UNIVERSIDADE BEIRA INTERIOR

Post-inflationary effects in primordial black hole formation and scalar-induced gravitational waves

Daniel del Corral Martínez

Tese para obtenção do Grau de Doutor em
Física
(3º ciclo de estudos)

Orientador: Prof. Doutor João Pedro de Jesus Marto
Co-orientador: Prof. Doutor Korumilli Sravan Kumar
Co-orientador: Prof. Doutor Javier Antonio Olmedo Nieto

Júri:
Prof. Doutor Paulo Jorge da Silva Almeida
Prof. Doutor Paulo Rodrigues Lima Vargas Moniz
Prof. Doutora Mar Bastero Gil
Prof. Doutor José Pedro Oliveira Mimoso
Prof. Doutor João Pedro de Jesus Marto
Prof. Doutor João Pedro Trancoso Gomes Rosa

28 de novembro de 2025

Declaração de Integridade

Eu, Daniel del Corral Martínez, que abaixo assino, estudante com o número de inscrição D3081 do curso de 3º ciclo em Física da Faculdade de Ciências, declaro ter desenvolvido o presente trabalho e elaborado o presente texto em total consonância com o **Código de Integridade da Universidade da Beira Interior**.

Mais concretamente afirmo não ter incorrido em qualquer das variedades de Fraude Académica, e que aqui declaro conhecer, que em particular atendi à exigida referenciação de frases, extratos, imagens e outras formas de trabalho intelectual, e assumindo assim na íntegra as responsabilidades da autoria.

Universidade da Beira Interior, Covilhã 26/06/2025

Firmado por DEL CORRAL MARTINEZ DANIEL - ***3014** el día 12/12/2025 con un certificado emitido por

(assinatura conforme Cartão de Cidadão ou preferencialmente assinatura digital no documento original se naquele mesmo formato)

I am grateful for the support of the grant UI/BD/151491/2021 from the Portuguese Agency Fundação para a Ciência e a Tecnologia. This research was funded by Fundação para a Ciência e a Tecnologia grant number UIDB/MAT/00212/2020

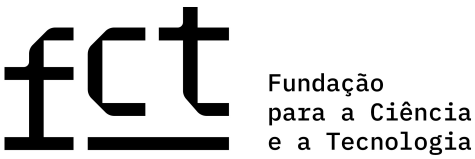

Acknowledgements

I would like to begin by expressing my deepest gratitude to my supervisor, João Marto, for his unconditional support and guidance throughout this journey. He has helped me not only academically but in every aspect of the PhD, always with patience, generosity, and dedication. I am truly grateful for all the things I have learned from him and for his constant encouragement and effectiveness during the most challenging moments.

My sincere thanks also go to my co-supervisor, K. Sravan Kumar, from whom I have gained invaluable insight into the research in physics and the publication of articles. His advice has been of great help, and I especially appreciated our scientific discussions, particularly during my stay in Portsmouth. The experiences and conversations we shared at the conferences "Spanish and Portuguese Relativity Meeting" and "Frontiers in Cosmology and Gravitational Physics" were truly enriching and had a lasting impact on my academic development.

I am especially thankful to both João and Sravan for their critical eye, thoughtful feedback, and patience, which consistently encouraged me to improve my work and approach problems with greater depth. Their guidance challenged me to grow as a researcher, and they always made me feel like a valued part of their team.

I would also like to warmly thank my other co-supervisor, Javier Olmedo, whose support during my Master's studies was crucial and naturally led to this PhD journey. His guidance during the early stages of the doctorate, as well as throughout the publication of my first article, was incredibly valuable and much appreciated. I would like to acknowledge and thank Professor Paolo Gondolo for the stimulating discussions on Primordial Black Holes. I learned a great deal from his explanations and truly enjoyed his way of sharing complex physics concepts with clarity and enthusiasm. My thanks also go to the University of Beira Interior for providing the resources and environment that made this research possible, and to the Fundação para a Ciência e a Tecnologia for the financial support through the research grant. Finally, I want to thank Professor Paulo Moniz for very useful comments on the preliminary document.

Resumo

Esta tese apresenta aspetos inéditos da formação de buracos negros primordiais (PBHs) a partir de instabilidades presentes no Universo primitivo, bem como da produção associada de ondas gravitacionais (OGs) induzidas. As principais contribuições inovadoras descritas neste trabalho são:

- A inclusão de efeitos significativos de perturbações em pequenas escalas que permanecem dentro do horizonte durante a inflação, frequentemente negligenciadas na literatura.
- Uma estimativa refinada da abundância de PBHs que vai além do formalismo padrão de Press-Schechter, incorporando a abordagem de Khlopov-Polnarev. Este último método, particularmente adequado para eras dominadas por matéria, captura efeitos cruciais como a supressão pela pressão e o impacto da não esfericidade na dinâmica das perturbações.

O foco principal recai sobre a fase de pré-aquecimento pós-inflacionária, predominantemente dominada por matéria, durante a qual o inflatão oscila em torno do mínimo de seu potencial antes de decair em partículas ultraleves (fase de reaquecimento). Essas oscilações induzem instabilidades paramétricas nas perturbações escalares por meio da equação de Mukhanov-Sasaki. Em particular, em pequenas escalas e com grandes desvios do potencial inflacionário em relação à forma quadrática, estas perturbações amplificam-se fortemente, podendo levar à formação de PBHs. Para caracterizar esse colapso de forma mais precisa, aplicamos três critérios complementares: (1) Os modos devem estar dentro de uma faixa de escalas específicas (banda de instabilidade) para serem afetados pelas instabilidades, (2) o tamanho físico dos modos deve ser maior do que o comprimento de Jeans, e (3) a definição de um limiar crítico baseado no tempo mínimo de colapso dessas perturbações. Cada um destes critérios permite melhorar a estimativa da fração de massa em PBHs.

As OGs induzidas, influenciadas por essas instabilidades em pequenas escalas por meio do acoplamento escalar-tensor de segunda ordem, apresentam uma amplificação rápida e significativa da densidade de energia em altas frequências. Adicionalmente, exploram-se as implicações de uma época de sobreprodução de PBHs e de dominação temporária da densidade de energia do Universo. Esta fase dominada por PBHs deixa também uma marca distintiva no espectro de OGs, fornecendo uma poderosa ferramenta para testar cenários com PBHs usando detetores atuais e futuros de ondas gravitacionais.

Estes resultados aprofundam a nossa compreensão da física do Universo primordial e abrem novas perspetivas para testar modelos inflacionários através da formação de PBHs e dos sinais de ondas gravitacionais.

Palavras-chave

Inflação, teoria de perturbações, pré-aquecimento, buracos negros primordiais, ondas gravitacionais, gravidade modificada

Abstract

This thesis explores new aspects of primordial black hole (PBH) formation from scalar perturbation instabilities in the early Universe and the associated production of induced gravitational waves (GWs). The key contributions of this thesis are:

- The inclusion of significant effects from small-scale perturbations that remain sub-horizon during inflation, which are often neglected in the literature.
- An alternative estimation to the standard Press–Schechter formalism for the PBH abundance is provided by the Khlopov–Polnarev formalism. This approach is particularly well-suited for inflaton matter-dominated era and accounts for critical effects such as pressure suppression and the influence of non-sphericity in the dynamics of perturbations.

The central focus is on the nearly matter-dominated post-inflationary preheating phase, where the inflaton oscillates at the minimum of its potential prior to its decay into ultra-light particles (reheating phase). These oscillations drive parametric instabilities in the scalar perturbations via the Mukhanov-Sasaki equation. Particularly, at small scales and with large deviations of the inflaton potential from a quadratic shape, these perturbations strongly amplify, potentially leading to PBH formation. To further characterize how these perturbations collapse into PBHs, we apply three complementary criteria: (1) the modes must lie within some specific range of scales (instability band) to be affected by the instabilities, (2) the physical size of the modes must be larger than the Jeans length and (3) a critical threshold based on the minimum time for collapse of these perturbations. Each of these criteria improves the estimation of the PBHs mass fraction.

The induced GWs, influenced by these small-scale instabilities through second-order scalar-tensor coupling, exhibit rapid and significant energy density amplification at high frequencies. Additionally, we explore the implications of an epoch of PBHs overproduction and the temporary domination of the energy density of the universe. This PBH-dominated phase also leaves a distinctive imprint on the GW spectrum, providing a powerful probe of PBH scenarios with current and future GW detectors.

These results enhance our understanding of early Universe physics and establish new avenues for testing inflationary models through PBH formation and gravitational wave signals.

Keywords

Inflation, perturbation theory, preheating, primordial black holes, gravitational waves, modified gravity

List of publications

This dissertation is based on the following publications:

[1] D. del Corral, P. Gondolo, K. Sravan Kumar, and J. Marto "Revisiting primordial black holes formation from preheating instabilities: the case of Starobinsky inflation", *JCAP* **02** (2025) 009, arXiv:2311.02754.

[2] D. del Corral "Self-resonance during preheating: The case of α-attractor models", *Annals Phys.*, vol. 470, p. 169824 (2024), arXiv:2406.04017.

[3] D. del Corral, P. Gondolo, K. Sravan Kumar, and J. Marto "Primordial black holes through preheating instabilities in α-attractor models" (2025), arXiv:2505.17790, *Submitted to a journal.*

[4] D. del Corral, P. Gondolo, K. Sravan Kumar, and J. Marto "Scalar-Induced Gravitational Waves from self-resonant preheating in α-attractor models" (2025), arXiv:2504.17602, *Submitted to a journal.*

[5] D. del Corral, K. Sravan Kumar, and J. Marto "Gravitational waves from primordial black hole dominance: The effect of inflaton decay rate", *Phys. Dark Univ.* **49** (2025) 101991, arXiv:2504.05875.

Other publications during these doctoral studies:

[6] D. del Corral and J. Olmedo, "Breaking of isospectrality of quasinormal modes in non-rotating loop quantum gravity black holes", *Phys. Rev. D*, vol. 105, no. 6, p. 064053 (2022), arXiv:2201.09584.

Contents

List of Abbreviations

CMB	Cosmic Microwave Background
GUTs	Grand unified theories
GR	General relativity
FLRW	Friedmann-Lemaître-Robertson-Walker
PBH	Primordial black holes
GWs	Gravitational waves
SIGWs	Scalar-induced gravitational waves
BBN	Big Bang Nucleosynthesis
DM	Dark matter
GGB	Galactic γ-ray background
EGB	Extragalactic γ-ray background
LSP	Lightest supersymmetric particles
EPTA	European Pulsar Timing Array
SKA	Square Kilometer Array
FAST	Five-hundred-meter Aperture Spherical radio telescope
LISA	Laser Interferometer Space Antenna
ASTROD-GW	Astrodynamical Space Test of Relativity using Optical Devices-Gravitational Wave
BBO	Big Bang Observer
DECIGO	Deci-hertz Interferometer Gravitational wave Observatory
ET	Einstein Telescope
KAGRA	Kamioka Gravitational Wave Detector
LIGO	Laser Interferometer Gravitational-Wave Observatory
OLS	Optically Levitated Sensor
BAW	Bulk Acoustic Wave
EDGES	Experiment to Detect the Global EoR Signature
ARCADE	Absolute Radiometer for Cosmology, Astrophysics, and Diffuse Emission
IAXO-SPD	International Axion Observatory (Single Photon Detectors)
IAXO-HET	International Axion Observatory (Heterodyne radio receivers)
IB	Instability band
MS	Mukhanov-Sasaki
PS	Press-Schechter
KP	Khlopov-Polnarev

1

Introduction

> *There never was a time when there was no motion, and there never will be a time when there will not be motion.*
>
> – Aristotle, *Physics (Book VIII)*

Aristotle viewed the universe as eternal, with no true beginning, governed by a continuous cycle and an "unmoved mover" that set it in motion. He saw the cosmos as without origin or end, reflecting a view of an eternal, unchanging order. In contrast, modern cosmology, through the Big Bang and Inflation theories, describes the early universe beginning in a well-defined initial state and evolving naturally into the cosmos we observe today. The study of the early universe is one of the cornerstones of physics, as it holds the key to the understanding of the origin and evolution of the cosmos.

1.1 The early universe

In 1915, Einstein formulated the field equations [7], which relate the geometry of spacetime to its matter content:

$$R_{\mu\nu} - \frac{1}{2} g_{\mu\nu} R = \frac{8\pi G}{c^4} T_{\mu\nu}. \tag{1.1}$$

Here, G is the gravitational constant, c is the speed of light, $R_{\mu\nu}$ and R denote the Ricci tensor and scalar, respectively, $g_{\mu\nu}$ is the metric tensor and $T_{\mu\nu}$ the energy-momentum tensor[1]. The left-hand side encodes spacetime curvature, whereas the right-hand side represents its energy content. In 1922, A. Friedmann showed that Einstein's equations naturally allowed for a dynamically evolving cosmos [8, 9], contrary to the static Universe model preferred by Einstein at that time. Friedmann found a solution to the Einstein equations that describes how the universe expands or contracts depending on its density, curvature, and energy content, which is known as the Friedmann equations. In 1927, and independently of Friedmann's work, G. Lemaître derived an expanding universe model based also on Einstein's Relativity and connected it to observations of galaxy redshifts [10]. Both proposed that the universe started from a small, dense state that has been

[1] Throughout the thesis we followed the metric signature $(-+++)$ and used the reduced Planck mass $M_{\rm Pl} = \sqrt{\frac{\hbar c}{8\pi G}} = 2.4 \times 10^{18}\text{GeV} = 4.34 \times 10^{-6}\text{g}$ with units of $\hbar = c = 1$.

expanding ever since. However, despite the profound implications of this idea, their work was unrecognized until E. Hubble's discovery in 1929, which provided direct observational evidence for an expanding universe. Using the 100-inch telescope at Mount Wilson Observatory, Hubble studied the emitted light from distant galaxies and found that they were receding from us. He formulated a relationship (Hubble's Law) showing that the velocity at which a galaxy moves away is directly proportional to its distance from us. This provided the first strong empirical evidence that the universe is expanding, validating the early works and ideas of Friedmann and Lemaître. H. P. Robertson and A. G. Walker also studied this problem in great detail during the 30's [11–14], offering a systematic classification of all possible metrics that are homogeneous and isotropic. Today, this result is known as the Friedmann-Lemaître-Robertson-Walker (FLRW) metric and describes an expanding, homogeneous, and isotropic universe. In spherical coordinates, the line element of the FLRW metric is given by

$$\mathrm{d}s^2 = -\mathrm{d}t^2 + a(t)\left[\frac{\mathrm{d}r^2}{1-kr^2} + r^2\mathrm{d}\theta + r^2\sin^2(\theta)\mathrm{d}\varphi^2\right], \tag{1.2}$$

where t represents cosmic time, $a(t)$ is the scale factor of the Universe, and $k = \pm 1, 0$ is the spatial curvature for a closed, open, or flat universe, respectively. This set a turning point in cosmology and paved the way for a theory of the origin of the Universe, what we know today as the Big Bang Theory[2]. But it was not until 1948 that these ideas came to solid grounds when G. Gamow, R. Alpher & R. Herman [15] predicted the existence of the cosmic microwave background radiation (CMB) as a remnant of this hot, dense, early stage, which was later discovered in 1965 by A. Penzias and R. W. Wilson [16]. In the early 70's, even before a concrete mechanism for generating fluctuations in the early Universe was known, E. Harrison and Y. Zeldovich independently proposed [17, 18] that the spectrum of these initial perturbations, a measure of their statistical distribution, should be scale-invariant. This assumption, based on simplicity and consistency with large-scale observations, led to what is now known as the Harrison-Zeldovich power spectrum. It describes a universe where fluctuations have equal amplitude on all logarithmic scales, an essential ingredient for the formation of cosmic structure. These precise discoveries, together with the development of Grand Unified Theories (GUTs) in the late 70's, posed several conceptual challenges to the Big Bang theory, such as:

- ***The horizon problem***: The observed statistical isotropy in the CMB suggests that regions of the universe separated by large distances share the same temperature. However, due to the finite nature of the speed of light, these regions should never have been in causal contact [19, 20].

[2]Actually, this name was coined by F. Hoyle, a defender of the Steady State theory. In a 1949 BBC radio broadcast, he mockingly referred to Lemaître's idea as the "Big Bang". However, despite Hoyle's skepticism, the term stuck and became widely accepted.

- ***The flatness problem***: The current density of the universe is close to the critical one for a flat ($k = 0$) geometry [20]. This seems to be an extremely rare situation without any deeper explanation.
- ***The magnetic monopole problem***: The Grand Unified Theories predict the production of magnetic monopoles in the early universe [21]. Yet, none have been observed.

Remarkably, a phase of exponential expansion (also known as de Sitter or inflationary expansion) preceding the Big Bang offers an elegant solution to these three cosmological problems. This idea can be realized through specific modifications to General Relativity (GR). In a pioneering work from the late 1970s, K. S. Stelle demonstrated that including curvature-squared terms such as R^2 renders gravity renormalizable [22, 23]. However, this approach introduces a massive tensor ghost, which violates unitarity. In response, various physicists explored alternative formulations, notably A. A. Starobinsky [24, 25]. In 1980, Starobinsky proposed a model in which the universe began in a highly symmetric state and, through the dynamics of an additional degree of freedom, evolved into the standard Big Bang cosmology [26]. This extra degree of freedom, known as the scalaron, naturally emerges in a renormalizable extension of gravity, often referred to as quadratic gravity [27, 28], which includes an R^2 term in the action. Unlike models that introduce a scalar field by hand, the Starobinsky theory of cosmic inflation is deeply rooted in the principles of quantum gravity, as the R^2 term arises from requiring that the theory is strictly renormalizable at high energy. By doing this, it avoids the use of parameters and recovers GR at low energies, still making strong predictions about the early universe. Moreover, the scalaron mass and the main inflationary observables (like the spectral index or the tensor-to-scalar ratio) seem to align well with the results from the Planck mission [29–31] (a space observatory that measured the cosmic microwave background with high precision). This primordial state can be described by a de Sitter phase, which represents a maximally symmetric spacetime that consists of a solution to the Einstein field equations in vacuum with a positive cosmological constant, effectively producing exponential expansion [26]. Yet, there was another challenge, such as the transition from the inflationary phase to the Big Bang expansion, often referred to as the "graceful exit of inflation". To address this, the cosmological expansion is presumed to be *almost* exponential, thereby defining a quasi-de Sitter spacetime. However, it was not until 1981 that A. Guth [32] unified all these ideas into a consistent framework of Cosmic Inflation. This was later addressed by A. Linde, who proposed in 1982 the New Inflation Theory [33], and established inflation as a compelling paradigm for the description of the early universe. Later in 1983, Linde proposed the Chaotic Inflation [34], which made Inflation a more generic theory.

During the inflationary phase, the scale factor of the universe increases nearly exponentially, and the Hubble rate, defined as $H(t) = \frac{\dot{a}}{a}$, remains almost constant. Here and in what follows, an overdot represents differentiation with respect to cosmic time t. The basic idea of Inflation is that the exponential expansion is driven by the potential energy of a

scalar field, which is introduced in Einstein's field equations either as a hypothetical matter field, called inflaton or, similar to Starobinsky's theory, as a modification of gravity, in which case it is called scalaron. Furthermore, inflationary cosmology naturally incorporates elements of quantum theory in the form of metric and matter fluctuations in the quasi-de Sitter expansion. The simplest model of inflation can be described by minimally coupling this scalar field to gravity through the following action

$$S = \int \mathrm{d}^4x\sqrt{-g}\left[\frac{M_{\mathrm{Pl}}^2}{2}R - \frac{1}{2}g^{\mu\nu}\partial_\mu\phi\partial_\nu\phi - V(\phi)\right], \tag{1.3}$$

where g is the determinant of the metric $g_{\mu\nu}$, ϕ is the scalar field, $V(\phi)$ its potential, and M_{Pl} the reduced Planck mass (see Footnote 1). Typically, we utilize the flat FLRW to characterize the spacetime during exponential expansion, as any initial deviation from a flat universe would be washed away by the inflationary expansion. To specifically reproduce such a period of exponential expansion, we need the potential term $V(\phi)$ to dominate over the kinetic term $\frac{1}{2}g^{\mu\nu}\partial_\mu\phi\partial_\nu\phi$, which is achieved by what is called slow-roll approximation, where the equation of motion of the field

$$\ddot{\phi} + 3H\dot{\phi} + \frac{\mathrm{d}V(\phi)}{\mathrm{d}\phi} = 0, \tag{1.4}$$

is simplified by neglecting higher-order derivatives such as $\ddot{\phi}$. The validity of this approximation is usually controlled by two slow-roll parameters, defined as [35]

$$\varepsilon = \frac{d}{dt}\left(\frac{1}{H}\right) = -\frac{\dot{H}}{H^2} \ll 1, \qquad \eta = \frac{\dot{\varepsilon}}{H\varepsilon} \ll 1, \tag{1.5}$$

where ε essentially measures the change in the Hubble horizon $1/H$ and η the change in ε. The smallness of these parameters (and thus the slow-roll approximation) is what characterizes the quasi-de Sitter spacetime. For exact de Sitter, the Hubble rate is constant, which implies $\varepsilon = \eta = 0$, and thus the universe never stops expanding exponentially. Therefore, $\varepsilon = 1$ and $|\eta| \sim 1$ constitutes the graceful exit of inflation. Under these assumptions, one can easily compute the power spectrum of curvature perturbations $\mathcal{R}$, defined as

$$\mathcal{P}_{\mathcal{R}}(k) \simeq \left.\frac{H^2}{8\pi^2\varepsilon M_{\mathrm{Pl}}^2}\right|_{k=aH}, \tag{1.6}$$

where k represents the wavenumber of the perturbation (in Fourier space) and the evaluation is performed at the moment each mode enters the Hubble radius $R_H = H^{-1}$, when the relation $k = aH$ holds. As anticipated earlier, these curvature perturbations, generated by quantum fluctuations of the inflaton during inflation, are the seeds of all large-scale structures and constitute one of the key observables from inflation. Appendix A shows the standard computations carried out during the inflationary phase to obtain the power spectrum of curvature perturbations. One can check that this power spectrum is al-

most scale-invariant, which is essentially what Harrison and Zeldovich observed, now explained within the inflationary context, but more importantly, it implies that all the scales experience the same expansion, a prediction of many inflationary models and one that is also consistent with observations of the CMB [29–31]. The power spectrum represents one of the key predictions of the inflationary theory and one of the most relevant concepts in cosmology. Furthermore, the theory of inflation has not only solved the observational challenges of the Big Bang model but also provided a framework for understanding the origin of cosmic structure: The quantum fluctuations of the scalar field during inflation were stretched to macroscopic scales, seeding the density perturbations that eventually grew into galaxies and large-scale structures, as studied by V. Mukhanov, G. Chibisov, and S. Hawking [36, 37] in the 80s.

After inflation, and in many single-field models, the scalar field reaches the minimum of its potential and begins to oscillate. At this point, exponential expansion halts and the universe transitions to a phase that is nearly matter-dominated, *i.e.* mainly characterized by an (averaged) negligible pressure. This period, called *preheating*[3], was first studied in the 90s by A. D. Dolgov, D. P. Kirilova, J. H. Traschen and R. H. Brandenberger [38–40] and some years later extended in the seminal papers of L. Koffman, Linde, and Starobinsky [41, 42], where the oscillations of the scalar field were found to lead to the growth of density perturbations through *parametric resonance*[4] [2, 43–46] that, under certain conditions, may collapse to form primordial black holes (PBHs). These black holes, believed to be formed in the early universe, are a powerful probe of the earliest moments of the universe, providing information about the conditions that prevailed immediately after inflation, and constitute one of the central elements of the thesis, see Section 1.2 for further details. The formation of PBHs during preheating can also leave behind imprints that may be detectable through gravitational wave (GW) signals. For instance, as density perturbations are amplified, they can generate scalar-induced gravitational waves (SIGWs) [47–50] which, although not necessarily, could serve as proof of the formation of PBHs. Moreover, PBHs can merge [51], cluster [52–56], accrete [57, 58], evaporate [45, 59], or dominate [60–63] the energy density budget of the Universe, producing also a characteristic signal in the form of GWs. These GWs, potentially detectable by future or even current high-frequency detectors, would provide a unique signature of the physics of the early universe and are therefore of particular interest. For this reason, it also constitutes one of the main focuses of this thesis, see Section 1.3 for further details. We will explore these PBH and GW effects through the remaining chapters of the thesis.

The preheating stage is not expected to be a long phase, since the Universe needs to transition into the standard hot and dense Big Bang picture. This is achieved by allowing

[3] Not to confuse with the reheating (radiation-dominated) period, defined below.

[4] The term *parametric resonance* originally referred to the scenario in which the inflaton field ϕ is coupled to an external field χ, such that the oscillations of ϕ backreact on the equation of motion for χ, leading to the exponential growth of its fluctuations and therefore to particle creation, as explained below. Today, parametric resonance more broadly describes the phenomenon wherein the oscillations of the inflaton at the bottom of its potential amplify perturbations through resonance effects.

the energy transfer from the oscillations of the inflaton into particles throughout a decay process into the Standard Model particles, a phase dubbed *reheating* [41] for obvious reasons. This process, in general, is extremely efficient, as shown in [42]. In the simplest model, where the inflaton couples to another scalar field χ through an interaction term $g^2\chi^2\phi^2$, the parametric resonance is very broad and occurs in a stochastic rather than regular manner, due to the rapid expansion of the universe causing phase decoherence between successive oscillations. Despite this stochasticity, the χ field fluctuations grow exponentially. Preheating evolves through distinct stages [42]: initially, particle backreaction is negligible, but it becomes significant later, increasing the oscillation frequency of the inflaton and enhancing particle production before ultimately terminating the resonance via rescattering processes. For a successful description of reheating, this decay has to occur at a temperature higher than 4 MeV so that the first elements start to form in a process called Big Bang Nucleosynthesis (BBN). If the temperature at which this decay occurs is lower, then it will spoil the abundance of light elements such as Hydrogen, Helium, or Lithium, of which we have accurate measurements. Therefore, the temperature limits the decay rates of the inflaton, which also has implications in the allowed abundance of PBHs [64, 65] or even in the energy density of GWs [66, 67] produced during preheating, as we will see in what follows.

Thesis synopsis

In this Section, we have provided a general overview of the early Universe, which serves as the background framework for our discussion. Several key phenomena occur in this context, as will be described in the following sections. However, before delving into the details, we present a schematic illustration of these effects in Fig. 1.1. The blue cone represents the growth of the universe, with classical time flowing from left to right and going through the different stages mentioned in this introduction (inflation, preheating, reheating, and BBN). The latter standard radiation and matter-dominated eras are not shown for simplicity, and the dark blue curves represent the production of GWs in three different scenarios. First, during preheating, these correspond to the amplification of perturbations via self-resonance (Chapter 3) that couple to the tensor perturbations at third-order in the perturbed expansion of the action and induce a background of GWs (Chapter 5). Then, the perturbations collapse into PBHs and, if these are produced abundantly, dominate the universe (PBH domination). In this scenario, the Poissonian energy-density fluctuations of the PBH fluid induce a gravitational potential that also produces a background of GWs (Chapter 6), similar to the preheating case. This phase ends with the Hawking evaporation of the PBHs, which also sources GWs and reheats the universe. These backgrounds of GWs travel unperturbed after reheating until today (represented by the wave-like blue curves) and potentially reach current and planned detectors. Below the blue cone, we represent the evolution of the density perturbations, shown as the wave-like red curves. During inflation, these are stretched to superhorizon scales, losing causal contact.

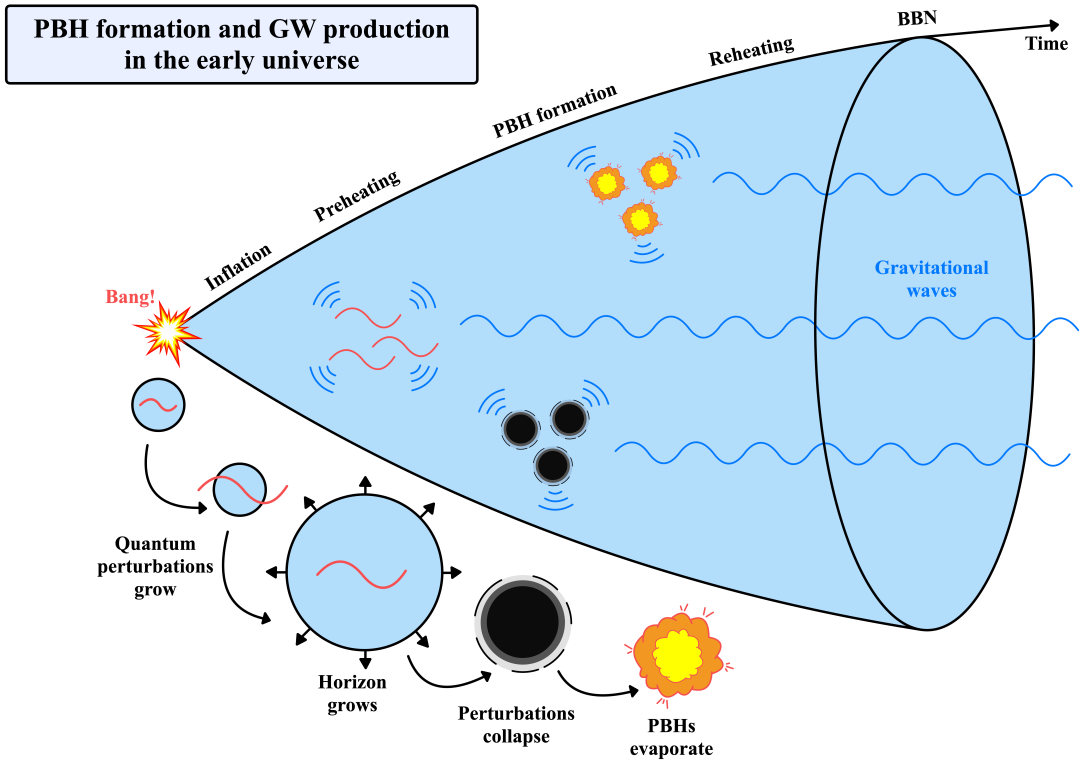

Figure 1.1: Scheme of the main new features studied in this thesis. The red curves represent the inflationary fluctuations that grow during inflation when the horizon (black circumference) remains fixed. These perturbations induce GWs (blue curves) via two different mechanisms: (1) during preheating by coupling to tensor perturbations, and (2) by collapsing into PBHs (black circles). The Hawking evaporation of PBHs also induces GWs, and in the three cases, these GWs propagate freely until today. The blue cone represents the growth of the universe, with time flowing from left to right. See text for details.

However, during preheating, the horizon (represented as a blue circle with black edges) grows and these perturbations enter the horizon, being affected by parametric resonance (Chapter 2) or self-resonance effects (Chapter 4), potentially collapsing into PBHs that ultimately evaporate via Hawking radiation. This scheme tries to encompass the main features of this investigation and therefore represents a heuristic picture of the universe in terms of perturbations and their associated effects. Furthermore, it ignores other effects and/or stages in the early universe. In the following two sections, we give further details about PBHs and GWs.

1.2 Primordial black holes: the birth of an idea

Usually, black holes are thought to have been theorized only after Einstein's GR. However, the concept of objects so dense that even light cannot escape from them can be traced back to the 18th century. In particular, John Michell's work [68], presented in the *Philosophical Transactions of the Royal Society of London* in 1783, introduced the idea of what he called *dark stars*. Building upon Newtonian gravity and the corpuscular theory of light,

Michell proposed that if a star were sufficiently massive, its escape velocity could exceed the speed of light, making it effectively invisible to an observer. Independently, Pierre-Simon Laplace reached a similar conclusion in his 1796 book *Exposition du Système du Monde* [69]. He demonstrated that as the radius of a celestial body contracts while its mass remains constant, its escape velocity increases. If this escape velocity exceeds the speed of light, the object will no longer emit detectable radiation. Despite their intriguing nature, these ideas were largely abandoned in the 19th century as the wave theory of light gained acceptance, casting doubt on whether gravity could influence electromagnetic waves.

It was not until the publication of Einstein's GR in 1915 [7] that gravity was redefined as the curvature of spacetime rather than a force, marking a significant departure from Newtonian gravity. Shortly after, K. Schwarzschild discovered the first exact solution to Einstein's field equations [70]. This solution describes the spacetime around a spherically symmetric, non-rotating, uncharged mass in a vacuum. At first glance, Schwarzschild's metric describes any isolated massive object, such as a star or a planet. However, a fundamental aspect of this solution is the existence of a critical radius, now known as the Schwarzschild radius:

$$r_S = \frac{2GM}{c^2}, \tag{1.7}$$

where M is the mass of the object. If the mass of an object is confined within this radius, an event horizon forms, beyond which any form of matter and light cannot escape[5]. This corresponds to the modern realization of Michell's dark star, now better understood within the framework of GR. Further developments came in 1939 when R. Oppenheimer and H. Snyder [72] revisited Schwarzschild's solution and demonstrated that a sufficiently massive star, upon exhausting its nuclear fuel, could undergo gravitational collapse to form a singularity[6]. However, at the time, the implications of this result were not fully appreciated, and many physicists regarded such objects as mere mathematical artifacts rather than physical entities. This also occurred for another exact solution to the Einstein equations, found in 1963 by R. P. Kerr [73]. The Kerr solution describes the geometry of spacetime around a rotating object, a much more realistic model than the non-rotating Schwarzschild black hole. In fact, most black holes observed in X-ray binaries or active galactic nuclei are rotating.

The term *black hole* was not introduced until 1967 by J. A. Wheeler, as interest in the subject resurged due to R. Penrose's singularity theorem [74]. The theorem provided the

[5] In this sense, a black hole is a particular case of the Schwarzschild metric; a concept usually misunderstood in the literature. This is related to Birkhoff's theorem [71], which states that any spherically symmetric solution of the vacuum Einstein field equations must be static and asymptotically flat, and is uniquely given by the Schwarzschild solution.

[6] We remark here that the star must be massive enough so that no known force can stop the collapse. Otherwise, gravitational collapse can be halted by electron degeneracy pressure, leading to the formation of a white dwarf, or, for more massive stars, by neutron degeneracy pressure, resulting in a neutron star.

first rigorous, general proof that singularities were not merely a peculiarity of special symmetric solutions but rather a fundamental feature of GR. This result was later extended to cosmological scenarios in collaboration with Hawking in 1970 [75], clearing doubts about the physical existence of black holes and providing strong theoretical evidence for their formation in nature.

In 1971, Hawking proposed that black holes could also have formed in the early universe [76], an idea that had first been explored in 1967 by Y. Zeldovich and I. Novikov [77]. Initially, they argued that such PBHs could not exist, as they would have accreted mass at extreme rates, rapidly reaching masses on the order of $10^{17} M_\odot$, which would be inconsistent with observations. However, their analysis ignored the role of the expansion of the universe, an aspect that significantly suppresses accretion. This issue was addressed in 1974 by B. Carr and Hawking [78], who demonstrated that in General Relativity, there is no self-similar solution in which a black hole can grow at the same rate as the cosmic horizon. Furthermore, they systematically analyzed how density perturbations in the early universe could give rise to small black holes, showing that if the overdensity in a region exceeded a critical threshold, it would collapse into a black hole rather than expanding with the universe. This clever idea laid the foundation for the concept of PBHs, and it is still nowadays the standard criterion used in the literature to determine whether or not PBHs can form. Although the precise estimation of the threshold is determined from the specific details of the model, as we show next, it constitutes the first of the three criteria we employ in the selection of perturbations able to collapse.

Fluctuations are usually characterized by the density contrast $\delta_{\boldsymbol{k}} = \delta\rho_{\boldsymbol{k}}/\rho$, where $\delta\rho_{\boldsymbol{k}}$ is the density perturbation and ρ the background energy density. The suffix "$_{\boldsymbol{k}}$" indicates we are working with the Fourier components, where $\boldsymbol{k}$ is the wavenumber vector and k is its modulus. As said above, the formation of PBHs depends on whether these perturbations exceed a characteristic threshold δ_c. This, in a medium with an equation of state $p = w\rho$, is approximately w, which in essence defines what is known as Carr's criterion [79] for perturbations

$$\delta_c \simeq w. \tag{1.8}$$

It is mainly based on the Jeans length criterion, which establishes the minimum amplitude the fluctuation must have so that gravity can counteract pressure and therefore collapse. Additionally, since PBHs form before BBN, they behave as non-baryonic objects and can span a vast range of masses, from the Planck mass ($M_{\rm Pl} \sim 10^{-5}$g) onwards[7], unlike astrophysical black holes that form from stellar collapse and thus have masses $\gtrsim M_\odot$. Since the rate of accretion of a black hole depends on its mass, this implies that PBHs, in general[8],

[7] Initially, the lower mass limit for PBHs was thought to be the Planck mass, but with the advent of inflationary cosmology in the 1980s, this limit shifted to approximately 10 g, corresponding to the energy density at the end of inflation. Any PBHs forming before this time would have been exponentially diluted by inflation, making their abundance negligible.

[8] The accretion rate depends both on the PBH mass and the density of the surrounding medium. A smaller

do not accrete enough to reach masses of the order of the solar mass [57,58], and therefore typically retain the mass they had at the time of formation. This is a crucial aspect as it allows us to relate the mass of the PBHs with the time of formation, since the typical mass of a PBH is determined by the Hubble horizon mass at the time the perturbation reenters the horizon, given by:

$$M = \gamma M_H. \tag{1.9}$$

Here, γ quantifies the fraction of the horizon mass that ends up in the PBH, which varies depending on the model and the equation of state of the universe at the moment of collapse, but usually is taken to be of order $\mathcal{O}(1)$. In this sense, the earlier the period we consider, the smaller the PBHs that can be formed. Thus, the study of post-inflationary scenarios, such as preheating, involves very small PBHs of 10^{15}g or less.

Another way of characterizing PBHs is through their abundance, usually estimated via the mass fraction. This is represented by $\beta(k)$, and defined as

$$\beta(k) = \frac{\mathrm{d}\Omega_{\mathrm{PBH}}(k)}{\mathrm{d}\ln M}, \tag{1.10}$$

where $\Omega_{\mathrm{PBH}} = \rho_{\mathrm{PBH}}/\rho$ is the fractional energy density of PBHs, that is, the fraction of the energy density in PBHs, ρ_{PBH}, with respect to the total energy density ρ. The mass fraction $\beta(k)$ represents the fraction of the total mass in the form of PBHs per logarithmic mass interval. Given some realization of the density field, the computation of the mass fraction usually relies on (1) the identification of the regions where the perturbation can potentially collapse and (2) the associated probability of collapse, that is, $\beta(k)$ itself [81]. The first question is difficult to tackle without using some approximations. Usually, one can consider the threshold criterion (1.8). The second question is typically addressed using the standard statistical *Press-Schechter* (PS) formalism [82], originally developed in 1973 for structure formation. This framework provided the first quantitative predictions for PBH formation and has since played a crucial role in evaluating their potential abundance and astrophysical consequences. After this, more formalisms followed, such as the *Khlopov-Polnarev* (KP) one, as we will see next. These two formalisms, along with their mathematical details, are detailed Appendices B.1 and B.2, as they constitute the two main mass fraction approaches used in this thesis.

The concept of small black holes captured Hawking's attention and motivated him to investigate their quantum properties. This led, in 1974, to his groundbreaking discovery: *Hawking radiation* [83]. Hawking demonstrated that black holes would not be entirely black, but instead they could emit thermal radiation due to quantum effects near the event

black hole embedded in a dense environment can, in principle, accrete efficiently, although a large sound speed in such media suppresses the inflow because gas pressure counteracts gravitational attraction. Recent numerical-relativity simulations [80] show that even when primordial black holes form with non-negligible initial spin, subsequent accretion of non-rotating background matter efficiently reduces their dimensionless spin, illustrating how sensitive PBH evolution is to the properties of the ambient medium.

horizon. This implied that black holes would lose mass over time and eventually "evaporate" on a characteristic timescale given by:

$$\tau \sim 10^{64} \left(\frac{M}{M_\odot} \right)^3 \text{s}. \tag{1.11}$$

Hawking radiation, although still highly theoretical, is widely regarded as one of the most profound discoveries of 20th-century physics, as it elegantly combines general relativity, quantum mechanics, and thermodynamics. Prior to Hawking's work, related ideas had been explored. For instance, Zeldovich proposed in 1971 that a rotating absorbing body could amplify incident electromagnetic waves, thereby extracting energy from its rotation [84]. This phenomenon, now known as *superradiance*, was later extended to rotating black holes. Building on this, Starobinsky in 1973 investigated the amplification of waves scattered by rotating black holes and discussed the possibility of a quantum analog involving spontaneous particle creation [85]. While not equivalent to Hawking radiation, these earlier insights laid important conceptual groundwork for understanding quantum processes in strong gravitational fields.

On the other hand, Hawking radiation implies that PBHs with masses below 10^{15} g (which we referred to as evaporating PBHs) would have fully evaporated by the present day, making direct detection at present impossible. This includes, for instance, PBHs formed during preheating. Nevertheless, based on the effects of Hawking radiation, their existence can still be constrained through a pair of indirect observational methods. The first such approach was proposed in 1976 by D. Page and Hawking [86], who noted that PBHs with masses near 10^{15}g would emit photons with characteristic energies of around 100 MeV. This insight led to the idea of using constraints on the extragalactic γ-ray background to limit their abundance. Their analysis showed that the fraction of the universe's energy density contained in PBHs of this mass must be below 10^{-8} times the critical density, significantly limiting their potential contribution to dark matter (DM). However, for lower-mass evaporating PBHs, these constraints are less stringent, allowing for a higher abundance. This idea was further developed in 1979 by Novikov *et al.* [87], who compiled various constraints on PBH evaporation across different mass ranges. In particular, evaporating PBHs can emit high-energy particles that affect the CMB and may alter the production of light elements during BBN [88, 89]. These constraints are illustrated in Fig. 1.2a, which shows, for example, that the abundance of PBHs is tightly constrained to be less than $\beta \simeq 10^{-25}$ for $M_{\text{PBH}} \simeq 10^{15}$ g. The second indirect method for probing evaporating PBHs arises from the *black hole information paradox* [90], formulated by Hawking in 1976. The paradox stems from the fact that Hawking radiation is a thermal process, meaning the emitted radiation is entirely random and carries no information about the matter that formed the black hole. If a black hole evaporates completely, the information it contained would be irretrievably lost, violating the principles of quantum mechanics. This paradox sparked extensive debate and inspired further theoretical investigations.

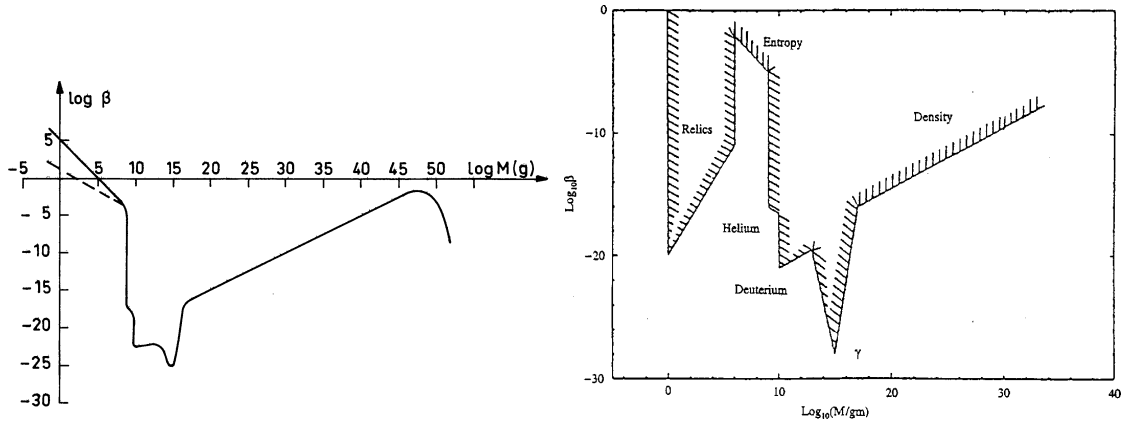

(a) **(b)**

Figure 1.2: Constraints on the abundance of PBHs from **(a)** 1979 and **(b)** 1994 (Refs. [87, 91], respectively) as a function of the masses of the PBHs. The quantity β represents the mass fraction of PBHs.

In subsequent years, researchers proposed possible resolutions to the paradox, including the idea that black holes might leave behind stable Planck-scale remnants. Works by M. A. Markov and P. C. West [92] and J. H. MacGibbon and Carr [93], suggested that as a black hole evaporates down to the Planck mass scale ($M_{\rm Pl} \sim 10^{-5}$g, $l_{\rm Pl} \sim 10^{-33}$cm), quantum gravity effects could prevent complete Hawking evaporation, leaving behind a small remnant that keeps the lost information. This possibility introduced a novel approach to constraining evaporating PBHs, as these remnants could contribute to DM. Further works [91, 94] extended these ideas and refined previous constraints, modifying the limits originally proposed by Novikov *et al.*, as illustrated in Fig. 1.2b. These developments demonstrated that Hawking radiation not only provided a theoretical foundation for PBH Hawking evaporation but also offered practical avenues for their detection and constraints on their abundance. Note that the argument in favor of black hole remnants, though said to be motivated by quantum gravity theories, emerges from multiple ad hoc assumptions to resolve the information paradox. Alternatively, recent investigations of a unitary formulation of quantum field theory in curved spacetime in consideration with gravitational backreaction effects offer a potential resolution to the information paradox at the foundational level [95, 96].

PBHs gained renewed interest following the development of the theory of inflation in the early 1980s. As shown in Section 1.1, inflation predicts that quantum fluctuations in the early universe generate density perturbations, which, upon horizon re-entry, could become sufficiently overdense to collapse into PBHs. This may provide a mechanism for PBH formation. In fact, inflationary models can be constrained by requiring that they do not overproduce PBHs, as different models predict different PBH mass spectra. This allows PBHs again to serve as unique probes of the early universe [97], even if they are not detected. Consequently, after the development of inflation, evaporating PBHs were no longer seen merely as relics but as potential tracers of inflationary physics.

The amplitude of primordial fluctuations at CMB scales is approximately constrained to

$\delta_k \sim 10^{-5}$. This value is too low to lead to significant PBH formation on those scales. Therefore, for PBHs to form in appreciable numbers, one of these two conditions must be met: either the power spectrum of fluctuations has a blue tilt, meaning it increases towards smaller scales [98], or it features a sharp peak at some sub-CMB scale, where constraints on the power spectrum are weaker. In the standard literature, the latter scenario can be realized if a period of ultra-slow-roll expansion occurs during inflation, leading to a drastic amplification of perturbations around a particular scale. This possibility was explored in detail by P. Ivanov *et. al.* in 1994 [99] and summarized as follows. In inflationary models where the potential contains an intermediate plateau, the inflaton field slows down significantly while traversing this region. As a result, its velocity $\dot{\phi}$ decreases sharply, leading to a corresponding reduction in the first slow-roll parameter ε. Now, since ε is related to the inflaton velocity through

$$\varepsilon = \frac{\dot{\phi}^2}{2H^2 M_{\rm Pl}^2}, \tag{1.12}$$

a small value of ε implies a significant enhancement in the power spectrum at the scales that exit the horizon during this phase, see Eqn. (1.6). This amplification increases the probability of PBH formation at those specific scales. Following Ivanov's pioneering work, numerous alternative mechanisms have been proposed to generate PBHs through inflationary dynamics, including features in the potential, phase transitions, and non-standard reheating scenarios. For a comprehensive review of these mechanisms, see [100]. However, in this thesis, we focus on a non-standard approach that considers the amplification of perturbations during preheating, due to instabilities produced from the oscillations of the inflaton at the bottom of the potential. Although this is a common feature in many single-field inflationary models, it has not received much attention in the literature. This last method is explained in Chapters 2, 3, and 4, whereas the standard inflation-amplified perturbations scenario is studied in Chapter 6.

Although out of the scope of this thesis, massive ($\gtrsim 10^{15}$g) PBHs are also interesting from the point of view of large-scale structure. This was motivated by the works of Mukhanov and Chibisov (1981) and Hawking (1982) [36, 37], where it was proposed that massive PBHs formed in the early universe could act as gravitational seeds for the rapid accumulation of matter. These PBHs would grow by accreting surrounding gas and merging with other black holes, potentially reaching supermassive scales over cosmic time [101–103]. This mechanism provides a natural explanation for the formation of supermassive black holes (SMBHs) at high redshifts. However, recent observations from the *James Webb Space Telescope* (JWST) have posed new challenges to our understanding of early SMBH formation. JWST has identified SMBHs [104, 105] and quasars [106, 107] at redshifts $z \simeq 8.5-10.6$, corresponding to roughly 500 million years after the Big Bang. The inferred masses of these objects appear to be too large for their formation epoch, given conventional models of black hole growth through standard Eddington-limited accretion [108]. These findings suggest that alternative scenarios, such as the direct collapse of smaller

primordial black holes into SMBHs or periods of super-Eddington accretion, may be required to explain the existence of such massive objects at such early times. An additional, often-overlooked possibility is that SMBHs may originate from the collapse of "dark stars," hypothetical early-universe stars powered by dark matter annihilation rather than nuclear fusion [109–111].

The interest in PBHs continued to grow in the late 1990s and early 2000s due to their potential role in explaining DM. PBHs naturally exhibit properties compatible with DM: they are non-luminous, non-baryonic, and stable over cosmological timescales. Consequently, during this epoch, PBHs started to attract attention among traditional dark matter candidates, such as weakly interacting massive particles and axions, even though interest in PBHs as DM had existed since the early days. During this period, PBH formation mechanisms were studied in greater detail. A significant breakthrough came from M. W. Choptuik's discovery of critical phenomena in gravitational collapse [112], which showed that the mass of a black hole depends on the amplitude of the perturbation from which it forms, following the scaling relation:

$$M = M_H \kappa (\delta_{\boldsymbol{k}} - \delta_c)^{\gamma}, \tag{1.13}$$

where γ is a coefficient dependent on the equation of state and κ depends on the model. This result was further explored through numerical studies by the works of J. C. Niemeyer and K. Jedamzik [113,114], who computed the resulting PBH mass function, and by I. Musco *et. al.* [115–117], who verified the mass scaling behavior for small $(\delta_{\boldsymbol{k}} - \delta_c)$ and studied a range of equation-of-state parameters ($0 < w < 0.6$). However, an important remark must be done here. This method applies to $(\delta_{\boldsymbol{k}} - \delta_c) \ll 1$, which is called critical regime, whereas for $(\delta_{\boldsymbol{k}} - \delta_c) \gtrsim 1$, perturbations enter the super-critical regime, where this estimation fails.

In 2013, T. Harada *et al.* [118] refined the old threshold estimation from Carr ($\delta_c \simeq w$) by deriving a new analytical formula based on more solid physical arguments. Their formula expresses the threshold as a function of the parameter of the equation of state. It is given by:

$$\delta_c = \frac{3(1+w)}{5+3w} \sin^2\left(\frac{\pi\sqrt{w}}{1+3w}\right). \tag{1.14}$$

This result (and Carr's criterion) revealed that in a pressureless universe ($w = 0$), the threshold vanishes, largely increasing the probability of PBH formation. However, this special case required further investigation, leading to subsequent studies by Harada *et al.* in 2016 and 2017 [119, 120], which built upon earlier works by M. Y. Khlopov and A. G. Polnarev from the 1980s [121–125]. They demonstrated that in a matter-dominated era ($w = 0$), pressure is negligible in preventing collapse. However, in realistic scenarios, non-spherical effects such as inhomogeneities, anisotropies, or angular momentum play a crucial role in halting collapse. Otherwise, perfectly spherical overdense regions would

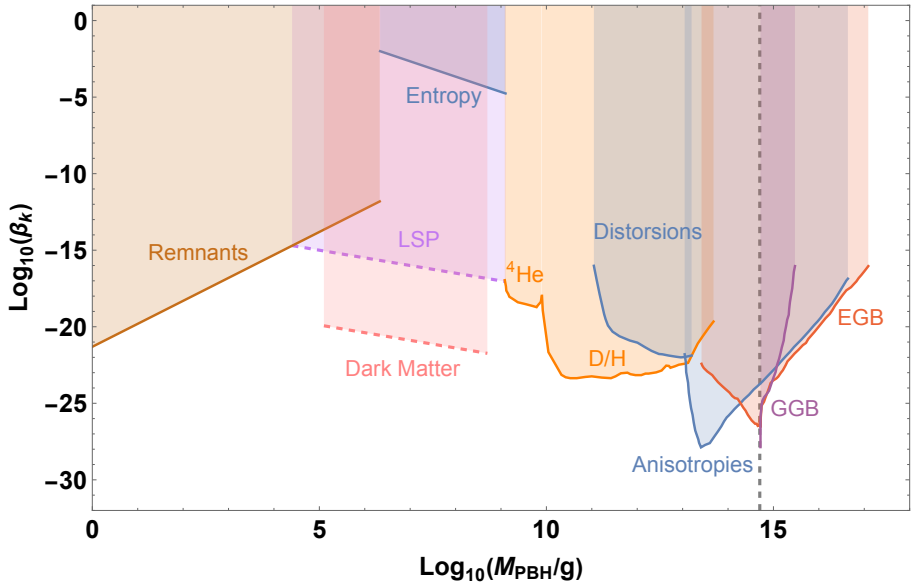

Figure 1.3: Constraints on the abundance of PBHs adapted from Refs. [126, 127] in 2020 as a function of the masses of the PBHs. The quantity β represents the mass fraction, and the vertical dashed line at $\sim 10^{15}$g is the critical mass below which PBHs should have been evaporated by now. These constraints are based on standard cosmologies, which assume that following inflation, there is the standard radiation-domination phase. See [128] for updated constraints that assume non-standard cosmologies, such as an early matter-dominated phase.

readily form black holes. This necessitated a modification of the standard PS formalism, leading to what is now known as the KP formalism, which is particularly relevant for PBH formation during the preheating phase, an aspect explored in subsequent chapters. For mathematical details about the derivation of the KP formalism, see Appendix B.2.

Studies on PBH Hawking evaporation effects also intensified during this period, leading to refined and new constraints, as shown in Fig. 1.3. Particularly significant were the improved constraints of CMB effects (entropy increase, distortions, and anisotropies) [129–131], as well as the update on the γ-ray limits. These last were further categorized into galactic and extragalactic backgrounds, labeled GGB and EGB in Fig. 1.3. Additionally, constraints from BBN were improved, placing stringent bounds on evaporating PBHs and their effects on the ^{4}He and ^{2}D abundances [64, 131]. Further, new constraints based on particle production from Hawking evaporation were added. This is the case of the lightest supersymmetric particles (LSP) [132], motivated by theories beyond the standard model, and dark matter [127]. For a comprehensive description of each of these constraints, see Chapter 4.

Since in this thesis we mainly focus on the production of PBHs from the collapse of perturbations during the preheating stage, we describe schematically this scenario in Fig. 1.4. In the upper panel, we show the evolution of some representative comoving scales. Particularly, the *instability band* (IB) is the range of k where the instabilities occur and the density contrast δ_k grows. It constitutes the second of the criteria we employ for the determination of the perturbations that can collapse, the first one being the threshold criterion

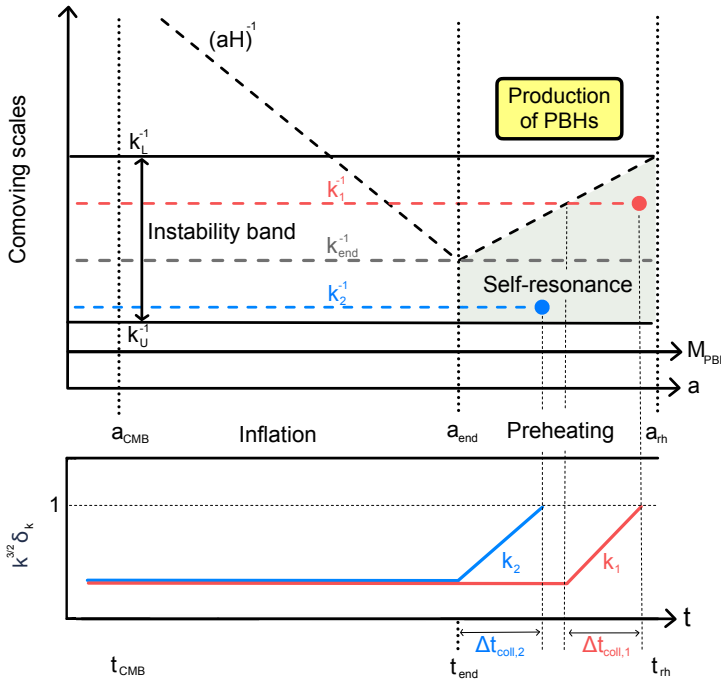

Figure 1.4: Schematic representation of the collapse of perturbations into PBHs during preheating due to instabilities in the scalar perturbations. The upper panel shows some particular comoving scales involved, and the lower panel shows the evolution of the density contrast associated with two particular scales.

defined above. Essentially, the IB corresponds to the range between two characteristic scales: k_L (lower) and k_U (upper). The lower bound, k_L, corresponds to the last mode entering the horizon during preheating and is defined as $k_L = a(t_{\rm rh})H(t_{\rm rh})$, where $t_{\rm rh}$ marks the end of the preheating phase. The upper bound, k_U, denotes the largest mode affected by self-resonance and is determined using Floquet theory [2]. For a sufficiently long preheating, the inflationary potential can be approximated by a parabola, so that k_U can be defined as follows [45]

$$\left(\frac{k_U}{a}\right)^{-1} = \frac{1}{M}\left(\frac{2}{3\phi_{\rm end}}\left(\frac{a}{a_{\rm end}}\right)^3\right)^{1/4}. \tag{1.15}$$

Here M is the mass of the scalar field ϕ, and the suffix "$_{\rm end}$" stands for evaluation at the end of inflation. Also shown for comparison is the scale $k_{\rm end} = a(t_{\rm end})H(t_{\rm end})$, defined as the last scale to exit the horizon during inflation. Amplification is assumed to occur as soon as a mode enters the IB, which is the region labeled self-resonance (green-shaded area) in Fig. 1.4. Also shown as an example are the two scales k_1 (red) and k_2 (blue). The former enters the IB after the end of inflation, whereas the latter is already inside by the end of inflation. Once inside the IB, their density contrast (plotted in the lower panel) grows until it reaches non-linearity in a time $\Delta t_{\rm coll}$. If the time they spent growing inside the IB is long enough so that the collapse occurs during preheating, *i.e.* $\delta_{\boldsymbol{k}} > \delta_c(k)$, then we say

that the mode has collapsed into a PBH (represented by a circle). The reason behind this amplification essentially resides in the mathematical structure of the Mukhanov-Sasaki (MS) equation, whose derivation is detailed in Appendix. A.2. Basically, the MS equation is a wave equation, and instabilities in the MS variable, $v_{\boldsymbol{k}}$, occur when $k^2 \simeq z''/z$, where z is given by $z = a\sqrt{2\varepsilon}M_{\rm Pl}$. The MS variable, as shown through Eqns. (A.11), (A.14), and (A.16) is directly related to $\delta_{\boldsymbol{k}}$, implying that their instabilities are carried into the density contrast. Still, there is one last criterion we employ to select the perturbations that can collapse. As shown in Appendix A.4, the fluctuations that could lead to a collapse into PBHs are the ones whose physical wavelengths are larger than the Jeans length. If this is the case, the modes evolve by gravitational collapse instead of developing acoustic oscillations. This constitutes our last criterion to select the perturbations that can collapse, which we summarize in what follows:

- ***Density Contrast Criterion:*** The density contrast $\delta_{\boldsymbol{k}}$ must exceed the threshold $\delta_c(k)$, to allow for the collapse of perturbations into PBHs. This threshold depends on the specific model under consideration.
- ***Instability Band Criterion:*** Modes must lie within the IB to be affected by the instabilities that favor the collapse.
- ***Jeans Length Criterion:*** The physical wavelength of the modes must be larger than the Jeans length to ensure that during the collapse, the pressure does not counteract gravity. The speed of sound and its derivation can be found in Appendix A.4.

During this whole dissertation, these three criteria are taken into account when considering the collapse of perturbations into PBHs. For more details about instabilities during preheating and their collapse, see Chapters 2 and 3. To conclude the discussion on PBHs, Table 1.1 summarizes the main differences between astrophysical and primordial black holes. Still, an essential aspect of PBH physics remains to be explored: their connection to gravitational waves. This topic is addressed in the next section.

1.3 Gravitational Waves: A window to the early universe

Before Einstein's GR, there were some attempts to describe GWs as an analog to electromagnetic waves, as shown by the works of O. Heaviside and H. Poincaré [133–136]. These were based on Maxwell's electromagnetic theory, which treats the electric and magnetic fields separately, and on Newton's gravitation, where gravity is assumed to propagate at infinite speed. Under these assumptions, a successful treatment of GWs is not possible.

Maxwell unified electricity and magnetism into a single classical electromagnetic theory in the 19th century, showing that electric and magnetic fields are interrelated components of the electromagnetic field. Building on this, Einstein's 1905 theory of special relativity [137] revealed that electric and magnetic fields transform into each other depending on

Feature	Astrophysical black hole	Primordial black hole
Time of formation	After the first generation of stars (200 million years after the Big Bang)	Early universe (before recombination)
Formation mechanism	Stellar collapse	Collapse of primordial density fluctuations
Mass range	Stellar ($1M_\odot$) to supermassive ($10^{12}M_\odot$)	From $\sim$ 1g onwards
Role in cosmology	Final state of massive stars	Potential dark matter candidates, supermassive BHs at high redshift
Hawking radiation	Negligible	Significant for $M_{\rm PBH} < 10^{15}g$, leading to Hawking evaporation
Accretion rates	Significant, forming bright accretion disks	Negligible or compared to mass loss from Hawking evaporation
Detection methods	Gravitational lensing, X-rays, gravitational waves	Microlensing, γ-ray, Hawking radiation signatures

Table 1.1: Summary of differences between astrophysical and primordial black holes.

the observer's motion, demonstrating their unity from a relativistic standpoint. However, after proposing his principle of equivalence in 1907 [138], Einstein recognized that special relativity could not be straightforwardly extended to include gravity, motivating the development of GR in 1915 [7]. After this, he thought, just as Poincaré did, that there could be gravitational waves similar to electromagnetic waves. However, in the electromagnetic case, what is usually found is dipole radiation, produced by the oscillations of two (positive and negative) electric charges, which generate electromagnetic waves. In the gravitational case, this analogy breaks down since there are no negative masses. This failure of the analogy made Einstein remain skeptical about GWs, as he wrote in a letter to Schwarzschild in 1916: "*There are no gravitational waves analogous to light waves*". However, a few months later, he published the work "*Approximate Integration of the Field Equations of Gravitation*" [139], where he predicted GWs and (incorrectly) monopole radiation. It was G. Nordström who pointed out Einstein's mistake and led him to correct it in 1918 [140]: gravitational waves are of a type technically known as quadrupole radiation, which makes them incredibly weak. This, added to the inherent weakness of the gravitational force, caused Einstein to remain skeptical about the reality of GWs. Further, this work was made under some approximations, which he revised in 1936 in a work with N. Rosen [141], arguing that the fully developed equations of the theory proved that GWs could not exist after all. However, as pointed out by I. Robinson, this conclusion was made under a poor choice of coordinates, showing that Einstein and Rosen correctly proved the prediction of GWs. Despite all these events, this was not enough for Einstein, who still refused to believe in the existence of GWs. He thought that, even if GWs were real, they would be so faint and their interaction with matter so weak that they would never be detected. Much less useful enough for science.

The skepticism rubbed off on the scientific community until Einstein died in 1955. After that, the seminal work of F. A. E. Pirani [142] in 1956 changed the general thought. He developed a mathematical formalism for the deduction of physically observable quantities, such as the Riemann curvature tensor, applicable to gravitational waves. This turned the attention toward the idea of whether or not GWs carry energy and thus if they could be detected, which was discussed at the Chapel Hill conference in 1957. This conference played a central role in the future development of classical and quantum Gravity and many of the ideas discussed there are still up for debate nowadays. Motivated by this conference, J. Weber, one of the attendees, proposed in 1960 [143] the first device for GWs based on the vibrations they induce in a mechanical system, a sort of "antenna" that was completed in 1966. Although several detectors were built across the globe, none detected a clear GW signal, producing some kind of disappointment in the scientific community. However, hope was raised with the first indirect detection of GWs in 1974 by J. H. Taylor and R. A. Hulse. They discovered a binary pulsar that was radiating gravitational energy, confirming the prediction of Einstein's GR. The announcement of the detection of gravitational radiation was not made until 1979 [144], which led them to win the Nobel Prize in Physics in 1993. Also in 1979, Starobinsky [145] predicted for the first time a nearly scale-invariant spectrum of relic GWs generated by quantum effects during a quasi-de Sitter phase of the early universe, laying the foundation for the modern search for stochastic GW backgrounds (GWBs). From this year on, the construction of new GW detectors was proposed. Among them, the most promising ones were the ones based on laser interferometry, such as the European Virgo and American LIGO collaborations, whose constructions began in 1993 and 1994, and started acquiring data in 2003 and 2002, respectively. These detectors joined in 2007 in a collaborative search for GWs, but again, none of these detectors reported any observation of GWs, and in 2011, both were shut down for some improvements. LIGO finished its improvements in February 2015, and by September of the same year, the first direct observation of a GW was made [146], which came from a pair of 30 solar-mass black holes orbiting around their common center of mass, slowly coming together and releasing gravitational energy. The peak of the signal was the end of this event when both black holes merged in the inspiral process. In 2017, Virgo also finished their improvements, and some months later, the LIGO-Virgo collaboration reported the first detection of GWs [147], also coming from a binary black hole merger. These two groundbreaking detections enabled Wiss, Thorne, and Barish to win the Nobel Prize in Physics in 2017 for their contribution to the detection of GWs. Further, in 2020, the Japanese KAGRA detector joined the LIGO-Virgo collaboration (from now on LVK collaboration). These three detectors operate on the High-Frequency Band (HF, 10 Hz-100 kHz) of the spectrum (see [148] for the classification of GWs in terms of their frequency), and thus they are restricted to GWs on that frequency range. This limitation arises mainly because detecting lower frequencies requires larger detectors, which already span 3–4 km for the LVK collaboration.

In 2016, the International Pulsar Timing Array (IPTA) collaboration released its first mea-

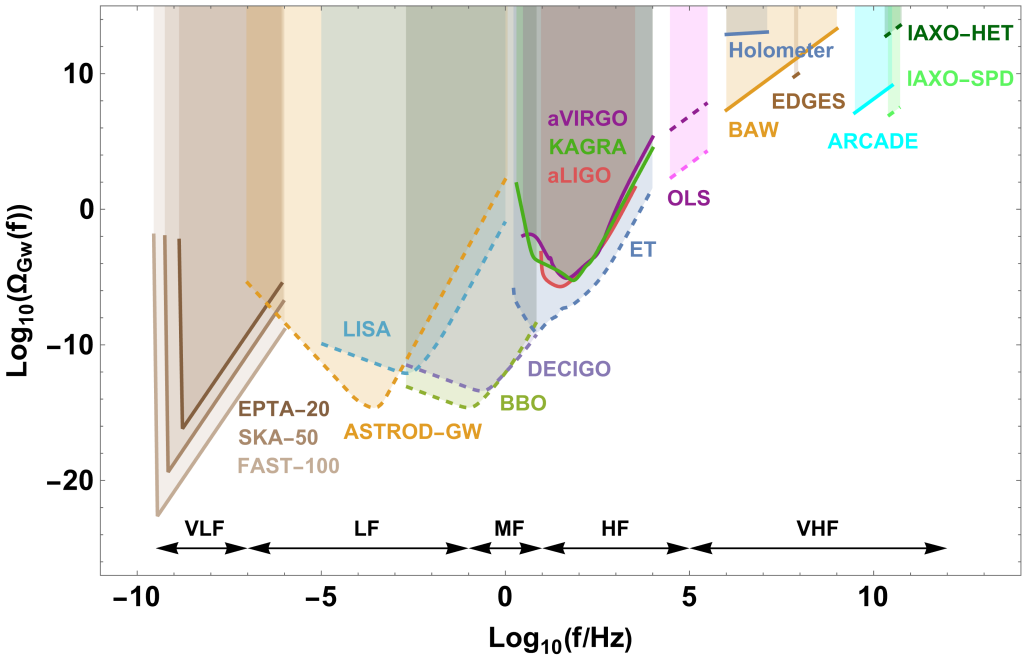

Figure 1.5: Sensitivity curves of several GW detectors as a function of the frequency, from the VLF to the VHF bands. The quantity Ω_{GW} represents the fractional energy density in the form of GWs. Continuous (dashed) curves represent current (planned) detectors. The image is reproduced from [148, 149].

surement of the amplitude of the GWB, which is a continuous, stochastic signal resulting from the superposition of numerous unresolved GW sources. This is the kind of signals that PBHs produce in the early universe and contrasts with the discrete and resolvable signals detected by the LVK collaboration, which originate from compact object mergers. While LVK measures transient, high-frequency GW events, the IPTA is sensitive to a persistent, low-frequency background signal, analogous to the CMB in the electromagnetic spectrum. Although not a GW detector in the conventional sense, the IPTA employs a distinct detection methodology based on identifying correlated deviations in the arrival times of pulsar signals, induced by passing GWs. Additionally, due to its detection approach and the spatial scale over which it operates, the IPTA is sensitive to the Very-Low-Frequency Band (VLF, 300 pHz–100 nHz), significantly lower than the frequency band accessible to LVK.

Still, there is a gap in frequencies between IPTA and LVK, which corresponds to the Low-Frequency-Band (LF, 100 nHz-0.1 Hz) and the Middle-Frequency-Band (MF, 0.1 Hz-10 Hz). Upcoming space-based detectors are planned to fill the gap: the Laser Interferometer Space Antenna (LISA) [150], planned for 2035, and others such as ASTROD-GW [151], BBO [152], and DECIGO [153], which are still in the design phase. Other third-generation ground-based detectors will also operate in the HF band, such as the Einstein Telescope (ET) [154], planned for 2035, and the Cosmic Explorer (CE) [155], which is in the design phase. These new detectors are expected to push the boundaries of GW detection even further and test Einstein's GR in the strong gravity regime. Fig. 1.5 shows the sensitivity curves of all these current (solid lines) and planned (dashed lines) detec-

tors, reproduced from the analysis made in Refs. [148, 149]. The ranges of the frequency bands are represented at the bottom by black arrows, following the classification of [148]. The curves labeled aVirgo and aLIGO correspond to the updated sensitivities of Virgo and LIGO after the improvement of 2011, while those labeled EPTA, SKA, and FAST correspond to IPTA, the European Pulsar Timing Array, the Square Kilometer Array, and the Five-hundred-meter Aperture Spherical Telescope.

The evaporating PBHs of interest in this thesis cannot be detected by a direct GW measurement, as they have already evaporated. However, what is measurable is the GWB they produce in the early universe when they are formed, which travels unperturbed through spacetime after that moment. As we will see, the characteristic frequency of the GWB produced by PBHs depends, in general, on their mass and production mechanism, with smaller PBHs associated with higher frequencies. For the case of evaporating PBHs ($\lesssim 10^{15}$g) and the effects studied in this thesis, their associated GWB spectrum will lie, in general, on the Very-High-Frequency Band (VHF, 100 kHz-1 THz) of the spectrum. Therefore, the current IPTA and LVK collaborations, as well as the future planned detectors meant to fill the gap in between, are excluded as possible candidates for detections of these GWBs. For this reason and completeness, we also included the detectors in the VHF band in Fig. 1.5 and direct the reader to Chapter 5, where these VHF detectors and the physics they use for detection are explained in detail. Finally, let us explain under what circumstances these evaporating PBHs can produce a GWB that could be measurable by these VHF detectors. Three scenarios are proposed in what follows; the first two of them are studied in the thesis, and the last is left for future work:

Scalar-Induced Gravitational Waves (SIGWs). In the standard scenario, primordial curvature perturbations, amplified during inflation, induce GWs at third-order in the perturbed expansion of the action when they reenter the horizon. However, as explained above, we consider a non-standard situation where the amplification of perturbations occurs during preheating, which we also expected to induce GWs [47–49]. In fact, since the density perturbations grow during this phase, the production of SIGWs is particularly efficient [50]. The resulting spectrum of SIGWs provides indirect evidence of PBH formation (since the amplified perturbations can collapse into PBHs) and is sensitive to the shape of the primordial power spectrum, making it a crucial observational probe. A schematic representation of this scenario is shown in Fig. 1.6. The key aspect is the definition of the relevant scales involved in the instability, as in the case of Fig. 1.4, the IB. When the modes enter the self-resonance instability (green shaded area), the scalar perturbations, such as $\Phi_{\boldsymbol{k}}$, grow. This is again related to the instabilities in the MS variable $v_{\boldsymbol{k}}$, as shown in Appendix A through Eqns. (A.11) and (A.14). Their behavior is illustrated in the bottom panel of Fig. 1.6 for two distinct scales, k_1 and k_2, separated by the scale $k_{\rm end}$. The first, shown in red, remains approximately constant after reentering the Hubble horizon $(aH)^{-1}$ during preheating. Although this may appear as non-amplification, it actually counteracts the usual decay of the gravitational potential at subhorizon scales in an expanding universe, ensuring $\Phi_{\boldsymbol{k}}$ remains stable during this phase. The mode k_2, shown

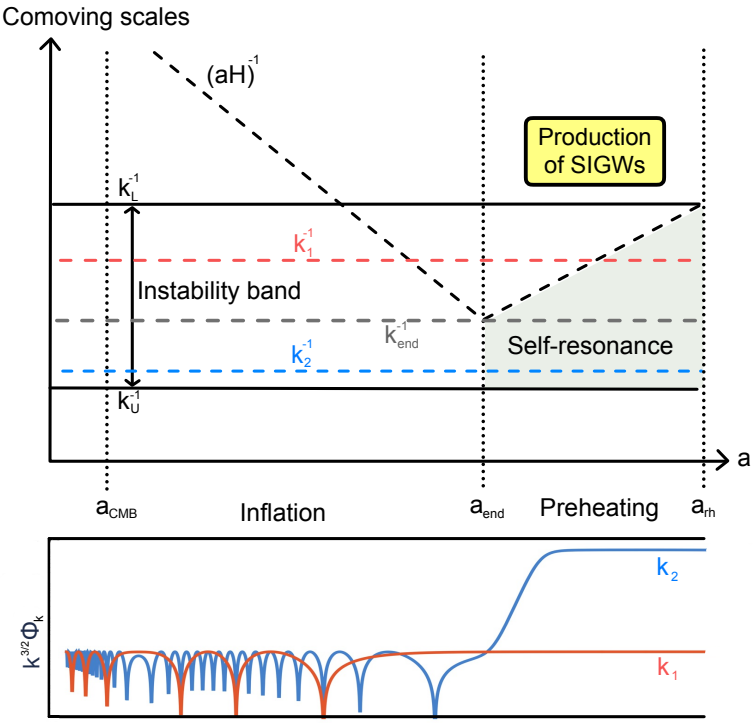

Figure 1.6: Schematic representation of the production of SIGWs during preheating. The upper panel shows some particular comoving scales involved, and the lower panel shows the evolution of the metric perturbation associated with two particular scales.

in blue, experiences stronger amplification as it spends more time within the region of instability of self-resonance. It should be noted that the Floquet exponent, responsible for amplification, is not the same for all modes within the IB [2], implying a stronger amplification for modes $k > k_{\rm end}$. For more details about the production of SIGWs during preheating, see Chapter 5.

Primordial Black Hole Domination. If PBHs form with a sufficiently high abundance, they can temporarily dominate the energy density of the universe, behaving as pressureless matter. During this phase, the PBHs induce Poissonian (shot-noise) energy density fluctuations, which act as an additional source of gravitational waves through third-order perturbation effects, similar to SIGWs but arising from the discrete nature of PBHs rather than a continuous power spectrum [60, 61, 63]. This mechanism generates a distinctive stochastic GW background that could be measured by detectors in the HF-VHF band. If such a signal is observed, it would provide direct evidence of a PBH-dominated era, although the details from the inflationary model generating these PBHs would get diluted.

Primordial Black Hole Evaporation. When PBHs reach the final stages of their evolution, they are theorized to evaporate via Hawking radiation, rapidly producing high-energy particles that act as radiation. In fact, this process would induce a violent transition from matter domination to radiation domination, leading to turbulent motion, shock waves, and non-linear density perturbations [59]. Such sudden transitions, analogous to

first-order phase transitions, act as powerful sources of gravitational waves [59–63], although at smaller frequencies compared to the SIGWs and PBHs domination effects, since this effect occurs later in time. Moreover, if PBHs undergo mergers before evaporating, the resulting Kerr PBHs can radiate a significantly enhanced fraction of their mass into high-energy gravitons, producing a "hot graviton background" and potentially contributing to the effective number of relativistic species [156].

1.4 Overview of the thesis

In this thesis, we examine the following aspects of the formation of PBHs and some of their associated GWBs:

- **Chapter 2**. *PBH formation during preheating in Starobinsky inflation*

  One plausible formation scenario for PBHs is the post-inflationary preheating stage, where the field oscillates at the bottom of the potential, causing the universe to behave as nearly matter-dominated. These oscillations induce instabilities in the density perturbations, referred to as Mathieu instability, and, consequently, the perturbations are amplified at a rate proportional to the scale factor. We study the two formalisms for studying the collapse of perturbations into PBHs presented in Section 1.2: PS and KP. Results for the mass fraction of PBHs are provided for the Starobinsky model. This chapter is primarily based on [1].

- **Chapter 3**. *Self-Resonance during preheating in Starobinsky-like models*

  When the inflationary potential deviates from a quadratic shape, the Mathieu instability becomes particularly strong, leading to perturbations that grow exponentially rather than linearly in the scale factor. In this context, the instability is commonly referred to as self-resonance. This chapter examines this effect for a generic potential expanded in powers of the inflaton field ϕ. It emphasizes the importance of including additional terms in the expansion beyond the quadratic term ϕ^2. We present results for the Starobinsky-like α-attractor models of inflation, where self-resonance is significantly stronger for small values of α, and propose two applications of this effect, studied in Chapters 4 and 5. This work builds on [2].

- **Chapter 4**. *PBH formation from self-resonant preheating in Starobinsky-like models*

  The self-resonant effects make perturbations grow faster as the value of α decreases, which translates into a lower threshold and, consequently, into a higher mass fraction and PBH masses. In this chapter, we explore these effects also for the α-attractor models, following again the PS and KP formalisms for the mass fraction, which can be seen as an extension of Chapter 2. This study is based on [3].

- **Chapter 5**. *SIGWs from self-resonant preheating in Starobinsky-like models*

In this chapter, we study the GWs induced from the amplification of the scalar perturbations during preheating also via the self-resonance mechanism. The results are shown for the α-attractor models. By varying the parameter α, we propose a lower bound based on the energy density of SIGWs constrained by BBN, which ultimately translates into a lower bound on the tensor-to-scalar ratio that differs from the one derived in previous works. The chapter is mainly based on [4].

- **Chapter 6**. *GWs from PBH dominance: The effect of the inflaton decay rate*

  When the fractional energy density of PBHs is the dominant one, it is usually called a PBH-dominated era, during which the Poissonian density fluctuations of the PBHs can induce GWs in a similar way as during preheating, due to the matter-dominated behavior. We propose a simple parametrization of the power spectrum based on a Starobinsky-like inflationary model, where the perturbations are amplified during inflation. Further, we assume that the PBHs are formed during preheating under the KP formalism, and that the field decays into radiation via a decay rate Γ_ϕ. By studying the parameter space of the model, we show that these assumptions help relax previous constraints. This chapter is mainly based on [5].

2

Primordial black hole formation during preheating in Starobinsky inflation

> *A luminous star, of the same density as the Earth, and whose diameter should be 250 times larger than that of the Sun, would not, in consequence of its attraction, allow any of its rays to arrive at us; it is therefore possible that the largest luminous bodies in the universe, may, through this cause, be invisible.*
>
> – Pierre-Simon Laplace [69] in 1796.

Laplace's proposition of massive celestial bodies whose gravitational pull prevents light from escaping is one of the studies that laid the conceptual groundwork for what would later be understood as black holes. Although formulated within Newtonian mechanics, this idea foreshadowed the implications of GR and quantum gravity in describing extreme astrophysical phenomena. In the modern era, these considerations have extended beyond stellar remnants to the early universe, where the formation of PBH is of significant interest. Moreover, since the inflationary phase constitutes the most important phase of the primordial Universe [24–26, 32], it is vital to understand if the PBH formation makes a significant contribution within the scope of inflationary cosmology.

The latest observations of the CMB from Planck data [30] are compatible with the single-field inflationary scenario. Thus, it is adequate to restrict ourselves to the detailed study of the primordial Universe within a single-field setup. Based on the available Planck data, Starobinsky and Higgs inflationary scenarios have become the favorite models as they fit so far, with the spectral index and tensor-to-scalar ratio constraints. The success of Starobinsky inflation, in particular, has gained a lot of attention because it is the first model of inflation in the modified gravity context, which has emerged from the foundations of quantum gravity [24, 157]. Starobinsky-like models have become a basis for building UV-completions around them because exponentially flat potentials happen to explain more naturally the observation of near scale-invariance of the CMB power spectra [157, 158]. For these reasons, we choose to work within the framework of Starobinsky inflation.

Recently, the preheating stage has been explored and projected to give small-scale PBH formation [43–46]. However, these studies only consider the possible collapse of (type I) modes that are super-horizon during inflation and experience resonance instabilities when they enter the horizon during the preheating stage. The fate of the other (type II) modes that remain in the subhorizon evolution after inflation is argued to be highly quantum mechanical. Thus, their contribution to PBH formation is an open question and therefore not considered in those studies. However, our primary aim here is to study all the fluctuations that can experience preheating instabilities and potentially collapse into PBH. This includes both type I and type II modes. The relevance of quantum-to-classical effects in generating preheating instabilities and collapse dynamics is important to mention. In the preheating stage, we may have a situation where classical modes can coexist with quantum ones. Whether quantum modes can trigger instabilities and contribute to classical collapse is a broader and non-trivial question. Without any indication that this can be the case, one valid approach would be to ignore them, as it is commonly done in the standard literature. However, we choose not to do so to estimate the impact of type II modes in PBH formation.

Furthermore, we identify a subclass of type II modes (type IIa) that, for all purposes, behave exactly as type I ones by growing and experiencing instabilities during the preheating phase. Thus, to be more precise, our focus is on all the modes that can become unstable and lead to the universal growth of density perturbations. Therefore, one motivating idea of this chapter is to revisit the preheating stage carefully and explore these type I and type IIa modes that evolve identically during preheating despite their evolution history during inflation. The other subset of modes (type IIb) remains unimportant, as they are unaffected by the instabilities or do not satisfy the criteria we define for the collapse into PBH.

Regarding the collapse of perturbations into PBH, one of these criteria is the consideration of a threshold (Eqns. (1.8) and (1.14)) above which the perturbations collapse [159] and then one applies the PS formalism [82] (Appendix B.1). This threshold is defined in terms of the pressure, as this is what stops the collapse. However, the preheating stage is characterized by negligible pressure, and thus the threshold estimation should be reconsidered. This is done in [45], where a scale-dependent threshold $\delta_c(k)$ is defined in terms of the time a perturbation needs to collapse compared to the time the reheating stage lasts. We, although closely following this work, also consider the KP formalism and compare both formalisms. This, as explained in Appendix B.2, suits better for a matter-dominated scenario, as it considers non-spherical effects that indeed restrict the probability of formation. Further, to determine the PBH masses, we consider the scale-dependent threshold $\delta_c(k)$ in the critical collapse framework (1.13).

The contents of this chapter are organized as follows: In Section 2.1, we review the dynamics of the scalar perturbations during preheating in the Starobinsky model. Section 2.2 describes the numerical procedure used to compute the background and perturbations

equations, exploring some range of comoving wavenumbers k meaningful to the density perturbations amplification. The process of PBH formation is explained in Section 2.3, where, for the Starobinsky potential, we present numerical estimations of the PBH mass fraction and associated mass. A summary is presented in Section 2.4.

2.1 Inflation and preheating in Starobinsky inflation

The inflaton potential, according to Starobinsky's $R + R^2$ theory, is given by

$$V(\phi) = V_0 \left(1 - e^{-\sqrt{\frac{2}{3}}\frac{\phi}{M_{\rm Pl}}}\right)^2 , \tag{2.1}$$

where $V_0 = \frac{3}{4}M^2 M_{\rm Pl}^2$ is related to the scalaron mass $M \sim 1.3 \times 10^{-5} M_{\rm Pl}$ in the Jordan frame, obtained by normalizing V_0 to the amplitude of the inflationary power spectrum from Planck results [29–31]. ϕ is also expressed in units of Planck mass, $M_{\rm Pl}$. The main mathematical details about inflation and preheating can be found in Appendix A. Here, we give the intuition about the new elements of our investigation. To do so, we start with the equation for the evolution of the comoving curvature perturbation, Eqn. (A.14). This can be solved numerically, although it requires some suitable initial conditions for Φ_k. These are obtained by considering the behavior of the curvature perturbation $\mathcal{R}_k$ in two different regimes of k. The first one (type I modes) is defined by the modes that exited the horizon during inflation and entered the particle horizon during preheating. The second one (type II modes) involves wavenumbers that have never exited the horizon. For the former, we can define the last scale to enter the Hubble radius during preheating, $k_{\rm min}$, which, using the Hubble radius crossing condition, can be computed as

$$k_{\rm min} = a(t_{\rm rh}) H(t_{\rm rh}). \tag{2.2}$$

Since the preheating duration depends on the inflaton coupling to matter fields and its decay process, we will consider various arbitrary periods of preheating. These type I modes belong therefore to the interval $k \in [k_{\rm min}, k_{\rm end}]$.

Regarding type II, these usually are not considered in the literature because of their sub-horizon (quantum-mechanical) evolution during inflation. Our investigation reveals that despite their history, a subclass of type II modes during preheating gets amplified like type I, which we call type IIa. The collapse of type I modes is considered as they enter the particle horizon and fall into the IB during preheating. Meanwhile, type IIa modes never exit the horizon during inflation but still can fall into the IB and get amplified. Therefore, both type I and IIa modes are on equal footing when inside the IB and can potentially contribute to PBH formation, as explained in the later part of the section. The remaining type II modes are labeled as type IIb. For illustration, in Fig. 2.1, we have plotted the evolution of the MS variable v_k and the density contrast δ_k for a type I and a type IIa mode,

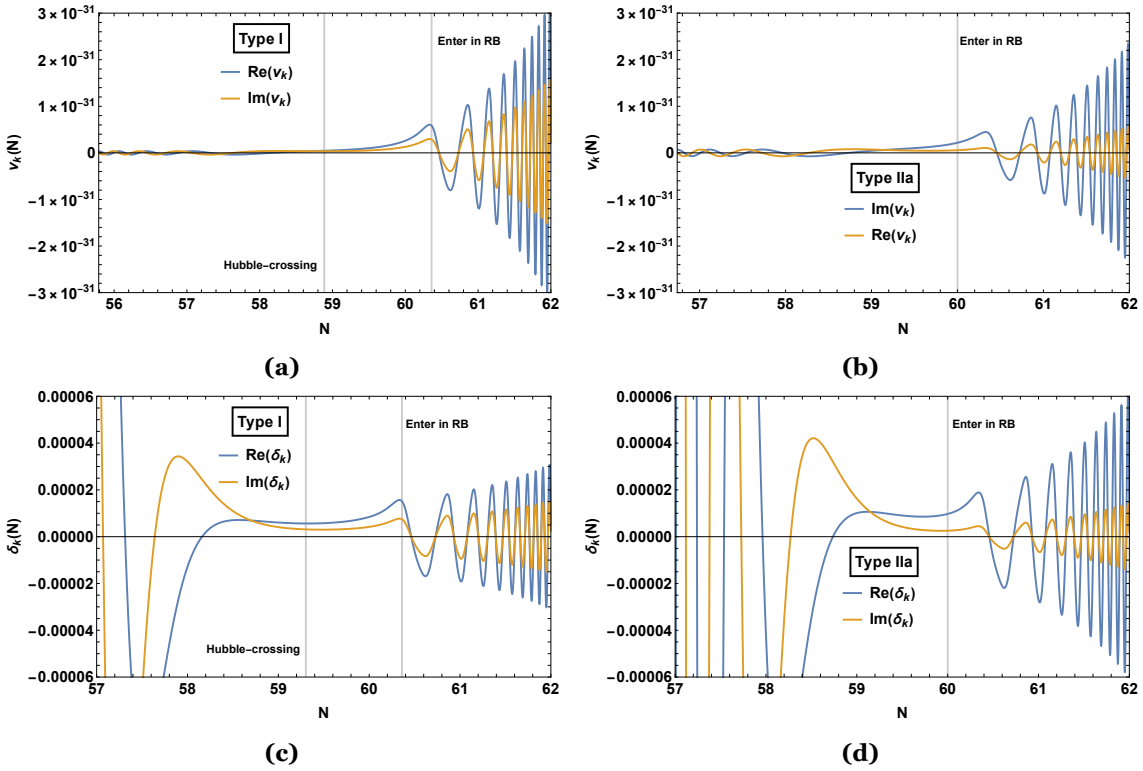

Figure 2.1: (a) Time evolution of the Mukhanov-Sasaki variable for a type I mode ($k \simeq 0.7k_{\rm end}$). Vertical gray lines mark the points where the mode exits the horizon during inflation (left one) and where it reenters back (right one). **(b)** The same but for a type IIa mode ($k = 1.35k_{\rm end}$). Vertical gray line marks, in this case, the point where the mode enters the RB, and thus, it starts to amplify. **(c)** Time evolution of the density contrast for the same type I mode. **(d)** Time evolution of the density contrast for the same type IIa mode.

both real and imaginary parts. We assumed the standard Bunch-Davies initial conditions, described in the next section. The question of the quantum aspects of these modes that could potentially collapse remains, we nonetheless explore all the modes classically in this work leaving the quantum treatment for future investigations. We fix an upper limit $k_{\rm max}$ (based on our numerical evaluation of density perturbations for the Starobinsky model) for the type II modes, given by

$$k_{\rm max} = 10^{-30} M_{\rm Pl}, \tag{2.3}$$

where the density perturbations typically reach the non-perturbative regime, at least for the Starobinsky model, see Fig. 2.6. These type II modes belong to the interval $k \in [k_{\rm end}, k_{\rm max}]$. In Fig. 2.2, these scales are shown, as well as the Hubble radius H^{-1}. Bear in mind that H^{-1} is a physical scale (in contrast to the conformal scale $(aH)^{-1}$) and, therefore, when plotted together with the scales a/k, those scales must be physical too. We define physical scales as

$$k_{\rm phys}^{-1} = \frac{a}{k_{\rm com}}, \tag{2.4}$$

where $k_{\rm com}$ is the comoving wavenumber.

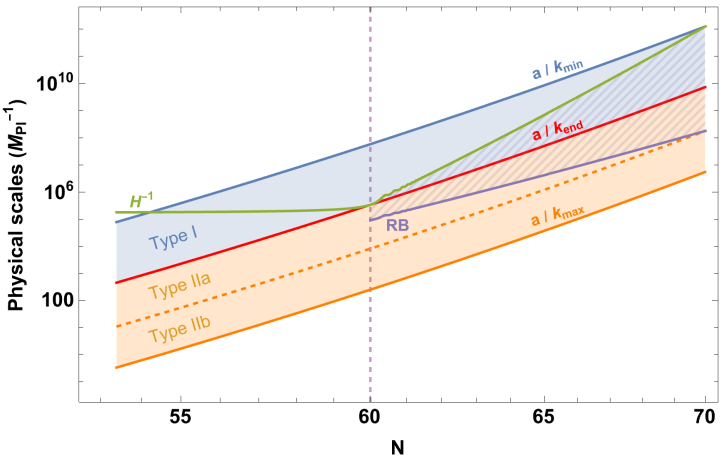

Figure 2.2: Physical scales of interest for the Starobinsky model as well as the physical Hubble radius H^{-1} as a function of the number of e-folds from the beginning of inflation. The small oscillations in H^{-1} after $N = 60$ are part of the solution, not an artifact. The Blue shaded area corresponds to the type I modes, whereas the orange shaded area corresponds to the type IIa and type IIb modes, separated by the last scale to enter the RB, the hatched area.

One last remark is needed before solving for the equation for the evolution of the comoving curvature perturbation, Eqn. (A.14), the effect of parametric resonance. This will help us gain a clearer understanding of how curvature perturbations behave during preheating and explicitly define the IB, a concept that is further studied in Chapter 3. Since, during this phase, the inflaton field oscillates around the bottom of the potential (2.1), one can approximate it by a quadratic one[9], that is, $V \sim \frac{M^2}{2}\phi^2$. Doing so, and neglecting fast-decaying terms, makes it possible to rewrite the Mukhanov-Sasaki equation (A.9) as a Mathieu-like equation of the type

$$\frac{\mathrm{d}^2\tilde{v}_k}{\mathrm{d}z^2} + \left[A_k - 2q(z)\cos(2z)\right]\tilde{v}_k = 0, \tag{2.5}$$

where $\tilde{v}_k = a^{1/2}v_k$ is the re-scaled MS variable, $z = Mt + \pi/4$ and the parameters

$$\begin{aligned} A_k &= 1 + \frac{k^2}{a^2M^2}, \\ q &= \frac{1}{M_{\mathrm{Pl}}}\sqrt{\frac{3}{2}}\phi_{\mathrm{end}}\left(\frac{a_{\mathrm{end}}}{a}\right)^{3/2}, \end{aligned} \tag{2.6}$$

depend on the background solution [43, 45, 46]. Now, since $q \sim \phi_{\mathrm{end}} < 1$ we are in the narrow resonance regime, and the first IB is given by the condition $1-q < A_k < 1+q$ [43], which corresponds to

$$0 < \frac{k}{a} < \sqrt{3HM}\,\frac{M\phi_{\mathrm{end}}}{\sqrt{6}H_{\mathrm{end}}M_{\mathrm{Pl}}} \simeq \sqrt{3HM}. \tag{2.7}$$

[9] It is important to mention that approximating the potential (2.1) by a parabola reflects the true behavior of the Starobinsky model for prolonged preheating stages. However, during the first moments of preheating, the Starobinsky potential differs from the quadratic one (see Fig. A.1 for high values of ϕ). This difference is further explored in Chapter 3.

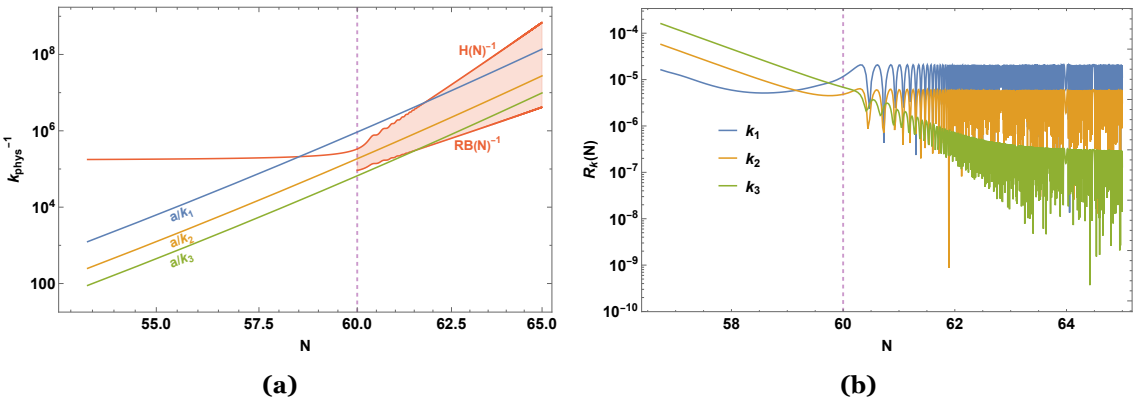

(a) **(b)**

Figure 2.3: a) Instability band (red shaded area) (2.8) as well as some examples of physical scales during the end of inflation and the beginning of preheating. **b)** Curvature perturbation for the physical scales selected. The vertical purple dashed line marks the end of inflation. The ε parameter is set to $\varepsilon = 3/2$ for visual purposes due to its high oscillating behavior.

If we now consider physical scales (in length units) and the fact that the mode has to be inside the horizon so that causality applies, we have that for a mode to be in the IB means the following

$$\frac{1}{H} > \frac{a}{k} > \frac{1}{\sqrt{3HM}}. \tag{2.8}$$

The important thing here is that for the modes satisfying (2.8), the re-scaled MS variable grows as $\tilde{v}_k \simeq e^{\int \mu(z)\mathrm{d}z} \simeq a^{3/2}$, where $\mu(t) \sim \frac{q(z)}{2}$ is the so-called Floquet exponent. All this is equivalent to $v_k \simeq a$, which implies a constant curvature perturbation by the definition of (A.11). That is: *modes satisfying* (2.8) *(inside the IB) have a constant curvature perturbation*. Fig. 2.3 confirms numerically this fact, where we depict the IB with some examples of physical scales (Fig. 2.3a), and the curvature perturbation associated with those physical scales as a function of the number of e-folds (Fig. 2.3b). For the type I mode labeled as k_1, the curvature perturbation decays during inflation until it exits the horizon and gets fixed to a constant value even after entering the horizon (or, equivalently, entering the IB). We also observe the curvature perturbation for type IIa modes k_2 and k_3, which enter the IB at different times. The mode k_2 decays until the end of inflation, and as it enters the IB at this point, it evolves towards constant value. On the other hand, the mode k_3 decays until approximately $N = 62$, then it enters the IB and eventually approaches a constant value.

Now that we have specified the two ranges of k and understood the behavior of the curvature perturbation during preheating, we can solve (A.14) analytically. For type I, since the modes exit the horizon during inflation, the curvature perturbation becomes and remains nearly constant even when the mode reenters the particle horizon during preheating, since it enters the IB, see Fig. 2.3 for k_1. We can thus fix the value of $\mathcal{R}_k$ to $\mathcal{R}_k^{\mathrm{hc}} \sim \mathcal{R}_k^{\mathrm{end}}$, the magnitude it had when it crossed the Hubble scale (hc stands for Hubble crossing). Therefore,

(A.14) can be solved analytically to give

$$|\Phi_{\boldsymbol{k}}| = \frac{3}{5}|\mathcal{R}_{\boldsymbol{k}}^{\rm end}| + C_1(k)\left(\frac{a_{\rm end}}{a}\right)^{5/2}, \tag{2.9}$$

where $C_1(k)$ is a constant of integration and we have considered $H \sim \frac{2}{3t}$ and $w_{\rm eff} \sim 0$ during preheating (see Appendix A.3). Ignoring the decaying mode, we see that the perturbation $\Phi_{\boldsymbol{k}}$ also remains constant during preheating in this interval. Regarding the derivative of $\Phi_{\boldsymbol{k}}$, by direct inspection of Eqn. (A.14) one can deduce that $|H^{-1}\dot{\Phi}_{\boldsymbol{k}}| \ll |\Phi_{\boldsymbol{k}}|$, so that $|\Phi_{\boldsymbol{k}}| = \frac{3}{5}|R_{\boldsymbol{k}}^{\rm end}|$ applies. Using this into (A.16) (ignoring the decaying term), we have that the density perturbation during preheating and for the type I modes is given by

$$|\delta_{\boldsymbol{k}}^{\rm I}| \sim \frac{2}{5}\left(\frac{k^2}{a^2H^2}+3\right)|\mathcal{R}_{\boldsymbol{k}}^{\rm end}|. \tag{2.10}$$

If the mode is super-Hubble, the term k^2/a^2H^2 is negligible, and the density perturbation is constant. However, once the mode enters the particle horizon during preheating, this term grows as

$$\frac{k^2}{a^2H^2} \sim \left(\frac{k}{k_{\rm end}}\right)^2\left(\frac{a}{a_{\rm end}}\right), \tag{2.11}$$

which implies the growth of density perturbation as $\delta_{\boldsymbol{k}} \sim a$ [46]. This increase will depend on both the value of k with respect to $k_{\rm end}$ and a with respect to $a_{\rm end}$. For example, if the mode enters the particle horizon at the beginning of preheating, then $k \sim k_{\rm end}$, and therefore the increase will be maximum. However, if the mode enters the particle horizon by the end of preheating $k \ll k_{\rm end}$, then the increase will be minimal. Therefore, among the type I modes, those that enter the particle horizon closely after the end of inflation ($k \approx k_{\rm end}$) are more likely to create overdense regions that can potentially collapse and form PBH. These are the modes studied earlier by [45].

Let us now study type II modes. In this case, the MS variable is still approximately given by the vacuum solution during inflation. However, as these modes enter the IB, the curvature perturbation sets to a constant value, and we retrieve solutions (2.9) and (2.10) again. This would be the case of mode k_2 in Fig. 2.3, the mode k_3 after $N \sim 62$ or, in general, any type IIa mode that falls into the IB, for which the density perturbation grows as

$$|\delta_{\boldsymbol{k}}^{\rm IIa}| \sim \frac{2}{5}\left(\frac{k^2}{a^2H^2}+3\right)|\mathcal{R}_{\boldsymbol{k}}^{\rm end}|. \tag{2.12}$$

For the remaining type IIb modes, the curvature perturbation $\mathcal{R}_{\boldsymbol{k}}$ decay as

$$|\mathcal{R}_{\boldsymbol{k}}| \sim \left(\frac{a_{\rm end}}{a}\right)|\mathcal{R}_{\boldsymbol{k}}^{\rm end}|, \tag{2.13}$$

which translates into an also decaying $\Phi_{\boldsymbol{k}}$. Using (2.13) into (A.14) and solving for $\Phi_{\boldsymbol{k}}$ we

obtain

$$|\Phi_{\boldsymbol{k}}| \sim \left(\frac{a_{\rm end}}{a}\right)|\mathcal{R}^{\rm end}_{\boldsymbol{k}}| + C_2(k)\left(\frac{3H}{2}\right)^{5/2}, \tag{2.14}$$

where again $C_2(k)$ is a constant of integration. Using this into (A.16) and ignoring the decaying term, the density perturbation is approximately given by

$$|\delta^{\rm IIb}_{\boldsymbol{k}}| \sim \frac{2}{3}\frac{k^2}{a^2H^2}\left(\frac{a_{\rm end}}{a}\right)|\mathcal{R}^{\rm end}_{\boldsymbol{k}}| \sim \frac{2}{3}\left(\frac{k}{k_{\rm end}}\right)^2|\mathcal{R}^{\rm end}_{\boldsymbol{k}}|, \tag{2.15}$$

where in the last step, we have used (2.11). Equation (2.15) tells us that the density perturbations corresponding to the type IIb modes remain constant in time and therefore do not suffer from instabilities, so we exclude them[10]. In essence, the modes that are of interest to us are the types I and IIa, which as we saw are the ones affected by the instabilities ($\delta^{\rm IIa}_{\boldsymbol{k}} \sim \delta^{\rm I}_{\boldsymbol{k}} \sim a$).

Now that we know the relation between $\mathcal{R}_{\boldsymbol{k}}$ and $\delta_{\boldsymbol{k}}$ we can use (2.10) and (2.12) to obtain the density perturbations. This is done by numerically solving for $v_{\boldsymbol{k}}$, shown in the next section.

2.2 Numerical approach

This section presents the numerical procedure used to compute the background evolution and scalar perturbations, along with their respective initial conditions.

2.2.1 Background solution and initial conditions

To solve for the background, usually, one substitutes the first Friedmann equation from (A.5) into (A.2) so that there is just one second-order ordinary differential equation at the end. This kind of equation needs two initial conditions to be completely solved, one for ϕ and one for $\dot{\phi}$, which we derive from the slow-roll approximation. First, from the Friedmann equations (A.5) we obtain the relation

$$\dot{H} = -\frac{\dot{\phi}^2}{2M_{\rm Pl}^2}. \tag{2.16}$$

Now, the first slow-roll parameter ε is defined in terms of the Hubble factor as $\varepsilon = -\dot{H}/H^2$. Substituting this into (2.16) we have

$$\frac{H}{\dot{\phi}} = \frac{1}{\sqrt{2\varepsilon}M_{\rm Pl}}. \tag{2.17}$$

[10] Actually, these modes can be further excluded by other criteria we define in the next sections.

This implies that the number of e-folds can be expressed as $\mathrm{d}N = H\mathrm{d}t = \frac{H}{\dot{\phi}}\mathrm{d}\phi$ and thus, substituting this into (2.17) we obtain

$$\mathrm{d}N = \frac{1}{\sqrt{2\varepsilon}M_{\mathrm{Pl}}}\mathrm{d}\phi. \tag{2.18}$$

Another common way of defining the first slow-roll parameter is in terms of the inflationary potential, given by

$$\varepsilon_V = \frac{M_{\mathrm{Pl}}^2}{2}\left(\frac{V_{,\phi}}{V}\right)^2, \tag{2.19}$$

where the subscript "$_{,\phi}$" refers to derivation with respect to the field ϕ. During inflation, the slow-roll parameters can be approximated, $\varepsilon \simeq \varepsilon_V$, so substituting (2.19) into (2.18) gives us an integral relation between the field and the number of e-folds, that is:

$$N = -\frac{1}{M_{\mathrm{Pl}}^2}\int_{\phi}^{0}\left(\frac{V}{V_{,\phi'}}\right)\mathrm{d}\phi'. \tag{2.20}$$

Usually, the number of e-folds is counted backward, with $N = 60$ marking the beginning of inflation, and $N = 0$ the end. To obtain $\varepsilon(N)$, we have to go back to (2.17) and use the relation $\mathrm{d}N = H\mathrm{d}t$ again to transform the derivative with respect to t to a derivative with respect to N. Then, using (2.20) we obtain

$$\varepsilon(N) = \frac{1}{2M_{\mathrm{Pl}}^2}\left(\frac{\mathrm{d}\phi}{\mathrm{d}N}\right)^2 = \frac{1}{2}\left(\frac{V_{,\phi}}{V}\right)^2. \tag{2.21}$$

Let us finally see how to obtain $\frac{\mathrm{d}\phi}{\mathrm{d}N}$. Using the Klein-Gordon equation (A.2), neglecting $\ddot{\phi}$ and transforming $\dot{\phi}$ into a derivative with respect to N we have

$$\frac{\mathrm{d}\phi}{\mathrm{d}N} = -\frac{V_{,\phi}}{3H^2}. \tag{2.22}$$

Now, using (A.5) to substitute H^2 and using the slow-roll approximation ($V \gg \dot{\phi}^2$) we obtain:

$$\frac{\mathrm{d}\phi}{\mathrm{d}N} = -M_{\mathrm{Pl}}^2\frac{V_{,\phi}}{V}. \tag{2.23}$$

For the Starobinsky model with potential given by (2.1), we have the following expressions

$$\phi \simeq \sqrt{\frac{3}{2}}\ln\left(\frac{4N}{3}\right)M_{\mathrm{Pl}}, \qquad \frac{\mathrm{d}\phi}{\mathrm{d}N} \simeq -\sqrt{\frac{2}{3}}\frac{M_{\mathrm{Pl}}}{N}, \qquad \varepsilon \simeq \frac{3}{4N^2}, \tag{2.24}$$

valid during the slow roll regime, and where $N = 60$ marks the beginning of inflation and $N = 0$ its end. We can now use (2.24) as initial conditions for the background equations (A.5) and (A.2). Even though our computations are made in cosmic time, it is more intuitive to make the plots with respect to the number of e-folds, for which we use the standard

relation

$$N(t) = \ln\left(\frac{a(t)}{a(t_0)}\right), \tag{2.25}$$

where $a(t_0)$ is the scale factor at the beginning of inflation, labeled as t_0. This is evaluated by using the Hubble-crossing condition at the pivot scale ($k_{\rm pivot} = 0.05{\rm Mpc}^{-1} = 1.33 \times 10^{-58} M_{\rm Pl}$), that is:

$$a_0 = \frac{k_{\rm pivot}}{H(t_0)}, \tag{2.26}$$

where $H(t_0)$ is the Hubble rate evaluated at the beginning of inflation, obtained via the normalization of the power at the pivot scale. From the Planck data [30, 31] we have

$$\mathcal{P}_{\mathcal{R}}(k_{\rm pivot}) \simeq 2.2 \times 10^{-9} \simeq \frac{H^2}{8\pi^2 M_{\rm Pl}^2 \varepsilon(N_{\rm inf})}. \tag{2.27}$$

Notice that one should not confuse t_0 with the initial time t_i of the computations. The times t_i and t_0 do not necessarily need to coincide. Imposing initial conditions from the slow-roll approximation gives an approximate (but somewhat accurate) estimation of the initial conditions for the field and seldom produces exactly 60 e-folds of inflation. This means that imposing initial conditions at t_i can give more or less than 60 e-folds, but then we normalize the scale factor at t_0 (so that from t_0 to the end of inflation we have exactly 60 e-folds). If this cosmic time is expressed in Planck mass units, it is enough to take $t_i = 10^5 M_{\rm Pl}^{-1}$ to be accurate, but numerically there is no difference so that we can take $t_i = 1 M_{\rm Pl}^{-1}$ as initial computational time. The scale factor $a(t)$ can be obtained by solving Friedmann equation (A.5) with an arbitrary initial condition. After that, it is just a matter of defining a rescaling using (2.26).

2.2.2 Scalar perturbations and initial conditions

As previously explained, we study perturbations with the MS equation written in cosmic time (A.9). Following [160], it is better (for numerical purposes) to solve this equation separately for the real and imaginary parts of the MS variable. This means we must specify real and imaginary initial conditions when solving Eqn.(A.9) in addition to an initial time. We derive these quantities in what follows.

Generally, initial conditions for all the fluctuations during inflation are imposed when the modes are deep inside the horizon $k \gg aH$, where the MS variable is usually expanded as

$$\hat{v}(\eta, \mathbf{x}) = \int \frac{d^3k}{(2\pi)^{3/2}} \left[a_{\mathbf{k}} v_{\boldsymbol{k}} e^{i\mathbf{k}\cdot\mathbf{x}} + a^{\dagger}_{\mathbf{k}} v^*_{\boldsymbol{k}} e^{-i\mathbf{k}\cdot\mathbf{x}} \right], \tag{2.28}$$

and where $a_{\mathbf{k}}$, $a^{\dagger}_{\mathbf{k}}$ are the creation and annihilation operators that satisfy the canonical

commutation relations. In this regime, the general solution of the MS equation (A.8) is given by

$$v_{\boldsymbol{k}}(\eta) = \frac{A_{\boldsymbol{k}}}{\sqrt{2k}}\left(1 - \frac{i}{k\eta}\right)e^{-ik\eta} + \frac{B_{\boldsymbol{k}}}{\sqrt{2k}}\left(1 + \frac{i}{k\eta}\right)e^{ik\eta}, \tag{2.29}$$

where $A_{\boldsymbol{k}},\ B_{\boldsymbol{k}}$ are the Bogoliubov coefficients and η represents conformal time. The canonical commutation relation of the MS field leads to [35]

$$v_{\boldsymbol{k}} v_{\boldsymbol{k}}^{*\prime} - v_{\boldsymbol{k}}^{*} v_{\boldsymbol{k}}^{\prime} = i, \tag{2.30}$$

where a prime denotes differentiation with respect to conformal time. This equation yields conditions on the coefficients

$$|A_{\boldsymbol{k}}|^2 - |B_{\boldsymbol{k}}|^2 = 1. \tag{2.31}$$

The Bunch-Davies vacuum, usually assumed for inflationary initial conditions, is defined as the one for which $A_{\boldsymbol{k}} = 1$ and $B_{\boldsymbol{k}} = 0$, which corresponds to the positive energy state when the mode is subhorizon $k \gg aH$, that is

$$v_{\boldsymbol{k}}\Big|_{k\gg aH} = \frac{1}{\sqrt{2k}}e^{-ik\eta}. \tag{2.32}$$

To understand the choice we make for the real and imaginary initial conditions of $v_{\boldsymbol{k}}$, this equation is written in a trigonometric form as:

$$v_{\boldsymbol{k}}(\eta) = \frac{1}{\sqrt{2k}}\left[\cos(k\eta) - i\sin(k\eta)\right]. \tag{2.33}$$

Let us further define the following two conditions:

i) Real and imaginary parts must be synchronized, in the sense that

$$\cos(k\eta)^2 + \sin(k\eta)^2 = 1,$$

so that the amplitude does not get affected.

ii) The initial computational time must be such that we let the mode evolve for a sufficient number of e-folds before the freezing (Hubble-crossing) point is reached.

As long as these two conditions apply, then the choice of initial computational time (conformal or cosmic) should have no impact on the final result for the modulus of Mukhanov's variable $|v_{\boldsymbol{k}}|$ (see Fig. 2.4 for details). This is because the freezing point acts as an attractor and always occurs at the same time and with the same amplitude, provided conditions i) and ii) are satisfied and that we refer to $|v_{\boldsymbol{k}}|$. We will choose the following simple initial

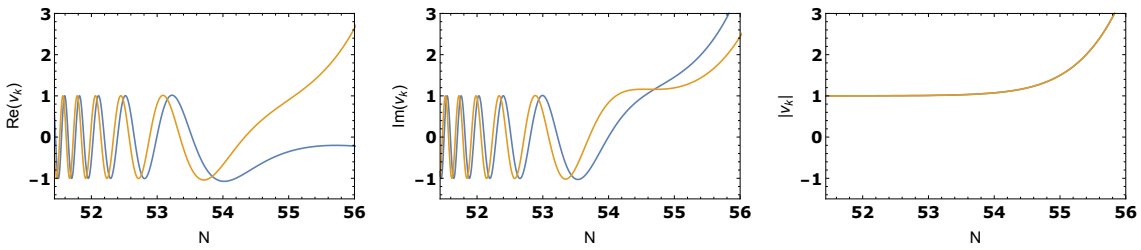

(a) **(b)** **(c)**

Figure 2.4: Evolution of the Mukhanov variable for two different choices of conformal time and for $k = 10^{-34} M_{\rm Pl}$. Hubble-crossing occurs at approximately 54 e-folds. In blue, conformal time is set to zero at the end of inflation $\eta(t_{\rm end}) = 0$ and in orange $\eta(t_{\rm end}) = \frac{\pi}{4}$. In **(a)** the real part is plotted, in **(b)** the imaginary part, and in **(c)** the modulus $|v_{\boldsymbol{k}}|$. In this last plot, both plots are superimposed, showing that the choice of conformal time does not affect $|v_{\boldsymbol{k}}|$, but indeed, it affects the real and imaginary parts. $v_{\boldsymbol{k}}$ is rescaled to have unitary amplitude while sub-Hubble.

condition[11] for all modes:

$$v_{\boldsymbol{k}}(t_i) = \frac{1}{\sqrt{2k}}. \tag{2.34}$$

This, of course, satisfies condition i) (see footnote 11) and, if t_i is such that it lets the mode evolve for some e-folds, then also condition ii). Following [160, 162], the starting time for the computations can be set for each mode to just a few e-folds before Hubble crossing, usually 2 or 3. This is because, at this point, the mode is still well described by the Bunch-Davies vacuum. Also, in doing so, we avoid the computation of unnecessary oscillations that the mode does. This consumes memory, which translates into more waiting time.

Let us see now how to obtain the initial condition for $\dot{v}_{\boldsymbol{k}}$. Using the definition of conformal time we have

$$\mathrm{d}\eta = \frac{\mathrm{d}t}{a(t)} \qquad \rightarrow \qquad \dot{\eta}(t) = a(t)^{-1}. \tag{2.35}$$

Differentiating (2.32) with respect to cosmic time and using (2.35) we have

$$\frac{\mathrm{d}}{\mathrm{d}t} v_{\boldsymbol{k}}(\eta(t)) = -\frac{ik}{a(t)} v_{\boldsymbol{k}}(\eta(t)). \tag{2.36}$$

Evaluating again at the same initial time t_i than in (2.34) we have, for all modes, that

$$\dot{v}_{\boldsymbol{k}}(t_i) = -\frac{i}{a(t)} \sqrt{\frac{k}{2}}\, e^{-ik\eta(t)}. \tag{2.37}$$

Therefore, from Eqns. (2.34) and (2.37) we have the following real and imaginary initial

[11] In essence, this is like setting t_i such that $k\eta(t_i) = 2n\pi$, with $n \in \mathbb{N}$. This fully satisfies condition i). We can always do that since conformal time is defined up to a constant and therefore is rather arbitrary [161].

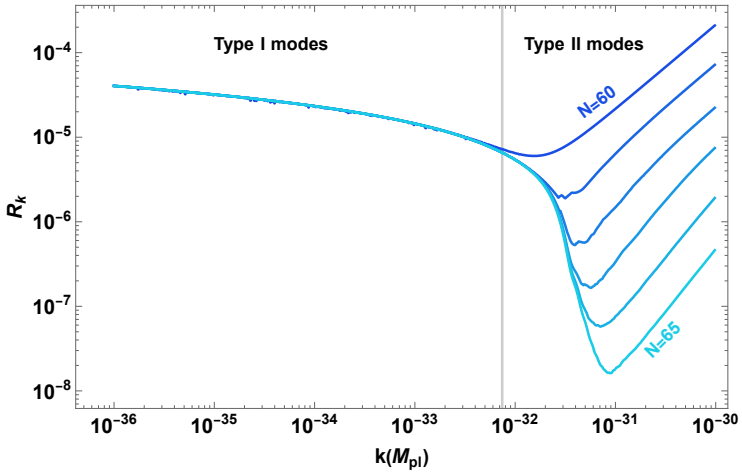

Figure 2.5: Averaged values of curvature perturbation as a function of the comoving wavenumber k evaluated from $N = 60$ (darker blue) to $N = 65$ (lighter blue) and normalized using the factor $k^{3/2}$. The vertical grey line at k_{end} separates the type I from the type II modes. This plot is entirely evaluated numerically.

conditions

$$\text{Re}\left[v_{\boldsymbol{k}}(t_i)\right] = \frac{1}{\sqrt{2k}}, \qquad \text{Re}\left[\dot{v}_{\boldsymbol{k}}(t_i)\right] = 0, \qquad \text{Im}\left[v_{\boldsymbol{k}}(t_i)\right] = 0, \qquad \text{Im}\left[\dot{v}_{\boldsymbol{k}}(t_i)\right] = -\frac{1}{a}\sqrt{\frac{k}{2}}. \tag{2.38}$$

Using these as initial conditions for (A.9) allows us to solve for the MS variable $v_{\boldsymbol{k}}$ and then for the curvature perturbation $\mathcal{R}_{\boldsymbol{k}}$, defined in (A.11). Fig. 2.5 shows the evolution of the comoving curvature perturbation for the two types of modes. In figures 2.5 and 2.6, time grows from the curve marked as $N = 60$ to the curve $N = 65$. Also, all quantities represented in the figures are averaged and normalized with the factor $k^{3/2}$ [35]. We can observe in Fig. 2.5 how, for type I modes, the curvature perturbation is constant (the curves are superposed). This happens because those modes have exited the horizon during inflation. Therefore, the value of the curvature perturbation is frozen, remaining nearly constant even after they enter the particle horizon during the preheating stage. For some type II modes, the curvature perturbation decays as a^{-1}, but as they enter the IB, it evolves towards a constant value (type IIa), whereas for others, the curvature perturbation always decays (type IIb).

Once we have computed $\mathcal{R}_{\boldsymbol{k}}$, we can numerically obtain the density perturbations using Eqns. (A.14) and (A.16). The results are presented in Fig. 2.6. For type I modes, we observe that $\delta_{\boldsymbol{k}}$ grows proportionally to the scale factor as they enter the particle horizon, consistent with Eqn. (2.10). As previously discussed, modes with smaller wavenumbers (k) spend less time inside the horizon, leading to minimal amplification. In contrast, modes with k close to the last scale that exited the horizon, k_{end} (indicated by the vertical grey line in Fig. 2.6), remain sub-Hubble for a longer period, resulting in greater amplification. For type II modes, smaller wavenumbers also experience amplification because the curvature perturbation remains nearly constant while they reside inside IB during pre-

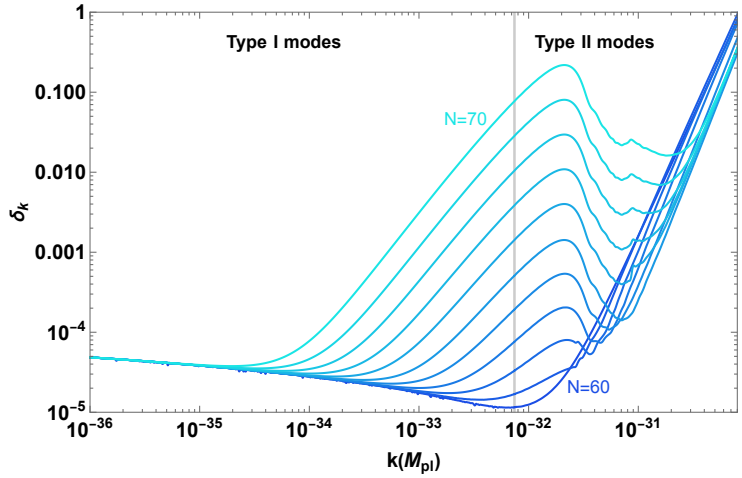

Figure 2.6: Averaged values of density perturbations δ_k as a function of the comoving wavenumber k evaluated from $N = 60$ (darker blue) to $N = 70$ (lighter blue). The vertical grey line at $k_{\rm end}$ separates the type I from the type II modes. This plot is made numerically up to $N = 65$. Then, since at this point the potential (2.1) is well approximated by a quadratic one, we have used the parametric instability described in [45] to extrapolate the evolution of the density perturbations by using the definition of RB.

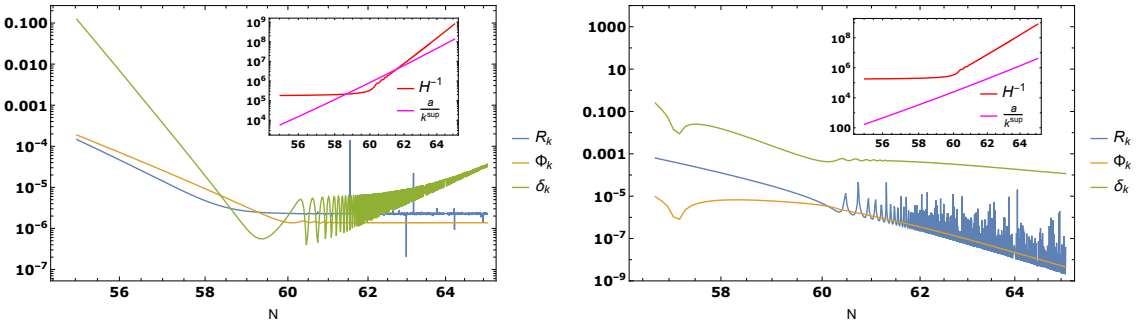

Figure 2.7: a) Evolution of $\mathcal{R}_k$, Φ_k and δ_k during the end of inflation and preheating for a type I mode with comoving wavenumber $k^I = 3 \times 10^{-33} M_{\rm Pl}$. b) The same but for a type II with comoving wavenumber $k^{II} = 10^{-31} M_{\rm Pl}$.

heating. However, as k increases, the perturbations remain approximately constant over time since they are outside the RB, in agreement with Eqn. (2.12).

To have a better understanding, Fig. 2.7 illustrates the evolution of $\mathcal{R}_k$, Φ_k, and δ_k for two specific modes: a type I mode with wavenumber $k^{\rm I} = 3 \times 10^{-33} M_{\rm Pl}$ and a type II mode with $k^{\rm II} = 10^{-31} M_{\rm Pl}$. For the type I mode (Fig. 2.7a), both the curvature perturbation $\mathcal{R}_k$ and the potential perturbation Φ_k remain constant, whereas the density perturbation δ_k grows. On the other hand, for the type II mode (Fig. 2.7b), $\mathcal{R}_k$ and Φ_k decay, while δ_k remains nearly constant.

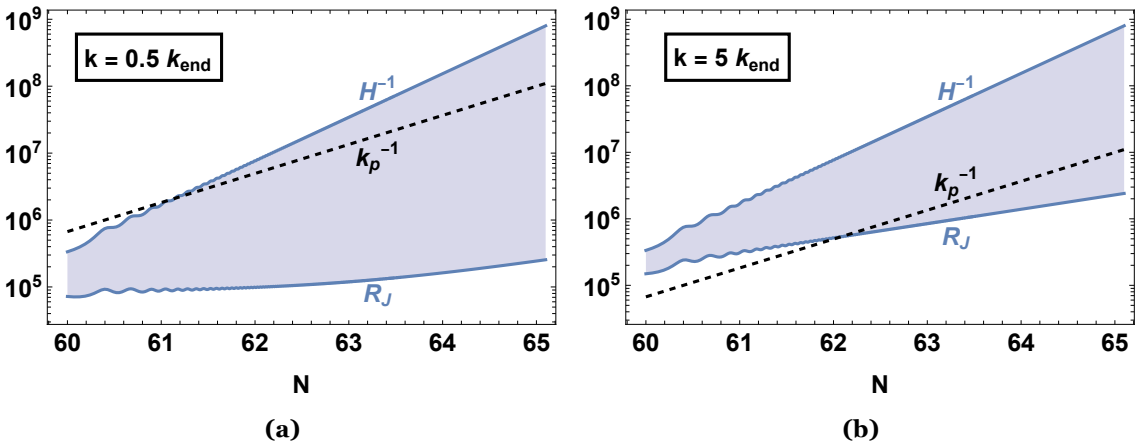

Figure 2.8: Time evolution of Jeans length for two modes (left panel corresponds to a type I mode while the right panel corresponds to a type II mode.

2.3 Numerical characterization of PBH formation

In this section, we give an account of PBH formation in the Starobinsky model, employing numerical calculations. First, we discuss the PS and the KP formalisms and compute the mass fraction. Then, we compute the PBH masses using the critical scaling method for both formalisms.

2.3.1 Mass fraction estimations

We have already defined the IB criterion. However, before going into details on the mass fraction and defining the threshold criterion, we introduce in detail the second criterion used for the selection of modes that can potentially collapse: The Jeans length criterion. From the definition of the Jeans length in Appendix A (see Eqn. (A.30)), we have that perturbations collapse if the following criterion is satisfied

$$R_J < \frac{\lambda_p}{2} < R_H \qquad \Rightarrow \qquad \frac{R_J}{\pi} < \frac{a}{k} < R_H. \tag{2.39}$$

This condition means the only modes that can potentially collapse are those with physical wavelengths two times larger than the Jeans length, and this is what we call the Jeans length criterion. This gives us a lower bound on the wavenumbers we must consider, which might collapse during the preheating. In Fig. 2.8, we show the evolution of R_J/π as a function of the number of e-folds for two different wavenumbers k in the Starobinsky inflationary scenario. We observe that for modes with small k, Jeans length is unimportant since it is too small for them, and thus, as soon as they enter the horizon, they can potentially collapse. However, as we increase k, we see that it takes some time for the mode to grow and be able to collapse. We can notice from Fig. 2.8 that the Jeans length grows at a smaller rate than H^{-1}. This makes some type II modes take some time before they grow enough and can collapse, which provides a physical mechanism to separate the

non-linear regime induced by the smallest scales (high k) from our considerations.

Press-Schechter formalism: This formalism is given by Eqn. (B.13), where the power spectrum for the density perturbations, $\mathcal{P}_\delta(k)$, is defined as

$$\mathcal{P}_\delta(k) = \frac{k^3}{2\pi^2}|\delta_{\boldsymbol{k}}|^2, \tag{2.40}$$

and evaluated at the end of preheating for each mode. As previously said, we will explore different preheating spans. Regarding the threshold values, as stated in Chapter 1, from the original analysis by Carr [79] and Harada [118], one obtains an analytical formula for the threshold as a function of w. However, this is valid just for a perfect fluid formulation and for $w \neq 0$. Since our context is a scalar field during preheating, we will use the formulation given in [45], based on time assumptions, to estimate the threshold. Following the spherical collapse model, the time a perturbation $\delta_{\boldsymbol{k}}$ needs to collapse into a PBH is given by [45, 163]

$$\Delta t_{\rm coll} = \frac{\pi}{H[t_{\rm bc}(k)]\delta_{\boldsymbol{k}}^{3/2}[t_{\rm bc}(k)]}, \tag{2.41}$$

where $t_{\rm bc}(k)$ is the time at which each mode (type I or II) enters the RB. Now, requiring that this time is equal to the time the mode is inside the RB, $\Delta t_{\rm in} = t_{\rm r} - t_{\rm bc}(k)$, where t_r is the end of preheating, one can obtain an estimation for the threshold, the minimum value of $\delta_{\boldsymbol{k}}$ that can produce a PBH, which we call the threshold criterion. Assuming that $\delta_{\boldsymbol{k}} \sim a$, one obtains [45]

$$\delta_c(k) = \left(\frac{3\pi}{2}\right)^{2/3}\left[e^{3(N_{\rm rh}-N_{\rm bc}(k))/2} - 1\right]^{-2/3}, \tag{2.42}$$

where $N_{\rm rh}$ is the number of e-folds at which preheating ends and $N_{\rm bc}(k)$ is the number of e-folds at which a perturbation enters the IB. Note that this equation assumes that $\delta_{\boldsymbol{k}} \sim a$ inside the IB, which is close to the Starobinsky case. However, this growth can be larger for other Starobinsky-like scenarios, such as α-attractors, as shown in Chapters 3 to 5.

Using the PS formalism from (B.13) we have computed in Fig. 2.9 the mass fraction of collapsed objects. We have taken the threshold defined through time constraints using (2.42), and only modes that satisfy (2.39) have been selected. Evaluation is made at different numbers of e-folds, from $N = 71$ to $N = 73$. As can be seen, as we increase the duration of preheating, the mass fraction increases since the modes have more time to collapse. Vertical dashed lines correspond to the smallest scale able to collapse for each duration of preheating and are computed using Jeans length argument. The vertical gray line marks the last scale to exit the horizon during inflation, $k_{\rm end}$. We see that for $k < k_{\rm end}$, we recover the results of [45]. However, in our case, a shorter preheating is enough to obtain a similar mass fraction because of the contribution from type II modes.

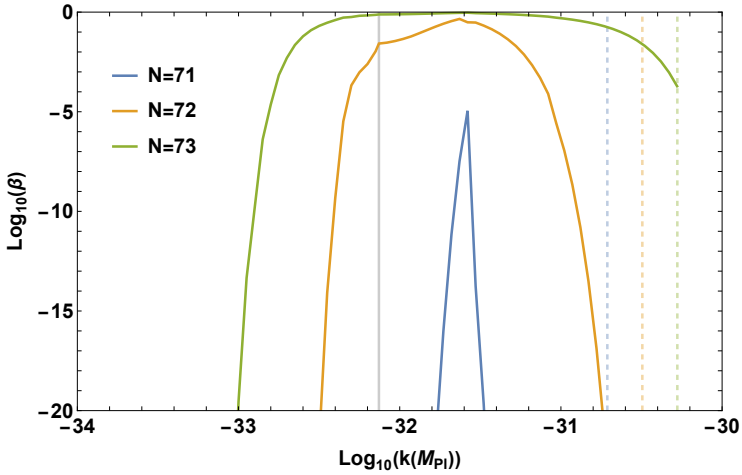

Figure 2.9: Mass fraction of collapsed objects for different durations of preheating, computed using PS formalism. The threshold is obtained through time constraints with (2.41), and only modes that satisfy (2.39) have been selected. Vertical dashed lines correspond to the smallest scale able to collapse at each evaluation step (with the same color code), computed using Jeans length argument.

Khlopov-Polnarev formalism: This formalism, suited for matter-dominated scenarios, is described in Appendix B.2. For small perturbations, we use the anisotropy estimation $\beta^{\rm KP}_{\rm aniso}(\sigma_k \lesssim 10^{-2})$, Eqn. (B.27), whereas for large amplified perturbations we instead use the estimation from inhomogeneity $\beta^{\rm KP}_{\rm inhom}(\sigma_k \gtrsim 10^{-2})$, Eqn. (B.32). To be more consistent, one could use instead the estimation for large perturbations from the anisotropy criterion $\beta^{\rm KP}_{\rm aniso}(k)$, Eqn. (B.28). However, at the moment this investigation was done, the authors were not aware of how this last estimation could be achieved.

Although considering $\beta^{\rm KP}_{\rm inhom}(\sigma_k \gtrsim 10^{-2})$ instead of $\beta^{\rm KP}_{\rm aniso}(k)$ does not take into account the anisotropy effects, which are the dominant ones, it captures the main differences with the PS formalism, which is what we try to show here. Furthermore, both approaches do not differ too much in this regime, so the results are valid in this sense. The estimates are depicted in Fig. 2.10, where we plot the estimates from KP formalism using both approaches (B.27) (continuous) and (B.32) (dahsed). We can notice that the KP formalism is very sensitive to the number of e-folds of preheating. The mass fraction drastically increases as we increase the number of e-folds during the preheating. It is worth noting that the KP formula only applies to the exact matter-dominated era, and the preheating cannot be strictly taken as that. However, given the smallness of the effective equation of state during preheating (see Appendix A.3), we get estimates subjected to negligible effects of non-zero pressure, providing reasonable bounds of PBH formation using the KP formalism. We can see in Fig. 2.11 that for lower values of σ_k the KP formula (B.27) (orange continuous) gives a higher estimate than the PS formalism (B.13) (blue). However, as σ_k increases, the latter has a higher estimate for the PBH abundance, unless the expression for high σ_k, Eqn. (B.32) is used (orange dashed).

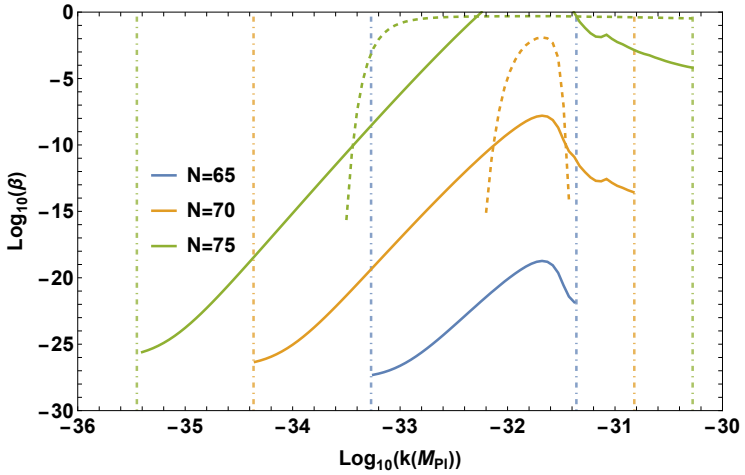

Figure 2.10: KP formalism evaluated for different lengths of preheating. Vertical dotted-dashed lines correspond to the comoving Hubble radius (left) and smallest scale able to collapse (right), computed using Jeans length argument. The color code is the same as for the time steps.

2.3.2 PBH associated mass

Let us turn to determining the mass associated with these PBHs. As shown in Chapter 1, for $\delta_{\boldsymbol{k}} \geq \delta_c$, and $\delta_{\boldsymbol{k}} \simeq \delta_c$, the PBH mass follows a scaling relation with $\delta_{\boldsymbol{k}}$ given by

$$M_{\rm PBH}(k) = M_{\rm H}\kappa(\delta_{\boldsymbol{k}} - \delta_c)^{\gamma}, \tag{2.43}$$

where κ, γ are constants (γ being dependent on the equation of state parameter w), and $M_{\rm H}$ is the horizon mass at the time of PBH formation, which is given by

$$M_{\rm H} = \frac{4\pi}{3}\rho H^{-3} \simeq \frac{4\pi}{3}\rho_{\rm end}a_{\rm end}^3\left(\frac{1}{aH}\right)^3. \tag{2.44}$$

We have used the fact that the energy density, during matter-domination, decays as

$$\rho \simeq \rho_{\rm end}\left(\frac{a}{a_{\rm end}}\right)^{-3}. \tag{2.45}$$

References [113–117, 164–166] present a vast account of numerical studies where (2.43) was derived. Parameter κ ranges from $\kappa \simeq 2.4$ to $\kappa \simeq 12$ [114]. We will consider $\kappa = 4$ to estimate the mass. Regarding the exponent γ, the scenario where $w = 0$ corresponds to a singular point, in the sense stated in [164]. However, in the present case, γ seems to approach a non-vanishing value when $w \to 0$. This situation was first analyzed in [166], where a $\gamma = 0.1057$ was obtained. We will use this value in our numerical evaluation of the PBH-associated mass, accounting for the smallness of our effective equation of state $w_{\rm eff}$ (see App. A.3).

In Fig. 2.12, we illustrate the mass fraction as a function of PBH mass, obtained using (2.43) for the PS and KP frameworks. The modes chosen to create this plot must fulfill

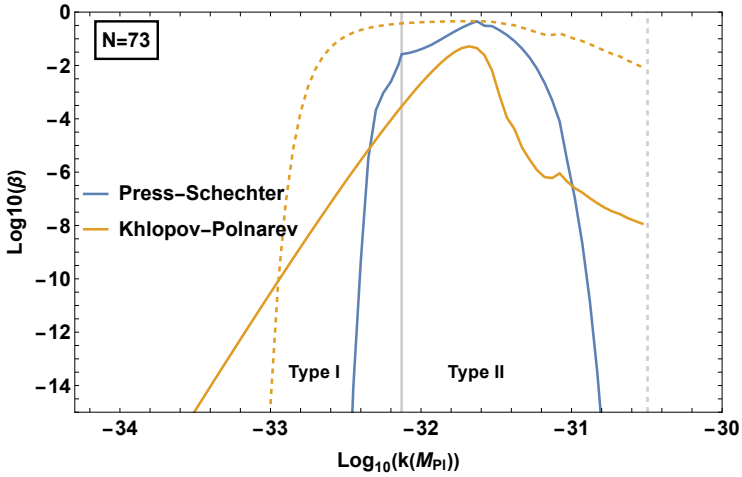

Figure 2.11: Comparison between Press-Schechter formalism (blue) and Khlopov-Polnarev for small σ_k (orange continuous) and for high σ_k (orange dashed). The vertical grey line is at k_{end}, marking the limit between type I and II modes. The vertical grey dashed line is at the smallest scale and can collapse, following Jeans length argument.

two criteria. First, only modes with $\delta_k \gtrsim \delta_c$ are considered, allowing (2.43) to be applied. Second, we must adhere to the Jeans instability requirement, which entails satisfying the inequality (2.39). Further, in Fig. 2.12, it is evident that the mass fraction is somewhat broadly distributed for PS compared to the KP formalism. As we prolong the preheating duration, the PBH mass increases as horizon mass grows over time (see (2.44)), and the shape of $\beta(k)$ does not appear to change notably. We conclude that PBH formation exceeds previous estimates [45] by more than 5 orders of magnitude, even with a reduced preheating duration. This results from the additional non-negligible contribution from the type II modes, which is somewhat anticipated in [45].

2.4 Summary

In this chapter, we carefully revisit the PBH formation criteria during the preheating stage and extend the study made previously in [45]. There, the authors studied PBH formation for type I modes in the context of chaotic inflation, which is ruled out by observations. We instead consider a more realistic scenario, such as the Starobinsky model, and further extend the formation of PBHs to type II modes (smaller scales), see Fig. 2.2 for details. Particularly, we found a subclass of these, type IIa, which behaves identically to type I, since these also fall inside the IB (2.8) and their density contrast grows as $\delta_k \propto a$. The difference between them is that type I modes become super-horizon during inflation and reenter during preheating, whereas type II remain in the subhorizon regime (see the discussion at the beginning of this chapter about their quantum nature). This extension to smaller scales (higher k) highlights the need for a criterion to select the modes able to collapse, and thus to avoid the non-linear regime. To do so, we employ the Jeans length argument (2.39).

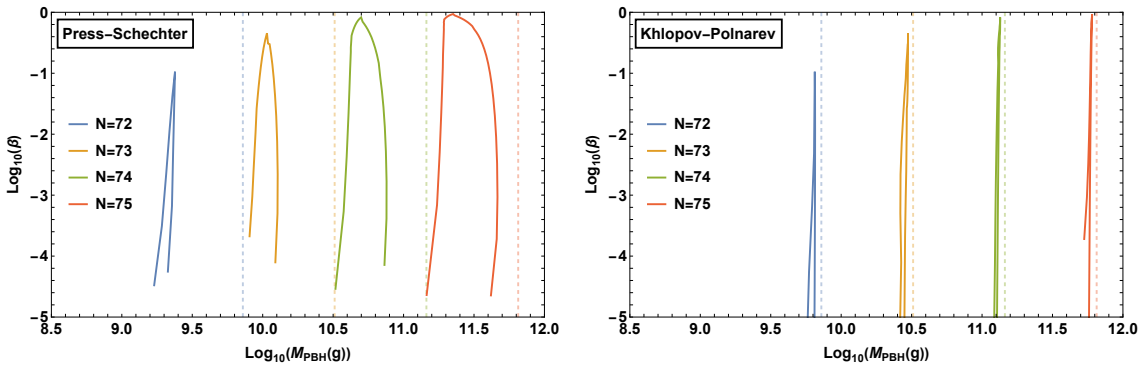

(a) **(b)**

Figure 2.12: Mass fraction of collapsed objects evaluated at different points after inflation for the two estimations under consideration, Press-Schechter (B.13) (a) and Khlopov-Polnarev (B.32) (b). Thresholds are obtained by imposing time constraints by (2.41), and only modes that satisfy (2.39) have been selected. The vertical dotted lines represent the horizon mass at the evaluation time, following the same color code of the mass fractions.

To compute the mass fraction, we employ two formalisms, the standard PS one (B.13), where the threshold is obtained via time assumptions (2.42), and the KP one, where we take the estimations from (B.27) and (B.32), and which is independent of any threshold and considers non-spherical effects. The differences between both formalisms are significant (see Fig. 2.11), especially for small values of perturbations, where the PS rapidly drops to zero. The PBH mass is computed under the critical collapse method (2.43), which is supported by numerical simulations. We found that considering the collapse occurring at the end of preheating, one obtains PBH masses of the order of $10^9 - 10^{12}$g (see Fig. 2.12), with not very much differences between formalisms, apart from a broader distribution for the PS case. Although not large enough, these masses could impact the early history of the universe by dynamical effects such as early accretion, clustering, or merging, as discussed in Chapter 1. Other effects include PBH dominating the universe before evaporating, with the consequent production of gravitational waves, which is the subject discussed in Chapter 6.

This study gives more precise estimates for the mass fraction of PBHs during the inflaton-like matter-dominated era by extending the formation to smaller scales and, also, by considering non-spherical effects in their formation, achieved via the KP formalism.

In the next chapter, we extend the study of the preheating instabilities to the case when the inflationary potential deviates from a quadratic (parabolic) shape. This is explored for the case of the Starobinsky-like inflationary models of α-attractors. Where, for small values of the parameter α, these instabilities are strong.

3

Self-Resonance during preheating in Starobinsky-like models

If you wish to understand the Universe, think of energy, frequency, and vibration.

– Nikola Tesla

At the fundamental level, the evolution of the early universe is governed by oscillations of fields, densities, and perturbations. Particularly interesting is this concept for this chapter, since the oscillatory behavior of the inflaton field at the end of inflation drives the amplification of density perturbations through instabilities. In this way, the physics of preheating resonates with Tesla's vision. To describe these effects, we work in the framework of the Starobinsky-like cosmological models known as α-attractors [167–170], which show an excellent agreement with Planck data [30] and have universal predictions of observables. For this reason, they have gained a lot of attention, as well as from the point of view of supergravity, where they are most naturally formulated. These models are characterized by the positive, real, dimensionless parameter α, where $\alpha = 1$ recovers Starobinsky inflation. Furthermore, for large field values, where the inflationary phase takes place, all these models behave identically to the Starobinsky model [158]. As we saw in Chapter 2, during preheating and due to the oscillations of the scalar field at the bottom of the potential, the density perturbations amplify due to parametric instabilities. This has been extensively studied in the literature, see for instance [41–46], and particularly for the case of the α-attractor models [171–181], where the potential is approximated by a parabola (quadratic). However, as we decrease the value of α in these models, the potential starts to deviate from the quadratic behavior, and the instabilities can be so strong that the non-linearity regime is reached in $\mathcal{O}(1)$ e-folds after the end of inflation, rendering the quadratic approximation as non-valid. In this scenario, the instabilities are called self-resonance effects.

Specifically, and contrary to the usual procedure, our focus lies on the study of the amplification of curvature perturbations through the MS equation. We consider these perturbations to be more relevant from the observational point of view and thus we find it necessary to develop the analytical tools necessary to explain its amplification during preheating. We perform a series expansion of the potential and posterior transformation of the MS equation into a Hill equation [182, 183], which gives us the Floquet's exponents governing the amplification of the perturbations. This Hill equation, which frequently

emerges in the context of preheating, has never been solved (in the context of preheating) including the terms coming from both the cubic and quartic contributions of the expansion of the potential.

The contents of this work are organized as follows. We begin in Section 3.1 by revisiting the α-attractor models. Then, in Section 3.2 we study the effect of self-resonance on a generic potential and compute the Floquet's exponents. Next, in Section 3.3 we show specifically for a T- and E-model the amplification of curvature perturbations and compare the results with a numerical computation. Section 3.4 focuses on the importance of considering higher order terms in the expansion of the potential by comparing with the parabola approximation. Then, Section 3.6 gives some applications and Section3.5 the time until the non-linearity regime is reached. A summary is given in Section 3.7.

3.1 α-attractor models

There are two types of α-attractors, the so-called T- and E-models, whose potentials are given, respectively, by [170]

$$V_T(\phi) = 3\alpha M^2 \tanh^2\left(\frac{\phi}{\sqrt{6\alpha}}\right), \tag{3.1a}$$

$$V_E(\phi) = \frac{3\alpha M^2}{4}\left(1 - e^{-\sqrt{\frac{2}{3\alpha}}\phi}\right)^2. \tag{3.1b}$$

Here, M is the inflaton mass, to be fixed by CMB normalization, ϕ is the scalar field, and α is the parameter characterizing the models, wich has some constraints[12]. Expanding the potentials around $\phi = 0$ we get

$$V_T(\phi) = \frac{M^2}{2}\phi^2 + \frac{\lambda_T}{4}\phi^4 + \dots, \tag{3.2a}$$

$$V_E(\phi) = \frac{M^2}{2}\phi^2 + \frac{\lambda_3}{3}\phi^3 + \frac{\lambda_E}{4}\phi^4 + \dots, \tag{3.2b}$$

where the coefficients of the cubic and quartic terms, responsible for the anharmonic behavior of the field, are given in terms of the parameter α by

$$\lambda_T = -\frac{2M^2}{9\alpha}, \qquad \lambda_3 = -M^2\left(\frac{3}{2\alpha}\right)^{1/2}, \qquad \lambda_E = \frac{7M^2}{9\alpha}. \tag{3.3}$$

[12] In this chapter, we focus just on the mathematical description of the self-resonance. Thus, we do not consider any specific value for α. The bounds on α are described in the next chapter, and here we just restrict to $\alpha > \mathcal{O}(10^{-4})$.

This, as we pointed out above, indicates that decreasing the parameter α enhances the importance of the cubic and quartic terms, even for relatively small values of ϕ. The results obtained here can be extrapolated to any potential whose Taylor expansion is given by a quadratic part + higher order terms.

3.2 Self-resonance for a generic potential

To obtain a general result for both T- and E-models, we will study self-resonance in potentials of the form

$$V(\phi) = \frac{M^2}{2}\phi^2 + \frac{\lambda_3}{3}\phi^3 + \frac{\lambda}{4}\phi^4. \tag{3.4}$$

The analysis is general and valid for every potential that can be written in this form, regardless of the presence of higher-order terms such as ϕ^5, ϕ^6, ...

3.2.1 Perturbation theory for anharmonic oscillators

As shown in Appendix A, the background dynamics of the inflaton field ϕ are governed by the equation of motion of the field (A.2) and Friedmann equations (A.5). After inflation, the friction term in (A.2) is sub-dominant and thus we can neglect it. Later, we will revisit the issue of considering the Hubble expansion. Under this assumption, Eqn. (A.2) can be solved using perturbation theory [182, 183]. Among all the perturbative methods available, we choose to work with the Lindsted-Poincaré Method [182][13]. First, we change the differential equation (A.2) to a time domain where the solution is simple harmonic and of period 2π. This is achieved by considering $\tau = \omega t$, where ω is the real frequency of oscillation of ϕ. Due to the presence of higher-order terms in the expansion of the potential, the frequency is not simply given by $\omega^2 = M^2$. Instead, we parametrize it as $\omega^2 = M^2(1-\beta^2)$, where β is a small, real parameter that carries the information about the departure of the system from quadratic behavior. We are assuming a negative sign in the parametrization of ω^2 due to the negative sign in the parameters λ_T and λ_E, which makes the potential, in general, wider than quadratic, thus decreasing the frequency of oscillations of the field. Next, the field is expanded into powers of the same small parameter β as follows

$$\phi = \beta\,\phi_1 + \beta^2\phi_2 + \beta^3\phi_3 + \dots, \tag{3.5}$$

with initial conditions $\phi_i(\tau_{\rm end}) = \Phi_i$ and $\phi_i'(\tau_{\rm end}) = 0$ for $i = 1, 2, \dots$ and where $\tau_{\rm end} = \omega\, t_{\rm end}$. If we now substitute this expansion into (A.2) and use (3.4), we find that at the

[13] Other methods include the Time Transformation Method [184], the Modified Lindsted-Poincaré Method [185], the Multiple Scales Method [183], or some methods based on Jacobian elliptic functions [186]. We, however, restrict ourselves to the Lindsted-Poincaré method due to its simplicity and good results.

lowest order in β the system behaves as a simple harmonic oscillator

$$\phi_1 = \Phi_1 \cos\tau. \tag{3.6}$$

Now, going to the next order, $\mathcal{O}(\beta^2)$, we observe that ϕ_2 is a combination of the zeroth, first and second harmonics, that is

$$\phi_2 = \frac{\lambda_3 \Phi_1^2}{6M^2}\left(\cos(2\tau) - 3 + 2\cos(\tau)\right) + \Phi_2 \cos(\tau). \tag{3.7}$$

Following the approach of the time transformation method [183–185], the initial conditions for ϕ_i ($i > 1$) can be chosen arbitrarily, as long as the main initial condition $\phi(\tau_{\text{end}}) = \phi_0$ holds. Thus, we can choose the amplitude Φ_2 to cancel out the first odd harmonic. In this sense, the second-order solution contains only even harmonics, which enable us to obtain a more accurate solution [185]. Going now to the next order, $\mathcal{O}(\beta^3)$, we encounter that in the differential equation, there are some terms proportional to $\cos(\tau)$ depending on λ_3 and λ, which produces a secular behavior [182]. This is because some of the driving terms in the differential equation have exactly the fundamental frequency of the system. To avoid this, we choose the following value for the amplitude

$$\Phi_1 = \frac{2M}{\sqrt{3\left|\lambda - \frac{10\lambda_3^2}{9M^2}\right|}}, \tag{3.8}$$

so that now the solution ϕ_3 does not contain secular terms. Choosing again Φ_3 so that it cancels out the first odd harmonic, we obtain a solution for ϕ_3 in terms of just the third odd harmonic as

$$\phi_3 = \Phi_1^3\left(\frac{\lambda}{32M^2} + \frac{\lambda_3^2}{48M^4}\right)\cos(3\tau). \tag{3.9}$$

We find it enough for our purposes to work up to order $\mathcal{O}(\beta^2)$, for which the solution is

$$\phi = \beta\Phi_1\cos(\tau) + \beta^2\frac{\lambda_3\Phi_1^2}{6M^2}(\cos(2\tau) - 3). \tag{3.10}$$

For the initial condition $\phi(\tau_{\text{end}}) = \phi_0$ to hold, we must solve for β at $\tau = \tau_{\text{end}}$ which, as previously said, is the correction to the frequency, which we defined as $\omega^2 = M^2(1-\beta^2)$. Once solved it will be given in terms of the anharmonic terms of the potential, namely λ_3 and λ, and in terms of the amplitude of the field ϕ_0. The larger the amplitude, the larger the correction to the frequency since the anharmonic terms became more dominant. For a small amplitude, we have $\omega^2 \simeq M^2$ and thus we recover the quadratic case (parabolic potential). In this sense, we see that including the friction term, and thus the decay of the field, the correction term β decreases and the system moves towards the quadratic approximation of the potential. Therefore, one can approximate this situation by choosing

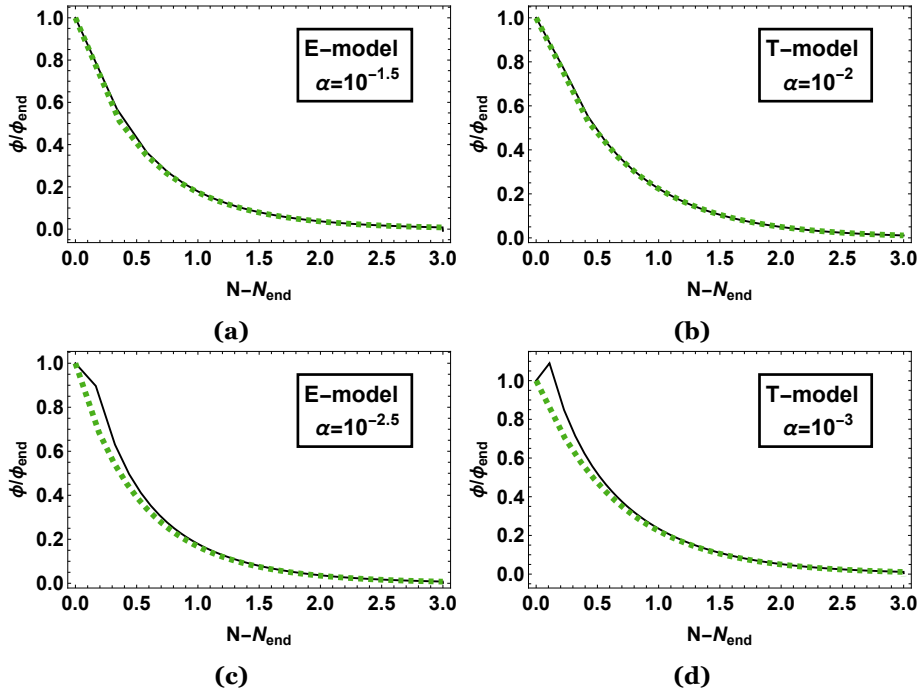

Figure 3.1: Amplitude of the field for E- and T-models with different values of alpha. In each case, the perturbative expansion (3.10) is shown in dotted green and the numerical solution is in continuous black.

a β that decays at the same rate as the field. That is

$$\beta(\tau) = \beta_{\text{end}} \left(\frac{a_{\text{end}}}{a} \right)^{3/2}, \tag{3.11}$$

where β_{end} is obtained from (3.10) at $\tau = \tau_{\text{end}}$ and $a_{\text{end}} = a(\tau_{\text{end}})$. To simplify notation, we omit the argument of β and neglect its derivatives since it is assumed to vary slowly compared to the rate of expansion of the universe. Fig. 3.1 shows the decay of the normalized amplitude of the field for the T- and E-models with different values of α using the perturbative expansion (3.10). For comparison, it has also been included the amplitude of the numerical solution of the equation of motion of the field, eqn, (A.2), which has been solved self-consistently with the Friedmann equation (A.5). As one can observe, the agreement is good, but as we decrease the values of α the analytic and numerical solutions deviate during the first e-fold of preheating. This is due to the lack of higher order terms in the expansion (3.10), which contribute more as α decreases. However, as Fig. 3.2 shows, working up to second order in β is enough for our purposes.

The term $\beta^2 \lambda_3 \Phi_1^2 / 2M^2$ in the solution for ϕ_2 is often called the drift or steady streaming term [183], characteristic of systems with even non-linearities ($\lambda_3 \phi^2$). It carries information about the asymmetry of the potential, since as we observe it is directly proportional to λ_3. Thus we clearly see that the asymmetry of the potential is transferred to the solution of the field, which will have a significant impact on the self-resonance effect, as we will see. For symmetric potentials ($\lambda_3 = 0 \neq \lambda$), this self-resonance effect is not as pronounced as in the asymmetric case, since the solution is given naturally in terms of odd harmonics,

which is closer to the quadratic case.

3.2.2 Floquet theory for perturbations

As we saw in Chapter 2, the MS equation (A.9) allows one to study the perturbations thoroughly. In this chapter, we also work with this equation and transform the MS equation to the time variable $\tau = \omega\, t$. Further, using the perturbative solution found in (3.10), and the expansion of the α-attractor potentials, Eqns. (3.2a) and (3.2b) into (A.9) we obtain, up to order $\mathcal{O}(\beta^2)$

$$\frac{\mathrm{d}^2\tilde{v}_{\boldsymbol{k}}}{\mathrm{d}\tau^2} + \left(A_k + 2q_1\cos(z) + 2p_1\sin(z) + 2q_2\cos(2z) + 2p_2\sin(2z) + h.h.\right)\tilde{v}_{\boldsymbol{k}} = 0, \quad (3.12)$$

where we have used trigonometric power-reduction identities to express the powers of sines and cosines as sums of harmonics. The term $h.h.$ denotes higher harmonics[14], and the coefficients are given by:

$$A_k = \frac{k^2}{a^2M^2} + 1 + \left(1 + \left(\frac{3}{2} + \frac{3\lambda}{2M^2} - \frac{\lambda_3^2}{M^4}\right)\Phi_1^2\right)\beta^2, \quad (3.13a)$$

$$q_1 = \frac{\lambda_3\Phi_1\beta}{M^2}, \quad (3.13b)$$

$$p_1 = -\left(\sqrt{\frac{3}{2}} - \sqrt{\frac{25}{6}}\right)\frac{\lambda_3\Phi_1^2\beta^2}{2M^2}, \quad (3.13c)$$

$$q_2 = \left(\frac{3\lambda}{2M^2} + \frac{\lambda_3^2}{3M^4} - \frac{3}{2}\right)\frac{\Phi_1^2\beta^2}{2}, \quad (3.13d)$$

$$p_2 = -\sqrt{\frac{3}{2}}\Phi_1\beta. \quad (3.13e)$$

To derive (3.12) we have used that the Hubble rate is given up to $\mathcal{O}(\beta^2)$ by

$$H^2 = \frac{1}{3}\left(\frac{\dot{\phi}^2}{2} + V\right) = \frac{\beta^2M^2\Phi_1^2}{6}. \quad (3.14)$$

Additionally, to eliminate the damping term, we rescale the MS variable as $\tilde{v}_{\boldsymbol{k}} = a^{1/2}v_{\boldsymbol{k}}$ [45, 46]. Eqn. (3.12) is known as a Hill equation, a generalization of a Mathieu equation (2.5) [188, 189]. Depending on the values of the parameters A_k, q_i, and p_i the physical modes $(k/a)^{-1}$ experience instability or stability as they evolve and thus using Floquet Theory, we can study the amplification of perturbations.

Following Floquet's theorem, the re-scaled MS variable evolves as $\tilde{v}_{\boldsymbol{k}} \sim \exp\left[\int \mu_k(\tau)\mathrm{d}\tau\right]$ [43], where μ_k are the so-called *Floquet exponents*. For $\Re(\mu_k) > 0$ we have exponential growth and the mode is said to be unstable. The Floquet exponents of the Hill equation

[14] We do not consider higher harmonics since doing so would introduce a higher order in β when calculating the Floquet exponent [187]

are generally unknown but can be computed using the harmonic balance method [183], where the MS variable $\tilde{v}_{\boldsymbol{k}}$ is expanded into harmonics as

$$\tilde{v}_{\boldsymbol{k}} = \sum_{n=0}^{\infty} e^{in\tau} C_n(\tau). \tag{3.15}$$

By substituting this into (3.12) and expressing the trigonometric functions as complex exponential functions, the following recurrence relation is obtained

$$\begin{aligned} C_n' = \frac{i}{2n}\Big[&(A_k - n^2)C_n + q_1(C_{n+1} + C_{n-1}) + ip_1(C_{n+1} - C_{n-1}) \\ &+q_2(C_{n+2} + C_{n-2}) + ip_2(C_{n+2} - C_{n-2})\Big], \end{aligned} \tag{3.16}$$

where we are neglecting the C_n'' since we assume that C_n are slowly varying compared to the rate of expansion of the universe. The first instability band emerges from examining the fundamental frequencies $n = \pm 1$ in (3.16). Typically, to order β^2, the coefficients $C_{\pm 1}$ are coupled just to each other. However, in our case, the presence of q_1 and p_1, along with q_1 and p_2 being of order β, the coefficients $C_{\pm 1}$ are being coupled to C_0, $C_{\pm 2}$ and $C_{\pm 3}$ to order β^2. This additional coupling complicates the computation of the Floquet exponents. Nonetheless, we have found that it suffices for our purposes to consider the fundamental frequencies $n = \pm 1$ and their corresponding couplings with the nearest harmonics $n = 0, 2$ and $n = -2, 0$, respectively, up to order β^2. By doing this, we derive the following differential matrix equation

$$\begin{pmatrix} C_1' \\ C_{-1}' \end{pmatrix} \simeq \frac{i}{2} \begin{pmatrix} A_k - 1 - \frac{q_1^2+p_1^2}{A_k} - \frac{q_1^2+p_1^2}{A_k-4} & q_2 - ip_2 - \frac{(q_1-ip_1)^2}{A_k} \\ -q_2 - ip_2 - \frac{(q_1+ip_1)^2}{A_k} & 1 - A_k + \frac{q_1^2+p_1^2}{A_k} + \frac{q_1^2+p_1^2}{A_k-4} \end{pmatrix} \begin{pmatrix} C_1 \\ C_{-1} \end{pmatrix}. \tag{3.17}$$

Finally, the Floquet exponents $\mu_k(\tau)$ are given by the eigenvalues of this matrix. Up to order β^2, these are given by:

$$\begin{aligned} \mu_k = \frac{1}{2}\Bigg[&q_2^2 + p_2^2 - (A_k - 1)^2 + 2q_1^2\Big(\frac{A_k - 1}{A_k} + \frac{A_k - 1}{A_k - 4} - \frac{q_1^2}{2(A_k-4)^2} - \\ &- \frac{q_1^2}{A_k(A_k-4)}\Big) + 2p_1^2\left(\frac{A_k - 1}{A_k} + \frac{A_k - 1}{A_k - 4}\right) - \frac{2q_1^2 q_2}{A_k} - \frac{4p_1 p_2 q_1}{A_k}\Bigg]^{1/2}. \end{aligned} \tag{3.18}$$

Using (A.11), we can relate the MS variable to the comoving curvature perturbation $\mathcal{R}_{\boldsymbol{k}}$ by

$$\mathcal{R}_{\boldsymbol{k}} = \frac{v_{\boldsymbol{k}}}{\sqrt{2\varepsilon}a} = \frac{\tilde{v}_{\boldsymbol{k}}}{\sqrt{2\varepsilon a^3}}, \tag{3.19}$$

Eqns. (3.18) and (3.19) give us the time-evolution of the curvature perturbation as a function of the anharmonic coefficients of the potential. This allows us to efficiently give an estimation of the amplification of perturbations along with the position of the peak in terms of the comoving wavenumber k. The Floquet's exponents of the curvature perturbations are, to our knowledge, shown for the first time for an inflationary potential presenting

both cubic and quartic terms in its expansion. This implies a great advantage from the numerical point of view since traditionally the codes designed to compute Floquet's exponents must deal with highly oscillatory functions that increase the computational time and become rather inefficient. From (3.19) we see that when the amplification of $\tilde{v}_{\boldsymbol{k}}$ exceeds $a^{3/2}$, the curvature perturbation will grow. Typically, for potentials close to parabolic, this amplification is as high as $a^{3/2}$, causing $\mathcal{R}_{\boldsymbol{k}}$ to remain approximately constant for the modes inside the instability band [45].

3.3 Characterization of self-resonance

Here we present the specific Floquet's exponents for both T- and E-models and compare them with numerical results. These findings can be generalized to any potential whose expansion around $\phi = 0$ matches either the expansion of a T- or an E-model.

3.3.1 T-model

In this case we have that $\lambda_3 = 0$ and thus $q_1 = p_1 = 0$, which greatly simplifies the expression for the Floquet's exponent

$$\mu_k^{(T)} = \frac{1}{2}\sqrt{q_2^2 + p_2^2 - (A_k - 1)^2}. \tag{3.20}$$

To check the validity of this approximation, we have computed the curvature perturbations numerically, using (A.9) with Bunch-Davies initial conditions and (3.19). Then, we have used the Floquet theory derived here, where the scale factor, needed to parametrize the decay of the field, is obtained by self-consistently solving the Friedmann equation (A.5), together with the equation of motion of the field (A.2). This is important, since considering that the time dependence of the scale factor follows a matter-dominated power-law, that is, $a \sim t^{2/3}$, is incorrect during the first e-folds of preheating, which is precisely where this study mainly focuses. Both methods are evaluated 5 e-folds after the end of inflation. Results are displayed in Figs. 3.2b and 3.2d for $\alpha = 10^{-2}$ and $\alpha = 10^{-3}$ and it shows a good agreement between both methods. Going to smaller values of α implies entering into the non-linear regime, where perturbations backreact and spoil the linear evolution. See Section 3.5 for further details and a comparison with previous estimations. The peaks to the right of the highest peak in Fig. 3.2 correspond to the amplification in higher instability bands. One could study these bands by considering the frequencies $n = \pm 2, \pm 3 \ldots$ and their corresponding couplings. However, to do so, one has to increase each time the order in ε, increasing the number of harmonics that come into play. We find it sufficient for our purposes to focus on the first instability band, as it is where the amplification is most pronounced. Finally, in Fig. 3.3a we display $\Re(\mu_k^{(T)})$ for $\alpha = 10^{-2.5}$ as a function of q_2 and A_k, as well as the trajectories of some modes in the (q_2, A_k) plane.

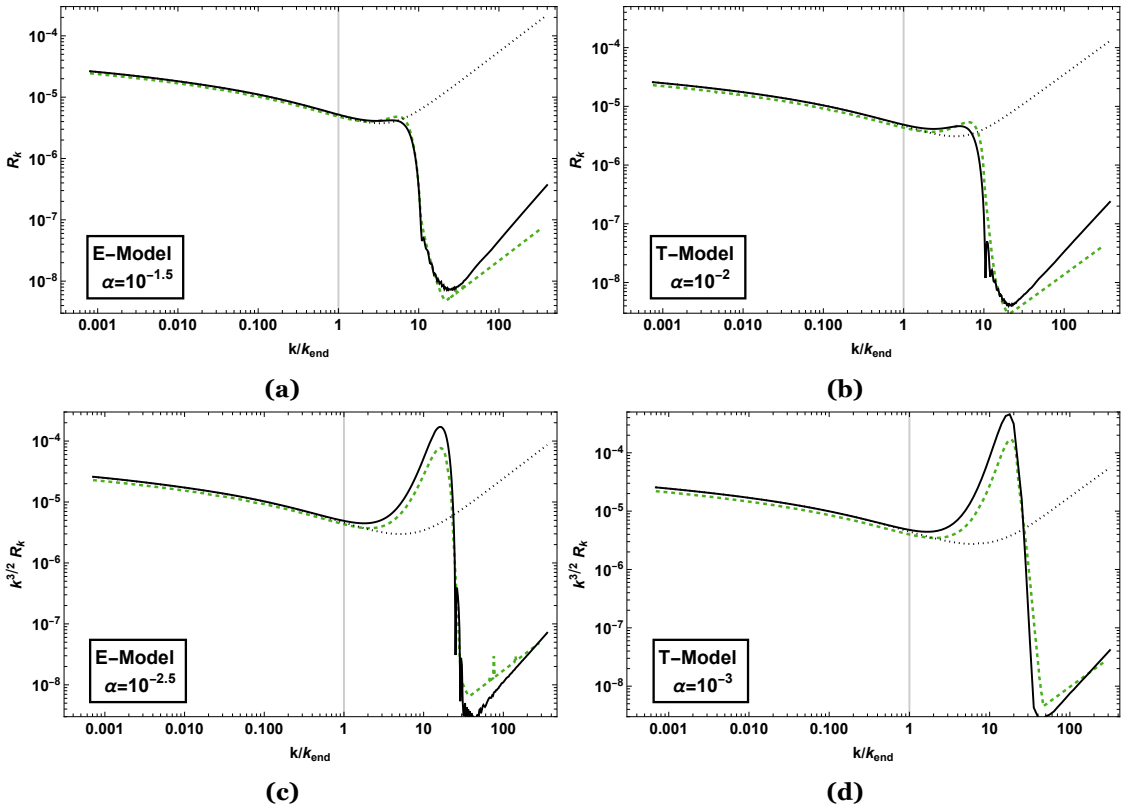

Figure 3.2: Curvature perturbations for **(a)** E-Model $\alpha = 10^{-1.5}$, **(b)** T-Model $\alpha = 10^{-2}$, **(c)** E-Model $\alpha = 10^{-2.5}$ and **(d)** T-Model $\alpha = 10^{-3}$ evaluated 5 e-folds after the end of inflation. Numerical computation is shown in continuous black and Floquet theory as described in this work in dashed green. The vertical grey line marks the scale that exits the horizon at the end of inflation, $k_{\rm end}$. For comparison, black dotted curves show the numerical computation of curvature perturbations at the end of inflation.

We remark that in Fig. 3.3a, $p_2 = 0$ and thus the $\mu_k^{(T)}$ shown does not correspond to the real time-evolution. However, it is enough to understand why the peak is produced for scales around $k \simeq 10\, k_{\rm end}$. Those scales cross the (q_2, A_k) plane throughout the maximum of $\mu_k^{(T)}$. Also, it is possible to give an analytical estimation of the position of the peak from the Floquet's exponent (3.20). For $k < k_{\rm end}$, all scales show the same evolution in the (q_2, A_k) plane. This is the reason why all of them are amplified by the same amount.

3.3.2 E-model

Now we have that $\lambda_3 \neq 0$ and thus the expression for the Floquet exponent is the full one given in (3.18), we will call it $\mu_k^{(E)}$. Figs. 3.2a and 3.2c display the curvature perturbations computed using the same method as in Figs. 3.2b and 3.2d (see previous section), this time for the E-model and for $\alpha = 10^{-1.5}$ and $\alpha = 10^{-2.5}$. Despite a numerical factor of $\mathcal{O}(1)$ of discrepancy between the numerics and Floquet theory, we find it enough to explain at which scales occur the maximum amplification, which could be also obtained analytically from the full expression (3.18). The discrepancy between numerics and the analytical result could be because we are neglecting some higher harmonics, which in

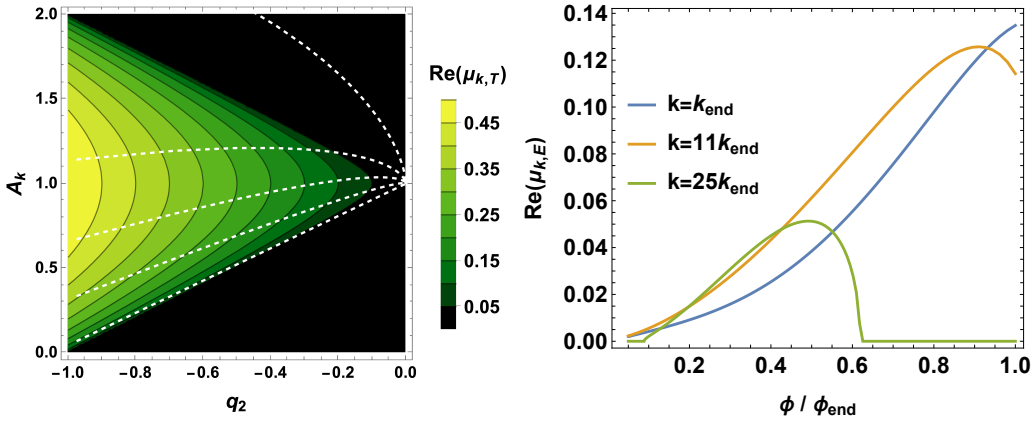

(a) **(b)**

Figure 3.3: (a) Floquet chart for a T-model with $p_2 = 0$ (just for graphical purposes) and $\alpha = 10^{-2.5}$. White dashed lines correspond to the evolution of the modes in the (q_2, A_k) plane and are, from bottom to top: 1, 10, 15, 20, 30, in units of $k_{\rm end}$. **(b)** Evolution of $\Re(\mu_{k,E})$ for an E-model with $\alpha = 10^{-2.5}$ as a function of the amplitude of the field and for different values of k.

the case of the E-model could contribute more significantly than in the T-model, as well as more couplings between them. We have observed analytically and also numerically that the amplification of $\mathcal{R}_{\boldsymbol{k}}$ is higher for the E-model compared to a T-model with the same value of α. This is due to the asymmetry of the potential since the perturbative solution for the E-model has even harmonics and, particularly, a drift term that appears already at order β^2. This fact makes the Floquet's exponent (3.18) have more contributions that enhance the amplification of the perturbations. Additionally, we have also observed that the position of the peak of maximum amplification is at higher k for the E-model, compared to a T-model with the same α. Now, regarding the time evolution of $\mu_k^{(E)}$ for each k-mode, a plot like Fig. 3.3a would not be sufficiently illustrative, given that $\mu_k^{(E)}$ depends on 5 parameters. This makes it challenging to understand why the peak is around $k \sim 11\, k_{\rm end}$. Instead, Fig. 3.3b shows $\Re(\mu_k^{(E)})$ for $\alpha = 10^{-2.5}$ as a function of the amplitude of the field for different values of k, expressed in units of $k_{\rm end}$. Here, we observe that for scales around $k \simeq 11\, k_{\rm end}$, the Floquet exponent exceeds that of other k-modes, resulting in higher amplification.

3.4 Contrast with quadratic approximation

During preheating, the potential is usually approximated by a parabola ($\lambda_3 = \lambda = 0$), where the solution for the field is just given by $\phi \simeq \phi_{\rm end} \left(\frac{a_{\rm end}}{a}\right)^{3/2} \cos(\tau)$ [42–46]. Considering this and keeping just the dominant terms, (A.9) is easily reformulated into the following Mathieu equation

$$\tilde{v}_{\boldsymbol{k}}'' + \big(A_k + 2p_2 \sin(2z)\big)\tilde{v}_{\boldsymbol{k}} = 0, \tag{3.21}$$

where now $\tau = Mt$ and

$$A_k = \frac{k^2}{a^2 M^2} + 1, \qquad p_2 = -\sqrt{\frac{3}{2}}\phi_{\text{end}} \left(\frac{a_{\text{end}}}{a}\right)^{3/2}. \tag{3.22}$$

Following the steps of Section 3.2.2, the Floquet exponent is given by

$$\mu_k^{(Q)} = \frac{1}{2}\sqrt{p_2^2 - (A_k - 1)^2}. \tag{3.23}$$

Let us now introduce the concept of *instability scale*, denoted as l_{inst}, which represents the spatial scale above which $\tilde{v}_{\boldsymbol{k}}$ experiences growth. For this growth to occur, the Floquet exponent must be real and positive. Imposing this in (3.23) and solving for $\left(k/a\right)^{-1} \sim l_{\text{inst}}$, one obtains

$$l_{\text{inst}}^{(Q)} = \frac{1}{M}\left(\frac{2}{3\phi_{\text{end}}^2}\left(\frac{a}{a_{\text{end}}}\right)^3\right)^{1/4} \simeq \frac{1}{\sqrt{3HM}}. \tag{3.24}$$

This is the standard preheating scenario. However, this approximation is not accurate for some potentials, even if they behave as quadratic at first order, such as the case of α-attractors with $\alpha \ll 1$. Fig. 3.4 corroborates this fact. It shows the Floquet exponent for both the T- and E-models and compares, in each case, $l_{\text{inst}}^{(Q)}$ (dashed red) with the corresponding spatial scale $l_{\text{inst}}^{(T,E)}$ (cyan) of the full expansion (3.4). For the T-model, imposing again that $\Re\left(\mu_k^{(T)}\right) > 0$ in (3.20) we obtain

$$l_{\text{inst}}^{(T)} = 2\left(-(4M^2 + 6M^2\Phi_1^2 + 6\lambda\Phi_1^2)\varepsilon^2 + \sqrt{24M^4\Phi_1^2\varepsilon^2 + 9(M^2 - \lambda)^2\Phi_1^4\varepsilon^4}\right)^{-1/2}. \tag{3.25}$$

Looking at the expression for $\mu_k^{(E)}$, Eqn. (3.18), one can observe the difficulty in obtaining an analytical expression for the instability scale in this case. For that reason, in Fig. 3.4b, $l_{\text{inst}}^{(E)}$ is obtained numerically. White dotted lines represent the evolution of the physical modes (from left to right), and at the moment those modes cross the instability scale, they start to amplify. These crossing points are different if one uses the full expansion (3.4) or just the quadratic term, pointing out the importance of considering higher-order terms. Moreover, the enhancement of perturbations can be physically explained with the negativity of the coefficients of the expansion, λ_3 or λ_T. If we treat them as self-interactions of the field, a negative coefficient implies an attractive force, which induces a negative pressure and makes some modes unstable. Nonetheless, as the field decays, the cubic and quartic terms of the expansion (3.4) became less dominant and one recovers the usual preheating scenario [1, 42–46] where the potential is well approximated by a parabola and $\tilde{v}_{\boldsymbol{k}} \sim a^{3/2}$. This can be seen in Fig. 3.4a, where for small amplitudes of the field $l_{\text{inst}}^{(Q)} \sim l_{\text{inst}}^{(T)}$. For Fig. 3.4b, one should go to smaller amplitudes to have this parallelism. Both of these figures are made using $\alpha = 10^{-2.5}$. Lastly, it is important to note that not all perturbations with $\left(k/a\right)^{-1} > l_{\text{inst}}$ undergo amplification. The upper limit is set by the Hubble

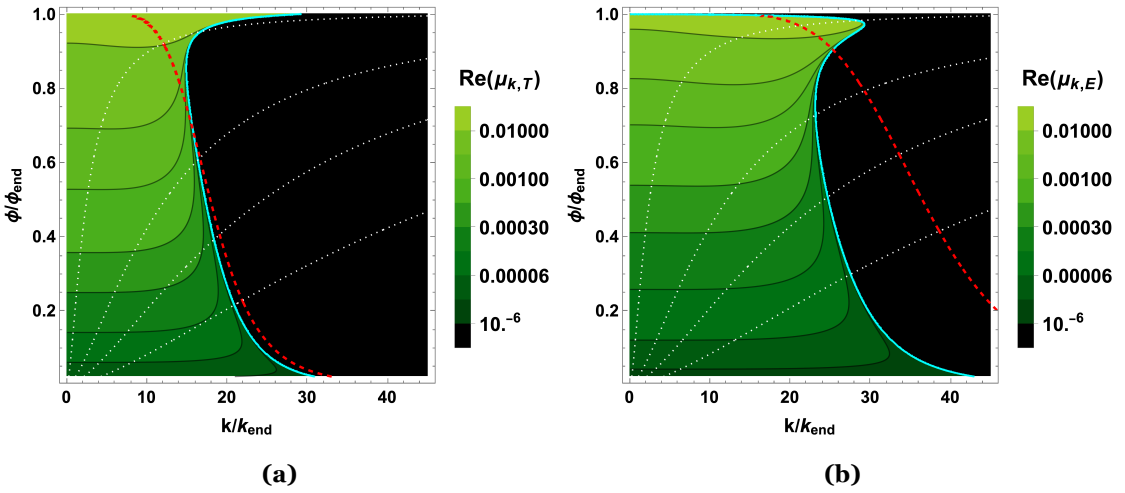

Figure 3.4: Floquet exponents for **(a)** T-model and **(b)** E-model with $\alpha = 10^{-2.5}$ as a function of physical wavenumbers and field amplitudes. Red dashed lines represent the instability scale (3.24) and continuous cyan lines the corresponding instability scales for the full expansion (3.4). For the T-model, this last is given by (3.25), whereas for the E-model is obtained numerically. White dotted lines mark the evolution of the physical k-modes. The black region represents the points where $\Re(\mu_k^{(T,E)}) = 0$.

radius $R_H = H^{-1}$ and the set of modes defined by $R_H > \left(k/a\right)^{-1} > l_{\rm inst}$ is what we have been refering to as *instability band* (IB). Figs. 3.5a and 3.5b show the IB (blue shaded area) for a T- and an E-model with $\alpha = 10^{-2.5}$, respectively. We see again that, for the T-model, $l_{\rm inst}^{(T)}$ approaches $l_{\rm inst}^{(Q)}$ sooner than in the E-model case. This is mainly because the former one is closer to the parabola, given the absence of the asymmetric coefficient λ_3. Suppose we neglect the higher-order terms in the expansion of the potential. In that case, we are not considering the amplification of some modes that enter the IB around the beginning of preheating, indicated by the lower gray dashed lines, which could lead to wrong estimations.

3.5 Backreaction and non-linearity

The α-attractor models have been studied in the context of parametric resonance. See, for instance, [171–174]. Typically, these works employ lattice methods to compute the growth of scalar field perturbations, $\delta\phi_{\boldsymbol{k}}$. Once these perturbations reach $\mathcal{O}(1)$, they start to backreact on the field evolution, leading to its rapid decay. However, a common limitation of lattice methods is that, although they consider the non-linear evolution of $\delta\phi_{\boldsymbol{k}}$, they often neglect metric fluctuations, $\Phi_{\boldsymbol{k}}$, which can influence the overall evolution of the perturbations. In contrast, the approach of this work is restricted to the linear regime but considers both field and metric fluctuations.

The main intention of this section is twofold. First, we want to find the exact point where the linear analysis of our approach becomes not valid and improve earlier estimations in this context by considering the evolution of the MS variable $v_{\boldsymbol{k}}$, which contains both metric

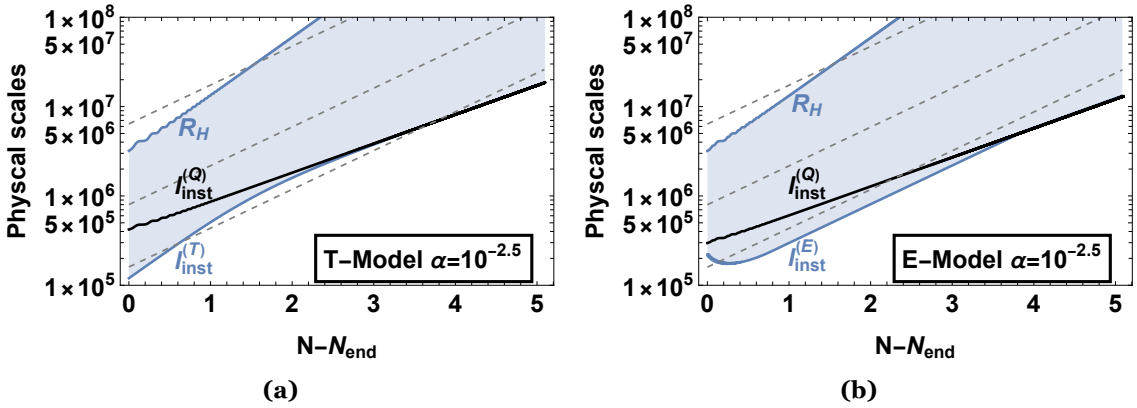

Figure 3.5: Instability band (blue shaded area) and instability scales, $l_{\rm inst}$, for the quadratic case and for a **(a)** T-model and **(b)** E-model. Also plotted are the Hubble radius R_H and the evolution of some physical modes $(\frac{k}{a})^{-1}$ (gray dashed lines). The horizontal axis represents the number of e-folds elapsed from the end of inflation.

and field fluctuations, and is related to the curvature perturbation $\mathcal{R}_k$ (see Eqn. (3.19)). Second, we want to highlight the limitations of some of the lattice methods that ignore metric fluctuations.

For comparison, Fig. 3.6a shows the number of e-folds, ΔN_{nl}, until non-linearity (backreaction) is reached for both T- and E-models and different values of α, computed using Floquet theory. The evolution is tracked for 5 e-folds after the end of inflation and the results in Fig. 3.6a demonstrate that the non-linearity regime is reached within $\mathcal{O}(1)$ e-fold, except for $\alpha > 10^{-3}$. For such values, while self-resonance is still significant, perturbations do not grow sufficiently to reach non-linearity, as can be seen from Fig. 3.2. Conversely, for smaller values of α, the non-linearity regime is reached more quickly, within $\mathcal{O}(1)$ e-fold. Although this estimation is similar to the one provided in [174], around Eqns. 10-14, our analysis makes the distinction between the T- and E-models clearer, as it considers a polynomial expansion of the potential instead of a monomial or parabolic approach (see for instance Eqns. 2-4 of [174]). In this sense, Fig. 3.6a shows that, due to the asymmetry in the E-model, perturbations amplify faster, reaching the non-linearity regime earlier. Nonetheless, for $\alpha < 10^{-4}$, both models exhibit similar behavior.

To further clarify the point, we present in Fig. 3.6b the curvature perturbations for a T-model, evaluated 0.5 e-folds after the end of inflation, for several values of the parameter α. We observe that as α decreases, the growth of the curvature perturbations become significantly more pronounced within the same time interval, reaching the non-linear regime sooner (pointing where our analysis cease to be valid). While our semi-analytical approach has limitations, as it ignores the non-linear interactions among the perturbations, it is specifically designed to probe the linear regime, where the equations governing the system remain tractable and the influence of metric perturbations can be consistently included.

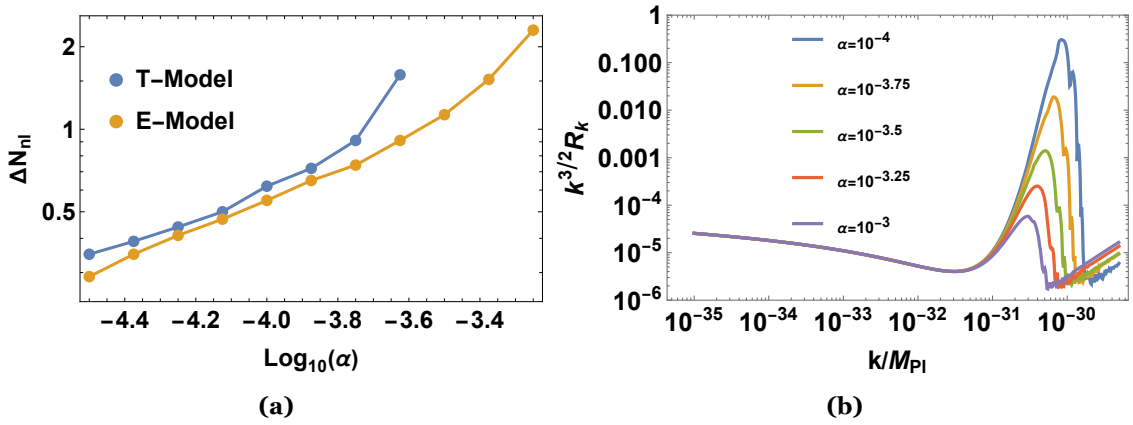

(a) **(b)**

Figure 3.6: (a) Number of e-folds, ΔN_{nl}, until non-linearity (backreaction) regime is reached as a function of the parameter α and for both T- and E-models. **(b)** Curvature perturbations for a T-model evaluated at 0.5 e-folds after the end of inflation for several values of the parameter α.

We performed a series of lattice simulations to shed some light on this argument. Due to its ease of use, we choose to work with the publicly available $\mathcal{C}\texttt{osmo}\mathcal{L}\texttt{attice}$ code [190,191]. In all simulations, we used a lattice size of $N = 128$, with an infrared cut-off of $\tilde{k}_{IR} = 0.05$, and parallelized computations across 8 cores. To facilitate the numerical simulations, we introduced the following dimensionless variables:

$$\tilde{\phi} = \frac{\phi}{M_P}, \qquad \tilde{k} = \frac{k}{M}, \qquad \mathrm{d}\tilde{t} = M\,\mathrm{d}t, \qquad \mathrm{d}\tilde{x}^i = M\,\mathrm{d}x^i, \tag{3.26}$$

where M_P is the Planck mass and M the mass of the scalar field. For further details, refer to the $\mathcal{C}\texttt{osmo}\mathcal{L}\texttt{attice}$ documentation [190, 191].

Fig. 3.7 shows the computation of the field perturbations $\delta\phi_k$ for two models, a T-model with $\alpha = 10^{-4}$ in Fig. 3.7a, and a E-model with $\alpha = 10^{-2.5}$ in Fig. 3.7b. For the former one, since $\alpha < 10^{-3}$, we see that at $N - N_{\text{end}} \sim 0.5$ the non-linearity regime is reached since the spectrum of perturbations loses its peaked shape and smooths, which confirms our results from Fig. 3.6a in the sense of the time until non-linearity is reached. This is explained as follows. Just after the end of inflation, the resonance is strong and around a specific scale. However, as time evolves, and due to the backreaction, the modes start to interact with each other, leading to a redistribution of the energy across different scales, which flattens the spectrum. At this point, our analysis would not be valid anymore, since we enter the non-linear regime. However, the lattice approach, which does go non-linear is not valid either, because it ignores metric fluctuations. As we can see in Fig. 3.6b, curvature perturbations are strongly amplified to $\mathcal{O}(1)$ for $\alpha < 10^{-3}$ and can influence the dynamics during preheating. A full non-linear numerical treatment of both metric and field fluctuations would clarify further this scenario. We leave this for future work.

For the E-model case, where $\alpha > 10^{-3}$, the non-linearity regime is not reached, consistent again with our predictions from Fig. 3.6a. This is evident from the fact that the perturbation spectrum retains its peaked structure as it evolves in Fig. 3.7b. This figure resembles

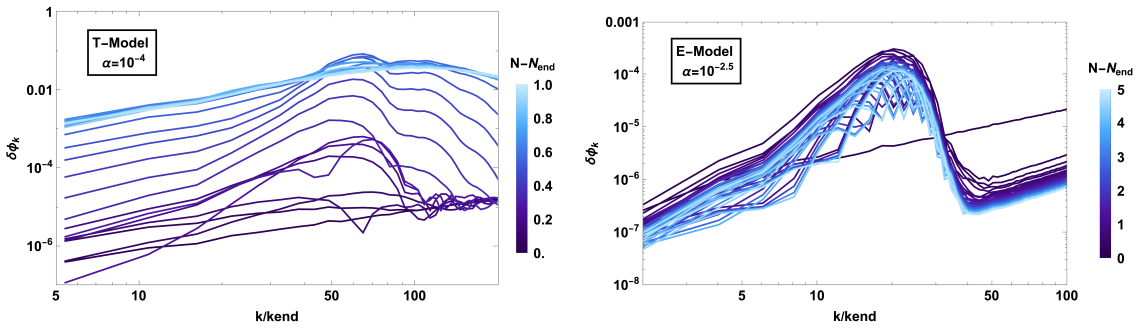

(a) **(b)**

Figure 3.7: Lattice simulations during preheating for **(a)** a T-model with $\alpha = 10^{-4}$ and **(b)** an E-model with $\alpha = 10^{-2.5}$. See text for specifications.

Fig. 3.2c, since the perturbations in both cases reach similar amplifications and around the same wavenumber $k/k_{\rm end} \sim 10 - 20$. Therefore, Fig. 3.7 suggests that the analytical method developed in this work is in good agreement with the numerical lattice simulations, when both approaches remain within linear perturbation theory.

3.6 Applications

Floquet theory offers a significant advantage: it allows us to forget about numerical computations and use the analytical results to estimate how the curvature perturbations are amplified. This approach accelerates computations, which typically imply long computational times associated with the highly oscillatory regime of preheating. Furthermore, the amplification process can lead to intriguing phenomena, as we briefly outline in the following discussion.

- ***Primordial Black Holes***: Using general relativity one can study the collapse into a black hole (BH) of a real, minimally coupled, massive scalar field in an asymptotically Einstein-de Sitter spacetime background. In [45, 163, 192] and Chapter 2, it is shown that density perturbations $\delta\rho_{\boldsymbol{k}}$ can collapse into a BH provided that the time the k-mode spends inside the IB exceeds the time it needs to collapse, defined as

$$\Delta t_{\rm coll} = \frac{\pi}{H[t_{\rm bc}(k)]\delta_{\boldsymbol{k}}^{3/2}[t_{\rm bc}(k)]}, \tag{3.27}$$

  which we called the threshold criterion. In our specific scenario, perturbations amplify faster with decreasing α values. This suggests that PBHs form more rapidly and consequently with smaller masses. However, a critical threshold should exist where PBHs may become overproduced, thereby establishing a lower bound for α. This is explored in Chapter 4.

- ***Scalar-Induced Gravitational Waves***: At third-order in the perturbed expansion of the action, the scalar perturbations couple to the tensor ones, inducing the production of GWs [193–195]. The resulting differential equation for the tensor perturbations $h_{\boldsymbol{k}}(\eta)$ in conformal time t is given by

$$h''_{\mathbf{k}}(\eta) + 2\mathcal{H}h'_{\mathbf{k}}(\eta) + k^2 h_{\mathbf{k}}(\eta) = \mathcal{S}(\mathbf{k}, \eta), \tag{3.28}$$

  where $\mathcal{H} = aH$ is the conformal Hubble rate and $\mathcal{S}(\mathbf{k}, \eta)$ is the so-called source function, which directly depends on the metric scalar perturbation $\Phi_{\boldsymbol{k}}$. This last can be related to the curvature perturbation $\mathcal{R}_{\boldsymbol{k}}$ [1] and thus with $v_{\boldsymbol{k}}$, which again suggests that for decreasing values of α the fractional energy density of GWs, $\Omega_{\rm GW}(k)$, can be high enough to reach the range of detection of some actual and future GWs detectors [149, 196]. The fractional energy density is defined as [193]

$$\Omega_{\rm GW}(k) \equiv \frac{1}{\rho}\frac{\mathrm{d}\rho_{\rm GW}}{\mathrm{d}\ln k} = \frac{k^2}{12\mathcal{H}^2}\sum_{\theta}\mathcal{P}_{h,\theta}(k), \tag{3.29}$$

  where $\rho_{\rm GW}$ is the energy density of GWs and $\mathcal{P}_{h,\theta}(k)$ the power spectrum of tensor perturbations, with θ accounting for both polarization states. This is explored in Chapter 5.

3.7 Summary

This chapter introduces an analytical model to explain the amplification of curvature perturbations at small scales during the post-inflationary preheating phase, based on the phenomenon of self-resonance. We consider both symmetric and asymmetric inflationary potentials, *i.e.*, T and E-models [167–170]. Initially, we solve perturbatively for the inflaton field and expand the inflationary potential up to fourth order. Then, we transform the MS equation into a Hill's one (3.12) and provide an explicit formula (3.18) for Floquet's exponents of the MS variable. The analytical results allow us to estimate, avoiding time-consuming numerical codes, the magnitude of the amplification of curvature perturbations during preheating, as well as the position of the peak in terms of comoving wavenumber k and the instability scale above which perturbations grow. Traditionally, self-resonance has been studied primarily within the framework of the perturbed equation of motion of the field [41–46, 171–181]. However, this approach is applied to the MS equation, which captures the dynamics of the curvature perturbations.

While applicable to any potential that can be expressed as (3.4), we focus our analysis on α-attractor models, given their observational preference [30]. Particularly, for $\alpha \ll 1$, our model reveals a pronounced self-resonance effect, leading to a rapid and substantial enhancement of the curvature perturbations, specifically for asymmetric potentials such as E-models due to the drift term. Also, we stress the importance of avoiding the stan-

dard parabola approximation during preheating for some models, specifically during the transition from inflation to preheating, as illustrated in Figs. 3.4 and 3.5. Moreover, we stress that this mechanism of amplification of perturbations is inherent to preheating in α-attractor models and does not require any fine-tuning.

As explained in Section 3.6, in the next two chapters, we will apply the self-resonance mechanism to the case of PBH formation and production of scalar-induced gravitational waves during preheating, Chapters 4 and 5, respectively. These effects are also studied for the Starobinsky-like α-attractor models.

4

Primordial black hole formation from self-resonant preheating in Starobinsky-like models

> *For a singularity brings so much arbitrariness into the theory that it actually nullifies its laws...Every field theory, in our opinion, must therefore adhere to the fundamental principle that singularities of the field are to be excluded.*
>
> – Einstein and Rosen [141] in 1936.

While we still do not have a definitive answer to the existence of singularities, the concept of black holes, which represent solutions to Einstein's equations with a singularity at their core, has been embraced in modern cosmology. Today, black holes are not just theoretical constructs, their existence is well-established, and their study has evolved, especially concerning the early universe.

In Chapter 2, we investigated PBH formation during preheating in Starobinsky inflation, based on earlier studies in this area [43, 45, 45]. In this Chapter, we extend that analysis to the broader class of Starobinsky-like inflationary α-attractor models introduced in Chapter 3, where the strong self-resonance effect during preheating provides the necessary amplification of perturbations to lead to the potential formation of PBHs.

To ensure phenomenological viability, it is essential to consider realistic constraints on the parameter α. There are multiple investigations in the literature that have derived lower bounds on the parameter α. In [197] it was found constraints on α from the study of reheating equation of state as $\log_{10}(\alpha) = -4.2^{+5.4}_{-8.6}$ (95% C.L.). According to [198], considerations of the overproduction of a light moduli field also implied some constraints on α in the context of the T-model. In [173] $\alpha \gtrsim 10^{-3}$ is obtained based on the effects of heavy fields in the α-attractor supergravity framework, and the subsequent geometric destabilization phenomenon during inflation. In our recent study [4] (see Chapter 5), we obtained stringent bounds $\log_{10}(\alpha) > -3.54$ for the T-model and $\log_{10}(\alpha) > -3.17$ for the E-model using the possible production of scalar-induced gravitational waves during preheating and applying the bound from the BBN constraint. In this Chapter, we consider these values of α to study PBH production during preheating in both E- and T-models.

Regarding PBH formation, in this chapter we also follow both PS and KP formalism to compute the mass fraction (see Appendix B.1 and B.2 for details). Furthermore, as described in detail in Chapter 2, we employ three criteria to restrict PBH formation, which

are summarized in Section 4.2. To estimate PBH masses, we adopt the standard approach of considering that the mass is roughly given by the horizon mass at the time the perturbation reenters the horizon, Eqn. (1.9).

This chapter is organized as follows. In Section 4.1, we revisit and elaborate upon the key constraints on evaporating PBHs, first introduced in Chapter 1 (see Fig. 1.3). Section 4.2 reviews the PBH formation criteria introduced in Chapter 2, updated for the self-resonance dynamics discussed in Chapter 3. Section 4.3 presents a detailed discussion of PBH properties, including their abundance and mass spectra. Finally, we summarize the main findings in Section 4.4.

4.1 Constraints on evaporating primordial black holes

As shown in Chapter 1, assuming the validity of Hawking radiation, one can impose some constraints on evaporating PBHs. These constraints, summarized in Fig. 1.3, fall into five main categories that we describe below.

Planck Remnants: The usual assumption is that the evaporation of a PBH proceeds until it vanishes [83]. Based on the uncertainty principle [92, 93], the information loss paradox [83, 90, 199], and some quantum gravity setups [200, 201], it was proposed that black holes could stop evaporating at the Planck scales. Although we do not know what form of quantum gravity corrections should take as one approaches the Planck mass, the black hole remnant is an interesting hypothesis[15] which we can test with observations [91]. In the case of PBHs with $M_{\rm PBH} \lesssim 10^6 g$, the rapid evaporation process could imply a significant population of remnants in the early universe. Still, their abundance must be limited as their density does not exceed the critical density of the universe [91].

Particle production from Hawking evaporation: The evaporation of PBHs could produce any particle predicted by theories beyond the standard model of particle physics. In particular, the evaporation of PBHs may produce the lightest supersymmetric particles (LSP), predicted in supersymmetry and supergravity models, which are stable and may contribute to the dark matter abundance. This affects PBHs with masses $M_{\rm PBH} \lesssim 10^{11} (m_{\rm LSP}/100\,{\rm GeV})^{-1}$g [132]. This bound depends on the mass of the LSP particle and, therefore, can vary. In Fig. 1.3 it is plotted for $m_{\rm LSP} = 100\,{\rm GeV}$ in magenta color. Since in this work, we consider α-attractor models that belong to the class of supergravity theories, we find it interesting to contemplate this constraint. In [127], it is considered that the PBHs produce DM particles during their evaporation, and constraints are obtained based on the actual abundance of DM. We examine this scenario in Fig. 1.3 for the case of

[15] Note that the argument in favor of black hole remnant, though said to be motivated from quantum gravity theories, emerges from multiple ad-hoc assumptions to resolve information paradox. Alternatively, recent investigations of a unitary formulation of quantum field theory in curved spacetime in consideration with gravitational backreaction effects offer a potential resolution to the information paradox at the foundational level [95, 96].

the Hawking temperature ($T_{\rm BH}$) of the PBH being $T_{\rm BH} > m_\chi$ and for a DM particle mass of $m_\chi = 10^8$ GeV. These constraints are shown in dashed lines as they depend on the mass of the particle emitted.

Cosmic Microwave Background (CMB): If PBHs emit high-energy photons during evaporation, these would contribute to the photon-to-baryon, as first pointed out in [130]. Particularly, the photons from evaporating black holes of $M_{\rm PBH} \lesssim 10^9 g$ would have enough time to thermalize, contributing to the photon-to-baryon ratio and thus increasing the entropy. However, this constraint is very weak, as can be seen in Fig. 1.3. On the other hand, as also pointed out in [130], for $10^{11} g \lesssim M_{\rm PBH} \lesssim 10^{13} g$, the photons are emitted after the freeze-out of double-Compton scattering, which implies that the CMB photons develop a non-zero chemical potential, leading to a μ-distortion. Another constraint related to CMB is the damping of small-scale anisotropies. If, during the evaporation process, the PBHs also emit high-energy electrons, these can scatter with the CMB photons, contributing to the temperature anisotropy power spectrum. This constraint affects PBHs in the range $2.5 \times 10^{13} g \lesssim M_{\rm PBH} \lesssim 2.4 \times 10^{14} g$ [131], and is particularly strong. All the constraints related to CMB effects are shown in blue in Fig. 1.3.

Big-bang nucleosynthesis (BBN): The PBHs of masses $10^9 g \lesssim M_{\rm PBH} \lesssim 10^{13} g$ evaporate around the time of BBN. If during this process they inject high-energy particles into the plasma, these would modify the standard BBN scenario in two ways [64, 65]: (1) high-energy mesons and antinucleons modify the neutron-to-proton ratio, (2) high-energy hadrons and photons dissociate light elements such as ^{4}He, thus increasing the abundance of others like D, T, ^{3}He, ^{6}Li and ^{7}Li. These constraints are shown in orange in Fig. 1.3 for the ^{4}He and D cases.

γ-ray backgrounds: If the PBHs with masses near $M_{\rm crit}$ are evaporating today, then they can contribute to the extragalactic γ-ray background (EGB), as first pointed out by Page and Hawking in 1976 [202]. They used observations of the EGB to constrain the mean number density of PBHs evaporating at present, shown in red in Fig. 1.3. Also, if PBHs are clustered within our galactic halo, then one would expect an anisotropic galactic γ-ray background (GGB), separable from the EGB. This constraint is shown in purple. Since these constraints are obtained through direct observations, as in the anisotropies case, they are very strong. Actually, one of the strongest constraints in the entire range of PBH masses, see for instance [126, 203, 204].

4.2 Revisiting PBH formation during self-resonant preheating

In this section, we summarize the findings of Chapters 2 and 3. That is, we describe how scalar perturbations can collapse to form PBHs from instabilities produced by self-resonance effects during preheating. First, concerning the IB, we know that the upper

limit is always determined by the Hubble radius $R_H = H^{-1}$, and the lower limit depends on the specific form of the potential. This last, from Chapter 3 is what we refer to as the *instability scale* $l_{\rm inst}$, which for a sufficiently long preheating ($> \mathcal{O}(1)$ e-folds) is given by Eqn. (3.24), where the value of the field at the end of inflation for the α-attractor models is obtained using slow-roll conditions and is given by [177]

$$\phi^T_{\rm end} \approx M_{\rm Pl}\sqrt{\frac{3\alpha}{2}}\,\text{arcsinh}\left(\frac{2}{\sqrt{3\alpha}}\right), \qquad \phi^E_{\rm end} \approx M_{\rm Pl}\sqrt{\frac{3\alpha}{2}}\log\left(\frac{2}{\sqrt{3\alpha}}+1\right), \tag{4.1}$$

for the T- and E-models, respectively. Therefore, the characteristic scale $l_{\rm inst}$ defines the IB as the range of modes satisfying:

$$l_{\rm inst} < \frac{a}{k} < R_H(t_{\rm rh}), \tag{4.2}$$

This is what we called the IB criterion in Chapter 2, now adapted to the α-attractor scenario. It implies that perturbations whose comoving wavenumber k is such that $a/k < l_{\rm inst}$ during preheating, decay, and therefore do not favor the collapse. Using (4.1), we observe that as α decreases, so does the instability scale $l_{\rm inst}$, and thus the IB gets broadened, increasing the number of modes that are affected by the self-resonance, and potentially the abundance of PBHs.

Next, we consider the Jeans' length criterion, which remains unaffected by the α-attractor scenario, but we summarize it in what follows. In essence, it states that the size of a perturbation must be larger than the Jeans' length so that pressure cannot counteract gravity and be able to collapse while remaining smaller than the Hubble radius in order to preserve causality. This condition is expressed as:

$$\frac{R_J}{\pi} < \frac{a}{k} < R_H, \tag{4.3}$$

where $R_J \simeq \sqrt{2c_s^2(k)/3}\,R_H$ is the Jeans' length [205–207] and $c_s^2(k)$ denotes the speed of sound, defined in Appendix A.4. This criterion imposes an upper limit on the wave numbers k that can potentially collapse, which competes with $l_{\rm inst}^{-1}$. The lower bound for the IB is chosen as the larger of these two scales, ensuring both criteria are met. In the high-k limit, both density and pressure perturbations average to zero, leading to $\langle c_s^2(k)\rangle = 1$, which holds both for the full expression (A.28) and the analytical approximation (A.29). This implies that a subhorizon mode must initially be of the order of the Hubble radius to collapse, which, by definition, is impossible. To validate this approximation, Fig. 4.1 compares the full numerical calculation of $\langle c_s^2(k)\rangle$ from (A.28) (red) with the analytical result (A.29) (black dashed) for two cases: a mode whose wavelength is closer to the horizon size ($k = 50k_{\rm end}$, Fig. 4.1a) and a mode well inside the horizon ($k = 350k_{\rm end}$, Fig. 4.1b). One can check that as the modes evolve, the speed of sound decreases towards zero, starting from $\langle c_s^2(k)\rangle = 1$ during inflation. This occurs sooner for $k = 50k_{\rm end}$ compared to $k = 350k_{\rm end}$, indicating that higher-k modes take longer to exceed the Jeans length and collapse.

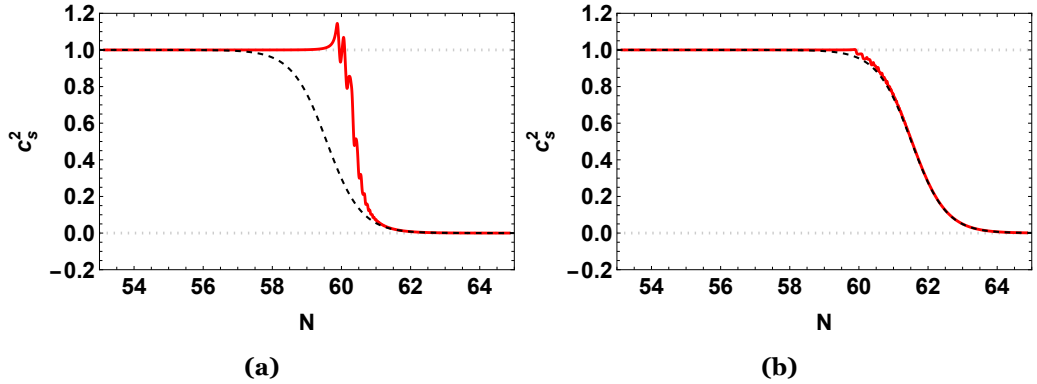

Figure 4.1: Numerically averaged (red) and analytical (dashed black) sound speeds, Eqns. (A.28) and (A.29), respectively, for two different modes: **a)** $k = 50\,k_{\rm end}$ and **b)** $k = 350\,k_{\rm end}$. The underlying model is an E-model with $\alpha = 10^{-2.5}$ and the horizontal dotted lines mark the limiting values of the sound speed, *i.e.*, $\langle c_s^2(k)\rangle = 1$ during inflation and $\langle c_s^2(k)\rangle = 0$ during preheating.

Lastly, a perturbation will collapse into a PBH if the density contrast $\delta_{\boldsymbol{k}}$ exceeds a threshold value δ_c, which we called the threshold criterion. We saw in Chapter 1 that the simplest estimate for δ_c arises from Carr's original analysis [79, 208], which gives $\delta_c \simeq w$. However, instead of using Carr's criterion (suitable for a fluid description), we computed the threshold in Chapter 2 using time constraints [1, 43, 45, 209], as defined in Eqn. (2.42). Nevertheless, this assumption for the threshold holds when self-resonance is weak. As we have seen, this assumption breaks down for small values of α [2]. Thus, instead of using (2.42) we numerically compute, for each value of α and k, the minimum value of the density perturbation that reaches $\mathcal{O}(1)$. This minimum value serves as the threshold $\delta_c(k)$, which is now k-dependent by construction. Thus, if $\delta_{\boldsymbol{k}}$ is larger than its corresponding minimum value $\delta_c(k)$, then the mode has enough time to reach $\mathcal{O}(1)$ and potentially collapse. In essence, this implies that due to the self-resonance effects, the threshold is expected to decrease as α decreases, since the perturbations grow faster and the minimum value that each mode needs to collapse decreases, which ultimately enhances the production of PBHs.

To be precise, we summarize now the three criteria we use to select the modes that can collapse into PBHs:

- ***Instability Band Criterion:*** Modes must lie within the IB to be affected by the instabilities that favor the collapse, satisfying (4.2).
- ***Jeans' Length Criterion:*** Modes must satisfy (4.3) to ensure that during the collapse, the pressure does not counteract gravity. The speed of sound is given in Appendix A.4.
- ***Density Contrast Criterion:*** The density contrast $\delta_{\boldsymbol{k}}$ must exceed the threshold $\delta_c(k)$, to allow sufficient time for PBH formation.

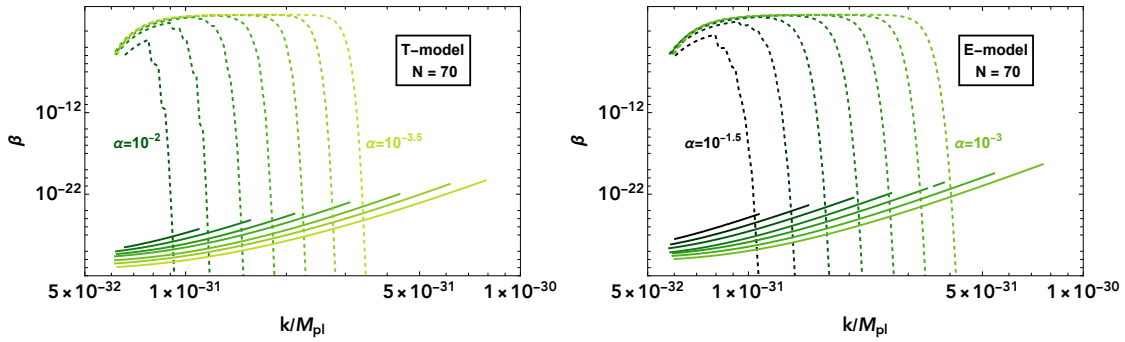

(a) **(b)**

Figure 4.2: Mass fraction for **(a)** T-model and **(b)** E-model using both KP (B.27) and PS (B.13) formalisms in dashed and continuous, respectively. The evaluation is made 10 e-folds after the end of inflation and values of α go from 10^{-2} to $10^{-3.5}$ for the T-model and from $10^{-1.5}$ to 10^{-3} for the E-model, in both cases with incremental steps of $10^{0.25}$. The color code of each value of α is the same in both plots. The lower value for α in each model is taken as the lower bound on α obtained in [4].

4.3 Primordial black hole characterization

After obtaining the evolution of the perturbations following the scheme outlined in Chapters 2 and 3, we now proceed to characterize the PBHs by calculating their mass fraction and corresponding masses.

4.3.1 Mass fraction

The mass fraction $\beta(k)$ is the main quantity used to characterize the abundance of PBHs. It is also common to express it normalized to the fractional density of dark matter, $\Omega_{\rm DM}$. In that case, it is typically represented by $f(M)$. We do not take into account for this work the dark matter and thus restrict ourselves to $\beta(k)$. As advanced at the beginning of this chapter, we employ the PS and KP formalisms to compute the mass fraction.

Press-Schechter: The estimation is obtained via Eqn. (B.13), and expressed in Fig. 4.2. There, we plot the mass fraction following the PS formalism (dashed curves) as a function of k for both T- and E-models and different values of α. Only the modes that satisfy the three criteria defined in Sec. 4.2 are considered, with evaluations performed 10 e-folds after the end of inflation. The results reveal that as α decreases, the mass fraction shifts toward higher values of k, since for each model the expansion after inflation (before setting to matter-dominated) is not exactly the same. Further, we observe that (1) as α decreases, more modes enter the IB, broadening the distribution, and (2) these modes grow faster, leading to a lower threshold $\delta_c(k)$, and consequently to a higher $\beta(k)$. Overall, this results in a broader mass fraction that grows for smaller values of α. If one increases the duration of preheating, we have checked that the value of α becomes irrelevant since almost the majority of the perturbations have enough time to collapse, resulting in an overproduction of PBHs. This occurs for a duration of preheating of approximately 12-13 e-folds

since at this stage the IB broadens to the point of including the modes belonging to the non-linear regime of the power spectrum. In that case, the mass fraction $\beta(k)$ becomes flat and fixed at 1 for the PS formalism, independently of α. This is what we refer to as an overproduction of PBHs.

Khlopov-Polnarev: We employ in this case the estimation for the anisotropy effect and small sigma, that is, Eqn. (B.27). In Fig. 4.2, the mass fraction computed using the KP formalism (continuous curves) is shown for both T- and E-models and various values of α. The three criteria defined in Sec. 4.2 are used to determine the range of modes that can collapse, with calculations performed at 10 e-folds after the end of inflation. The results show a tendency similar to the PS formalism: as α decreases, the mass fraction increases and shifts to higher values of k. However, a notable distinction is observed: in contrast to the PS formalism, the KP mass fraction decreases with decreasing α, for the same value of k. However, the modes affected cover a higher range due to the broadened IB and the smaller threshold from the fast amplification. Furthermore, in this case, the effect of increasing the duration of preheating does not necessarily translate into an overproduction of PBHs, as the mass fraction $\beta(k)$ broadens but remains small, in general. However, as discussed in the PS case, the modes belonging to the non-linear regime of the power spectrum, enter the IB and thus still it is not very clear if one can trust the KP estimation in this scenario.

One can observe differences in the mass fractions with respect to the results of Chapter 2, particularly in the case of the KP formalism. This is because we are following a different approach in terms of the collapse time. In Chapter 2, the collapse time is considered for all modes to be at the end of preheating when the density contrast has grown due to the parametric instabilities in Starobinsky inflation, which translates into a higher mass fraction. Some studies adopt this approach [113, 210–212]. In contrast, we consider a distinct collapse time for each mode, evaluating the density contrast at the moment of entering the IB, as some other works do [43, 45, 45]. Despite these methodological differences, we find it valuable to explore both alternatives, given the limited research on PBH formation during early matter-dominated eras such as preheating. Further investigation in this area is essential to improve our understanding of the collapse of perturbations in these scenarios.

4.3.2 PBH mass

To compute the mass of the PBHs forming, we estimate it roughly as the horizon mass M_H at the moment these modes enter the IB [45], $M_{\rm PBH} = \gamma M_H$ (Eqn. (1.9)). Here, the parameter γ specifies the fraction of the horizon mass that ends up in the PBH. It represents the uncertainties of the collapse in matter-dominated scenarios, and for simplicity, we take it to be $\gamma = 1$. This estimation for $M_{\rm PBH}$ also differs from the one in Chapter 2, where the critical scaling model is used instead [210]. However, in the present study, the

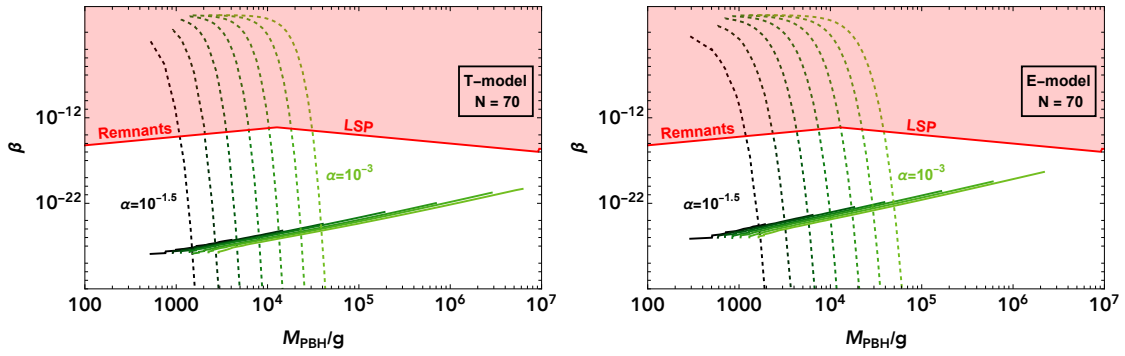

(a) **(b)**

Figure 4.3: Mass fraction for **(a)** T-model and **(b)** E-model using PS (dashed) and KP (continuous) formalisms as a function of the mass of the PBHs formed, Eqn. (2.43). Evaluations are made at 10 e-folds after the end of inflation. The red-shaded region represents the values of $\beta(k)$ constrained by the remnants and LSP constraints. The color code for α is the same as in Fig. 4.2.

differences $(\delta_k - \delta_c(k)) \gg 1$ are due to the rapid growth of perturbations (which lowers the value of the thresholds). In this sense, perturbations are in the super-critical regime, where the critical scaling does not apply. For this reason, we compute the PBH mass following (1.9).

Figure 4.3 displays the mass fraction as a function of the PBH mass for different values of the parameter α and for both the T- and E-models, using the PS and KP formalisms. The effect of the parameter α is also noteworthy here; a decrease in α leads to higher PBH masses. Furthermore, the range of masses of the PBHs formed is affected only by the constraints of Planck remnants and LSP, which, as stated in the introduction, are highly theoretical. Particularly, the PS formalism is highly disfavored in this scenario if one assumes that Hawking radiation produces stable Planck remnants as the end products of evaporation. In contrast, the KP estimation is consistent with all the current constraints. Further, these significant differences between the PS and KP formalisms emphasize the importance of accounting for nonspherical effects during the collapse of perturbations. Neglecting such effects can lead to an overestimation of the mass fraction or a rule-out of the model. Due to the lack of a definitive method, this analysis highlights the further need for accurate numerical simulations of PBHs formation during preheating.

4.4 Summary

In this Chapter, we have explored the formation of PBHs during the preheating phase of the early universe in the context of α-attractor models of inflation [170, 197, 213, 214], focusing on their mass fraction and mass spectrum under the frameworks of the PS [82,205] and KP [215–217] formalisms. We found effects of self-resonance during the preheating that are particularly strong for $\alpha \ll 1$ [2] and induce instabilities that could lead to the collapse of overdensities and form PBHs. Using Floquet theory, we define a band of modes

affected by the self-resonance effects, which we call the instability band (IB). By incorporating the dynamics of the density perturbations within the IB, we have defined three essential criteria that the density perturbations must fulfill to collapse into a PBH. Our approach not only refines previous analyses [43, 45, 45] but also crucially extends our previous results in the context of Starobinsky inflation [1] to all the Starobinsky-like scenarios like α-attractor models. The major highlight of this study is that we considered the impact of small-scale instabilities and non-spherical effects in the formation of PBHs by incorporating the KP formalism for the first time into generalized Starobinsky-like models. We quantitatively compared the PBH mass fraction $\beta(k)$ estimates from the PS formalism, which is widely followed, against the KP formalism.

Using the PS formalism (B.13), we computed the mass fraction $\beta(k)$ of PBHs, taking into account Gaussian statistics for perturbations and a k-dependent variance derived from the power spectrum. Our results are shown in Fig. 4.2 and indicate that, as the parameter α decreases, the mass fraction shifts to higher values of k and broadens. However, the PS formalism overestimates PBH abundance in a matter-dominated universe, as it neglects nonspherical effects (although it considers a threshold value for the perturbations). On the other hand, the KP formalism (B.27), which accounts for the anisotropy criterion and is independent of any threshold, offers a more realistic estimate of PBH formation during preheating. Our analysis shows in Fig. 4.2 that the KP estimation is, in general, lower compared to the PS case. Also, the tendency with α differs from the PS formalism. Smaller values of α lead to a smaller abundance of PBHs for the same value of k, although it affects a broad range of modes. This analysis is slightly different from the one in Chapter 2, where the formation of PBHs by the overdensities of all k is considered to occur at the end of the preheating phase. In this Chapter, we considered different times of PBH formation depending on the minimum time for each fluctuation to collapse and the corresponding threshold of density contrast for each k. To be precise, the former approach considers an instant of time for PBH formation, i.e., the end of preheating, whereas our investigation in this Chapter explores different times of PBH formation for each scale before the end of preheating. We find both approaches interesting and offer new insights into the phenomenon of PBH formation.

Finally, we compared our results with observational constraints [64, 65, 91, 126, 127, 130–132, 204], such as those from PBHs remnants, LSP and DM production, CMB effects, BBN, and γ-ray backgrounds (see Fig. 1.3 or red-shaded region in Fig. 4.3). For this particular scenario, the range of masses is only affected by the Planck scale remnants, LSP, and DM constraints, which are highly theoretical, and the last two of them actually depend on the mass of the particle emitted by the PBHs. Still, our analysis demonstrates that the interplay between the non-spherical and self-resonance effects during preheating plays a crucial role in determining the formation of PBHs.

In the next Chapter, we apply the self-resonance effects to the generation of SIGWs also in the context of the inflationary α-attractors to obtain a lower bound on the parameter

α, which is different for the T- and the E-models.

5

Scalar-induced gravitational waves from self-resonant preheating in Starobinsky-like models

> *It seems certain that gravitational waves exist. However, there is no reason to think that they will ever be observable.*
>
> – Henri Poincaré [134] in 1905.

This statement clearly reflects the skepticism regarding the observability of GWs that persisted for much of the 20th century among the scientific community, especially Einstein. Today, thanks to his theory of General Relativity, GWs are not only detectable but also crucial probes of the early universe, particularly in the context of inflationary cosmology.

After the Planck 2013-2018 data, there has been a surge in the building of single-field Starobinsky-like inflationary scenarios [218] in various frameworks of quantum gravity due to stringent constraints on multifield inflation. The vanilla models of single-field inflation predict the scalar spectral index (n_s) and tensor-to-scalar ratio (r) as [158, 219]

$$n_s \approx 1 - \frac{2}{N}, \quad r = \frac{12\alpha}{N^2}\,, \tag{5.1}$$

where α is a parameter that depends on the framework for the ultra-violet (UV) completion of gravity. In the context of α-attractor inflation, the α parameter indicates the curvature of the Kähler geometry in supergravity [167–170, 197, 213, 214, 220]. It is important to note that models of α-attractors could predict, in general, any smaller value for the tensor-to-scalar ratio compatible with the latest bound $r < 0.032$ [221, 222]. Although future observations aim to detect primordial gravitational waves, there is a lack of a theoretical lower bound on the value of α except through considerations of reheating [197]. However, one can use the preheating stage to obtain a lower bound on α, since as this parameter decreases, we have seen in Chapter 3 that the self-resonance effects become increasingly stronger and make the perturbations grow. The resulting amplified scalar perturbations couple at third-order[16] in the perturbed expansion of the action to the tensor fluctuations and induce GWs, the SIGWs we described in Chapter 1. These SIGWs can

[16] At the level of first order perturbed Einstein equation (or at the level of second order action) scalar and tensor modes do not couple, whereas the perturbed Einstein equations at the second-order (i.e., at the level of 3rd order perturbed action) we can have scalar modes acting as additional source to the generation of gravitational waves on top of the background as (5.2) illustrates.

be so efficiently produced to reach the BBN bound, which is precisely what our investigation utilizes here to derive a new lower bound on α, based solely on the considerations of preheating instabilities and the consequent generation of SIGWs. Our result is robust even for a small duration of preheating of 1-2 e-folds, as one can realistically expect after the end of inflation.

We have shown that these instabilities during preheating could lead to the generation of PBH [1–3] in Starobinsky as well as in α-attractor inflationary models (see Chapters 2, 3, and 4). However, the study in this chapter focuses on SIGWs produced irrespective of whether or not PBH are generated during preheating. It is also important to note that SIGWs are a secondary effect. At the linearized level, both scalar and tensor perturbations decouple. Therefore, we compute the linearized effect, which we call BGWs, and the non-linear (secondary) effect, *i.e.*, the SIGWs. A schematic representation of the scenario described above is shown in Fig. 1.6 (see Section 1.3 for further details).

Depending on the specific range of scales affected by the self-resonance, the SIGWs will have an imprint in a particular span of frequencies. In general, these scales are small and around the last scale to exit the horizon during inflation, which implies that we lie on the Very-High-Frequency (VHF) region of the GW spectrum (100 kHz – 1 THz) [148, 149, 223, 224]. This VHF region has been explored in the literature in the contexts of GUT scale, PBH, and quantum gravity [225–227]. Although some detectors (in operation and/or planned) work on the VHF band of the GW spectrum, their sensitivities are too low to detect a stochastic background of SIGWs. These sensitivities are shown in Fig. 5.1 in terms of the fractional energy density of gravitational waves, $\Omega_{\rm GW}$. One can observe that all of them lie above the cosmological bound coming from Big Bang nucleosynthesis (BBN) [66, 67], making it impossible to detect a stochastic background of GWs formed during preheating (otherwise, it would conflict with BBN predictions). Within the VHF band, one of the regions of interest in this work, the most promising prospects for detecting GWs are provided by:

- ***Optically levitated dielectric sensors***: These are based on the use of optically trapped and cooled dielectric microspheres or microdisks that experience a force when a GW passes through. A 1-meter prototype, the Optically levitated sensor (OLS) [228], is under construction at Western University in the USA.
- ***Bulk acoustic wave (BAW) devices***: The vibrations of a resonant mass detector due to the passage of a GW could be read through the piezoelectric effect and Superconducting Quantum Interference Devices (SQUIDs) [229]. A BAW device has been running since 2018 at the University of Western Australia [229, 230].
- ***Interferometers up to 100 MHz***: The quantum Cramér-Rao bound implies that, for a given laser power, higher bandwidth is needed to increase the sensitivity [231]. This implies that a broadband interferometer with the VIRGO, LIGO, or KAGRA-level sensitivity is not viable in the MHz region. However, there are several other

interferometers in this bandwidth, such as the Holometer experiment at Fermilab [232]. It consists of two co-located power-recycled Michelson interferometers with 40-meter-long arms, which increase sensitivity in the search for stochastic GWs.

- ***Gertsenshtein effect***: This consists of the conversion of photons into GWs (and vice versa) in the presence of a magnetic field. Although these kinds of detectors are not yet built, Ref. [149] points out the possibility of using existing experiments originally designed to search for axion-like particles from the Sun, such as IAXO [233]. Ref. [234] explores this possibility using Single Photon Detectors (SPD) and Heterodyne radio receivers (HET). Another possibility is to rely on observations of large-scale cosmic regions, where magnetic fields may extend over kpc to Mpc scales, thereby increasing the effective detector volume. Thus, using the astrophysical data from radio telescopes, such as EDGES or ARCADE [235, 236], one can constrain $\Omega_{\rm GW}$.

Apart from the VHF band, we also show for comparison in Fig. 5.1 the sensitivity curves of GW detectors in lower frequency bands: the Very-Low-Frequency (VLF), the Low-Frequency (LF), the Middle-Frequency (MF), and the High-Frequency (HF). See [148, 228] and references therein for details about the detectors and the acronyms. The two curves labeled as $r = 0.028$ and $r = 2.25 \times 10^{-6}$ in Fig. 5.1 correspond to the energy density of GWs (background + induced) from an E-model with $\alpha = 8.4$ and $\alpha = 10^{-3.17}$, respectively, where r is the tensor to scalar ratio (5.1). The upper bound on r corresponds to the one obtained using 10 datasets from the BICEP/Keck Array 2015 and 2018, Planck releases 3 and 4, and LIGO-Virgo-KAGRA Collaboration [237]. The lower bound is obtained in this work using SIGWs and the BBN bound. See Sec. 5.1.2 for details.

The inflationary models we study in this chapter are the well-known Starobinsky-like α-attractor models [167–170,197,213,214,220]. Beyond their inflationary observables (5.1), we show that these models are also particularly interesting from the perspective of SIGWs. As the value of α decreases, the minimum of the potential (at $\phi = 0$) starts to deviate from the quadratic (parabola) behavior, triggering the self-resonance phenomenon and amplifying the scalar perturbations. Fig. A.1 compares both potentials for several values of α, revealing an evident asymmetry in the E-model case. This, as shown in [2], makes the self-resonance effect stronger in this class of potentials, ultimately imposing a tighter constraint on α for the E-models and, consequently, on the tensor-to-scalar ratio. These differences will be further analyzed in Sec. 5.1, where their impact on tensor perturbations is clarified.

This chapter is organized as follows: In Sec. 5.1, we examine the generation of SIGWs from these scalar perturbations and numerically compute the energy density of GWs for different values of α. Then, a summary is presented in Sec . 5.2, and Appendixes C.1 and C.2 show some complementary computations, such as the derivation of the equation of motion for the SIGWs or its power spectrum.

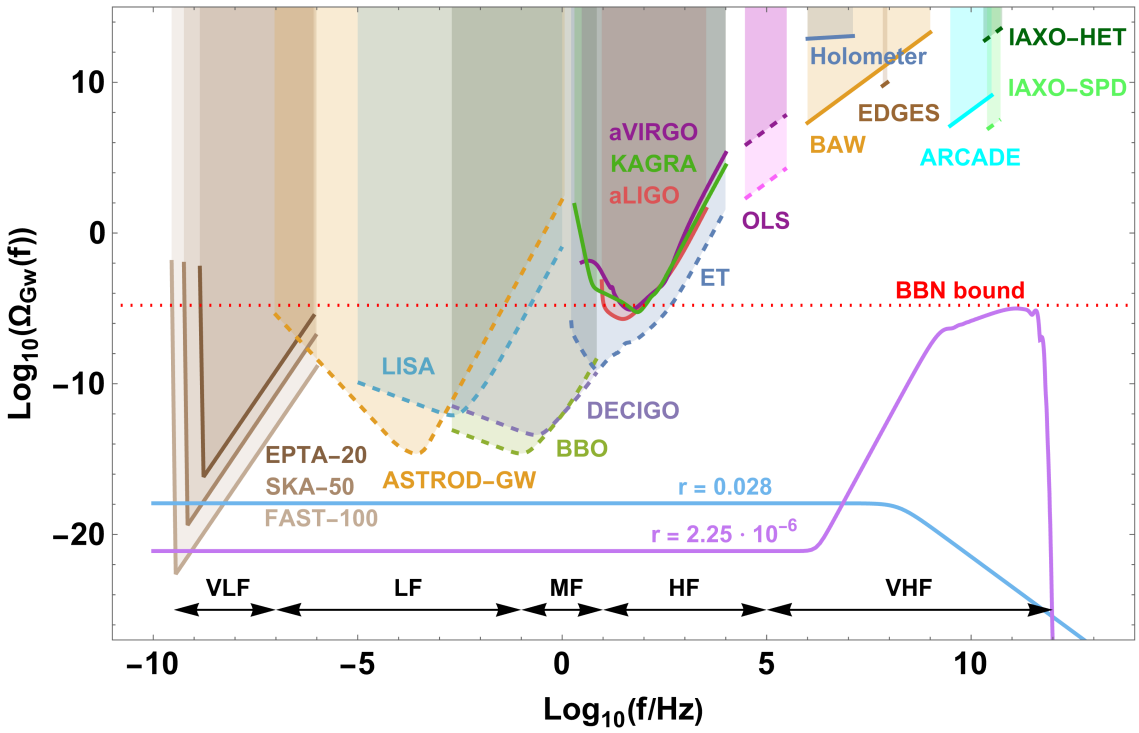

Figure 5.1: Sensitivity curves of some GW detectors (in terms of Ω_{GW}) as a function of the frequency in Hertz. Also shown is the BBN bound, taken from [66, 67]. Solid (dashed) lines represent operative (planned or theorized) GW detectors. The figure is produced from the analysis of [148,149] and references therein. The bottom lines with arrows mark the limits of the standard frequency bands of GWs, as defined in [148]. The blue and magenta curves labeled as $r = 0.028$ and $r = 2.25 \times 10^{-6}$ represent two spectra of GWs computed from the upper and lower bounds on the tensor-to-scalar ratio; see the text for details. These are computed using the method outlined in this work.

5.1 Tensor perturbations

After computing the scalar perturbations during preheating, for which we employ the procedure described in Chapters 2 and 3, and Appendix A, we aim to analyze the tensor perturbations to determine whether the amplification of scalar perturbations leaves an imprint on the power spectrum of SIGWs. We first use perturbation theory in Sec. 5.1.1 to estimate the energy density of gravitational waves and then, in Sec. 5.1.2, we explain the numerical strategy followed to achieve that goal.

5.1.1 Energy density of gravitational waves

Going to the 3rd order perturbation of the action (1.3) in scalar (Φ, $\delta\phi$) and tensor (h_{ij}^{λ}) fluctuations, we obtain the third-order equations of motion for the tensor modes $h_{\mathbf{k}}$ in Fourier space as [48, 50, 193, 195]

$$\ddot{h}_{\boldsymbol{k}}^{(\lambda)}(t) + 3H\dot{h}_{\boldsymbol{k}}^{(\lambda)}(t) + \frac{k^2}{a^2}h_{\boldsymbol{k}}^{(\lambda)}(t) = \frac{\mathcal{S}(\boldsymbol{k},t)}{a^2}, \tag{5.2}$$

where $\lambda = +, \times$ denotes the two polarization states, a dot means derivative with respect to cosmic time, and $\mathcal{S}(\boldsymbol{k},t)$ is the source term, given by

$$\mathcal{S}(\boldsymbol{k},t) = \int \frac{\mathrm{d}^3\tilde{k}}{(2\pi)^{3/2}}\tilde{k}^2(1-\mu^2)\left(4\Phi_{\tilde{\boldsymbol{k}}}\Phi_{\boldsymbol{k}-\tilde{\boldsymbol{k}}} + 2\delta\phi_{\tilde{\boldsymbol{k}}}\delta\phi_{\boldsymbol{k}-\tilde{\boldsymbol{k}}}\right). \tag{5.3}$$

The above source term contribution originates from the scalar-scalar-tensor vertex interaction term in the third-order perturbed expansion of the action (1.3). Here, we neglect 4th and higher-order contributions on the expectation that any further scalar self-interactions are negligible. As we can see from Fig. 3.2, the curvature perturbation, which is a combination of metric and scalar field fluctuation, remains smaller than unity even in the regime of self-resonance amplification during the preheating phase. If we consider the scales of full non-linear regime, then the effects of non-Gaussianities are important [238, 239], which we defer for future investigations. Since the source term (5.3) on the right-hand side of (5.2) reflects the fact that these GWs are no longer free-propagating waves but rather a metric distortion arising from terms quadratic in the scalar perturbations [50], they are called SIGWs. Moreover, the integral over $\tilde{k}$ reflects that the computation of SIGWs involves a convolution of different modes, meaning the contribution from any individual mode is diluted and mixed with contributions from other modes. Consequently, the amplification of the gravitational waves arises from the collective contribution of all modes within the Hubble horizon. In our case, the significant contribution to the amplification comes from the modes $k > k_{\mathrm{end}}$ (See Fig. 3.2). In Appendix C.1 we show the derivation of the source term $\mathcal{S}(\boldsymbol{k},t)$ from the perturbed Einstein equations and how to express it in terms of the metric scalar perturbations, as shown in Eqn. (5.3).

We can compute the energy density of GWs as the 00 component of the pseudo-energy momentum tensor of GWs [193], that is

$$\rho_{\rm GW} = M_{\rm Pl}^2 \int \mathrm{d}\ln k \frac{k^3}{16\pi^2} \left\{ \sum_\lambda \langle \dot{h}_{\boldsymbol{k}}^{(\lambda)} \dot{h}_{-\boldsymbol{k}}^{(\lambda)} \rangle' + \frac{k^2}{a^2} \langle h_{\boldsymbol{k}}^{(\lambda)} h_{-\boldsymbol{k}}^{(\lambda)} \rangle' \right\}, \tag{5.4}$$

where the notation "!" indicates that the Dirac delta has been factored out and thus $\langle h_{\boldsymbol{k}}^{(\lambda)} h_{-\boldsymbol{k}}^{(\lambda)} \rangle'$ is directly related to the power spectrum $\mathcal{P}_h(k,t)$, defined as

$$\langle h_{\boldsymbol{k}}^{(\lambda)}(t) h_{\boldsymbol{k}'}^{(\lambda)}(t) \rangle = \frac{1}{2} \frac{2\pi^2}{k^3} \delta^3(\boldsymbol{k} + \boldsymbol{k}') \mathcal{P}_h(k,t), \tag{5.5}$$

where the $1/2$ factor comes from the fact that $\mathcal{P}_h(k,t)$ includes contributions from both polarizations. For our case, this power spectrum can be computed as follows

$$\mathcal{P}_h^{\rm SI}(k,t) = \frac{16 g^2(k,t)}{k} \int_0^\infty \mathrm{d}\tilde{k} \int_{-1}^1 \mathrm{d}\mu \, \frac{\tilde{k}^3 (1-\mu^2)^2}{|k-\tilde{k}|^3} \mathcal{P}_\Phi(\tilde{k}) \mathcal{P}_\Phi(|k-\tilde{k}|), \tag{5.6}$$

where SI stands for scalar-induced, μ is the cosine of the angle between ingoing and outgoing scales, and $\mathcal{P}_\Phi(k)$ is the power spectrum of the scalar perturbations $\Phi_{\boldsymbol{k}}$. It is defined similarly to (5.5), but a Heaviside function is introduced in this case to avoid the contribution to the integral coming from the non-linear regime of $\mathcal{P}_\Phi$ [50], that is

$$\langle \Phi_{\boldsymbol{k}}(t) \Phi_{\boldsymbol{k}'}(t) \rangle = \frac{2\pi^2}{k^3} \delta^3(\boldsymbol{k} + \boldsymbol{k}') \mathcal{P}_\Phi(k,t) \Theta(k_U - k), \tag{5.7}$$

where the function $g(k,t)$ is defined in Eqn. (C.13). Appendix C.2 shows the details about the derivation of (5.6) following the standard derivations of GWs production during matter-dominated scenarios as well as some analytical estimates for the spectral energy density of GWs. The latter, labeled as Ω_{GW}, is often used instead of ρ_{GW} to compare theoretical predictions with current constraints and future observations. It represents the energy density per logarithm of k over the critical density and is given by

$$\Omega_{\rm GW}(k,t) = \frac{1}{3 M_{\rm Pl}^2 H^2} \frac{\mathrm{d}\rho_{\rm GW}}{\mathrm{d}\ln k}. \tag{5.8}$$

After the preheating stage, where the radiation-dominated (reheating) period begins, the GWs behave as freely propagating waves. We assume that this transition occurs suddenly. This implies that the following approximation holds from the end of preheating onwards

$$\dot{h}_{\boldsymbol{k}}^{(\lambda)} \simeq i \frac{k}{a} h_{\boldsymbol{k}}^{(\lambda)}. \tag{5.9}$$

Thus using Eqns. (5.4), (5.8) and (5.9), the spectral energy density of SIGWs at the end of preheating is given by

$$\Omega_{\rm GW}^{\rm SI}(k, t_{\rm rh}) = \frac{\mathcal{P}_h^{\rm SI}(k, t_{\rm rh})}{12} \left(\frac{k}{k_L} \right)^2, \tag{5.10}$$

where we have used $a(t_{\rm rh})H(t_{\rm rh}) = k_L$. After the end of preheating, the fractional energy density redshifts at sub-Hubble scales as any non-interacting relativistic particles. Therefore, the present energy density of gravitational waves is approximated by [50]

$$\begin{aligned}\Omega_{\rm GW}^{\rm SI}(k,t_0) &\simeq \Omega_\gamma^0\,\Omega_{\rm GW}^{\rm SI}(k,t_{\rm rh})\\ &\simeq \frac{4\,\Omega_\gamma^0}{3}\left(\frac{k}{k_L}\right)^2\frac{g^2(k,t_{\rm rh})}{k}\int_0^\infty {\rm d}\tilde{k}\int_{-1}^1 {\rm d}\mu\,\frac{\tilde{k}^3\,(1-\mu^2)^2}{|k-\tilde{k}|^3}\,\mathcal{P}_\Phi(\tilde{k})\mathcal{P}_\Phi(|k-\tilde{k}|),\end{aligned} \tag{5.11}$$

where $\Omega_\gamma^0 \simeq 1.2\times10^{-5}$ is the present energy density of photons, t_0 represents the present epoch, and we have substituted in the last line the power spectrum from Eqn. (5.6), see [50] for details. This quantity is usually expressed as a function of the GW frequency f rather than the wave number k. The relationship between them is given by [240]

$$f = 1.55\times10^{-15}\left(\frac{k}{\rm Mpc^{-1}}\right)\,{\rm Hz}. \tag{5.12}$$

As previously mentioned, we are also interested in the BGWs, whose evolution equation is also (5.2) but with $\mathcal{S}_{\boldsymbol{k}} = 0$, indicating that BGWs behave as free waves. Inflation predicts an almost scale-invariant power spectrum of BGWs, given by

$$\mathcal{P}_h^{\rm inf}(k) = \mathcal{A}_h\left(\frac{k}{k_*}\right)^{n_t}, \tag{5.13}$$

where $k_* = 0.05{\rm Mpc}^{-1}$ is the pivot scale, $\mathcal{A}_h$ is the tensor amplitude, and n_t the tensor spectral index. These parameters are related to the tensor-to-scalar ratio (5.1) as $\mathcal{A}_h = r\mathcal{A}_\mathcal{R}$ and $n_t = -r/8$, where $\mathcal{A}_\mathcal{R} = 2.2\times10^{-9}$ is the amplitude of the scalar power spectrum at the pivot scale. Let us begin by studying the evolution of Eqn. (5.13) after inflation. To analyze this, let us solve (5.2) (with $\mathcal{S}_{\boldsymbol{k}} = 0$) under different expansion histories of the universe. Defining $h_{\boldsymbol{k}} = \tilde{h}_{\boldsymbol{k}}/a$ (omitting the polarization index λ) and using conformal time η, we can express (5.2) as

$$\tilde{h}_{\boldsymbol{k}}'' + \left(k^2 - \frac{\nu^2-\frac{1}{4}}{\eta^2}\right)\tilde{h}_{\boldsymbol{k}} = 0, \tag{5.14}$$

where $\nu = \frac{3(1-w)}{2(1+3w)}$, and we have assumed that $a \sim \eta^{\frac{2}{1+3w}}$, with w being the equation of state parameter of the universe. The solution to this equation is given in terms of Bessel functions:

$$h_{\boldsymbol{k}} = \sqrt{\eta}\left[A_k J_\nu(k\eta) + B_k Y_\nu(k\eta)\right]. \tag{5.15}$$

During preheating (reheating), we have $\nu \simeq 3/2$ ($\nu = 1/2$). Thus, for subhorizon modes, and in both cases, $J_\nu(k\eta) \sim Y_\nu(k\eta) \sim 1/\sqrt{k\eta}$, implying $h_{\boldsymbol{k}} \sim 1/a$. This allows us to define

the transfer function for the background tensor perturbations as:

$$\mathcal{T}_h^2(k,t) = \begin{cases} 1 & t < t_k \\ \frac{1}{2}\left(\frac{a_k}{a}\right)^2 & t > t_k \end{cases} \tag{5.16}$$

where a_k is the scale factor at the time the mode k enters the horizon, defined as t_k. The factor $1/2$ accounts for averaging over harmonic oscillations of modes deep inside the horizon [241]. The background tensor power spectrum evolves as follows after inflation:

$$\mathcal{P}_h^{\mathrm{B}}(k,t) = \mathcal{P}_h^{\mathrm{inf}}(k)\mathcal{T}_h^2(k,t), \tag{5.17}$$

and the background fractional energy density is computed using (5.8) as

$$\Omega_{\mathrm{GW}}^{\mathrm{B}}(k,t) = \frac{k^2}{12a^2H^2}\mathcal{P}_h^B(k,t) = \frac{\mathcal{P}_h^{\mathrm{inf}}(k)}{24}\frac{a_k^4H_k^2}{a^4H^2}. \tag{5.18}$$

If the mode enters during preheating, a suppression effect exists due to the $a^4H^2 \propto a$ term in Eqn. (5.18). This means that the fractional energy density gets suppressed as $\Omega_{\mathrm{GW}}^{\mathrm{B}} \propto a_k/a$ for the modes entering during preheating [241–245], that is, for $k > k_L$. This effect disappears when reheating begins. At this point, and as in the scalar-induced case, the fractional energy density redshifts as any non-relativistic particles. This implies we can use the following parametrization for the fractional energy density of BGWs evaluated at the present time:

$$\Omega_{\mathrm{GW}}^{\mathrm{B}}(k,t_0) = \Omega_\gamma^0\frac{r\mathcal{A}_\mathcal{R}}{24}\left(\frac{k}{k_*}\right)^{n_t}\begin{cases} \frac{a_k}{a_{\mathrm{rh}}}, & \text{if } k > k_L \\ 1, & \text{if } k \leq k_L \end{cases} \tag{5.19}$$

Further suppression effects exist for modes entering during the late matter- and dark-energy-dominated eras. However, the associated wavelengths are much smaller than those relevant during preheating and are, therefore, not considered here. Finally, the total fractional energy density of GWs evaluated at present is the sum of both contributions (i.e., (5.19) and (5.11))

$$\Omega_{\mathrm{GW}}^{\mathrm{TOT}}(k,t_0) = \Omega_{\mathrm{GW}}^{\mathrm{B}}(k,t_0) + \Omega_{\mathrm{GW}}^{\mathrm{SI}}(k,t_0), \tag{5.20}$$

where the numerical computation of $\Omega_{\mathrm{GW}}^{\mathrm{SI}}$ is detailed in the next subsection.

5.1.2 Numerical strategy

To numerically compute the total fractional energy density of SIGWs, we begin by computing the time evolution of the curvature perturbations $\mathcal{R}_k$, following the method outlined in Chapters 2 and 3, and Appendix A. The results are stored in k-space. Next, the power spectrum of the curvature perturbations, $\mathcal{P}_\mathcal{R}$, is computed and evaluated at the end of the

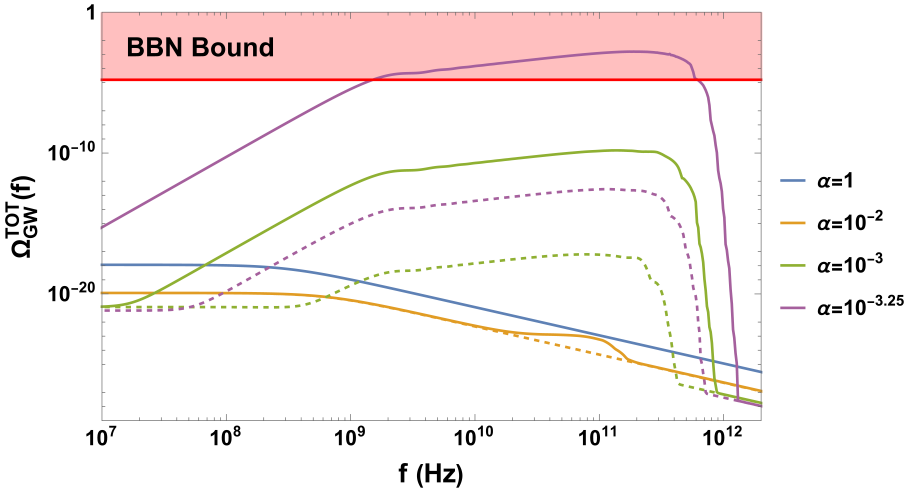

Figure 5.2: Total fractional energy density of GWs, Eqn. (5.20), evaluated today for a T-model (dashed lines) and an E-model (solid lines), with different values of α and as a function of the frequency of each mode, expressed in Hz. The red horizontal line represents the BBN bound. Preheating is assumed to last for 5 e-folds.

short self-resonance stage, as it remains constant for the modes of interest thereafter. At this stage, the universe behaves as matter-dominated, allowing us to use the following relation between $\mathcal{P}_\mathcal{R}$ and $\mathcal{P}_\Phi$ [48, 50]

$$\mathcal{P}_\mathcal{R}(k) = \frac{9}{25}\mathcal{P}_\Phi(k), \tag{5.21}$$

where $\mathcal{P}_\mathcal{R}$ is defined analogously to (5.7). This relation is then substituted into (5.11). Since the curvature perturbations can only be obtained numerically in discrete steps of k, the integral over $\tilde{k}$ in (5.11) is discretized. Specifically, the k-space integral is divided into 100 uniform points per logarithmic interval of k. This procedure is repeated for each value of k in $k \in [k_L, k_U]$ and evaluated at the end of the preheating stage, $t_{\rm rh}$, which we consider to last approximately 5 e-folds.

Fig. 5.2 shows the computation of the total fractional energy density of GWs for the two models under consideration (T-model as dashed lines and E-model as solid lines) and for different values of the parameter α. We have also included the Starobinsky model [24], which corresponds to an E-model with $\alpha = 1$, for comparison purposes. An interesting feature of Fig. 5.2 is that the amplification peak for high-k in the scalar perturbations of Fig. 3.2 is also present in the energy density of GWs for small α, since $\Omega_{\rm GW}^{\rm TOT} \sim \Omega_{\rm GW}^{\rm SI}$. However, for higher values of α, such as the Starobinsky case, the amplification of scalar perturbations is negligible and thus $\Omega_{\rm GW}^{\rm TOT} \sim \Omega_{\rm GW}^{\rm B}$. Nonetheless, due to the convolution mentioned earlier, this contribution from the peak gets diluted among the rest of the modes inside the horizon, and thus the peak in $\Omega_{\rm GW}^{\rm TOT}$ is not as sharp as it is in $\mathcal{P}_\mathcal{R}$, which makes it difficult to track back the initial feature in the power spectrum causing the amplification. In Appendix C.2 we show some analytical approximations that explain the shape of $\Omega_{\rm GW}^{\rm SI}$. We also remark here that, as anticipated, decreasing α leads to a growth of the met-

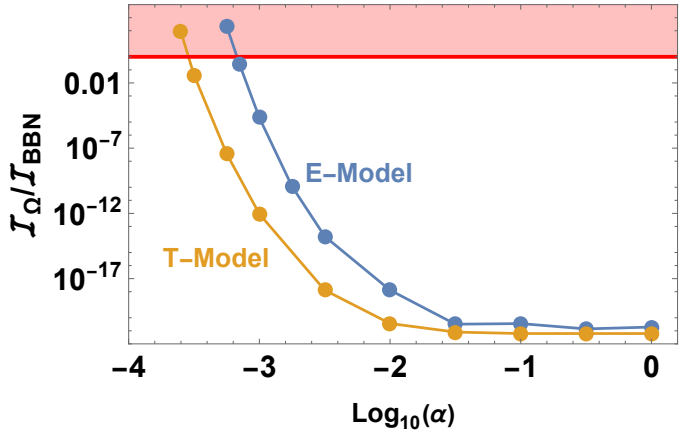

Figure 5.3: Integrated fractional energy density, Eqn. (5.11), normalized to $\mathcal{I}_{\rm BBN}$ as a function of α for the T- and E-models.

ric perturbations, which enhances gravitational wave production in the very VHF band. Although there is no current GW detector for the VHF band, we can use the BBN bound to restrict the model's parameters. This proceeds as follows. The GWs at the onset of the BBN contribute to the radiation density and can potentially change the expansion rate of the universe, and thus the abundance of the light elements. Measurements of this abundance lead to an equivalent number of additional relativistic species of 1.4 neutrino degrees of freedom, which translates into the following upper bound for the total fractional energy density of GWs [66, 67]

$$\mathcal{I}_\Omega = \int_0^\infty \Omega_{\rm GW}^{\rm TOT}(k)\, \mathrm{d}\ln(k) \leq 1.6\times 10^{-5} = \mathcal{I}_{\rm BBN}. \tag{5.22}$$

This bound is represented as the horizontal red band in Fig. 5.2, which is reached for the E-model with $\alpha = 10^{-3.25}$. It is important to remark that the bound is on the integral over the whole spectrum of modes, which implies that $\Omega_{\rm GW}^{\rm TOT}$ could present a peak above $\mathcal{I}_{\rm BBN}$, provided it is narrow so that $\mathcal{I}_\Omega < \mathcal{I}_{\rm BBN}$. Thus, Fig. 5.2, is not good enough to establish a lower bound on α. Instead, Fig. 5.3 shows the result of the numerical integration of the fractional energy density (5.11) as a function of α for the T- and E-models, normalized to $\mathcal{I}_{\rm BBN}$. Here, we clearly see a limiting value of α, for which the BBN bound is reached (red shaded area). This corresponds to $\log_{10}(\alpha) \simeq -3.54$ for the T-model and to $\log_{10}(\alpha) \simeq -3.17$ for the E-model. Since the amplification occurs rapidly ($\mathcal{O}(1)$ e-fold), this essentially restricts the duration of preheating. Also, we can use (5.1) to put a lower bound on the tensor-to-scalar ratio, that is

$$r_T > 9.61\times 10^{-7} \qquad \text{and} \qquad r_E > 2.25\times 10^{-6}, \tag{5.23}$$

where the suffixes $_T$ and $_E$ stand for the different bounds on α for each model. The lower bound on r_E rests on the fact that the E-model potential is asymmetric and thus self-resonance is stronger in this case, for the same value of α, due to the drift terms in the

potential expansion [2]. This lower bound, although far from the sensitivity of the future satellite observer LiteBIRD ($r \sim 1.0 \times 10^{-3}$) [246, 247], agrees with the bound using BICEP2 and Planck data [222].

In [248, 249], it is pointed out that the spectrum of SIGWs corresponding to the modes $k < k_{\text{end}}$ could be affected by the later transition from the preheating (inflaton matter domination) to the radiation era. In the case of a gradual transition from preheating to radiation, Ref. [248] indicates that the SIGWs enhancement gets suppressed because of the subsequent decay of the gravitational potential Φ_k. However, in the case of a sudden transition [249], the same conclusion does not apply; in fact, there is an additional enhancement in SIGW. By comparison to [248, 249], in this chapter, we also consider in addition the self-resonance effects in the $k > k_{\text{end}}$ region of the spectrum (i.e., the modes that never exit the horizon during inflation but fall into the instability band). Notably the enhanced contribution to SIGW $\Omega_{\text{GW}}^{\text{TOT}}$ is dominated by the modes $k \gg k_{\text{end}}$ as we can notice from Fig. 3.2 and Fig. 5.2. A recent study of this regime [250] shows the gravitational particle production contribution from the small wavelength modes $k \gg k_{\text{end}}$ is negligible because the vacuum associated with these modes during inflation is closer to the Minkowski vacuum rather than the de Sitter vacuum. This indicates that the decay of gravitational potential Φ_k for these modes is unlikely to happen. However, a precise analytical and numerical study of this scenario is left for future work.

5.2 Summary

In this chapter, we explored the production of SIGWs during the preheating phase in the context of α-attractor inflationary models. These models, characterized by the parameter α, deviate from a quadratic potential as α decreases (see Fig. A.1), which triggers a self-resonance effect and, rapidly and substantially, amplifies the scalar perturbations during preheating [2,188,189]. We particularly considered all the perturbations that fall into the preheating instability band, which include the modes that exit the horizon during inflation and the ones that remain in the subhorizon regime during preheating, i.e., $k < k_{\text{end}}$ and $k > k_{\text{end}}$, respectively. In particular, we found that the modes $k > k_{\text{end}}$ whose wavelength is larger than the Jeans length are significantly amplified, and these modes would not contribute to particle production in the post-preheating phase. This amplification, in turn, directly impacts the production of gravitational waves, since scalar perturbations couple to the tensor perturbations at third-order perturbed expansion of the action through the source term (See (6.42) and (6.43)). We computed the total fractional energy density of GWs (SIGWs + BGWs) for different values of α and our findings show that, for sufficiently small values of α, the integral of the total fractional energy density of GWs reaches the BBN bound (6.49), see Figs. 6.2 and 5.3. In particular, we observe that the growth in Ω_{GW}^{TOT} is extremely large (by several orders of magnitude) for small differences in α. See for instance Fig. 6.2 for $\alpha = 10^{-2} - 10^{-3}$. This is due to the fact that the fractional energy

density of SIGWs is, naively speaking, proportional to $\int \mathcal{P}_\Phi^2(k) \sim \int \mathcal{P}_\mathcal{R}^2(k)$ (See (6.48)), meaning small variations in $\mathcal{R}_k$ induce large changes in $\Omega_{GW}^{\rm SI}$ so that the secondary effect (SIGWs) dominates over the linear effect (BGWs). In contrast, this amplification mechanism is suppressed for higher values of α, including the Starobinsky case, where the effect becomes negligible.

We demonstrated, for the first time, that the lower limit on α imposed by the BBN constraint differs between T-models and E-models when considering the production of SIGWs during preheating instabilities. This approach relies on the assumption that the decay of the inflaton field is not instantaneous, with its coupling to the fields responsible for reheating the universe being sufficiently small to ensure that the preheating phase lasts under 5 e-folds before the inflaton decays into ultra-relativistic particles [41, 42].

The distinction in the lower bound on α arises from the additional amplification present in the E-model compared to the T-model, which can be attributed to the asymmetry of the potential [2]. These new bounds, although derived under different assumptions, should be compared with those reported in [197] based on the duration of reheating along with the current bounds on the scalar spectral index, where $\log_{10}(\alpha) = -4.2^{+5.4}_{-8.6}$ at 95% C.L, in [198] based on the overproduction of a light moduli field, where $\alpha \lesssim 10^{-8}$, or in [173] based on geometrical destabilization of a spectator field, where $\alpha \lesssim 10^{-3}$. Furthermore, they establish a new lower bound on the tensor-to-scalar ratio, as given in (5.23).

In conclusion, our analysis suggests that the amplification of scalar perturbations during self-resonant preheating offers an effective mechanism for generating GWs, particularly in the VHF band. These remarks highlight the need for increasing the sensitivity of gravitational wave detectors in the VHF range that could potentially test these theoretical predictions [148, 149, 223, 224] and offer new insights into the physics of the early universe. Furthermore, we derive for the first time a concrete lower bound on the tensor-to-scalar ratio for the single-field Starobinsky-like inflationary scenarios, which would be an important input for the future probes of B-mode polarization [251, 252].

The next chapter examines the combined effects analyzed throughout this dissertation within the context of a generic Starobinsky-like inflationary potential—specifically, the formation of PBHs during the preheating phase, followed by the subsequent generation of induced GWs during the PBH-dominated (matter-dominated) era, which ends through the evaporation of the PBHs via Hawking radiation, thereby reheating the universe.

6

Gravitational waves from primordial black hole dominance: The effect of the inflaton decay rate

> *It is suggested that there may be a large number of gravitationally collapsed objects of mass* $10^{-5}g$ *upwards which were formed as a result of fluctuations in the early universe.*
>
> – Stephen Hawking [76] in 1971

This marks the beginning of Hawking's work titled "*Gravitationally Collapsed Objects of Very Low Mass*." It was the first instance showing that PBHs could have formed in the early universe, leading to Hawking's discovery of Hawking Radiation in 1974 [83], by which PBHs can lose mass and eventually evaporate. Since then, these two concepts have been closely linked to explain the early universe, particularly in post-inflationary scenarios, and have also been used to place constraints on the abundance of PBHs. In this chapter, we investigate this precise relationship and examine the overproduction of PBHs during the preheating phase and the posterior generation of induced GWs.

For the formation of PBHs, we choose to work under the KP formalism [119, 121–125] as we understand, from the results of Chapters 2 and 4, that it better describes the collapse dynamics of perturbations in matter-dominated scenarios. This formalism was previously described in Appendix (B.2). However, we consider here two new elements: the decay of the inflaton field into radiation and the posterior evaporation of the PBHs via Hawking radiation [83], which we describe in what follows. Further, we will apply these considerations to an extended distribution of perturbations, contrary to the standard monochromatic assumption [59–63].

Moreover, we work only with modes that exited the horizon during inflation and were amplified by some mechanism. Therefore, a central element in its formation is the appearance of a pronounced peak in the inflationary power spectrum. Various inflationary scenarios can lead to such an amplification of curvature perturbations. For instance, in single-field models, mechanisms such as an inflection point [253–256] or a step-like feature in the potential [257–260] can generate the necessary peak. For multi-field, this peak can be produced through non-canonical kinetic terms [261–264], the interplay of multiple axion fields [265, 266], or waterfall trajectories in hybrid models [267–271]. For a comprehensive review of these mechanisms, see [100]. Although the parametrization of

the power spectrum via a Gaussian peak is introduced in an ad hoc manner in our study, adjusting its height and position effectively encapsulates the essential physics of almost every inflationary model mentioned earlier. This is the approach we will follow, remaining agnostic about the precise physical mechanism of the amplification of perturbations during inflation.

Interest in PBHs has grown recently due to their potential to answer several questions in cosmology. In particular, they have been proposed as candidates for dark matter, as generators of structure in the universe, or even as seeds for the formation of supermassive black holes in the center of galactic nuclei. See [272, 273] for a review. However, although observational data tightly constrain their abundance [203, 273], for small masses ($\lesssim 10^{10}$g), these constraints rely on the nature of Dark Matter, which is currently unknown [274], and on the details of Hawking evaporation [83] and the production of Planck remnants [91–94], a highly theoretical element. For this reason, the constraints can be relaxed to the point that PBHs come to dominate the energy density of the universe, a period called PBH-dominated, which behaves as pressureless matter. If this occurs, their inherent Poissonian fluctuations in density can source a stochastic background of gravitational waves, providing a unique observational window into the early universe. The frequencies associated with this background of GWs fall into the very-high frequency range, as shown in previous works in the context of PBHs in grand unified theories and supergravity [5, 225, 226]. In this range, the current and planned detectors still lack a sufficiently high sensitivity, further motivating their refinement.

To eventually recover the standard radiation-dominated era necessary for successful Big Bang Nucleosynthesis (BBN), we consider the inflaton decay into Standard Model particles, thereby reheating the universe. This is achieved by considering the scalar field's decay into radiation, with decay rate Γ_ϕ. However, if PBHs dominate before that, then the universe is reheated through Hawking evaporation [45,83,127], and the reheating temperature corresponds to the evaporation temperature of the PBHs. Refs. [59–63] considered that the PBH-dominated phase occurs due to the interplay between the different energy densities of PBHs (matter), and a background fluid with an arbitrary equation of state $w > 0$, ignoring the specific formation mechanism of the PBHs. We, however, consider that PBHs are produced during an early matter-dominated phase, under the KP formalism, and that the PBH-dominated phase occurs due to the decay of the scalar field into radiation, which modifies the actual constraints on the abundance of PBHs. Then, we analyze the production of induced GWs by the Poissonian fluctuations of the PBH fluid. To our knowledge, this is the first time it has been studied in the literature.

This chapter is organized as follows: We begin in Sec. 6.1 by defining an analytical expression for our power spectrum and giving some details on the preheating period and the parameters of the model. Then, in Sec. 6.2, we describe the dynamics of a PBH-dominated phase, from the collapse of perturbations to the power spectrum of the PBH density fluctuations. The results for the induced GWs are obtained in Sec. 6.3, as well as a comparison

with previous studies in the literature. Conclusions are given in Sec. 6.4, and appendices D.1 and D.2 show some analytical estimations of the mass fraction of PBHs and the fractional energy densities of PBHs and GWs, respectively.

6.1 Inflation and preheating

As stated above, we consider an inflationary power spectrum with a Gaussian peak. According to Planck's 2018 results [30, 31], the inflationary power spectrum of curvature perturbations $\mathcal{R}_k$ can be parametrized as follows

$$\mathcal{P}_{\mathcal{R}}^{\text{inf}}(k) = \mathcal{A}_s \left(\frac{k}{k_*}\right)^{n_s-1}, \tag{6.1}$$

where $\mathcal{A}_s = 2.1 \times 10^{-9}$ is the amplitude of the power spectrum at the pivot scale $k_0 = 0.05\text{Mpc}^{-1}$, and $n_s \simeq 0.965$ is the spectral index. Motivated by other works [100, 253–271] (see above), we introduce a Gaussian peak in the power spectrum, and choose to parametrize it as a log-normal-like distribution, given by

$$\mathcal{P}_{\mathcal{R}}^{\text{peak}}(k) = \mathcal{A}_{\text{peak}} \exp\left[-\frac{\left(\log_{10}(k/k_{\text{peak}})\right)^2}{\sigma^2}\right], \tag{6.2}$$

where $\mathcal{A}_{\text{peak}}$ is the amplitude at the peak scale k_{peak} and the standard deviation of the Gaussian is chosen to be $\sigma = 0.2$ to reduce the number of free parameters. Eqn. (6.2) is useful for this work as it avoids the tails of the Gaussian peak (due to the $\log_{10}$ term), and since it constitutes a two-parameter ($\mathcal{A}_{\text{peak}}$ and k_{peak}) model-independent parametrization that can reflect the physics of the models described in [100, 253–271]. The total power spectrum is the sum of the contributions from (6.1) and (6.2), that is

$$\mathcal{P}_{\mathcal{R}}(k) = \mathcal{P}_{\mathcal{R}}^{\text{inf}}(k) + \mathcal{P}_{\mathcal{R}}^{\text{peak}}(k). \tag{6.3}$$

In Fig. 6.1 we show some examples of the power spectrum (6.3) along with several current (continuous) and forecasted (dashed) constraints on the power spectrum. The dotted-dashed constraints from PBHs represent non-standard scenarios that depend on the detailed nature of Dark Matter, which is currently unknown, as well as on the details of the Hawking radiation [83] and the production of Planck-size remnants after PBH evaporation [91–94, 274]. We will remain agnostic about these last constraints and consider values of $\mathcal{P}_{\mathcal{R}}(k)$ that are both above and below them, as illustrated in Fig. 6.1. Furthermore, the positions of the Gaussian peaks of the power spectra shown in Fig. 6.1 correspond to scales that exit the horizon at a time close to the end of inflation, when the scalar field is of the order of the Planck mass.

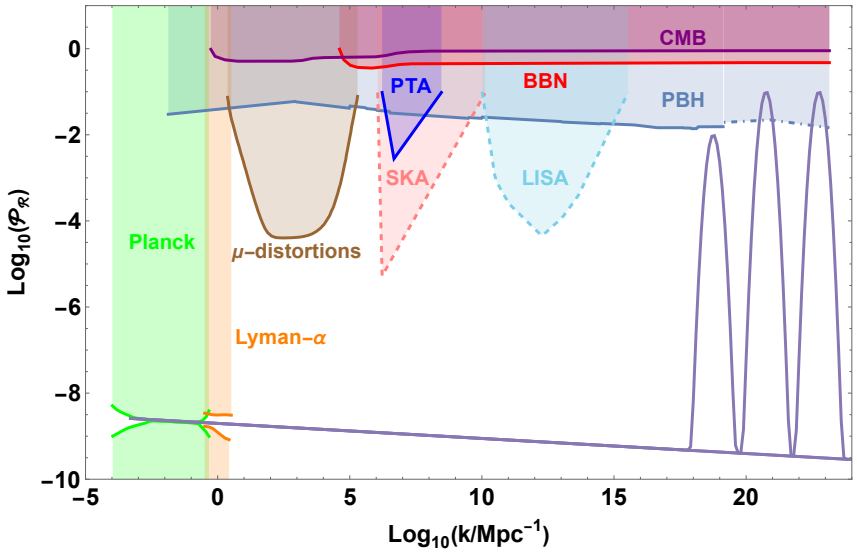

Figure 6.1: Three examples of inflationary power spectra + gaussian peak (corresponding to $A_{\rm peak} = 0.01,\ 0.1,\ 0.1$ and $k_{\rm peak} = 6\times10^{18}, 6\times10^{20}, 6\times10^{22}{\rm Mpc}^{-1}$ respectively), that we compare against the constraints on the power spectrum of curvature perturbations from PBHs [65, 273, 275], Planck observations on the CMB [31], Lyman-α forest [276], μ-distortions [277] and GWs [274, 278, 279] (PTA, SKA and LISA). The continuous (dashed) lines represent current (forecasted) constraints. The dotted-dashed lines for the PBH constraint represent the constraints associated with the non-standard scenarios like Hawking evaporation considerations and the possibility of PBHs remnants. The above Figure is produced from the data available in [65, 279].

According to Planck's results [30, 31], the upper limit on the energy density at the pivot scale is given by $\rho_{\rm inf} \lesssim 10^{16}$GeV, which translates into the following upper limit on the Hubble rate at the pivot scale $H_{\rm inf} \lesssim 2.5\times10^{-5}M_{\rm Pl}$. We further assume that H is constant during inflation and extrapolate that value till the end of inflation, where the preheating period begins. This phase is characterized by an oscillating scalar field at the bottom of the inflationary potential, which makes the universe (effectively) behave as being matter-dominated and implies that the scale factor can be parametrized as

$$a(t) \simeq a_{\rm end}\left(\frac{t}{t_{\rm end}}\right)^{2/3}, \tag{6.4}$$

where the suffix "$_{\rm end}$" means the quantity at the end of inflation and t is cosmic time. Also, the Hubble rate, defined as $H(t) = \dot{a}/a$, with an overdot denoting a derivative with respect to cosmic time, is given by

$$H(t) \simeq \frac{2}{3t}. \tag{6.5}$$

During this phase, the perturbations that enter the horizon collapse into PBHs, as shown in the next section. However, the quantity we use to compute the abundance of PBHs, *i.e.*, the mass fraction $\beta(k)$, is not the power spectrum of curvature perturbations, but the variance of the density perturbations, σ_k. For modes that enter the horizon after inflation,

the curvature perturbations are related to the density perturbations $\delta_{\phi,\boldsymbol{k}}$ as follows [17] [43, 45]

$$\delta_{\phi,\boldsymbol{k}} \simeq \frac{8}{5}\mathcal{R}_{\boldsymbol{k}}, \tag{6.6}$$

where a suffix "$_{\boldsymbol{k}}$" means Fourier component and k is the modulus of the wavenumber vector $\boldsymbol{k}$. Also, a suffix "$_{\phi}$" is introduced as a notation so that these fluctuations are not confused with the energy density fluctuation of the PBHs, which is defined below. Eqn. (6.6) is obtained from (2.10) evaluated at horizon-crossing time and implies that the power spectrum of the density perturbations should be written as

$$\mathcal{P}_{\delta_\phi}(k) \simeq \frac{64}{25}\mathcal{P}_{\mathcal{R}}(k), \tag{6.7}$$

and we can approximate the variance as follows

$$\sigma_k \simeq \sqrt{\mathcal{P}_{\delta_\phi}(k)}. \tag{6.8}$$

As explained above, to terminate the preheating stage and recover the usual reheating scenario, the inflaton field must decay into radiation via a decay rate Γ_ϕ, which occurs at a time $t_{\rm r} = \Gamma_\phi^{-1}$. At this point, the time evolution of the temperature of the radiation fluid is given by [41, 42, 280]

$$T_{\rm decay}(t) = \left(\frac{90}{\pi^2 g_*(T)}\right)^{1/4} \sqrt{\frac{\Gamma_\phi}{M_{\rm Pl}}} \left(\frac{a_{\rm r}}{a}\right) M_{\rm Pl}, \tag{6.9}$$

in units of Planck mass ($1M_{\rm Pl} = 1.22 \times 10^{19}$GeV). In this equation, $a_{\rm r} = a(t_{\rm r})$ and $g_*(T)$ is the number of relativistic degrees of freedom, which takes the value $g_* = 106.75$ for $T \gtrsim 100$GeV (assuming the Standard Model is valid at those energies, see Refs. [281, 282] for a review of the dependence of the effective degrees of freedom with temperature). However, if after the decay the abundance of PBHs is high enough, they will dominate due to the different redshifts of the energy densities of radiation and PBHs, a^{-4} and a^{-3}, respectively. In this case, since radiation becomes a subdominant component, the reheating occurs at a later stage and through the evaporation of PBHs due to Hawking radiation [83], with an associated temperature given by (see Eqn. (2.24) of [61])

$$T_{\rm eva} \simeq 2.76 \times 10^4 \text{GeV} \left(\frac{g_*(T_{\rm eva})}{106.75}\right)^{-1/4} \left(\frac{g_H}{108}\right)^{1/2} \left(\frac{M_{\rm PBH,0}}{10^4 \text{g}}\right)^{-3/2}, \tag{6.10}$$

with g_H being the spin-weighted degrees of freedom and $M_{\rm PBH,0}$ the mean mass of the PBH distribution, considered as the mass of the PBHs associated with the Gaussian peak (see

[17] In this chapter, since our focus is only on the scales that are amplified during inflation, we do not consider the subhorizon modes that never exit the horizon during inflation. Although they could contribute to PBH formation, as shown in [1, 3] (see Chapters 2, 3 and 4), their contribution is only toward very small scales in contrast to what we explore in this work.

Eqns. (6.15) and (6.20)). Taking into account that for a successful BBN the temperature of the plasma should be $T_{\rm BBN} > 4$MeV [283] and the upper limit on the energy scale of inflation, $H_{\rm inf}/M_{\rm Pl} \lesssim 2.5 \times 10^{-5}$ [30, 31], one obtains the following allowed range for the PBH masses, given by [59–63]

$$10\text{g} \lesssim M_{\rm PBH,0} \lesssim 10^{9}\text{g}. \tag{6.11}$$

Since the position of the Gaussian peak sets the mean mass of the distribution of PBHs, we choose $k_{\rm peak}$ to fit accordingly inside this mass range. Although the parametrization of the peak of the power spectrum is rather arbitrary, we, in essence, try to reproduce a Starobinsky-like model [24] with a feature in the potential that produces the peak, as explained above. This allows us to select the values of the decay rates in terms of the expected temperature of reheating of these models [284–286]. Thus, we consider the following range of inflaton decay rates for our analysis

$$\Gamma_\phi^{\rm min} = 10^{-25} M_{\rm Pl} < \Gamma_\phi < 10^{-19} M_{\rm Pl} = \Gamma_\phi^{\rm max}, \tag{6.12}$$

which implies reheating temperatures of 10^6GeV to 10^9GeV. We have checked that $\Gamma_\phi^{\rm max}$ does not conflict with the PBHs. That is, they form before the field decays. Also, for $\Gamma_\phi^{\rm min}$, we select the scenarios where PBHs dominate before their evaporation (otherwise they do not produce GWs). In any case, the decay rate of the inflaton should be considered carefully. It could be the case that when the PBHs dominate, the temperature of the surrounding radiation (6.9), due to the field's decay, is higher than the temperature of the PBHs themselves (6.10), which delays the evaporation process and allows a longer PBH-dominated phase. We consider this when computing the GWs from the PBH-dominated phase in Sec. 6.3. However, this effect on the production of GWs, if any, is minimal.

6.2 Primordial black hole dominance

In this section, we describe the collapse process of a perturbation into a PBH under the KP formalism and compute the fractional energy density $\Omega_{\rm PBH}$. Then, assuming that the scalar field decays into radiation, we study the evolution of the energy densities of the field, radiation, and the PBHs. Finally, after determining the conditions for a PBH-dominated era, we show the power spectrum of Poissonian fluctuations of the energy density of the PBH fluid.

6.2.1 Collapse of perturbations during preheating

As stated in Appendix B.2, in a matter-dominated era, the formation probability of a PBHs relies on the fraction of sufficiently spherical regions to undergo collapse. To compute it, we use the estimation from the anisotropy effect $\beta^{\rm KP}_{\rm aniso}(k)$, Eqn. (B.28), which is valid

for small and large perturbations and is the dominant contribution. This is the formula for the mass fraction that we are using in our computations. The mass fraction must be computed, for each k, at the time t_k when the mode enters the horizon. This is obtained by assuming that when a mode crosses the horizon the relation $k = a(t_k)H(t_k)$ is satisfied, which during a matter-dominated phase is given in terms of k by

$$t_k \simeq t_{\rm end}\left(\frac{k_{\rm end}}{k}\right)^3, \tag{6.13}$$

where we have used Eqns. (6.4) and (6.5), and defined $k_{\rm end} = a(t_{\rm end})H(t_{\rm end})$. Thus, using (B.28), we can compute the mass fraction as a function of time and then relate it to the fractional energy density in the form of PBHs as follows [82, 118]

$$\beta(M_{\rm f}) \equiv \frac{{\rm d}\Omega_{\rm PBH}(M_{\rm f})}{{\rm d}\ln(M_{\rm f})} \qquad \rightarrow \qquad \Omega_{\rm PBH}(M_{\rm f}) = \int_{M_{\rm H}^{\rm end}}^{M_{\rm f}} \beta(\tilde{M}_{\rm f}){\rm d}\ln(\tilde{M}_{\rm f}), \tag{6.14}$$

where $M_{\rm f}$ is the PBH mass at the moment of formation, and the lower limit of the integral is the horizon mass at the end of inflation, which corresponds to the smallest possible PBH mass. As explained above, to not to overestimate $\Omega_{\rm PBH}$, we must take into account the time at which each perturbation enters the horizon and collapses. To do this, we relate the mass of the PBHs at formation, $M_{\rm f}$, with the wavenumber k at the moment it crosses the horizon using equation (6.13) as follows

$$M_{\rm f}(k) \simeq \frac{4\pi\gamma}{H(t_k)} \simeq \gamma M_H^{\rm end}\left(\frac{k_{\rm end}}{k}\right)^3, \tag{6.15}$$

where γ determines the fraction of the horizon mass that goes into the PBHs (we assume $\gamma = 1$ for simplicity) and $M_H^{\rm end}$ is the horizon mass at the end of inflation. Using (6.15), the wavenumber k can be seen as a "measure of time" and the integral in (6.14) is rewritten as

$$\Omega_{\rm PBH}(k) = 3\int_{k}^{k_{\rm end}} \beta(\tilde{k}){\rm d}\ln(\tilde{k}), \tag{6.16}$$

where the lower limit represents the moment in cosmic time t at which the wavenumber k crosses the horizon, *c.f.* Eqn. (6.13), and the factor of 3 comes from the relation between ${\rm d}\ln(M_f)$ and ${\rm d}\ln(k)$, see Eqn. (6.15). The results for the numerical integration of (6.16) are shown in Fig. 6.2 as a function of the number of efolds N from the end of inflation ($N_{\rm end}$) for two values of the position of the Gaussian peak, $10^{-2}k_{\rm end}$, and $10^{-1}k_{\rm end}$, with its amplitude ranging from 10^{-3} to 1. We observe that as we move the Gaussian peak towards higher scales, it takes more time for $\Omega_{\rm PBH}$ to grow and (potentially) dominate. Moreover, we also observe the appearance of a plateau for high values of N, whose amplitude depends on $\mathcal{A}_{\rm peak}$, see Appendix D.1 for details. This clearly reflects the fact that the inflationary spectrum $\mathcal{P}_{\mathcal{R}}^{\rm inf}$ hardly contributes to the mass fraction, and once the peak has entered the horizon, $\Omega_{\rm PBH}$ stays fixed to a constant value. We consider that the totality

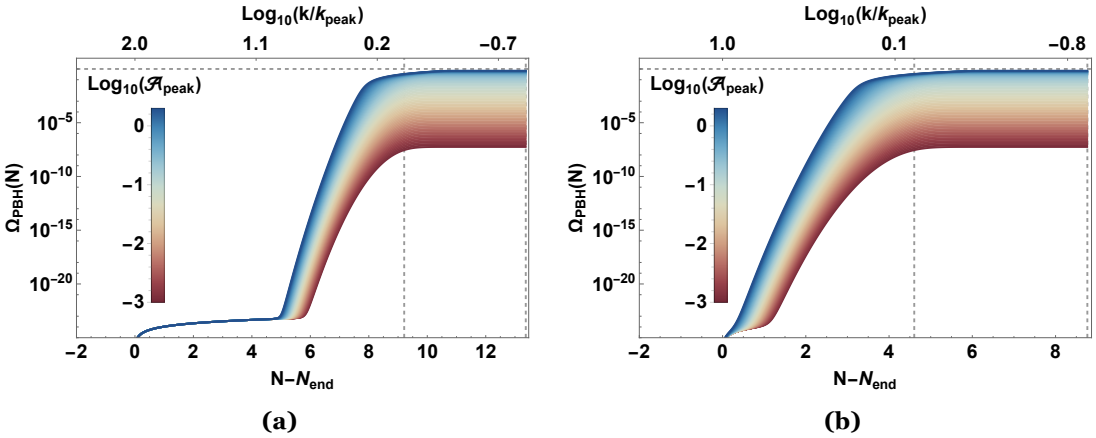

Figure 6.2: Fractional energy density of PBHs for **a)** $k_{\rm peak} = 10^{-2} k_{\rm end}$ and **b)** $k_{\rm peak} = 10^{-1} k_{\rm end}$ as a function of the number of efolds N. Here, $k_{end} = 5.7 \times 10^{24} \text{Mpc}^{-1}$ is the scale corresponding to the end of inflation, which exits the horizon approximately $N_{end} = 60$ e-folds after the pivot scale. The vertical dashed line to the left corresponds to the point where the peak enters the horizon and the one to the left when the scale $k_{\rm peak}/8$ enters the horizon. The horizontal dashed line corresponds to $\Omega_{\rm PBH}(t) = 1$.

of the peak has entered the horizon when the scale $k_{\rm peak}/8$ enters, which approximately corresponds to a distance of 10σ from the peak. This is the reason why the numerical computation of (6.14) is terminated at the moment $t_{k_{\rm peak}/8}$, represented by the vertical dashed line to the right, when the scale $k_{\rm peak}/8$ enters the horizon and $\Omega_{\rm PBH}$ is fixed on the plateau. However, we remark that the choice of 10σ is just orientative, and one could, in principle, choose either higher or lower values for this scale. In Appendix D.1, we show some analytical approximations to the fractional energy density of PBHs (6.16), where the dependence with the parameters of the model, specifically with $\mathcal{A}_{\rm peak}$, is revealed.

As stated in Appendix B.2, in principle, one could consider other non-spherical effects in the formation probability of the PBHs under the KP formalism, such as the inhomogeneity effect [119, 125, 287], or the angular momentum of the black holes [120]. If that is the case, the total mass fraction is computed as the product of the individual mass fractions associated with each effect. We however restrict this work to the anisotropy effect, as it is the dominant one.

6.2.2 Hawking evaporation

As seen in Fig. 6.2, once the Gaussian peak has entered the horizon, the fractional energy density of PBHs reaches a plateau and gets fixed to a constant value. For reasons obvious in the following, we call this time the "initial" time and label it as

$$t_{\rm in} = t_{k_{\rm peak}/8}. \tag{6.17}$$

According to Hawking [83], PBHs evaporate and emit particles with an approximate thermal spectrum corresponding to the temperature $T_{\rm PBH} = M_{\rm Pl}^2/M_{\rm PBH}$ (based on Hawking evaporation). However, due to this particle emission, the PBHs lose mass at a rate given

by [59, 288, 289]

$$\Gamma_{\rm PBH}(t) \equiv -\frac{{\rm d}\ln M_{\rm PBH}(t)}{{\rm d}t} = A\frac{M_{\rm Pl}^4}{M_{\rm PBH}^3(t)}, \tag{6.18}$$

where the constant A is given by

$$A = \frac{3.8\pi}{480} g_H, \tag{6.19}$$

where we assume $g_H \simeq 108$ (corresponding to standard model degrees of freedom) for $M_{\rm PBH} \ll 10^{11} g$. In our case, we have an extended mass distribution, contrary to the standard monochromatic case. To simplify, we assume that the mean PBH mass corresponds to the mass of the PBHs formed at the peak of the distribution, that is

$$M_{\rm PBH,0} = M_{\rm f}(k_{\rm peak}). \tag{6.20}$$

By integrating Eqn. (6.18), one obtains the following time-dependence of the mass

$$M_{\rm PBH}(t) = M_{\rm PBH,0}\left(1 - \frac{t}{t_{\rm eva}}\right)^{1/3}, \tag{6.21}$$

being $t_{\rm eva}$ the time at which the PBHs completely evaporate, given by

$$t_{\rm eva} = \frac{M_{\rm PBH,0}^3}{3AM_{\rm Pl}^4}. \tag{6.22}$$

6.2.3 Boltzmann equations for the evolution of the energy densities

Considering now the energy transfer from the inflaton field to the PBHs and then to radiation, we consider the following Boltzmann equations for the evolution of the energy densities [59]:

$$\begin{aligned} \dot{\rho}_{\rm PBH} + (3H + \Gamma_{\rm PBH})\,\rho_{\rm PBH} &= 0, \\ \dot{\rho}_\phi + (3H + \Gamma_\phi)\,\rho_\phi &= 0, \\ \dot{\rho}_{\rm r} + 4H\rho_{\rm r} - \Gamma_{\rm PBH}\,\rho_{\rm PBH} - \Gamma_\phi\,\rho_\phi &= 0, \end{aligned} \tag{6.23}$$

where $\rho_{\rm PBH}$, ρ_ϕ, and $\rho_{\rm r}$ represent the energy densities of PBHs, scalar field, and radiation, respectively. Note that in the set of equations (6.23) we neglect any backreactions associated with PBH evaporation. Therefore, we assume that inflaton energy densities are unaffected by PBH evaporation. To solve the system (6.23) we use the following set of

initial conditions

$$\begin{aligned}\rho_{\rm PBH}(t_{\rm in}) &= \Omega_{\rm PBH}(t_{\rm in})\rho_T(t_{\rm in}),\\ \rho_\phi(t_{\rm in}) &= (1-\Omega_{\rm PBH}(t_{\rm in}))\rho_T(t_{\rm in}),\\ \rho_{\rm r}(t_{\rm in}) &= 0,\end{aligned} \tag{6.24}$$

where the total energy density, ρ_T, follows from the Friedmann's equation

$$\rho_T = \rho_{\rm PBH} + \rho_\phi + \rho_{\rm r} = 3H^2M_{\rm Pl}^2. \tag{6.25}$$

Fig. 6.3 shows the solution of the system (6.23) together with the initial conditions (6.24) and for several values of Γ_ϕ and $\Omega_{\rm PBH}(t_{\rm in})$. Note that the values of $\Omega_{\rm PBH}(t_{\rm in})$ in our case are not arbitrary. Rather, they are determined from the PBH formation mechanism, which in our case is determined by the KP framework we explained in the previous section. The time $t_{\rm in}$ here can also be seen as the time when the PBH critical energy density $\Omega_{\rm PBH}$ gets saturated to a constant value (See Fig. 6.2). We have chosen $k_{\rm peak} = 0.1k_{\rm end}$ for all our computations. The left column in Fig. 6.3 shows the effect of changing Γ_ϕ, growing from top to bottom, whereas the right column shows the effect of a varying $\Omega_{\rm PBH}(t_{\rm in})$, also growing from top to bottom. We observe that the higher both of these parameters are, the longer the PBHs dominate. Since the position of the Gaussian peak is the same for all plots, which essentially sets the mean mass of the PBH distribution, evaporation occurs (approximately) at the same number of efolds, $N_{\rm eva}$[18]. Thus, setting $k_{\rm peak}$ towards higher scales increases the evaporation time and consequently decreases the temperature of the plasma after evaporation, which could conflict with BBN, as shown above (see Eqn. (6.11)).

The vertical dashed lines in Fig. 6.3 mark several relevant times, translated to number of efolds. From left to right: $t_{\rm in}$, ϕ-radiation equality ($t_{\rm r}$), radiation-PBH equality ($t_{\rm PBH}$), and PBH evaporation ($t_{\rm eva}$). The former and the latter are defined in Eqns. (6.17) and (6.22), respectively. The ϕ-radiation equality occurs approximately at $t_{\rm r} \sim \Gamma_\phi^{-1}$ and, to estimate the transition from radiation to PBHs we do the following. Initially, the scalar field dominates, and thus ρ_ϕ redshifts as

$$\rho_\phi(t) \sim \rho_\phi(t_{\rm in})\left(\frac{a(t_{\rm in})}{a(t)}\right)^3 \sim \rho_\phi(t_{\rm in})\left(\frac{t_{\rm in}}{t}\right)^2, \tag{6.26}$$

where we assume the standard matter-dominated power-law behavior of the scale factor, $a \sim t^{2/3}$. The decay into radiation occurs at a time $t_{\rm r} \sim \Gamma_\phi^{-1}$, which implies that

$$\rho_\phi(t_{\rm r}) \sim \rho_\phi(t_{\rm in})\left(\frac{t_{\rm in}}{t_{\rm r}}\right)^2. \tag{6.27}$$

[18] It is worth noting here that any modification of Γ_ϕ and/or $\mathcal{A}_{\rm peaks}$ turns into different expansion rates of the universe, depending on the amount of time matter (ϕ, PBHs) or radiation dominates. This means even though $t_{\rm eva}$ is fixed, $N_{\rm eva}$ could in principle differ based on the duration of PBH dominance (See (6.31)).

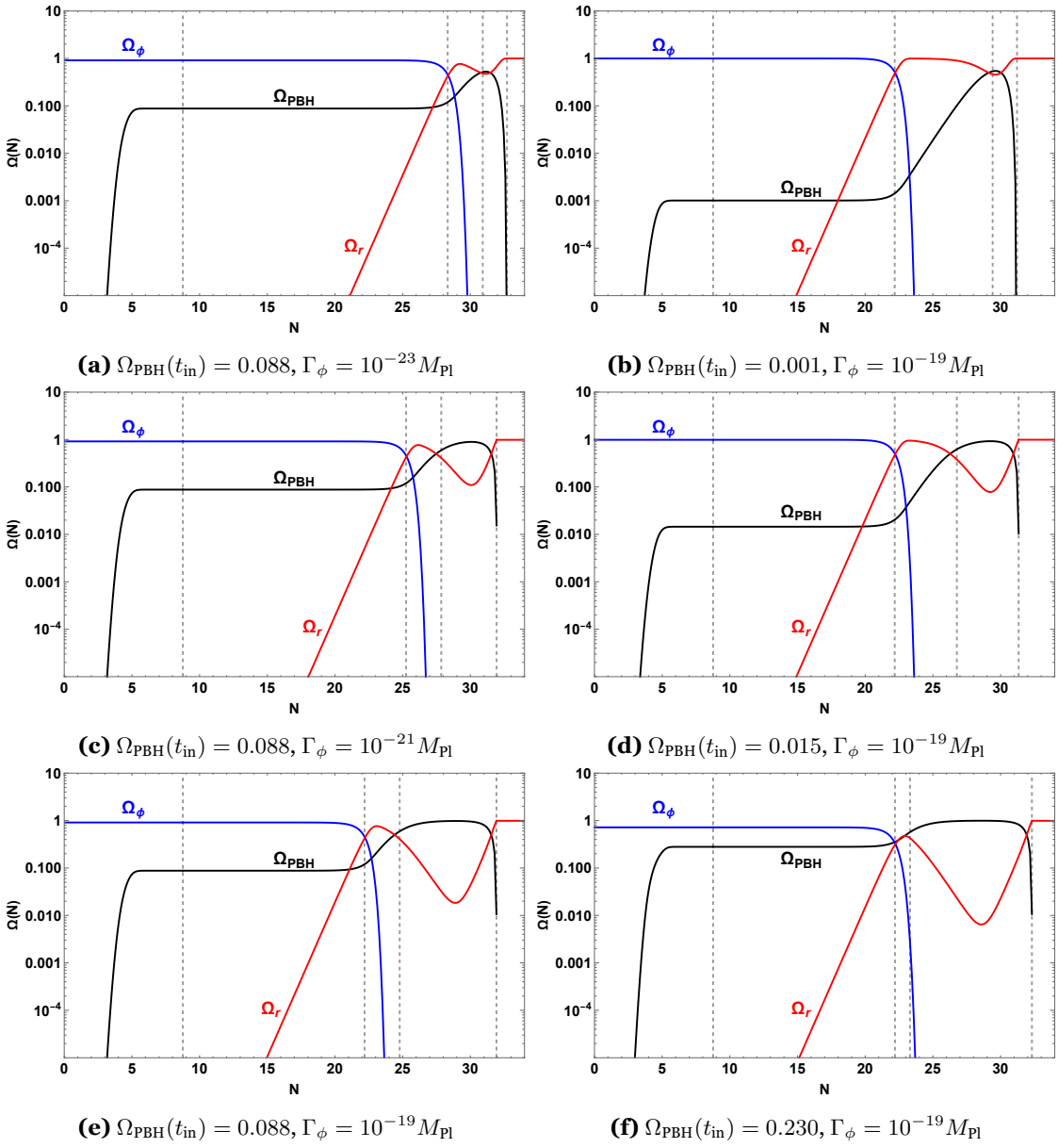

(a) $\Omega_{\rm PBH}(t_{\rm in}) = 0.088$, $\Gamma_\phi = 10^{-23} M_{\rm Pl}$

(b) $\Omega_{\rm PBH}(t_{\rm in}) = 0.001$, $\Gamma_\phi = 10^{-19} M_{\rm Pl}$

(c) $\Omega_{\rm PBH}(t_{\rm in}) = 0.088$, $\Gamma_\phi = 10^{-21} M_{\rm Pl}$

(d) $\Omega_{\rm PBH}(t_{\rm in}) = 0.015$, $\Gamma_\phi = 10^{-19} M_{\rm Pl}$

(e) $\Omega_{\rm PBH}(t_{\rm in}) = 0.088$, $\Gamma_\phi = 10^{-19} M_{\rm Pl}$

(f) $\Omega_{\rm PBH}(t_{\rm in}) = 0.230$, $\Gamma_\phi = 10^{-19} M_{\rm Pl}$

Figure 6.3: Evolution of the fractional energy densities for PBHs (black), the scalar field (blue), and radiation (red). The left column shows the effect of varying Γ_ϕ, growing from top to bottom, whereas the right column shows the effect of a varying $\Omega_{\rm PBH}(t_{\rm in})$, also growing from top to bottom. The vertical dashed lines marks from left to right: $t_{\rm in}$ (translated to efolds), ϕ-radiation equality, radiation-PBH equality, and $t_{\rm eva}$ (translated to efolds), respectively.

At this point, $\rho_\phi(t_{\rm r}) \sim \rho_r(t_{\rm r})$ and radiation becomes the dominant component. This implies that $\rho_{\rm r}$ redshifts as

$$\rho_{\rm r}(t) \sim \rho_{\rm r}(t_{\rm r}) \left(\frac{a(t_{\rm r})}{a(t)}\right)^4 \sim \rho_{\rm r}(t_{\rm r}) \left(\frac{t_{\rm r}}{t}\right)^2, \tag{6.28}$$

where now we used that $a \sim t^{1/2}$ during radiation-dominated. On the other side, $\rho_{\rm PBH}$ redshifts as follows during this radiation-dominated era

$$\rho_{\rm PBH}(t) \sim \rho_{\rm PBH}(t_{\rm in}) \left(\frac{t_{\rm in}}{t_{\rm r}}\right)^2 \left(\frac{t_{\rm r}}{t}\right)^{3/2}, \tag{6.29}$$

where we considered the redshift during the time ρ_ϕ dominates. Equating (6.28) and (6.29), we obtain, approximately, the time at which PBHs dominate, which is given by

$$t_{\rm PBH} \sim \Gamma_\phi^{-1} \left(\frac{1-\Omega_{\rm PBH}(t_{\rm in})}{\Omega_{\rm PBH}(t_{\rm in})}\right)^2. \tag{6.30}$$

Using this, the approximated time the PBH-dominated phase lasts is computed as the difference between eqns (6.22) and (6.30), that is

$$\Delta_{\rm PBH} = t_{\rm eva} - t_{\rm PBH} = \frac{M_{\rm f}^3}{3AM_{\rm Pl}^4} - \Gamma_\phi^{-1} \left(\frac{1-\Omega_{\rm PBH}(t_{\rm in})}{\Omega_{\rm PBH}(t_{\rm in})}\right)^2. \tag{6.31}$$

The longer the PBH-dominated phase lasts, the higher the induced GWs produced (See Sec. 6.3). In this sense, Eqn. (6.31) clearly reflects the impact that the different parameters of the model have on the production of GWs. For instance, a small decay rate (the scalar field decays late in time) reduces the time the PBHs dominate but can be compensated if their abundance is large. On the other hand, a large mean PBH mass increases this time since PBHs evaporate later. In essence, Eqn. (6.31) shows the rich interplay between the parameters of the model.

6.2.4 Power spectrum of primordial black hole fluctuations

In this section, we compute the power spectrum corresponding to the PBH domination phase. In order to do this, let us assume that PBHs are randomly distributed in space, meaning that the probability distribution of each PBH position is uniform and that the locations of different black holes are uncorrelated. This assumption effectively corresponds to Poissonian statistics. A key point to note is that this description breaks down at distances smaller than the mean comoving separation, $\bar{r}$, between neighboring black holes. Below $\bar{r}$, the discrete nature of the PBH distribution becomes significant, making the fluid approximation inadequate. This mean separation is computed as [62]

$$\bar{r} = \left(\frac{3M_{\rm PBH,0}}{4\pi\rho_{\rm PBH}}\right)^{1/3}. \tag{6.32}$$

The fact that PBHs are discrete objects introduces inhomogeneities, which can be quantified with the power spectrum of PBHs density fluctuations $\delta_{\mathrm{PBH},k}$. A detailed derivation is provided in Appendix A of [62]. Here, for completeness, we briefly summarize the main steps. For N PBHs of equal mass M_{PBH} in a volume V, the probability of finding n PBHs in a subvolume v is given by the binomial distribution

$$P_n^{\mathrm{bin}}(r) = \binom{N}{n} \left(\frac{v}{V}\right)^n \left(1 - \frac{v}{V}\right)^{N-n}, \tag{6.33}$$

which approaches a Poisson distribution in the large-N limit

$$\lim_{N\to\infty} P_n^{\mathrm{bin}}(r) = P_n^{\mathrm{Poiss}}(r) = \left(\frac{r}{\bar{r}}\right)^{3n} \frac{e^{-\frac{r^3}{\bar{r}^3}}}{n!}. \tag{6.34}$$

Using this distribution, one can compute the variance (two-point correlation function) of the PBH energy density fluctuations, which turns out to be proportional to a Dirac delta function [62]:

$$\left\langle \frac{\delta\rho_{\mathrm{PBH}}(\mathbf{x})}{\rho_{\mathrm{tot}}} \frac{\delta\rho_{\mathrm{PBH}}(\mathbf{x}')}{\rho_{\mathrm{tot}}} \right\rangle \propto \delta(\mathbf{x} - \mathbf{x}'), \tag{6.35}$$

implying uncorrelated (white noise) fluctuations. This proportionality with the Dirac delta resides in the fact that the density fluctuations are completely uncorrelated beyond the scale of individual points: there is non-zero correlation only at zero separation. Fourier transforming this result yields a constant power spectrum for the density contrast, $P_{\delta_{\mathrm{PBH}}}(k) =$ const, with the proportionality constant independent of k. The dimensionless power spectrum is then given by[19] [62]

$$\mathcal{P}_{\delta_{\mathrm{PBH}}}(k) = \frac{2}{3\pi} \left(\frac{k}{k_{\mathrm{UV}}}\right)^3 \Theta\left(k_{\mathrm{UV}} - k\right), \tag{6.36}$$

which scales as k^3 and where $k_{\mathrm{UV}} = a/\bar{r}$ is the ultraviolet cutoff of the power spectrum. This scaling reflects the Poisson nature of the PBH distribution and indicates that power increases with decreasing scale (increasing k), up to a UV cutoff set by the mean PBH separation. For scales larger than k_{UV}, the PBH fluid can be treated as non-relativistic matter, but as k approaches k_{UV}, the discrete nature of the PBHs leads to shot-noise effects and the fluid picture is no longer valid [59, 60]. One can compare this scale-dependent power spectrum with the scale-invariant power spectrum of curvature perturbations, defined in (1.6). The reason behind the k^3 scaling of Eqn. (6.36), as shown above, resides in the nature of a Poisson-distributed matter field like a gas of PBHs, contrary to the case of Gaussian inflationary perturbations. This k^3 scaling indicates that small-scale perturbations (high k) dominate the power, contrary to the inflationary power spectrum. These energy

[19] We are not considering possible deviation from Poisson statistics by non-Gaussianities that could further lead to primordial clustering [238, 239] because our consideration of the KP collapse mechanism is restricted to overdensities that are small enough.

density fluctuations correspond to isocurvature perturbations when the PBHs form. In other words, PBHs form in this case from the perturbations of the scalar field, and by conservation of energy, any missing part of the scalar field fluid that ends up into a PBHs is compensated by PBHs themselves, so that the fluctuations in both fluids are equal and opposite, *i.e.*, $\delta_{\text{PBH},\boldsymbol{k}} = -\delta_{\phi,\boldsymbol{k}}$, which is what mainly characterizes isocurvature perturbations. Initially, these isocurvature PBH perturbations do not induce GWs, but as the PBH become the dominant component of the universe, the isocurvature PBH perturbations source curvature perturbations, which have a gravitational potential associated, and this last is responsible for inducing GWs. Note that these induced GWs should not be confused with the induced GWs from amplified perturbations during, for instance, an early matter-dominated period [4, 48, 50, 193, 195]. In this case, the GWs are sourced by the gravitational potential of the Poissonian fluctuations associated with the overproduction (dominance) of the PBHs, instead of being sourced by the inflaton perturbations. In essence, the novelty of this approach resides in the fact that the isocurvature perturbations are sourced by the scalar field, contrary to the standard approach where the radiation fluid sources the isocurvature perturbations [59–63]. Moreover, we do take into account the whole evolution of the PBHs by considering their formation mechanism, instead of assuming an initial abundance of PBHs.

So now the problem at hand is to relate the initial isocurvature fluctuations $\delta_{\text{PBH},\boldsymbol{k}}$ to the gravitational potential $\Phi_{\text{PBH},\boldsymbol{k}}$ of the PBH fluid. Following [62], this relation is given by

$$\Phi_{\text{PBH},\boldsymbol{k}} \simeq -\frac{1}{5}\delta_{\text{PBH},\boldsymbol{k}} \tag{6.37}$$

on super-Hubble scales, and by

$$\Phi_{\text{PBH},\boldsymbol{k}} \simeq -\frac{9}{4}\left(\frac{k_{\text{PBH}}}{k}\right)^2 \delta_{\text{PBH},\boldsymbol{k}} \tag{6.38}$$

on sub-Hubble scales, where $k_{\text{PBH}} = a(t_{\text{PBH}})H(t_{\text{PBH}})$ is the scale that enters the horizon by the time PBHs dominate, where t_{PBH} is defined in (6.30). What Eqns. (6.37) and (6.38) tell us is that the gravitational potential is constant in time during a PBH-dominated era, as it is expected from a matter-dominated epoch. One can interpolate between the two equations to obtain a single expression that reflects the behavior on both super and sub-Hubble scales, that is

$$\Phi_{\text{PBH},\boldsymbol{k}} \simeq -\left[5 + \frac{4}{9}\left(\frac{k}{k_{\text{PBH}}}\right)^2\right]^{-1} \delta_{\text{PBH},\boldsymbol{k}}, \tag{6.39}$$

and use this in (6.36) to obtain the power spectrum of the gravitational potential associated with a dominating fluid of PBHs:

$$\mathcal{P}_{\Phi_{\text{PBH}}}(k) = \frac{2}{3\pi}\left(\frac{k}{k_{\text{UV}}}\right)^3 \left[5 + \frac{4}{9}\left(\frac{k}{k_{\text{PBH}}}\right)^2\right]^{-2}. \tag{6.40}$$

This spectrum presents a maximum at $k = \frac{3\sqrt{15}}{2} k_{\rm PBH}$ of order

$$\mathcal{P}^{\rm max}_{\Phi_{\rm PBH}} = \frac{27}{64\pi}\sqrt{\frac{3}{5}}\left(\frac{k_{\rm PBH}}{k_{\rm UV}}\right)^3 \simeq \frac{27}{64\pi}\sqrt{\frac{3}{5}}\gamma\left(\frac{\Gamma_\phi}{H_{\rm end}}\right)\frac{\Omega^2_{\rm PBH}(t_{\rm in})}{(1-\Omega_{\rm PBH}(t_{\rm in}))^3}\left(\frac{k_{\rm end}}{k_{\rm peak}}\right)^3, \tag{6.41}$$

where $\Omega_{\rm PBH}(t_{\rm in})$ can also be estimated from the parameters of the model. See Appendix D.1 and particularly Eqn. (D.12) for details.

6.3 Induced gravitational waves

Now that we have computed the power spectrum of the gravitational potential induced by the PBH density contrast, we can compute the associated GWs production due to the PBH domination [59–63]. Before going into detail, it is important to make some remarks. GWs are mainly produced in two ways:

- ***First-order GWs***: This signal corresponds to the stochastic background generated by the inflationary fluctuations $\mathcal{P}^{\rm inf}_{\mathcal{R}}$, with an almost flat power spectrum and usually very weak, which we call BGWs.
- ***Second-order GWs***: Scalar perturbations couple to the tensor ones at third-order in the perturbed expansion of the action and induce GWs. For this reason, these are called scalar-induced gravitational waves (SIGWs). Several mechanisms can produce amplified scalar perturbations, as we have seen. However, in this Chapter, we focus on the amplified scalar density fluctuations from the PBH-dominated phase and apply the approach in Refs. [48, 50, 195].

When considering both scalar and tensor fluctuations in the second-order perturbed Einstein equations, one derives the following equation of motion for the tensor perturbations

$$\ddot{h}^{(\lambda)}_{\boldsymbol{k}}(t) + 3H\dot{h}^{(\lambda)}_{\boldsymbol{k}}(t) + \frac{k^2}{a^2}h^{(\lambda)}_{\boldsymbol{k}}(t) = \frac{\mathcal{S}(\boldsymbol{k},t)}{a^2}, \tag{6.42}$$

where $\lambda = +, \times$ denotes the two polarization states of the tensor modes and $\mathcal{S}(\boldsymbol{k},t)$ is the source term, computed as a convolution of different modes. Here and in what follows, we work in the Newtonian gauge. The source term arises only at third-order in the perturbed expansion of the action and shows that the SIGWs are no longer free-propagating waves but rather a metric fluctuation arising from terms quadratic in the scalar perturbations [50]. In this case, it is given by

$$\mathcal{S}(k,t) = 4\int \frac{{\rm d}^3\tilde{k}}{(2\pi)^{3/2}}\tilde{k}^2(1-\mu^2)\Phi_{{\rm PBH},\tilde{\boldsymbol{k}}}\Phi_{{\rm PBH},|\boldsymbol{k}-\tilde{\boldsymbol{k}}|}. \tag{6.43}$$

As one can observe from this expression, the source term reflects that the contribution from any individual mode is diluted and mixed with the contributions coming from other

modes. The power spectrum of the tensor perturbations is given by

$$\langle h_{\boldsymbol{k}}^{(\lambda)}(t) h_{\boldsymbol{k}'}^{(\lambda)}(t)\rangle = \frac{1}{2}\frac{2\pi^2}{k^3}\delta^3(\boldsymbol{k}+\boldsymbol{k}')\mathcal{P}_h(k,t), \tag{6.44}$$

where the $1/2$ factor comes from the fact that $\mathcal{P}_h(k,t)$ includes contributions from both polarizations. During a PBH-dominated phase, the gravitational potential is constant in time for all scales, and so it is the source term (6.43). Therefore, one can attempt to obtain a particular solution of (6.42) and compute the correlator in (6.44) to obtain the power spectrum of GWs induced by PBH domination:

$$\mathcal{P}_h^{\text{PBH}}(k,t) = \frac{16 g^2(k,t)}{k}\int_{k_{\text{eva}}}^{k_{\text{UV}}} \mathrm{d}\tilde{k}\int_{-1}^{1}\mathrm{d}\mu\,\frac{\tilde{k}^3\,(1-\mu^2)^2}{|k-\tilde{k}|^3}\mathcal{P}_{\Phi_{\text{PBH}}}(\tilde{k})\mathcal{P}_{\Phi_{\text{PBH}}}(|\boldsymbol{k}-\tilde{\boldsymbol{k}}|), \tag{6.45}$$

where $k_{\text{eva}} = a(t_{\text{eva}})H(t_{\text{eva}})$ that corresponds to the smallest co-moving wavenumber that enters the horizon at the PBH evaporation time. The function $g(k,t)$ is known as the growth function for the tensor modes, defined as

$$g(k,t) = 1 + 3\,\frac{\frac{2k}{aH}\cos\left(\frac{2k}{aH}\right) - \sin\left(\frac{2k}{aH}\right)}{\left(\frac{2k}{aH}\right)^3}, \tag{6.46}$$

see [50] for details. $\mathcal{P}_{\Phi_{\text{PBH}}}(k)$ is given in (6.40), and the limits of the integral are chosen so that we consider just the relevant modes during PBH-dominated. Still, the main quantity characterizing this scenario is the spectral energy density of GWs, $\Omega_{\text{GW}}^{\text{PBH}}$, used to compare theoretical predictions with current constraints and future observations. It is computed as follows

$$\Omega_{\text{GW}}^{\text{PBH}}(k,t) = \frac{1}{\rho_c}\frac{\mathrm{d}\rho_{\text{GW}}}{\mathrm{d}\ln k}, \tag{6.47}$$

and represents the energy density per logarithm of k over the critical density $\rho_c = 3M_{\text{Pl}}^2 H^2$. Since GWs redshift at sub-Hubble scales as any non-interacting relativistic particles after being produced, the present spectral energy density of GWs is therefore approximated by [50]

$$\Omega_{\text{GW}}^{\text{PBH}}(k,t_0) \simeq \frac{\Omega_\gamma^0}{12}\left(\frac{k}{k_{\text{eva}}}\right)^2 \mathcal{P}_h^{\text{PBH}}(k,t_{\text{eva}}) \tag{6.48}$$

where $\Omega_\gamma^0 \simeq 1.2\times 10^{-5}$ is the present energy density of photons, and t_0 represents the present epoch. See Appendix D.2 for analytical estimations of (6.48) as a function of the parameters of the model. Particularly, Eqns. (D.22) and (D.23) show the approximations of $\Omega_{\text{GW}}^{\text{PBH}}(k,t_0)$ for $k \ll k_{\text{PBH}}$ and $k \gg k_{\text{PBH}}$, respectively. Now, these GWs are produced before BBN, and thus they cannot interfere with its predictions. If GWs are overproduced, then they contribute significantly to the radiation density and can potentially change the expansion rate of the universe, which modifies the abundance of light elements. To avoid

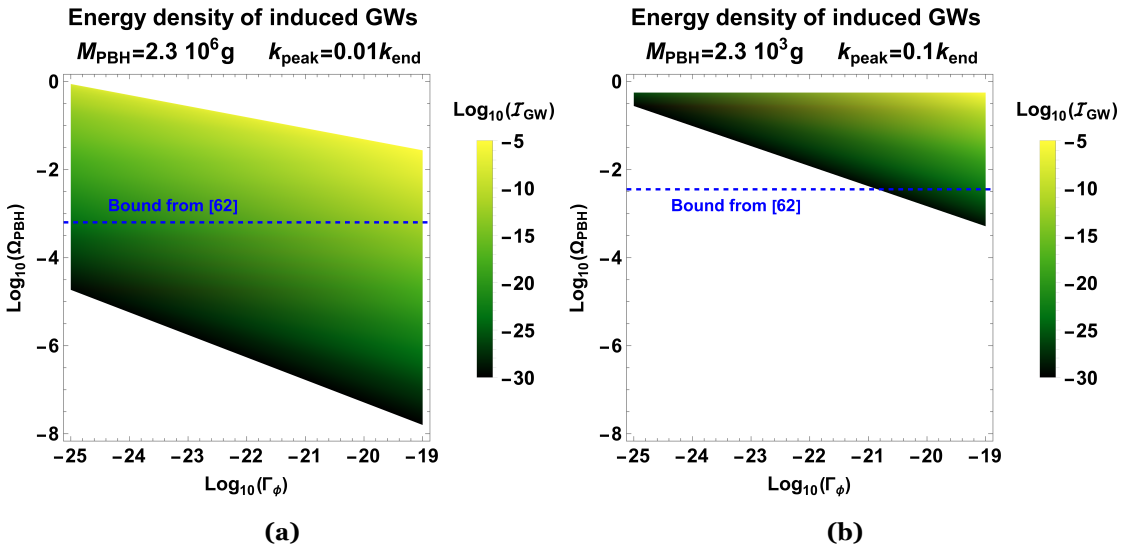

Figure 6.4: Total energy density of SIGWs (I_{GW}) for **(a)** $k_{\rm peak} = 10^{-2} k_{\rm end}$ and **(b)** $k_{\rm peak} = 10^{-1} k_{\rm end}$ as a function of the fractional energy density of PBHs ($\Omega_{\rm PBH}$) at formation and the decay rate of the field (Γ_ϕ). The dashed blue line corresponds to the bound from [62], given in Eqn. (6.50), which does not consider the effects of the decay rate. It corresponds to the maximum initial fractional energy density of PBHs that does not overproduce GWs and reaches the BBN bound. By considering the effect of the decay rate, we extend this bound to higher values of $\Omega_{\rm PBH}$.

this scenario, the total amount of energy in the form of GWs must satisfy this relation [66, 67]

$$\mathcal{I}_{\rm GW} = \int_0^\infty \Omega_{GW}^{\rm PBH}(k)\, \mathrm{d}\ln(k) \leq 1.6 \times 10^{-5} = \mathcal{I}_{\rm BBN}. \tag{6.49}$$

Fig. 6.4 shows the computation of $\mathcal{I}_{\rm GW}$ for the two values of $k_{\rm peak}$ considered in this work and as a function of the decay rate of the scalar field Γ_ϕ and the initial fractional energy density of PBHs, $\Omega_{\rm PBH}(t_{\rm in})$. This last, as shown in Appendix D.1, depends directly on $\mathcal{A}_{\rm peak}$ and σ (see Eqns. (D.7), (D.11), and (D.12)). To reproduce this plot we have selected the values of $\mathcal{I}_{\rm GW}$ that satisfy the BBN bound (6.49) and also the cases where PBHs dominate before their evaporation (otherwise the production of GWs is not possible through this mechanism). Further, as explained in Sec. 6.1, we consider the cases where the temperature of radiation is higher than the evaporation temperature of the PBHs. This effect mainly translates into a lower $k_{\rm eva}$ which, looking at (6.48), induces a higher amount of SIGWs, since PBHs dominate for a longer time. However, this scenario does not affect too much the production of SIGWs. Also, for comparison, the blue dashed line corresponds to the bound shown in [62], which translated to our notation is given by

$$\Omega_{\rm PBH}(t_{\rm in}) < 1.4 \times 10^{-4} \left(\frac{10^9 \mathrm{g}}{M_{\rm PBH,0}} \right)^{1/4}. \tag{6.50}$$

As can be seen, by considering an initially matter-dominated universe together with a decay rate of the scalar field into radiation, one can relax the constraints on the initial

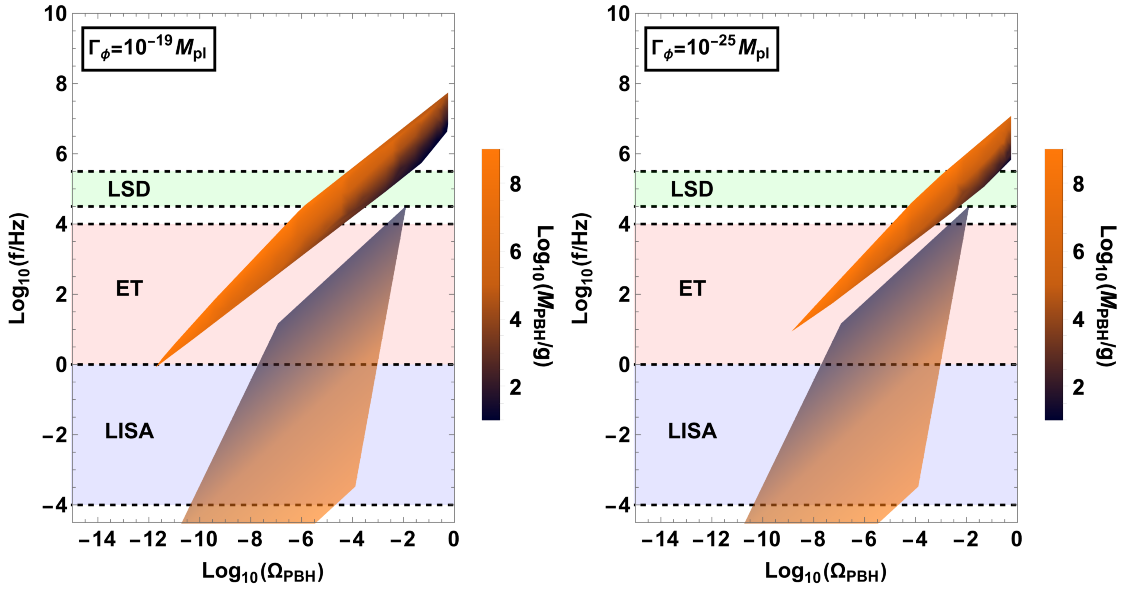

Figure 6.5: Mass of the PBHs as a function of the frequency at which the fractional energy density of GWs peaks and the initial fractional energy density of PBHs. The green, pink, and purple bands correspond to the range of detectable frequencies of the LSD, ET, and LISA GW detectors, respectively. Brighter orange-to-black colors correspond to our results, whereas lighter colors correspond to the results of ref. [62].

abundance of PBHs at production time. This means that high initial values of $\Omega_{\rm PBH}$ are allowed if the PBHs dominate for a short period, which is possible if Γ_ϕ is small. On the contrary, a small initial abundance of PBHs needs more time to reach the BBN bound and overproduce GWs, that is, small $\Omega_{\rm PBH}$ and high Γ_ϕ.

In Fig. 6.5, we show the mean mass of the PBHs distribution as a function of the fractional density of PBHs and the frequency of the peak of the SIGWs produced in each case. To compare, we also show the frequency ranges of some planned GW detectors, such as the Levitated Sensor Detector (LSD) [228], the Einstein Telescope (ET) [154], and the Large Interferometer Space Antenna (LISA) [150]. This reveals that, for some regions of the parameter space, the frequency of the GWs falls into the detectable range of the LSD and ET detectors. However, their sensitivity is insufficient to detect these GWs, which further motivates their refinement. In addition, we also show the effect of changing the decay rate. A larger decay rate (left plot) implies that PBHs have more time to dominate, as the scalar field decays sooner. As a consequence, GWs are produced more abundantly and on a wider span of frequencies. On the contrary, a smaller decay rate (right plot) implies a reduced production of GWs. To produce this plot, we have considered the PBHs that have enough time to dominate ($t_{\rm PBH} < t_{\rm eva}$), and excluded the scenarios where GWs are over-produced ($\mathcal{I}_\Omega^{\rm PBH} < \mathcal{I}_{\rm BBN}$). This plot is aimed to be compared with Plot. 3 of [62], where the authors study the production of GWs from a PBH-dominated phase without focusing on the production mechanism or the inflationary details. The results from Fig. 3 of [62] are shown in lighter colors in Fig. 6.5. These, in general, correspond to lower frequencies and are placed below our results, shown in brighter colors. In this work, in addition, we

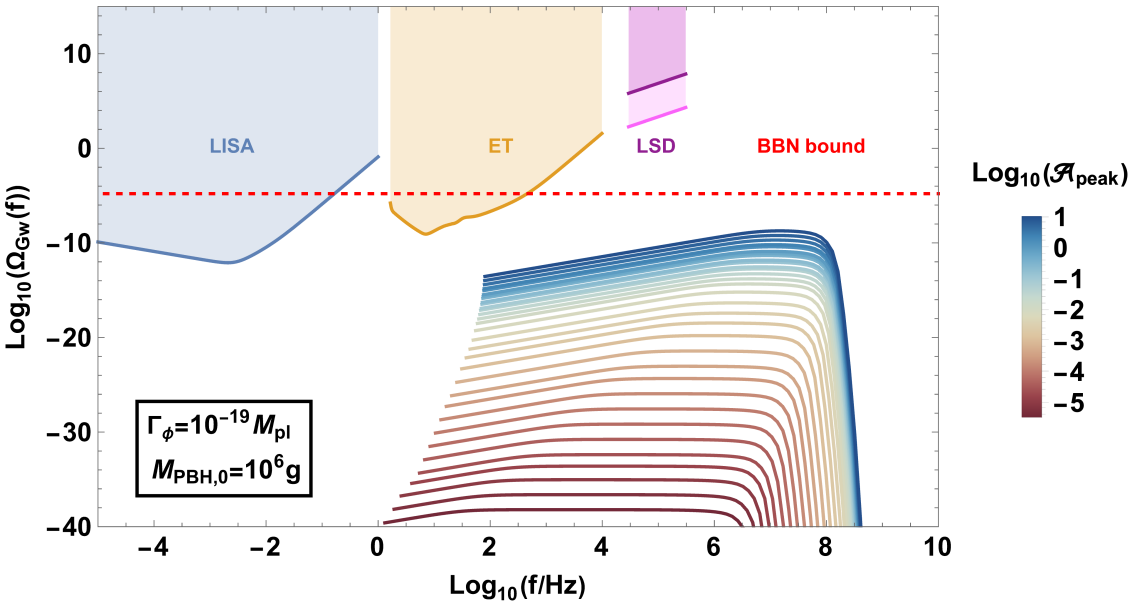

Figure 6.6: An example of GW spectra for the scenario where $\Gamma_\phi = 10^{-19} M_{\rm Pl}$ and $M_{\rm PBH,0} = 10^6$g shown for several values of the amplitude of the Gaussian peak $\mathcal{A}_{\rm peak}$.

consider the whole evolution of the PBH, from formation mechanism to their domination and final evaporation, along with details of inflaton decay. Since the energy density of SIGWs $I_{\rm GW}$ relies on the PBH domination duration determined by the inflaton decay rate (through (6.30)) and the PBH mass fraction (See (B.28) and (6.14)), our results are significantly different from [62]. Therefore, our considerations of PBH formation details and inflaton decay produce high-frequency GWs induced by PBH domination in contrast to the results in [62], which indicate a low-frequency domain. Note that the authors in [62] evaluate the plot at the late matter-radiation equality, whereas Fig. 6.5 is evaluated at the present time. Finally, and for completeness, we show in Fig. 6.6 the GW spectrum as a function of the frequency for the case of a decay rate of $\Gamma_\phi = 10^{-19} M_{\rm Pl}$ and a mean PBH mass of $M_{\rm PBH,0} = 10^6$g. The result is shown for several values of $\mathcal{A}_{\rm peak}$, which translates into different mass fractions of PBH, $\Omega_{\rm PBH}(t_{\rm in})$. As explained above, the GW spectrum lies below the sensitivity of the future GW detectors.

6.4 Summary

In this work, we have explored the formation and evolution of PBHs in an early matter-dominated universe, focusing on their potential dominance, which provides an alternative reheating mechanism through Hawking radiation. Our approach focuses on the KP formalism [119,121–125,204,273] to describe PBH formation during the preheating (matter-dominated) phase, considering an extended distribution of perturbations rather than a monochromatic one. This scenario differs significantly from the standard ones considered in the literature [59–63], where PBHs are considered to form during radiation domination

and the mass fraction is computed using the PS formalism [82]. To achieve a significant amount of PBH, we consider a Starobinsky-like inflationary model [24] with some feature in the potential that amplifies perturbations around a particular scale, parametrized with a Gaussian peak, Eqn. (6.3). PBH domination, in our framework, is affected by the inflaton field decay rate (Γ_ϕ) into radiation via a decay rate Γ_ϕ, whose values we choose according to the Starobinsky model [286]. Then, the evolution of the energy densities is solved with a system of coupled Boltzmann equations (6.23). If PBHs dominate for a sufficient amount of time (that depends on inflaton decay rate through (6.30)), the Poissonian density fluctuations they produce induce GWs at third-order in the perturbed expansion of the action [48,50,195] that could reach the BBN bound (6.49). Our study revealed that both the duration of the PBH-dominated phase and thus the production of the GW phase are highly sensitive to:

- ***The decay rate of the inflaton field,*** Γ_ϕ: A lower decay rate allows PBHs to dominate for longer and induce more GWs.
- ***The fractional energy density of PBH,*** $\Omega_{\boldsymbol{PBH}}$: If the PBHs are produced more abundantly, they dominate sooner and induce more GWs. This quantity is directly related to $\mathcal{A}_{\rm peak}$ and σ, see Appendix D.1.
- ***The mass of the PBH distribution,*** $M_{\boldsymbol{PBH},0}$: The higher the mass, the later evaporation occurs and a longer PBH-dominated phase, which induces more GWs. This is inversely related to $k_{\rm peak}$ (6.20).

We computed the power spectrum of these induced GWs and found that the resulting signal could be within the detectable range of future gravitational wave detectors such as the LSD and ET, see Fig. 6.5. Further, our results indicate that considering an early matter-dominated phase together with a decay rate for the inflaton field allows for a relaxation of earlier constraints on PBH, as Fig. 6.4 reveals. This suggests that PBHs could have played a more significant role in cosmic evolution than early studies indicate, which highlights the importance of considering the interplay between PBH formation during a matter-dominated phase using the Khlopov-Polnarev formalism, the inflaton decay to radiation, and the emission of induced gravitational waves in the early universe.

7

Conclusions and outlook

I've searched around the universe
Been down some black holes
There's nothing but space, man...

– Sam Ryder, UK's representative at Eurovision 2022

Conclusions

In this thesis, we have investigated the formation and evolution of PBHs and SIGWs during the post-inflationary phase of preheating in the context of Starobinsky-like models. Our findings provide new insights into the mechanisms driving these phenomena and their potential implications for the early universe and observational cosmology.

More specifically, in Chapter 2, we have revisited and extended the study of [45] about PBH formation during preheating. We worked under the framework of Starobinsky inflation and considered the role of two types of perturbations, type I and II, defined in terms of their wavenumber k. The type I modes have already been studied in [45], and are the usual ones considered in the literature. These correspond to modes that exited the horizon during inflation and then reenter during preheating into the IB and get amplified, with the density contrast growing as $\delta_{\boldsymbol{k}}^{\mathrm{I}} \sim a$. The type II modes, which remain subhorizon after inflation, are a new element in our study. We have demonstrated that a subclass of type II modes (labeled type IIa) can also lead to PBH formation, as these modes also fall into the IB, and therefore $\delta_{\boldsymbol{k}}^{\mathrm{IIa}} \sim a$. We employed the PS (B.13) and KP (B.27), (B.32) formalisms to estimate the mass fraction of the PBHs formed during preheating and analyze their differences. The former is usually utilized for the radiation-dominated scenario and demands the definition of a threshold for perturbations, δ_c. This is computed within the spherical collapse method by assuming the collapse of a massive scalar field in an Einstein-de Sitter universe [45, 163], which gives an estimation for the time each perturbation needs to collapse (2.42). The KP formalism, being threshold-independent, is well suited for matter-dominated scenarios, and as shown in Appendix A.3, preheating approximately corresponds to such a phase. To obtain the PBH mass, we used the critical collapse method (2.43) and assumed that PBH formation occurs at the end of preheating. Furthermore, to avoid the non-linear regime in the type II modes range, we imposed the

Jeans length criterion (2.39), which sets a higher bound on k. In essence, we established three key criteria to determine whether the perturbations collapse into PBH, summarized as follows: (i) the wavelength of the fluctuation must lie within the IB to be affected by the instabilities, (ii) its wavelength must be subhorizon and exceed the effective Jeans length so that gravity counteracts pressure, and (iii) the density contrast must be large enough to enable collapse before the end of preheating, which defines the threshold. Our analysis shows that PBH formation is significantly influenced by the duration of preheating, with longer preheating stages leading to higher and massive PBH production, see Fig. 2.12.

The instabilities during preheating are enhanced if the inflationary potential deviates from the quadratic shape during preheating. In this case, these are usually called self-resonance effects, as the main amplification comes from the terms $\phi^3, \phi^4 \dots$ in the expansion of the potential. In Chapter 3, we proposed an analytical model to describe the amplification of perturbations through self-resonance effects and provided new insights into the preheating dynamics of Starobinsky-like α-attractor inflationary models (although the analysis is valid for any inflationary potential that can be expanded in powers of the scalar field). Using perturbation theory for anharmonic oscillators, we transformed the MS equation (A.9) into a Hill equation (3.12) and obtained the Floquet exponents of the MS variable using Floquet theory. Then, we related the MS variable to the curvature perturbation $\mathcal{R}_k$ using (3.19). Particularly, and for the first time, we derived explicit formulas for the Floquet exponents of inflationary potentials having both cubic and quartic terms in their expansion, see Eqn. (3.18). Further, we demonstrated how perturbations are enhanced during preheating, particularly for asymmetric potentials such as E-models, see Fig. 3.2. Our results revealed a strong dependence of amplification on the parameter α. Smaller values of α make the potential to strongly deviate from the quadratic approximation, leading to a rapid growth of perturbations. This mechanism, intrinsic to α-attractors, suggests a physical lower bound on α, beyond which perturbations could reach the non-linear regime, potentially affecting PBH formation and SIGW production. These two effects are studied in Chapters 4 and 5, respectively.

In Chapter 4, we studied the formation of PBHs during preheating, within the framework of α-attractor models [170, 197, 213, 214]. As anticipated in Chapter 3, we identified strong self-resonance effects for $\alpha \ll 1$. To determine whether overdensities within the IB collapse into PBH, we applied the three key criteria defined in Chapter 2, extending previous results from Starobinsky inflation to generalized α-attractor scenarios. We quantified the PBH mass fraction $\beta(k)$ again using both PS and KP formalisms and found that while smaller α increases the range of affected modes, it reduces PBH abundance in the KP case, a behavior opposite to the PS formalism. Moreover, unlike the instantaneous collapse assumption at the end of preheating used in Chapter 2, this analysis allows for scale-dependent collapse times and thresholds. These results have also been compared with current observational constraints [64, 65, 91, 126, 127, 130–132, 204], including limits from PBHs remnants, LSP and DM production, CMB, BBN, and γ-ray backgrounds. In our case, only constraints from Planck remnants, LSP, and DM production are rele-

vant. Overall, this Chapter highlights the significant role of small-scale self-resonance instabilities and nonspherical effects during preheating in the context of the inflationary α-attractor models.

Since the scalar perturbations couple to tensor ones at third-order in the perturbed expansion of the action, we can analyze the impact of self-resonant amplification on GW production. This is studied in Chapter 5, and the GWs produced in this way are called SIGWs. Using the perturbed Einstein equations we derive an equation of motion for the tensor perturbations at third-order in the perturbed expansion of the action, see Eqns. (5.2) and (5.3). Then, using the approach of Chapters 2 and 3, and Appendix A, the curvature perturbations are obtained and used to finally compute the energy density of GWs (background + second order). The results are shown in Fig. 5.2. Our analysis revealed that for sufficiently small values of α ($\log_{10}(\alpha) \simeq -3.54$ for the T-model and $\log_{10}(\alpha) \simeq -3.17$ for the E-model), the energy density of SIGWs reaches the BBN bound (5.22), imposing new constraints on this parameter (see Figs. 5.2 and 5.3). This, as a consequence, translates into a lower bound for the tensor-to-scalar ratio: $r > 9.61 \times 10^{-7}$ for the T-model and $r > 2.25 \times 10^{-6}$ for the E-model. Notably, our approach provides this bound through a novel method, and should be compared with those reported in [197] based on the duration of reheating along with the current bounds on the scalar spectral index, where $\log_{10}(\alpha) = -4.2^{+5.4}_{-8.6}$ at 95% C.L, in [198] based on the overproduction of a light moduli field, where $\alpha \lesssim 10^{-8}$, or in [173] based on geometrical destabilization of a spectator field, where $\alpha \lesssim 10^{-3}$. Additionally, we found that the amplification of SIGWs is stronger in E-models than in T-models due to their asymmetric potential, which also explains the difference in the lower bound on α and the tensor-to-scalar ratio. Our results indicate that SIGWs generated during preheating fall within the frequency ranges of current and upcoming GW detectors, see Fig. 5.1. Furthermore, if the detector sensitivities improve, these signals could become observable, highlighting the importance of advancing GW detection in the VHF band.

The combination of the effects described in Chapters 2 to 5 is studied in Chapter 6. There, we analyze the production of GWs from an overproduction of PBHs during preheating, contrary to other works that focus on the radiation stage [59–63] and do not consider the PBH formation mechanism. We propose a generic power spectrum, parametrized in Eqns. (6.1), (6.2), and (6.3) with a Gaussian peak, which summarizes the different features that can produce PBH. Then, we evolve the perturbations during preheating and compute the mass fraction with a new analytic expression for the KP formalism, Eqn. (B.28). Preheating ends when the inflaton field decays into radiation via a decay rate Γ_ϕ. If the PBHs are abundant enough at this point, they dominate the energy density of the universe for a period that ends when they evaporate due to Hawking radiation, see Eqn. (6.18). During this PBH-dominated phase, the Poissonian density fluctuations of the PBH fluid can induce GWs at third-order in the perturbed expansion of the action, similar to the scenario described in Chapter 5. We found that the duration of the PBH-dominated phase and the induced gravitational wave production are highly sensitive to the inflaton decay

rate, the initial PBH fractional energy density, and the mean mass of the PBH distribution, as shown in Figs. 6.3 and 6.4. Our study suggests that PBHs could have played a more significant role in the early universe than previously thought [62], with the decay rate of the field influencing also the production of GWs and relaxing existing constraints on their abundance, see Eqn. (6.50).

Outlook

The collapse of perturbations in matter-dominated scenarios, such as preheating, is an active area of research. Further work is needed to understand how this process occurs and, specifically, which conditions lead to PBH formation. In this sense, a natural extension of the investigation presented in this thesis would be:

- The formation of PBHs is generally expected to occur when sufficiently large perturbations reenter the cosmological horizon during the radiation-dominated era. At this point, an overdense region, typically modeled as a contracting shell of matter, becomes gravitationally unstable in a background expanding universe. While traditional analyses often approximate the collapse process using the Oppenheimer-Snyder model [72], which assumes a static, asymptotically flat spacetime, this approach neglects the dynamic nature of the cosmological background, particularly the influence of expansion and time-dependent curvature. A more realistic treatment requires analyzing the collapse within an FLRW background, where the interplay between the local overdensity and the global expansion could significantly alter the conditions for black hole formation. Furthermore, we believe that the boundary terms of the Einstein–Hilbert action, such as the Gibbons–Hawking–York [290, 291], would be interesting to consider in dynamically evolving spacetimes. These terms can lead to modifications in the effective dynamics of collapse, potentially introducing corrections to the standard Oppenheimer-Snyder model predictions. Thus, a comprehensive study of gravitational collapse in an expanding background, accounting for both contributions to the action, is needed for accurately characterizing the formation of PBH.

- Understanding the mass fraction of PBHs formed during the early universe requires a detailed analysis of the nature and evolution of primordial perturbations. In particular, the role of anisotropies in the initial conditions is of critical importance, especially in matter-dominated scenarios. According to the KP formalism [119–123], such anisotropies can significantly alter the standard assumptions regarding the gravitational collapse of perturbations, leading to deviations from the spherically symmetric models typically assumed, for instance, in the PS estimation. These anisotropies may arise naturally from second-order effects in cosmological perturbation theory, particularly through the non-linear coupling between scalar and ten-

sor perturbations. These extra corrections introduce couplings that can lead to directional dependencies in the collapse dynamics. Such couplings can generate shear and tidal fields, which in turn produce anisotropic stress, modifying the effective gravitational potential experienced by the collapsing region. This theoretical framework offers a physical basis for the types of anisotropies that are otherwise introduced heuristically in the Zeldovich approximation [292], in which the anisotropic collapse is encoded through the deformation tensor and its associated eigenvalue structure (see Appendix B.2), but the origin of these anisotropies is not explicitly tied to the underlying cosmological perturbations. By connecting the KP formalism and second-order perturbation theory, it becomes possible to explain how anisotropies naturally emerge from inflationary initial conditions and evolve non-linearly, ultimately influencing the threshold for PBH formation and the resulting mass spectrum.

- We have applied the PS and KP formalism to the case of small-length perturbations (type II modes) during early matter-dominated scenarios. However, there exist more modern prescriptions to estimate the mass fraction of PBH. One of them is the *compaction function* formalism, first studied by M. Shibata and M. Sasaki in 1999 [293]. It involves evaluating a function that measures the excess mass (or energy density) enclosed within a spherical region relative to the background, normalized by the radius of that region [293–295]. This function is called the compaction function $\mathcal{C}$, and it is specifically defined as $\mathcal{C}(r) = \frac{\delta M(r)}{R(r)}$, where $\delta M(r)$ is the mass excess within a radius r, and $R(r)$ is the corresponding areal (or physical) radius. PBH formation is expected when $\mathcal{C}(r)$ exceeds a critical threshold $\mathcal{C}_c$, typically around 0.4-0.5, at its maximum over all radii, indicating that the local gravitational pull is strong enough to overcome pressure gradients and cosmic expansion. It would be fruitful to extend this formalism to the case of small-wavelength perturbations and/or improve the threshold estimation for an early matter-dominated scenario.

- An intriguing avenue for future investigation involves relaxing the assumption that PBHs decay exclusively into light Standard Model particles. While this assumption is well-motivated by the efficiency of Hawking radiation to emit particle species lighter than the PBH temperature ($T \sim M_p^2/M_{\rm PBH}$ in units where $k_B = 1$), it is theoretically plausible that, in the final stages of evaporation, PBHs could emit heavier particles, including inflaton quanta, provided their mass lies below the Hawking temperature. This scenario becomes particularly relevant for very light PBHs nearing the end of their evaporation, where T may approach the inflaton mass scale ($m_\phi \sim 10^{13}$ GeV in typical inflationary models). Although such emission is expected to be highly suppressed and energetically negligible under standard semi-classical assumptions, the extreme conditions in this regime may invite contributions from quantum gravitational effects, which could substantially alter the evaporation dynamics. Investigating whether inflaton particle production in this regime could lead to non-trivial phenomenological consequences, such as residual inflaton field exci-

tations or exotic reheating scenarios, may broaden our knowledge of PBHs physics. Given the speculative nature of physics near the Planck scale, such studies would necessarily involve going beyond the semi-classical framework of Hawking radiation.

- A natural extension of this work involves investigating the non-linear dynamics governing the collapse of overdense regions into primordial black holes. Linear and semi-analytical approaches, while insightful, may fail to capture critical non-linear effects that can significantly alter collapse thresholds and PBHs abundances. To address this, fully relativistic numerical simulations using tools such as `GRChombo` [296] or lattice simulations such as `CosmoLattice` [190, 191] offer a powerful framework to study PBH formation in a dynamically rich, nonperturbative regime, as demonstrated in recent works [297].

Personal note

Looking back at the historical development of PBH research, I am impressed by how far the field has progressed. The mechanisms for constraining and studying their abundance have evolved significantly since the early estimations in 1979. For me, the way PBHs connect quantum mechanics and general relativity with astrophysical observations makes them a fascinating probe of fundamental physics, and working on them has deepened my appreciation for the early universe.

A key motivation for this thesis is that historically limited attention has been paid to preheating in the context of PBH formation and GW production. I hope that the results from this investigation will help to garner more interest in probing the preheating stage as a crucial window into the physics of the early universe. Therefore, the preheating dynamics can shed new light on inflationary models and the mechanisms driving PBH formation.

In my opinion, GWs are among the most powerful messengers of the early universe. Unlike photons, whose observations are limited to post-recombination epochs, GWs can travel relatively uninterrupted from their sources, preserving information about the processes that generated them. This makes them a unique tool to test foundational aspects of cosmology.

As the history of GW detection has shown, theoretical progress is the key to technological innovation. I am hopeful that, as highlighted during this thesis, the need to probe higher-frequency GWs will continue to inspire new detectors and methodologies, bringing us closer to exploring the early universe.

Appendix A

Mathematical details about inflation and preheating

A common feature of the chapters of this thesis is the dynamical evolution of the background and the perturbations. This appendix summarizes the main mathematical details of both, as well as some details about the derivation of the effective equation of state.

A.1 Background

Starting with the background dynamics, these are well described by using a flat FLRW spacetime, whose line element is given by

$$\mathrm{d}s^2 = -\mathrm{d}t^2 + a^2\delta_{ij}\mathrm{d}x^i\mathrm{d}x^j, \tag{A.1}$$

and where δ_{ij} is the Kroneker delta. Using this, the cosmological evolution of a scalar field ϕ minimally coupled to gravity is given by varying the action (1.3) with respect to ϕ, which gives the equation of motion of the field

$$\ddot{\phi} + 3H\dot{\phi} + \frac{\mathrm{d}V(\phi)}{\mathrm{d}\phi} = 0\,. \tag{A.2}$$

Next, we consider that the matter content is described by this scalar field ϕ, which implies that the stress-energy tensor in (1.1) is given by

$$T_{\mu\nu} = \partial_\mu\phi\partial_\nu\phi - g_{\mu\nu}\left(\frac{1}{2}\partial^\lambda\phi\partial_\lambda\phi + V(\phi)\right), \tag{A.3}$$

with the following identifications for the energy density and pressure of the inflation field

$$\rho = \frac{1}{2}\dot{\phi}^2 + V(\phi) \tag{A.4a}$$

$$p = \frac{1}{2}\dot{\phi}^2 - V(\phi) \tag{A.4b}$$

With this, the 00-component of the Einstein equations (1.1) gives the first and second Friedmann equations

$$H^2 = \frac{1}{3M_{\rm Pl}^2}\left(V(\phi) + \frac{\dot{\phi}^2}{2}\right) \tag{A.5a}$$

$$\dot{H} + H^2 = -\frac{1}{3M_{\rm Pl}^2}\left(\dot{\phi}^2 - V\right). \tag{A.5b}$$

Eqns. (A.2) and (A.5) effectively describe the background dynamics of the scalar field and the expansion of the universe.

A.2 Perturbations

To study perturbations, we introduce a fluctuation in the scalar field as $\phi \to \phi + \delta\phi$. This sources scalar perturbations Φ, Ψ, E, and B in the metric, given now by the following perturbed FLRW line element

$$ds^2 = -(1+2\Phi)dt^2 + 2aB_{,i}dx^i dt + a^2\left[(1-2\Psi)\delta_{ij} + 2E_{,ij}dx^i dx^j\right]. \tag{A.6}$$

Using this, the perturbed Einstein's equations are now given by [298]

$$3H(\dot{\Psi} + H\Phi) + \frac{k^2}{a^2}\left[\Psi + H(a^2\dot{E} - aB)\right] = -\frac{\delta\rho}{2M_{\rm Pl}^2}, \tag{A.7a}$$

$$\dot{\Psi} + H\Phi = -\frac{\delta q}{2M_{\rm Pl}^2}, \tag{A.7b}$$

$$\ddot{\Psi} + 3H\dot{\Psi} + H\dot{\Phi} + (3H^2 + 2\dot{H})\Phi = \frac{1}{2M_{\rm Pl}^2}\left(\delta p - \frac{2}{3}k^2\delta\Sigma\right), \tag{A.7c}$$

$$(\partial_t + 3H)(\dot{E} - B/a) + \frac{\Psi - \Phi}{a^2} = \frac{\delta\Sigma}{M_{\rm Pl}^2}, \tag{A.7d}$$

where δq is the momentum density, δp is the pressure perturbation, $\delta\Sigma$ is the anisotropic stress and Ψ, Φ, E and B are the scalar metric perturbations. From now on, we will work in the Newtonian gauge to take $E = B = 0$. This is useful as the metric perturbation Φ in this gauge is identified as the Newtonian gravitational potential and, in the subhorizon limit, the equations reduce to the standard Newton-Poisson non-relativistic formulation. Moreover, since we are dealing with a scalar field, the anisotropic stress vanishes ($\delta\sigma = 0$) because there are no off-diagonal elements in the energy-momentum tensor (A.3). Using this in (A.7d) we obtain that the scalar metric perturbations are equal, that is, $\Phi = \Psi$.

By working with the perturbed Einstein equations, one can obtain a compact single equation for the evolution of perturbations when expressed in terms of conformal time η, related to cosmic time by $\mathrm{d}t = a\mathrm{d}\eta$. This is referred to as the Mukhanov-Sasaki (MS) equa-

tion [35, 298], expressed as

$$v_{\boldsymbol{k}}'' + \left[k^2 - \frac{z''}{z}\right] v_{\boldsymbol{k}} = 0\,, \tag{A.8}$$

where $v_{\boldsymbol{k}} = a\left[\delta\phi_{\boldsymbol{k}} + \phi'\Phi_{\boldsymbol{k}}/\mathcal{H}\right]$ is the so-called MS variable, a combination of the field and metric perturbations. Here and in what follows, a prime denotes derivative with respect to conformal time, $z \equiv \sqrt{2\varepsilon}\, a M_{\rm Pl}$, ε is the first slow-roll parameter, the suffix "$_{\boldsymbol{k}}$" denotes Fourier component, and k is the modulus of the wavevector $\boldsymbol{k}$ of each perturbation. For practical reasons, working in cosmic time t will be more efficient. Therefore, using the relationship between cosmic and conformal time, Eqn. (A.8) is now given by:

$$\ddot{v}_{\boldsymbol{k}} + H\dot{v}_{\boldsymbol{k}} + \left[\frac{k^2}{a^2} + \frac{\mathrm{d}^2 V}{\mathrm{d}\phi^2} - 2H^2 + \frac{2\dot{\phi}}{H M_{\rm Pl}^2}\frac{\mathrm{d}V}{\mathrm{d}\phi} + \frac{7\dot{\phi}^2}{2M_{\rm Pl}^2} - \frac{\dot{\phi}^4}{2H^2 M_{\rm Pl}^4}\right] v_{\boldsymbol{k}} = 0, \tag{A.9}$$

The reason behind this change is that all the terms in this equation remain non-singular after the end of inflation, when ϕ, $\dot{\phi}$ and ε periodically vanish as the field oscillates around the bottom of the potential. Once we have solved for $v_{\boldsymbol{k}}$, the Fourier component of the comoving curvature perturbation, defined as [298]

$$\mathcal{R}_{\boldsymbol{k}} = \Phi_{\boldsymbol{k}} - \frac{H}{\rho + p}\delta q_{\boldsymbol{k}}, \tag{A.10}$$

is related to the MS variable by

$$\mathcal{R}_{\boldsymbol{k}} = \frac{1}{M_{\rm Pl}^2}\frac{v_{\boldsymbol{k}}}{a\sqrt{2\varepsilon}}. \tag{A.11}$$

This is a very useful quantity since it allows us to easily compute the dimensionless power spectrum of curvature perturbations as

$$\mathcal{P}_{\mathcal{R}}(k) = \frac{k^3}{2\pi^2}|\mathcal{R}_{\boldsymbol{k}}|^2. \tag{A.12}$$

However, it should not be confused with the curvature perturbation in uniform-density hypersurfaces, labeled as $\zeta_{\boldsymbol{k}}$. It is defined as [299]

$$-\zeta_{\boldsymbol{k}} = \Phi_{\boldsymbol{k}} + \frac{H}{\dot{\rho}}\delta\rho_{\boldsymbol{k}}. \tag{A.13}$$

Both $\mathcal{R}_{\boldsymbol{k}}$ and $\zeta_{\boldsymbol{k}}$ measure the changes in the curvature, but from different hypersurfaces. While $\zeta_{\boldsymbol{k}}$ is defined on hypersurfaces where the energy-density perturbation vanishes ($\delta\rho = 0$), $\mathcal{R}_{\boldsymbol{k}}$ is defined on hypersurfaces where the scalar field perturbation vanishes ($\delta\phi_{\boldsymbol{k}} = 0$). This last is precisely what makes $\mathcal{R}_{\boldsymbol{k}}$ useful in our case. In subhorizon scales, the ones of interest for our study, the dynamics of the perturbations are governed by the fluctuations of the scalar field, since gravitational effects are small compared to the kinetic ones. Therefore, the comoving curvature perturbation essentially captures the dynamics of per-

turbations deep inside the horizon and evolves in a predictable manner up to horizon exit [299]. For this reason, it is usually chosen to set the initial conditions for perturbations and to compute the inflationary power spectrum.

Let us see now how to compute the fractional energy density perturbations or density contrast, $\delta_{\boldsymbol{k}} = \delta\rho_{\boldsymbol{k}}/\rho$, where $\delta\rho_{\boldsymbol{k}}$ is the Fourier component of the density perturbation and $\rho = 3H^2 M_{\rm Pl}^2$ is the background energy density. Using the perturbed Einstein equations, concretely the momentum constraint, which corresponds to (A.7b), we obtain the following relation between the metric potential $\Phi_{\boldsymbol{k}}$ and the comoving curvature perturbation

$$\mathcal{R}_{\boldsymbol{k}} = \frac{2}{3}\frac{H^{-1}\dot{\Phi}_{\boldsymbol{k}} + \Phi_{\boldsymbol{k}}}{1+w} + \Phi_{\boldsymbol{k}}, \tag{A.14}$$

where w is the parameter of the equation of state (or simply equation of state), defined as

$$w = \frac{p}{\rho} = \frac{\frac{\dot{\phi}^2}{2} - V(\phi)}{\frac{\dot{\phi}^2}{2} + V(\phi)}, \tag{A.15}$$

where p is the background pressure. In Section A.3, we show the computation procedure of the effective equation of state (see Eqn. (A.26)), which is plotted in Fig. A.2b. This shows that preheating is nearly a matter-dominated stage due to the smallness of the effective equation of state. If we now take (A.7a) and divide it by $3H^2$ we obtain

$$\delta_{\boldsymbol{k}} = -\frac{2}{3}\left(\frac{k^2}{a^2H^2} + 3\right)\Phi_{\boldsymbol{k}} - 2\frac{\dot{\Phi}_{\boldsymbol{k}}}{H}. \tag{A.16}$$

In this expression, we express the density perturbation $\delta_{\boldsymbol{k}}$ in terms of the perturbation $\Phi_{\boldsymbol{k}}$, which is obtained by solving the differential equation (A.14), where $\mathcal{R}_{\boldsymbol{k}}$ is given by (A.11) and (A.9).

A.3 Effective equation of state

In this section, we give an analytical parametrization of the equation of state for an oscillating scalar field. We call this the effective equation of state, $w_{\rm eff}$. The main reason to do this is because the universe does not behave as purely matter-dominated just right after the end of inflation. There is a transition period from inflation to matter-domination. In [300], the effective equation of state was derived using a potential of the form $V(\phi) = \frac{m^2}{2}\phi^n$, just after the end of inflation, giving

$$w_{\rm eff} = \frac{n-2}{n+2}. \tag{A.17}$$

For $n = 2$, we immediately see that $w_{\rm eff} = 0$, and thus, the universe is perfectly approximated by a matter-dominated one after inflation. However, as we will see, this is not

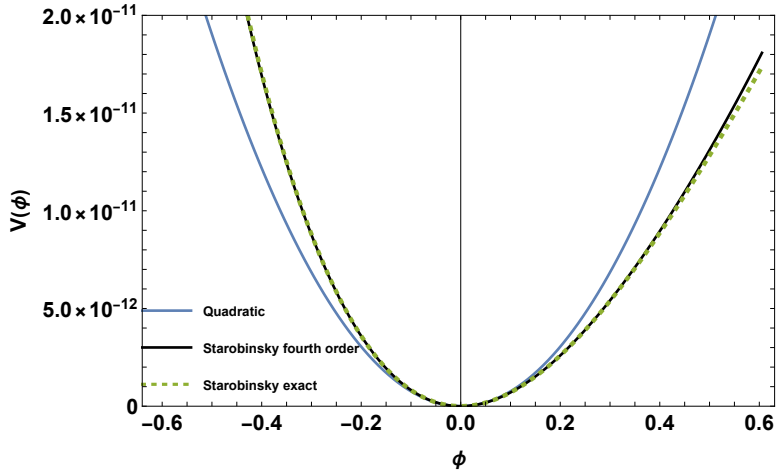

Figure A.1: Comparison between quadratic inflation ($V = \frac{M^2}{2}\phi^2$) in blue, the series expansion (A.18) of the Starobinsky potential in black and the full version of it (eqn. (2.1)) in dashed green.

the case for the Starobinsky model. Let us consider, for example, the potential (2.1). By making a series expansion around $\phi = 0$ up to the fourth order, we obtain

$$V(\phi) \simeq \frac{M^2}{2}\phi^2 + \frac{\lambda_3}{3}\phi^3 + \frac{\lambda}{4}\phi^4, \tag{A.18}$$

where M is the scalaron mass, to be normalized with CMB observations, and the parameters λ_3 and λ are defined as

$$\lambda_3 = -\sqrt{\frac{3}{2}}M^2 \qquad \lambda = \frac{7}{9}M^2. \tag{A.19}$$

Both of these parameters cause the potential to be different from the purely quadratic one (see Fig. A.1 for illustration). Multiplying the Klein-Gordon equation (A.2) by ϕ and averaging over one period of oscillation, we obtain the following expression for the potential (A.18)

$$\langle \phi V'(\phi) \rangle \simeq M^2\langle\phi^2\rangle + \lambda_3\langle\phi^3\rangle + \lambda\langle\phi^4\rangle, \tag{A.20}$$

where we have applied the virial theorem[20] $\langle \phi V'(\phi) \rangle \simeq \langle \dot{\phi}^2 \rangle$ and the brackets $\langle \dots \rangle$ mean averaging over one period of oscillation. More specifically, we define the average of a function $f(t)$ over one period T of oscillation as

$$\langle f(t) \rangle = \frac{1}{T}\int_{t_0}^{t_0+T} f(t)\mathrm{d}t, \tag{A.21}$$

[20] In the context of an oscillating scalar field, the virial theorem relates time-averaged quantities over one oscillation period. Specifically, it states that the average kinetic energy of the field, $\langle\dot{\phi}^2\rangle$, is approximately equal to its restoring force, $\langle\phi V'(\phi)\rangle$, a quantity determined by the shape of the potential. Physically, this reflects the idea that as the scalar field oscillates in its potential well, its kinetic and potential energies continuously exchange, but over time settle into a predictable balance. This makes it possible to express energy density and pressure in terms of averaged potential-dependent quantities, which simplifies the formulae.

where t_0 represents some arbitrary initial time. Using eqn. (A.20), the background energy density can be written as

$$\langle\rho\rangle \simeq \frac{\langle\dot{\phi}^2\rangle}{2} + \langle V(\phi)\rangle \simeq M^2\langle\phi^2\rangle + \frac{5}{6}\lambda_3\langle\phi^3\rangle + \frac{3}{4}\lambda\langle\phi^4\rangle, \tag{A.22}$$

and the background pressure as

$$\langle P\rangle \simeq \frac{\langle\dot{\phi}^2\rangle}{2} - \langle V(\phi)\rangle \simeq \frac{\lambda_3}{6}\langle\phi^3\rangle + \frac{\lambda}{4}\langle\phi^4\rangle. \tag{A.23}$$

Now, the evolution of the field ϕ is parameterized by [300]

$$\phi(t) \simeq \phi_0(t)T(t), \tag{A.24}$$

where $\phi_0(t) = \phi_{\text{end}}\left(\frac{a_{\text{end}}}{a}\right)^{3/2}$ encodes the decaying amplitude of the field due to the redshift of the universe and $T(t)$ is an oscillatory periodic asymmetric function (due to the λ_3 coefficient). Its average value can be computed as $\langle T(t)^n\rangle \simeq \frac{2}{n+2}$ for n even. Following [301], for n odd, the sinusoidal resulting function oscillates around zero and is suppressed by the averaging. Thus, we will only consider the average of even powers. Using the averaging of $\langle T(t)^n\rangle$ and (A.24) into the background energy and pressure we get

$$\begin{aligned}\langle\rho\rangle &\simeq \langle V(\phi_0)\rangle \\ \langle P\rangle &\simeq \frac{\lambda}{12}\langle\phi_0^4\rangle.\end{aligned} \tag{A.25}$$

Now, the effective equation of state can be computed as

$$w_{\text{eff}} = \frac{\langle P\rangle}{\langle\rho\rangle} \simeq \frac{\lambda}{12}\frac{\langle\phi_0^4\rangle}{\langle V(\phi_0)\rangle} = \frac{\frac{\lambda}{6M^2}\langle\phi_0^2\rangle}{1+\frac{\lambda}{2M^2}\langle\phi_0^2\rangle}. \tag{A.26}$$

Here, we can see that after the end of inflation, the effective equation of state is not exactly zero. It starts with small positive values and approaches zero as preheating continues, reaching the approximated matter-dominated stage. In Fig. A.2, we observe the effect of these extra terms in the expansion of the Starobinsky potential, where the effective version is compared with the numerical one, obtained from (A.15).

A.4 Jeans length and speed of sound

We are interested mainly in scales inside the horizon ($k > aH$) during the preheating phase. Since the effect of pressure is negligible, we can perform Newtonian perturbation theory, and the density contrast obeys the following differential equation [206, 207, 302]

$$\ddot{\delta}_{\boldsymbol{k}} + 2H\dot{\delta}_{\boldsymbol{k}} + \left(c_s^2k_p^2 - \frac{\rho}{2M_{\text{Pl}}^2}\right)\delta_{\boldsymbol{k}} = 0. \tag{A.27}$$

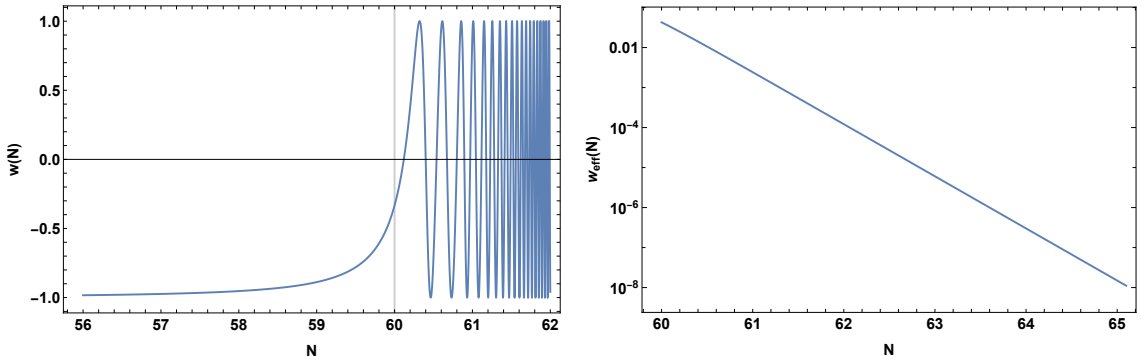

Figure A.2: a) The equation of state obtained numerically from (A.15) b) The effective equation of state (A.26) as a function of e-folds.

Here, c_s^2 is the (effective) speed of sound, and $k_p = k/a$ is the physical wavenumber, related to a physical wavelength by $\lambda_p = 2\pi/k_p$. For a perfect fluid we have $c_s^2 = w$ since w is constant [303, 304]. However, for a scalar field (Section A.3), the equation of state w is not constant in general. Therefore, the computation of the speed of sound is no longer trivial and must be done carefully. Following [301], the (effective) speed of sound for a general single-field case is

$$c_s^2 = \frac{\langle \delta p \rangle}{\langle \delta \rho \rangle} = \frac{\langle \frac{k^2}{a^2}\phi - V'(\phi) + V''(\phi)\phi \rangle}{\langle \frac{k^2}{a^2}\phi + 3V'(\phi) + V''(\phi)\phi \rangle}. \tag{A.28}$$

To obtain a simple expression for c_s^2, we will expand the Starobinsky potential around $\phi = 0$ and up to fourth order, as done in Appendix A.3. Then, we average the field using (A.24) and finally arrive at the expression

$$c_s^2 = \frac{\frac{k^2}{4M^2a^2} + \frac{\lambda}{4M^2}\langle \phi_0^2 \rangle}{\frac{k^2}{4M^2a^2} + 1 + \frac{3\lambda}{8M^2}\langle \phi_0^2 \rangle}, \tag{A.29}$$

which for high k it reaches $c_s^2 = 1$. This is shown in Fig. A.3, where we depict the speed of sound as a function of N for different values of k. Coming back to (A.27), we see that for a physical wavelength greater that $\lambda_p > \lambda_J = \frac{\sqrt{8}\pi c_s}{\sqrt{\rho}}$ the perturbations will grow by gravitational collapse and perturbations with $\lambda_p < \lambda_J$ will develop acoustic oscillations [305]. This essentially defines the Jeans length as half of the physical wavelength above which perturbations can collapse, i.e., $R_J = \frac{\lambda_J}{2}$. Using eqn. (A.29) we find the following expression for Jeans length

$$R_J = \left(\frac{2}{3} \frac{\frac{k^2}{4M^2a^2} + \frac{\lambda}{4M^2}\langle \phi_0^2 \rangle}{\frac{k^2}{4M^2a^2} + 1 + \frac{3\lambda}{8M^2}\langle \phi_0^2 \rangle} \right)^{1/2} \pi R_H, \tag{A.30}$$

where we have used $\rho = 3H^2 M_{\rm Pl}^2$ and λ is given in (A.19).

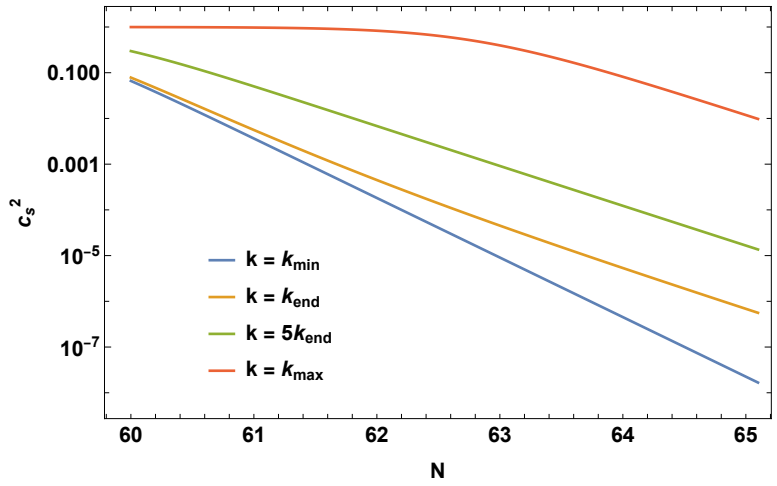

Figure A.3: The speed of sound as a function of N for different k.

Appendix B

Mass fraction of primordial black holes

To complement the discussion of PBH physics presented in the Introduction, this appendix provides the mathematical details of the two main formalisms used in this thesis for computing the mass fraction: the Press–Schechter and Khlopov–Polnarev approaches.

B.1 Press-Schechter formalism

In the context of PBH, the PS formalism [81, 82] is commonly used to compute the mass fraction in a radiation-dominated universe, where the equation of state parameter is $w = 1/3$. However, in this thesis, we also apply it to the case of a matter-dominated universe, with $w \simeq 0$, as shown in Chapters 2 and 4. Let us briefly explain the basics of this formalism. Given some density field in real space $\delta(\boldsymbol{x})$, one starts by coarse-graining it over a spherical region of radius R as

$$\delta_R(\boldsymbol{x}) = \left(\frac{a}{R}\right)^3 \int \mathrm{d}\boldsymbol{y}\delta(\boldsymbol{y})W\left(\frac{a|\boldsymbol{y}-\boldsymbol{x}|}{R}\right), \tag{B.1}$$

where $\boldsymbol{x}$ and $\boldsymbol{y}$ denotes comoving cordinates, R is a physical distance, and W is a window function such that $W(x) \simeq 1$ if $x \ll 1$, and $W(x) \simeq 0$ if $x \gg 1$. It is normalized in the sense:

$$4\pi \int_0^\infty W(x)\mathrm{d}x = 1, \tag{B.2}$$

and typically chosen to be a Heaviside step function[21] $W(x) = \frac{3}{4\pi}\theta(1-x)$. The eqn. (B.1) represents a convolution between the density field and the window function. Defining the rescaled window function as

$$W_R(x) = \left(\frac{a}{R}\right)^3 W\left(\frac{a|\boldsymbol{x}|}{R}\right), \tag{B.3}$$

we can express eqn. (B.1) as

$$\delta_R(x) = (\delta * W_R)(x), \tag{B.4}$$

[21] Depending on the specific context, different window functions may be employed. For example, one might use a Gaussian profile or a window function defined as a Heaviside step function in Fourier space rather than in real space.

where the symbol $*$ denotes convolution instead of standard multiplication. Now, using the convolution theorem, we can express the Fourier transform of the convolution of δ and W_R as the product of the individual Fourier transforms of δ and W_R, that is

$$\mathcal{F}\{\delta * W_R\}(k) = \mathcal{F}\{\delta\}(k)\mathcal{F}\{W_R\}(k). \tag{B.5}$$

See [306] for more details. Therefore, the Fourier transform of eqn. (B.4) is given by

$$\delta_R(k) = \delta_{\boldsymbol{k}}\widetilde{W}_R\left(k\right), \tag{B.6}$$

where $\delta_{\boldsymbol{k}}$ and $\widetilde{W}_R(k)$ represent the Fourier transforms of the density field and the rescaled window function, respectively. The latter is given by

$$\widetilde{W}_R(k) = 3\left(\frac{a}{kR}\right)^3\left[\sin\left(\frac{kR}{H}\right) - \frac{kR}{H}\cos\left(\frac{KR}{a}\right)\right]. \tag{B.7}$$

This allows us to relate the power spectrum of the coarse-grained density field

$$\mathcal{P}_{\delta_R}(k) = \mathcal{P}_\delta(k)\widetilde{W}_R^2(k), \tag{B.8}$$

in terms of the power spectrum of the density field, $\mathcal{P}_{\delta_R}(k)$, defined as

$$\langle\delta_{\boldsymbol{k}}\delta^*_{\boldsymbol{k}'}\rangle = \frac{2\pi^2}{k^3}\mathcal{P}_\delta(k)\delta_D(\boldsymbol{k}-\boldsymbol{k}'). \tag{B.9}$$

Then, the variance of the smoothed density field σ_k is obtained, by definition, via the following relation

$$\sigma_k^2 = \langle\delta_R^2(\boldsymbol{x})\rangle = \int_0^\infty \mathcal{P}_\delta(k)\widetilde{W}^2(k)\mathrm{d}\ln k. \tag{B.10}$$

Assuming that the density fluctuations $\delta_{\boldsymbol{k}}$, and therefore δ_R, follow a Gaussian probability distribution P with variance σ_k, we have

$$P(\delta_R) = \frac{e^{-\frac{\delta_R^2}{2\sigma_k^2}}}{\sqrt{2\pi\sigma_k}}. \tag{B.11}$$

Therefore, the probability of a given region undergoing collapse, that is, of a given δ_R being above the threshold, is computed as

$$\beta^{\mathrm{PS}}(k) = P[\delta_R \geq \delta_c] = 2\int_{\delta_c}^{\delta_{\max}} P(\delta_R)\mathrm{d}\delta_R = \mathrm{erfc}\left[\frac{\delta_c}{\sqrt{2\sigma_k^2}}\right] - \mathrm{erfc}\left[\frac{\delta_{\max}}{\sqrt{2\sigma_k^2}}\right], \tag{B.12}$$

where $\delta_{\max}$ is the maximum allowed threshold value, usually taken to be $\delta_{\max} = 1$ to avoid the formation of PBHs in the non-perturbative regime, where $\mathcal{P}_\delta(k) \gg 1$ [307]. In this sense, the enhanced perturbation modes will not contribute to increasing the mass frac-

tion as we go to high values of k. The factor of 2 in the last equality of (B.12) comes from the Press-Schechter theory itself. This equation can be further simplified by assuming a peaked power spectrum, for which the relation $\sigma_k \simeq \mathcal{P}_\delta(k)$ is satisfied, and therefore we have the following final expression for the mass fraction under the Press-Schecter formalism

$$\beta^{\mathrm{PS}}(k) = \mathrm{erfc}\left[\frac{\delta_c}{\sqrt{2\mathcal{P}_\delta(k)}}\right] - \mathrm{erfc}\left[\frac{\delta_{\max}}{\sqrt{2\mathcal{P}_\delta(k)}}\right]. \tag{B.13}$$

B.2 Khlopov-Polnarev formalism

Khlopov and Polnarev (KP) pioneered the study of PBH formation in a matter-dominated era [121–123], where the effect of non-sphericity in the gravitational collapse plays a crucial role. As the region containing the perturbation shrinks, any initial deviations from spherical symmetry can grow significantly, thereby avoiding collapse. These deviations are encoded in various effects that can be taken into account. In this appendix, we describe in detail the anisotropy effect, which is the dominant one, and make some comments on the inhomogeneity and angular momentum effects.

Let us begin with the anisotropy effect. In an almost spherical collapse, gravity pulls matter radially inward toward the center, but in an anisotropic collapse, matter collapses faster in some directions than in others. If these differences are significant, shear stresses can disrupt the formation of a PBH [308]. However, a moderate anisotropy can allow collapse. For instance, if a perturbation is slightly elongated or deformed but still retains a strong central gravitational potential, it can collapse into a PBH. To estimate the effectiveness of this collapse, we summarize here the results of [119], which employs (1) the Zel'dovich approximation for the nonlinear evolution of density perturbations, (2) Thorne's hoop conjecture, and (3) the probability distribution for nonspherical perturbations derived by Doroshkevich.

The Zel'dovich approximation is a semi-analytic method to track the evolution of matter in the universe by perturbing the motion of fluid elements from a uniform expansion [292]. It is particularly useful in describing the formation of structures. To formulate it, one parametrizes the comoving Eulerian coordinate of a fluid element by

$$r_i(t) = a(t)q_i + b(t)p_i(q_j), \tag{B.14}$$

where $a(t)$ is the scale factor, q_i ($i = 1, 2, 3$) are the Lagrangian coordinates, $p_i(q_j)$ is the deviation vector, and the function b(t) represents a linearly growing mode. The deformation tensor, defined as the Jacobian of the transformation between Eulerian and Lagrangian

coordinates, is given by

$$D_{ik} = \frac{\partial r_i}{\partial q_k} = a(t)\delta_{ik} + b(t)\frac{\partial p_i}{\partial q_k}. \tag{B.15}$$

Now, using the matrix $\partial p_i/\partial q_k$, one can define a set of fundamental axes and define the Lagrangian coordinates such that

$$\frac{\partial p_i}{\partial q_k} = \text{diag}(-\alpha, -\beta, -\gamma), \tag{B.16}$$

with α, β, and γ being functions of the Lagrangian coordinates. Furthermore, and without loss of generality, we assume that $\infty > \alpha \geq \beta \geq \gamma > -\infty$, and that the collapse occurs at least along one of the principal axes, so that $\alpha > 0$. Then, the deformation tensor is expressed as

$$D_{ik} = \text{diag}(a - \alpha b, a - \beta b, a - \gamma b), \tag{B.17}$$

whose determinant gives the local change in volume. Next, to determine how density evolves under gravitational collapse, we begin with the principle of mass conservation, which states that the mass of a fluid element remains constant as it deforms:

$$\mathrm{d}m = \rho \mathrm{d}^3 r = \bar{\rho} a^3 d^3 q. \tag{B.18}$$

Here, $\mathrm{d}^3 q$ represents a fixed Lagrangian volume element, and $\mathrm{d}^3 r$ is the corresponding deformed physical volume. The quantity ρ is the local physical (Eulerian) density of the fluid element at a given time, while $\bar{\rho}$ denotes the background (mean) density of the homogeneous Friedmann universe at the same epoch. Using eqns. (B.18) and (B.17), we obtain the following relation between the local and the background densities

$$\rho = \frac{a^3}{(a - \alpha b)(a - \beta b)(a - \gamma b)}\bar{\rho}, \tag{B.19}$$

which allows us to estimate the moment of collapse as the determinant of the deformation tensor being zero, producing an infinite density. This does not necessarily occur at the same time for each of the principal axes due to the anisotropies, producing what is known as a pancake collapse, where the mass becomes a two-dimensional ellipse. In fact, we can locally take the Lagrangian coordinates q_i as

$$r_1 = (a - \alpha b)q_1, \qquad r_2 = (a - \beta b)q_2, \qquad r_3 = (a - \gamma b)q_3. \tag{B.20}$$

Since $\alpha \geq \beta \geq \gamma$, the collapse occurs along the r_1 axis, and one can show that at the moment of collapse (t_c), the semi-minor and semi-major axes of the ellipse are given,

respectively, by

$$r_2(t_c) = 4\left(1-\frac{\beta}{\alpha}\right) r_{\max}, \qquad r_3(t_c) = 4\left(1-\frac{\gamma}{\alpha}\right) r_{\max}, \tag{B.21}$$

where $r_{\max}$ is the r_1 axis at the moment of maximum expansion.

Thorne's hoop conjecture [309, 310] states that a black hole forms when a mass M gets compacted into a region equal or smaller than a sphere of surface $4\pi r_S^2$, where $r_S = 2GM/c^2$ is the gravitational (Schwarzschild) radius. The hoop $\mathcal{C}$ of a region is defined as the largest of its circumferences in all directions. For the pancake collapse, it is computed as

$$\mathcal{C} = 16\left(1-\frac{\gamma}{\alpha}\right) E(e) r_{\max}, \tag{B.22}$$

where E is the complete elliptic integral of the first kind and e the eccentricity of the pancake, given by

$$e = \sqrt{1-\left(\frac{r_2(t_c)}{r_3(t_c)}\right)^2} = \sqrt{1-\left(\frac{\alpha-\beta}{\alpha-\gamma}\right)^2}, \tag{B.23}$$

where $r_2(t_c)$ and $r_3(t_c)$ are given in eqn. (B.21). The hoop conjecture is then expressed as $\mathcal{C} \leq 2\pi r_S$ or, using eqn. (B.22), as

$$h(\alpha,\beta,\gamma) \equiv \frac{8}{\pi}\left(1-\frac{\gamma}{\alpha}\right) E(e)\frac{r_{\max}}{r_S} \leq 1, \tag{B.24}$$

where the quotient $r_{\max}/r_S$ reflects how much the initial overdensity must shrink to collapse.

Finally, the Doroshkevich distribution [311] gives the joint probability distribution of the eigenvalues α, β, and γ of the deformation tensor in the Zel'dovich approximation. It represents how likely it is, in a Gaussian random field, that a collapsing region will have a particular shape defined by these eigenvectors. Its mathematical expression is given by

$$\begin{aligned} w(\alpha,\beta,\gamma)\mathrm{d}\alpha\mathrm{d}\beta\mathrm{d}\gamma = -\frac{3375}{8\sqrt{5}\pi\sigma_k^6}\exp\left[-\frac{3}{\sigma_k^2}\left(\alpha^2+\beta^2+\gamma^2-\frac{1}{2}(\alpha\beta+\beta\gamma+\gamma\alpha)\right)\right] \\ \times(\alpha-\beta)(\beta-\gamma)(\gamma-\alpha)\mathrm{d}\alpha\mathrm{d}\beta\mathrm{d}\gamma, \end{aligned} \tag{B.25}$$

where σ_k is the variance of the density perturbations (B.10). Then, the total production probability of PBHs is given by

$$\beta(k) = \int_0^\infty \mathrm{d}\alpha \int_{-\infty}^{\alpha} \mathrm{d}\beta \int_{-\infty}^{\beta} \mathrm{d}\gamma\, \theta(1-h(\alpha,\beta,\gamma))\omega(\alpha,\beta,\gamma). \tag{B.26}$$

where the Heaviside's θ function is introduced to account for the Zel'dovich approximation and Thorn's hoop conjecture; see [119] for details about this whole derivation. The

original analysis of Khlopov and Polnarev [121] was made in a heuristic way and gave $\beta(k) \simeq 0.02\sigma_k^5$, which was later refined in [119] to obtain eqn. (B.26). For this last, a semi-analytical formula can be obtained [119], giving

$$\beta^{\text{KP}}_{\text{aniso}}(\sigma_k \lesssim 10^{-2}) \simeq 0.056\sigma_k^5, \tag{B.27}$$

which is valid for $\sigma_k \lesssim 10^{-2}$ (small perturbations). Two important remarks are worth mentioning here (1) These estimations for $\beta(k)$ are based on analytical fits of full numerical computations under the assumption of small perturbations, so in this sense, they do not capture the physics of scenarios with amplified perturbations. Thus, for the case of amplified perturbations ($\sigma_k \gtrsim 10^{-2}$), we have derived for the first time, an improved semi-analytical formula for $\beta(k)$ valid for σ_k up to $\mathcal{O}(1)$ that recovers the previous one for $\sigma_k \lesssim 10^{-2}$, eqn. (B.27). This is given by:

$$\beta^{\text{KP}}_{\text{aniso}}(k) = \frac{A_1\,\sigma_k^5 + A_2\,\sigma_k^6}{1 + A_1\,\sigma_k^5 + A_3\,\sigma_k^6}, \tag{B.28}$$

where the values for the constants are $A_1 = 0.056$, $A_2 = 1.084$, and $A_3 = 6.536$. The derivation of this formula is explained in what follows. According to App. B of [119], the mass fraction (B.26) can be transformed to the following expression:

$$\beta(k) = -\frac{675\sqrt{5}}{2\pi\sigma_k^6}\int_{-\frac{1}{2}}^{\frac{1}{2}} \mathrm{d}u\,(2u-1)(2u+1)\int_{-1-\frac{2}{3}u}^{\infty} \mathrm{d}t\,\frac{2 + 2Az_*^2 + A^2 z_*^4}{A^3} e^{-Az_*}, \tag{B.29}$$

where A and z_* are both functions of (u,t). These are given by

$$A(t,u) = \frac{9}{2}\left(\frac{t}{\sigma_k}\right)^2 + 10\left(\frac{u}{\sigma_k}\right)^2 + \frac{15}{2}\left(\frac{1}{\sigma_k}\right)^2, \tag{B.30a}$$

$$z_*(t,u) = \frac{4}{\pi}\left(t + \frac{2}{3}u + 1\right)^{-2} E\left(\sqrt{1 - \left(u + \frac{1}{2}\right)^2}\right). \tag{B.30b}$$

Eqns. (B.29) and (B.30) have been adapted to our notation. To recover the equations from App. B of [119] consider $\sigma_3^2 = \frac{\sigma_k^2}{5}$. The numerical solution of (B.29) is shown in Fig. B.1 as the continuous black curve labeled β_{num} and as a function of the variance of the density perturbations σ_k. Also shown in Fig. B.1 is the analytical approximation $\beta^{\text{KP}}_{\text{aniso}}(\sigma_k \lesssim 10^{-2})$ (eqn. (B.27)) for small σ_k as the red dashed curve. One can observe that for $\sigma_k \gtrsim 10^{-2}$, this analytical estimation deviates from the numerical solution, with one order of magnitude of deviation for $\sigma_k \sim \mathcal{O}(1)$. Since in general, we study amplified perturbations, we find it useful to find a parametrization of the numerical solution valid also for high values of σ_k. This new parametrization is shown in Fig. B.1 as the green dashed curve, which fits better than the estimation for small σ_k. It corresponds to eqn. (B.28), which asymptotes to the estimation for small σ_k, and to the constant value A_2/A_3 for high σ_k. This

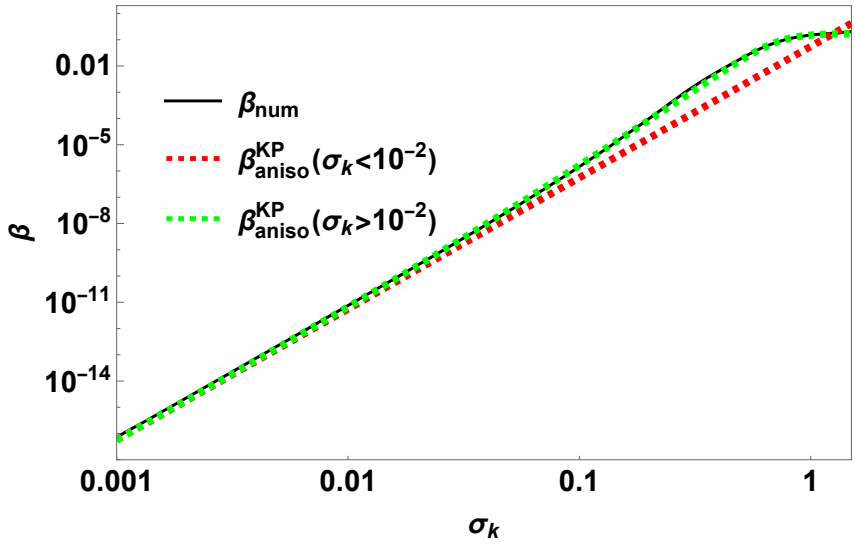

Figure B.1: Mass fraction under the KP formalism as a function of the variance of the density perturbations σ_k. The curves labeled as $\beta_{\rm num}$, $\beta^{\rm KP}_{\rm aniso}(\sigma_k \lesssim 10^{-2})$, and $\beta^{\rm KP}_{\rm aniso}(\sigma_k \gtrsim 10^{-2})$ corresponds to eqns. (B.29), (B.27), and (B.28), respectively.

last can be understood from the fact that strong anisotropy suppresses collapse, and then higher σ_k does not mean a higher $\beta(k)$. For instance, if a perturbation is highly anisotropic, *i.e.* very elongated, different regions of the perturbation will experience different gravitational forces and collapse at different rates. This leads to tidal shearing, since the perturbation stretches and deforms rather than forming a compact object, and to the formation of filaments or pancakes rather than PBHs [121–125]. Eqn. (B.28) offers, for the first time, a simple and rapid estimation of the mass fraction for the KP formalism over the whole range of σ_k that avoids numerically-cost computations.

Another effect that can be taken into account is inhomogeneity. Inhomogeneities influence the collapse by altering the conditions under which an apparent horizon forms before information from the central region can escape. In this sense, if density inhomogeneities are too strong, they can prevent PBH formation by dispersing the collapsing matter before a black hole can form. This was also considered by Khlopov and Polnarev in their original analysis [125], which obtained an estimation for the mass fraction that was later refined in [287] to give

$$\beta^{\rm KP}_{\rm inhom}(\sigma_k \lesssim 10^{-2}) \simeq 3.7\sigma_k^{3/2}, \tag{B.31}$$

which again is valid for small perturbations, $\sigma_k \lesssim 10^{-2}$. For larger perturbations, $\sigma_k \gtrsim 10^{-2}$, the following semi-analytical expression is found for the mass fraction [287]

$$\beta^{\rm KP}_{\rm inhom}(\sigma_k \gtrsim 10^{-2}) \simeq \frac{1}{2}\left[1 - {\rm Erf}\left(\frac{0.11}{\sqrt{2}\sigma_k}\right)\right]. \tag{B.32}$$

Further effects can be taken into account, such as the angular momentum of the perturba-

tions [312], where the centrifugal force effectively bounces back most collapsing masses, preventing direct black hole formation. Overall, the total mass fraction is computed as the product of the individual mass fractions associated with each of the considered effects.

Appendix C

SIGWs during matter-dominated scenarios

C.1 Source term for SIGWs

In this appendix, we closely follow the analysis presented in [193] and [48]. By considering both metric and field fluctuations, we can write the following line element for the perturbed FLRW metric

$$\mathrm{d}s^2 = g_{\mu\nu}\mathrm{d}x^\mu \mathrm{d}x^\nu = -(1+2\Psi)\mathrm{d}t^2 + a^2[(1-2\Phi)\delta_{ij} + h_{ij}]\mathrm{d}x^i \mathrm{d}x^j, \tag{C.1}$$

where h_{ij} is a gauge-invariant, symmetric, transverse, and traceless perturbation tensor. We are working in the Newtonian gauge. The most general form for h_{ij} is given by

$$h_{ij}(x,t) = \sum_{\lambda=+,\times} h^{(\lambda)}(t)\tau_{ij}^{(\lambda)}(x), \tag{C.2}$$

where $\tau_{ij}^{(\lambda)}$ are polarization tensors, which are symmetric, transverse, and traceless, and the index $\lambda = +, \times$ denotes the two polarization states. Using the metric defined in (C.1) we can derive the following field equation for h_{ij} from the third order perturbative expansion of the action (1.3) [47, 299]

$$\ddot{h}_{ij} + 3H\dot{h}_{ij} - \frac{\nabla^2 h_{ij}}{a^2} = -\frac{4}{a^2}\mathcal{T}_{ij}^{lm}\mathcal{S}_{lm}. \tag{C.3}$$

Here $\mathcal{S}_{lm}$ is the source term, which contains the information about scalar perturbations and is given by [193]

$$\mathcal{S}_{lm} = -8\partial_l(\Phi+\Psi)\partial_m\Phi + 4\partial_l\Phi\partial_m\Phi + 2\partial_l\delta\phi\partial_m\delta\phi. \tag{C.4}$$

The term $\mathcal{T}_{ij}^{lm}$ is the projection tensor, responsible for extracting the transverse and traceless components of any tensor and the terms involving second-order scalar and tensor perturbations [195]. It can be expressed in terms of the polarization tensors $\tau_{ij}^{(\lambda)}$ as [48]

$$\mathcal{T}_{ij}^{lm}\mathcal{S}_{lm} = \int \frac{\mathrm{d}^3\mathbf{k}}{(2\pi)^{3/2}} e^{i\mathbf{k}\cdot\mathbf{x}} \left(\sum_{\lambda=+,\times} \tau_{ij}^{(\lambda)}(\mathbf{k})\tau^{(\lambda)lm}(\mathbf{k}) \right) \mathcal{S}_{lm}(\mathbf{k}), \tag{C.5}$$

where $\mathcal{S}_{lm}(\boldsymbol{k})$ is the Fourier transform of $\mathcal{S}_{lm}(\boldsymbol{x})$. Additionally, the Fourier transform of h_{ij} is expressed as

$$h_{ij}(x,t) = \int \frac{\mathrm{d}^3\mathbf{k}}{(2\pi)^3} \sum_{\lambda=+,\times} h_{\mathbf{k}}^{(\lambda)}(t)\tau_{ij}^{(\lambda)}(\mathbf{k})e^{i\mathbf{k}\cdot\mathbf{x}}. \tag{C.6}$$

By applying eqns. (C.5) and (C.6), we can transform the equation of motion (C.3) into Fourier space, resulting in the following expression [48]

$$\ddot{h}_{\boldsymbol{k}}^{(\lambda)} + 3H\dot{h}_{\boldsymbol{k}}^{(\lambda)} + \frac{k^2}{a^2}h_{\boldsymbol{k}}^{(\lambda)} = -\frac{\tau^{lm}\mathcal{S}_{(\lambda)lm}(\boldsymbol{k})}{a^2}. \tag{C.7}$$

Next, we compute the Fourier transform of $\mathcal{S}_{lm}(\boldsymbol{x})$, for which we use the following property of the Fourier transforms, called the Convolution Theorem. Consider two functions, f and g. The Fourier transform of their product is given by [306]

$$\mathcal{F}\{f(\boldsymbol{x})g(\boldsymbol{x})\} \equiv \frac{1}{(2\pi)^{3/2}}(f * g)(\boldsymbol{k}), \tag{C.8}$$

where $\mathcal{F}$ represents the Fourier transform and $*$ the convolution, defined as

$$(f * g)(\boldsymbol{k}) = \int \mathrm{d}^3\tilde{\boldsymbol{k}}\, f(\tilde{\boldsymbol{k}})\, g(\boldsymbol{k} - \tilde{\boldsymbol{k}}). \tag{C.9}$$

Using this, the source term in (C.7) is now given by [48, 50, 195]

$$\mathcal{S}(\boldsymbol{k},t) = -\tau^{lm}\mathcal{S}_{lm}(\boldsymbol{k},t) = \int \frac{\mathrm{d}^3\tilde{k}}{(2\pi)^{3/2}}\tau^{lm}\tilde{k}_l\tilde{k}_m \left(4\Phi_{\tilde{\boldsymbol{k}}}\Phi_{\boldsymbol{k}-\tilde{\boldsymbol{k}}} + 2\delta\phi_{\tilde{\boldsymbol{k}}}\delta\phi_{\boldsymbol{k}-\tilde{\boldsymbol{k}}}\right), \tag{C.10}$$

where we are ignoring the anisotropic stress, which translates into $\Phi + \Psi = 0$. The meaning of (C.10) is that, since the source term consists of products of perturbations that interact in real space and thus their Fourier coefficients mix, the resulting mode of the product is influenced by all possible pairs of modes of the original perturbations, which translates into a convolution in $\boldsymbol{k}$. Using the properties of the projection tensors, we have that [48]

$$\tau^{(\lambda)lm}\tilde{k}_l\tilde{k}_m = \tilde{k}^2(1-\mu^2), \tag{C.11}$$

where μ is the cosine of the angle between the incoming and outgoing scales. Thus, the final expression for the source term in (C.10) is

$$\mathcal{S}(\boldsymbol{k},t) = \int \frac{\mathrm{d}^3\tilde{k}}{(2\pi)^{3/2}}\tilde{k}^2(1-\mu^2) \left(4\Phi_{\tilde{\boldsymbol{k}}}\Phi_{\boldsymbol{k}-\tilde{\boldsymbol{k}}} + 2\delta\phi_{\tilde{\boldsymbol{k}}}\delta\phi_{\boldsymbol{k}-\tilde{\boldsymbol{k}}}\right). \tag{C.12}$$

C.2 Power spectrum of SIGWs

As shown in [2], the self-resonance is brief for small values of α, followed by the usual, pressureless, matter-dominated preheating, where the scale factor evolves as $a \sim t^{2/3}$ and $\Phi_{\boldsymbol{k}} \sim \delta\phi_{\boldsymbol{k}} \sim C(k)$ for the modes of interest. We remark that this does not imply any fluid description since the matter content of the universe is still in the form of an oscillating scalar field. Under these assumptions, $\mathcal{S}(\boldsymbol{k}, t) = \mathcal{S}_{\boldsymbol{k}}$, and we can attempt to solve (6.42) semi-analytically. A particular solution is given by [50]:

$$h_{\boldsymbol{k}}^{(\lambda)}(t) = \frac{\mathcal{S}_{\boldsymbol{k}}}{k^2}\left[1 + 3\,\frac{x\cos x - \sin x}{x^3}\right] = \frac{\mathcal{S}_{\boldsymbol{k}}}{k^2} g(k,t), \tag{C.13}$$

where $x = \frac{2k}{aH}$, $g(k,t)$ is the growth function for the tensor modes, and we have used the following initial conditions

$$h_{\boldsymbol{k}}^{(\lambda)}(k \ll aH) = 0, \qquad \text{and} \qquad \dot{h}_{\boldsymbol{k}}^{(\lambda)}(k \ll aH) = 0, \tag{C.14}$$

since the typical assumption is that SIGWs are generated instantaneously when the relevant mode enters the horizon [48]. Using (C.13), the two-point correlation function for $h_{\boldsymbol{k}}$ can be written as

$$\begin{aligned}
\langle h_{\boldsymbol{k}}^{(\lambda)}(t) h_{\boldsymbol{k}'}^{(\lambda)}(t)\rangle &= \frac{g^2(k,t)}{k^4}\langle \mathcal{S}_{\boldsymbol{k}}\mathcal{S}_{\boldsymbol{k}'}\rangle \\
&\simeq \frac{16 g^2(k,t)}{k^4}\int \frac{\mathrm{d}^3\tilde{\boldsymbol{k}}}{(2\pi)^{3/2}}\int \frac{\mathrm{d}^3\tilde{\boldsymbol{k}}'}{(2\pi)^{3/2}}\tilde{k}^2\tilde{k}'^2(1-\mu^2)^2\langle \Phi_{\tilde{\boldsymbol{k}}}\Phi_{\boldsymbol{k}-\tilde{\boldsymbol{k}}}\Phi_{\tilde{\boldsymbol{k}}'}\Phi_{\boldsymbol{k}-\tilde{\boldsymbol{k}}'}\rangle \\
&\simeq \frac{8\pi g^2(k,t)}{k^4}\delta^{(3)}(\boldsymbol{k}+\boldsymbol{k}')\int \mathrm{d}^3\tilde{\boldsymbol{k}}\,\frac{\tilde{k}\,(1-\mu^2)^2}{|\boldsymbol{k}-\tilde{\boldsymbol{k}}|^3}\mathcal{P}_\Phi(\tilde{k})\mathcal{P}_\phi(|\boldsymbol{k}-\tilde{\boldsymbol{k}}|),
\end{aligned} \tag{C.15}$$

where in the second step we are neglecting $\delta\phi_{\boldsymbol{k}}$ since it is subdominant with respect to $\Phi_{\boldsymbol{k}}$, and in the last equality we used Wick's theorem to express the four-point correlation function of a Gaussian distribution of scalar perturbations as a function of two-point correlation functions [48, 50, 193]. Using the definition of the power spectrum of SIGWs, eqn. (6.44), we have

$$\mathcal{P}_h^{\mathrm{SI}}(k,t) = \frac{8 g^2(k,t)}{\pi k}\int \mathrm{d}^3\tilde{\boldsymbol{k}}\,\frac{\tilde{k}\,(1-\mu^2)^2}{|\boldsymbol{k}-\tilde{\boldsymbol{k}}|^3}\,\mathcal{P}_\Phi(\tilde{k})\mathcal{P}_\Phi(|\boldsymbol{k}-\tilde{\boldsymbol{k}}|). \tag{C.16}$$

Finally, decomposing the volume element into spherical coordinates as

$$\int_V \mathrm{d}^3\tilde{\boldsymbol{k}} = \int_0^\infty \tilde{k}^2\mathrm{d}\tilde{k}\int_0^\pi \sin\theta\mathrm{d}\theta\int_0^{2\pi}\mathrm{d}\varphi = \int_0^\infty \tilde{k}^2\mathrm{d}\tilde{k}\int_{-1}^1 \mathrm{d}\mu\int_0^{2\pi}\mathrm{d}\varphi, \tag{C.17}$$

we have

$$\mathcal{P}_h^{\rm SI}(k,t) = \frac{16 g^2(k,t)}{k} \int_0^\infty \mathrm{d}\tilde{k} \int_{-1}^1 \mathrm{d}\mu \, \frac{\tilde{k}^3 \, (1-\mu^2)^2}{|\boldsymbol{k}-\tilde{\boldsymbol{k}}|^3} \mathcal{P}_\Phi(\tilde{k}) \mathcal{P}_\Phi(|\boldsymbol{k}-\tilde{\boldsymbol{k}}|). \tag{C.18}$$

Now, to gain some insight into the behavior of the power spectrum, we analyze it in two different regimes. First, for the low-k modes, we have that considering $k \ll \tilde{k}$ in (C.18), then $|\boldsymbol{k}-\tilde{\boldsymbol{k}}| \sim \tilde{k}$, and thus we have

$$\mathcal{P}_h^{\rm SI}(k,t) \sim \frac{256 g^2(k,t)}{15k} \int_0^\infty \mathrm{d}\tilde{k} \, \mathcal{P}_\Phi^2(\tilde{k}) = \frac{256 g^2(k,t) \, \mathcal{I}_{\tilde{k}}}{15k}, \tag{C.19}$$

where $\mathcal{I}_{\tilde{k}}$ represents the integral of the square of the power spectrum over the whole range of $\tilde{k}$. This essentially depends on the amplitude of the peak, so the higher the peak, the higher the integral, which ultimately translates into an amplification for the low-k range, although the peak is in the high-k range. This clearly reflects the convolutive nature of the source term, as stated in Sec. 5.1.1. Regarding the growth function $g(k,t)$, let us write $x = \frac{2k}{aH}$. Then, the expansion of $g(x)$ for small x is $g \sim x^2/10$ and therefore, eqn. (C.19), evaluated at the end of preheating, is given by

$$\mathcal{P}_h^{\rm SI}(k \ll \tilde{k}, t_{\rm rh}) \sim \frac{2.7 \, \mathcal{I}_{\tilde{k}}}{k_L^4} k^3. \tag{C.20}$$

Using the definition of the fractional energy density, eqn. (6.48), we have

$$\Omega_{\rm GW}^{\rm SI}(k \ll \tilde{k}, t_{\rm rh}) \sim \frac{0.22 \Omega_\gamma^0 \, \mathcal{I}_{\tilde{k}}}{k_L^6} k^5. \tag{C.21}$$

For the modes higher than $k_{\rm end}$ the growth function has settled to unity and thus $\Omega_{\rm GW}^{\rm SI}$ is now given by

$$\Omega_{\rm GW}^{\rm SI}(k \sim k_{\rm end}, t_{\rm rh}) \sim \frac{1.4 \, \Omega_\gamma^0 \, \mathcal{I}_{\tilde{k}}}{k_L^2} k. \tag{C.22}$$

Finally, for the high-k modes, taking the limit $k \gg \tilde{k}$ in (C.18), we have that $|\boldsymbol{k}-\tilde{\boldsymbol{k}}| \sim k$, and the power spectrum is given by

$$\mathcal{P}_h^{\rm SI}(k \gg \tilde{k}, t_{\rm rh}) \sim \frac{16 \, \mathcal{P}_\Phi(k)}{k^4} \int_0^\infty \tilde{k}^3 \mathcal{P}_\Phi(\tilde{k}) = \frac{16 \, \mathcal{P}_\Phi(k) \mathcal{I}_k}{k^4}, \tag{C.23}$$

where $\mathcal{I}_k$ is defined in a similar way to $\mathcal{I}_{\tilde{k}}$ and the growth function is set to unity. This translates into the following expression for the fractional energy density

$$\Omega_{\rm GW}^{\rm SI}(k \gg \tilde{k}, t_{\rm rh}) \sim \frac{4 \Omega_\gamma^0 \, \mathcal{P}_\Phi(k) \mathcal{I}_k}{3 k_U^2 k^2}. \tag{C.24}$$

Fig. C.1 shows these approximations as the dashed black lines for two particular values of α in an E-model, $\alpha = 1$ (blue) and $\alpha = 10^{-3}$ (orange). For the latter, we observe that (C.22)

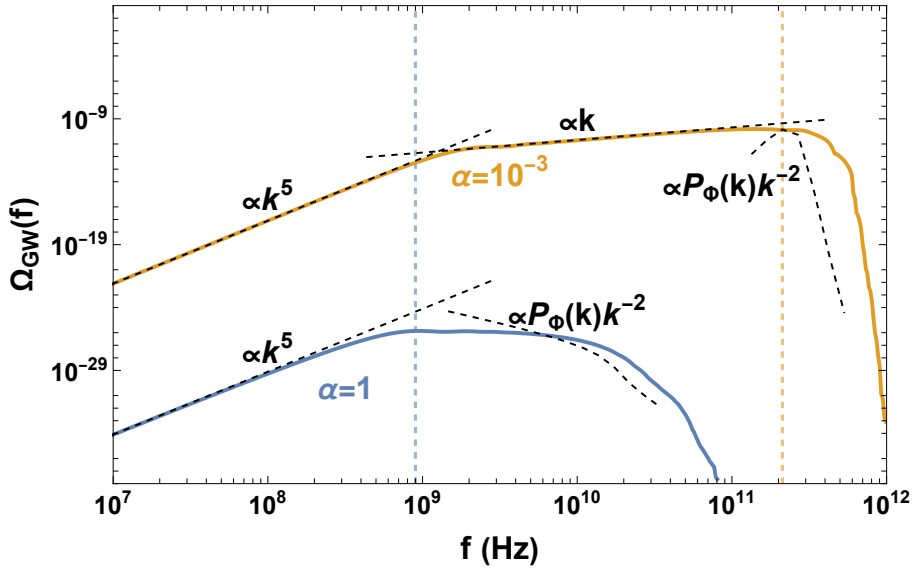

Figure C.1: Fractional energy density for an E-model and two values of α. Black dashed lines represent the analytical approximations given by eqns. (C.21), (C.22), and (C.24). Vertical dashed lines mark the frequency of the peak in each case, obtained with eqn. (C.26) for $\alpha = 1$ (blue) and from the peak of $\mathcal{P}_\mathcal{R}(k)$ for $\alpha = 10^{-3}$ (orange).

is useful to determine the amplitude of the peak. Considering that it is at the same scale as the peak in the power spectrum, *i.e.* k_p, then the maximum amplitude of the fractional energy density is computed as

$$\Omega_{\rm GW}^{\rm SI,max} \sim \frac{1.4\Omega_\gamma^0 \mathcal{I}_{\tilde{k}}}{k_L^2} k_p, \tag{C.25}$$

where $k_p \sim k_U/\sqrt{2}$ [188, 189]. Eqn. (C.25) is shown as the vertical blue dashed line of Fig. C.1. On the contrary, for $\alpha = 1$, since there is no amplification peak, the maximum is at the point where the growth function peaks. Again, considering $x = \frac{2k}{aH}$, these points are given by the roots of the equation

$$\tan x = \frac{3x}{3 - x^2}, \tag{C.26}$$

the first of which is given approximately by $x_0 \sim 5.76$, which implies $k_0 \sim 2.88 k_L$. This is shown as the vertical orange dashed line of Fig. C.1. Finally, for comparison purposes, we also show the fractional energy density of BGWs for the same values of α but in lighter colors. One can observe that, for the Starobinsky case, the background contribution is higher than the induced one, contrary to the case of $\alpha = 10^{-3}$.

Appendix C. SIGWs during matter-dominated scenarios

Appendix D

Analytical estimations for σ_k, $\Omega_{\mathbf{PBH}}$, and $\Omega_{\mathbf{GW}}^{\mathbf{PBH}}$

D.1 Analytical solutions for $\Omega_{\mathbf{PBH}}(k)$

We want to solve the integral

$$\Omega_{\rm PBH}(k) = 3\int_k^{k_{\rm end}} \beta(\tilde{k}) \mathrm{d}\ln(\tilde{k}), \tag{D.1}$$

where $\beta(k)$ is given by (B.28) in terms of σ_k. To simplify, let us consider that the power spectrum is given just by the Gaussian peak, that is, $\mathcal{P}_\mathcal{R}(k) \simeq \mathcal{P}_\mathcal{R}^{\rm peak}(k)$. Now, using this in (6.8), we obtain the following expression for the variance of the density perturbations

$$\sigma_k \simeq \frac{8\sqrt{\mathcal{A}_{\rm peak}}}{5} \exp\left[-\frac{\log\left(k/k_{\rm peak}\right)^2}{2\sigma^2}\right]. \tag{D.2}$$

To gain some insight into the behavior of $\Omega_{\rm PBH}(k)$, we will solve analytically the integral (D.1) in two regimes, small ($\sigma_k \lesssim 1$) and large ($\sigma_k \gtrsim 1$) variance. First, let us consider that the variance of the density perturbations is small for the whole range of k. In this case, we can safely consider

$$\beta(k) \simeq A_1\sigma_k^5 + A_2\sigma_k^6 \qquad (\sigma_k \lesssim 1), \tag{D.3}$$

and the integral (D.1) reduces to the integral of sum of two Gaussians, that is

$$\Omega_{\rm PBH}(x) \simeq 3\int_x^{x_{\rm end}} \left(B_1 e^{-\alpha_1 x^2} + B_2 e^{-\alpha_2 x^2}\right) \mathrm{d}x, \tag{D.4}$$

where we have applied the change of variable $x = \ln(k/k_{\rm peak})$ and defined

$$B_1 = A_1\left(\frac{8\sqrt{\mathcal{A}_{\rm peak}}}{5}\right)^5, \tag{D.5a}$$

$$B_2 = A_2\left(\frac{8\sqrt{\mathcal{A}_{\rm peak}}}{5}\right)^6, \tag{D.5b}$$

$$\alpha_1 = \frac{5}{2\sigma^2\ln(10)^2}, \tag{D.5c}$$

$$\alpha_2 = \frac{3}{\sigma^2\ln(10)^2}. \tag{D.5d}$$

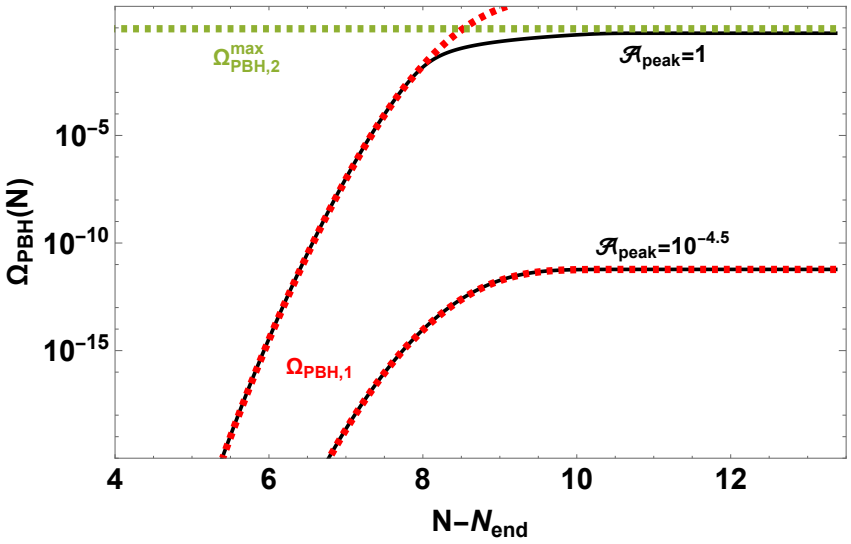

Figure D.1: Fractional energy density of PBHs as a function of the number of efolds from the end of inflation. The black curves show the numerical computation of (D.1), whereas the green and red curves the analytical approximation of (D.6) and (D.11), respectively. The peak of the power spectrum is centered at $k_{\rm peak} = 10^{-2} k_{\rm end}$.

The integral of (D.4) is now straightforward and gives

$$\Omega_{\rm PBH,1}(k, k_{\rm end}) \simeq \frac{3\sqrt{\pi}}{2} \left\{ \frac{B_1}{\sqrt{\alpha_1}} \left[\text{erf}\left(\ln\left(\frac{k_{\rm end}}{k_{\rm peak}}\right) \sqrt{\alpha_1} \right) - \text{erf}\left(\ln\left(\frac{k}{k_{\rm peak}}\right) \sqrt{\alpha_1} \right) \right] \right.$$
$$\left. + \frac{B_2}{\sqrt{\alpha_2}} \left[\text{erf}\left(\ln\left(\frac{k_{\rm end}}{k_{\rm peak}}\right) \sqrt{\alpha_2} \right) - \text{erf}\left(\ln\left(\frac{k}{k_{\rm peak}}\right) \sqrt{\alpha_2} \right) \right] \right\}, \tag{D.6}$$

where erf(x) is the error function. Here we observe that, as the value of k decreases (moving forward in time), the mass fraction reaches a constant value given by

$$\Omega^{\rm max}_{\rm PBH,1} = \frac{3\sqrt{\pi}}{2} \left(\frac{B1}{\sqrt{\alpha_1}} + \frac{B2}{\sqrt{\alpha_2}} \right). \tag{D.7}$$

This occurs after the Gaussian peak has fully entered the horizon, when the production of PBHs decreases drastically. The approximation (D.6) is shown in Fig. D.1 in red as a function of the number of efolds from the end of inflation. It shows a good agreement with the numerical solution for small $\mathcal{A}_{\rm peak}$. However, as $\mathcal{A}_{\rm peak}$ increases, a small portion of the Gaussian peak exceeds $\sigma_k \simeq 1$ and for those modes $\beta(k) \neq A_1 \sigma_k^5 + A_2 \sigma_k^6$. Instead, the mass fraction reaches a constant value

$$\beta(k) \simeq A_2/A_3 \qquad (\sigma_k \simeq 1). \tag{D.8}$$

Still, this approximation is only valid for the portion of the peak above the threshold value $\sigma_{\rm th} = 1$. Imposing $\sigma_k > \sigma_{\rm th}$ in (D.2), the following range of k is obtained

$$e^{-\sqrt{X(\sigma_{\rm th})}} \lesssim \frac{k}{k_{\rm peak}} \lesssim e^{\sqrt{X(\sigma_{\rm th})}}, \tag{D.9}$$

where

$$X(\sigma_{\rm th}) = -2\sigma^2 \ln(10)^2 \ln\left(\frac{5\sigma_{\rm th}}{8\sqrt{\mathcal{A}_{\rm peak}}}\right), \tag{D.10}$$

which is only valid when $\sigma_{\rm th} < \frac{8}{5}\sqrt{\mathcal{A}_{\rm peak}}$. In this interval, the integral (D.1) is easily computed, and gives

$$\Omega^{\rm max}_{\rm PBH,2} \simeq \frac{6A_2}{A_3}\sqrt{X(\sigma_{\rm th})}. \tag{D.11}$$

This is by definition the highest contribution to $\Omega_{\rm PBH}$, and thus serves as an upper bound on the mass fraction of PBH. It is shown in Fig. D.1 in green for the case when (D.10) is valid, that is, when the Gaussian peak is above $\sigma_k > 1$, and shows also good agreement with the numerical solution. In short, the maximum abundance of PBHs for our model can be estimated as follows

$$\Omega^{\rm max}_{\rm PBH} = \min\left\{\Omega^{\rm max}_{\rm PBH,1}, \Omega^{\rm max}_{\rm PBH,2}\right\}. \tag{D.12}$$

D.2 Analytical solutions for $\Omega^{\rm PBH}_{\rm GW}$

The fractional energy density of SIGWs is given by eqn. (6.48) as follows:

$$\begin{aligned}\Omega^{\rm PBH}_{\rm GW}(k) \simeq \frac{16\,\Omega^0_\gamma}{27\pi^2}\frac{k}{k^2_{\rm eva}k^6_{\rm UV}}\int_{k_{\rm eva}}^{k_{\rm UV}} {\rm d}\tilde{k}\int_{-1}^{1}{\rm d}\mu\,\tilde{k}^6(1-\mu^2)^2 \\ \cdot\left[5+\frac{4}{9}\left(\frac{\tilde{k}}{k_{\rm PBH}}\right)^2\right]^{-2}\left[5+\frac{4}{9}\left(\frac{|\boldsymbol{k}-\tilde{\boldsymbol{k}}|}{k_{\rm PBH}}\right)^2\right]^{-2},\end{aligned} \tag{D.13}$$

where we have substituted the power spectrum of SIGWs (6.45) and the power spectrum of PBHs density fluctutations (6.40). Further, we consider $g(k, t_{\rm eva}) \simeq 1$ for the modes of interest. We give now analytical estimations of (D.13) to understand the dependence of $\Omega^{\rm PBH}_{\rm GW}$ with the parameters of the model. Defining

$$x \equiv \frac{\tilde{k}}{k_{\rm PBH}}, \qquad y \equiv \frac{k}{k_{\rm PBH}}, \tag{D.14}$$

the integral in (D.13) is simplified to

$$\Omega_{\rm GW}^{\rm PBH}(y) \simeq \frac{16\,\Omega_\gamma^0}{27\pi^2}\frac{k_{\rm PBH}^8}{k_{\rm eva}^2 k_{\rm UV}^6} y \int_{x_{\rm eva}}^{x_{\rm UV}} {\rm d}x \int_{-1}^{1} {\rm d}\mu\, x^6 \left(5+\frac{4}{9}x^2\right)^{-2}\left(5+\frac{4}{9}(x^2+y^2-2xy\mu)\right)^{-2}, \tag{D.15}$$

where $x_{\rm eva}$ and $x_{\rm UV}$ are defined using (D.14). The main contribution to the integral in μ comes from $\mu = 0$, which further simplifies the integral to

$$\Omega_{\rm GW}^{\rm PBH}(y) \simeq \frac{16\,\Omega_\gamma^0}{27\pi^2}\frac{k_{\rm PBH}^8}{k_{\rm eva}^2 k_{\rm UV}^6} y \int_{x_{\rm eva}}^{x_{\rm UV}} {\rm d}x\, \upsilon(x,y), \tag{D.16}$$

where $\upsilon(x,y)$ is defined as

$$\upsilon(x,y) = x^6\left(5+\frac{4}{9}x^2\right)^{-2}\left(5+\frac{4}{9}(x^2+y^2)\right)^{-2}. \tag{D.17}$$

A primitive of $\upsilon(x,y)$ with respect to the variable x is given by

$$\begin{aligned}\Upsilon(x,y) = \frac{6561}{4096y^6}\Bigg[&-\frac{4050xy^2}{45+4x^2} - \frac{2xy^2(45+4y^2)^2}{45+4x^2+4y^2} + 675\sqrt{5}(9+y^2)\tan^{-1}\left(\frac{2x}{3\sqrt{5}}\right)\\ &+(y^2-45)(4y^2+45)^{\frac{3}{2}}\tan^{-1}\left(\frac{2x}{\sqrt{45+4y^2}}\right)\Bigg].\end{aligned} \tag{D.18}$$

Considering that $x_{\rm UV} \gg x_{\rm eva}$, we have that

$$\int_{x_{\rm eva}}^{x_{\rm UV}} {\rm d}x\, \upsilon(x,y) = \Upsilon(x_{\rm UV},y) - \Upsilon(x_{\rm eva},y) \simeq \Upsilon(x_{\rm UV},y). \tag{D.19}$$

Now, for the modes that enter the horizon during PBH domination ($y \ll 1$), and for a very large $x_{\rm UV}$, the function $\Upsilon(x_{\rm UV},y)$ asymptotes to

$$\Upsilon(x_{\rm UV}\gg 1, y\ll 1) \simeq \Upsilon(\infty,0) = \frac{2187\sqrt{5}\pi}{4096}. \tag{D.20}$$

On the contrary, for the modes that are already inside the horizon during PBH domination ($y \gg 1$), and again for a very large UV cut-off, the function $y\Upsilon(x_{\rm UV},y)$ asymptotes to the value

$$y\Upsilon(x_{\rm UV}\gg 1, y\gg 1) \simeq y\Upsilon(\infty,\infty) = \frac{6561\pi}{1024}. \tag{D.21}$$

Then, the fractional energy density of SIGWs can be estimated as

$$\Omega_{\rm GW}^{\rm PBH}(k\ll k_{\rm PBH}) \simeq \frac{81\sqrt{5}\,\Omega_\gamma^0}{256\pi}\frac{k\,k_{\rm PBH}^7}{k_{\rm eva}^2 k_{\rm UV}^6} \sim k \tag{D.22}$$

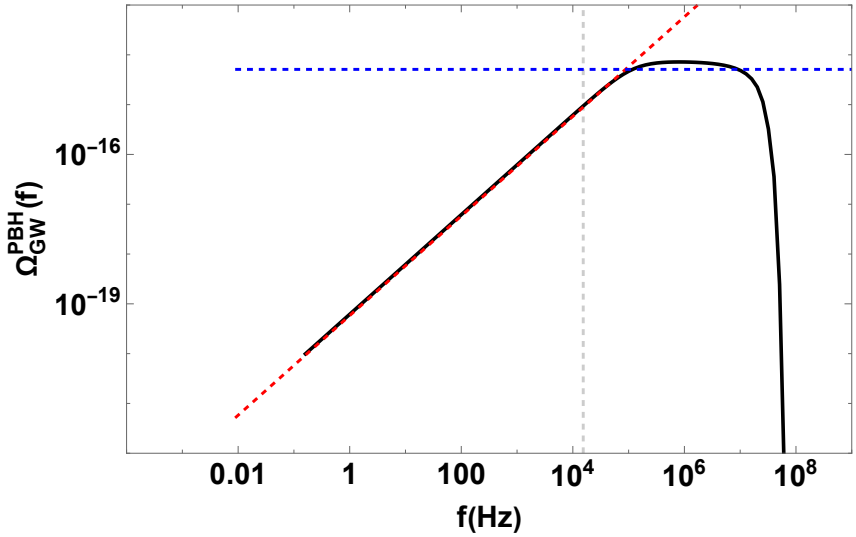

Figure D.2: Numerical solution (continuous black) of the fractional energy density of SIGWs, eqn. (D.13) and the analytical approximations for small (large) $k/k_{\rm PBH}$ in red (blue). The vertical gray dashed line corresponds to the frequency associated with the mode $k_{\rm PBH}$. The set of parameters chosen is: $k_{\rm peak} = 0.01 k_{\rm end}$, $\mathcal{A}_{\rm peak} = 0.1$, and $\Gamma_\phi = 4.5 \times 10^{-18}$.

for modes entering the horizon when PBHs dominate, and as

$$\Omega_{\rm GW}^{\rm PBH}(k \gg k_{\rm PBH}) \simeq \frac{243\,\Omega_\gamma^0}{64\pi} \frac{k_{\rm PBH}^8}{k_{\rm eva}^2 k_{\rm UV}^6} \sim \text{cte}, \tag{D.23}$$

for the modes that are already inside the horizon when the PBHs start dominating. This last serves us as an estimation of the maximum amount of GWs produced. Eqns. (D.22) and (D.23) are shown in Fig. D.2 in dashed red and blue, respectively, and for a particular choice of parameters, see the caption for details. We observe that both agree well with the full numerical solution of (D.13), shown in continuous black line.

Appendix D. Analytical estimations for σ_k, Ω_{PBH}, and Ω_{GW}^{PBH}

Bibliography

[1] D. del Corral, P. Gondolo, K. S. Kumar, and J. Marto, "Revisiting primordial black holes formation from preheating instabilities: the case of Starobinsky inflation," *JCAP* **02** (2025) 009, arXiv:2311.02754 [astro-ph.CO].

[2] D. del Corral, "Self-resonance during preheating: The case of α-attractor models," *Annals Phys.* **470** (2024) 169824, arXiv:2406.04017 [hep-th].

[3] D. del Corral, P. Gondolo, K. S. Kumar, and J. a. Marto, "Primordial black holes through preheating instabilities in α-attractor models," arXiv:2505.17790 [astro-ph.CO].

[4] D. del Corral, P. Gondolo, K. S. Kumar, and J. Marto, "Scalar-Induced Gravitational Waves from self-resonant preheating in α-attractor models," arXiv:2504.17602 [astro-ph.CO].

[5] D. del Corral, K. S. Kumar, and J. Marto, "Gravitational waves from primordial black hole dominance: The effect of inflaton decay rate," arXiv:2504.05875 [astro-ph.CO].

[6] D. del Corral and J. Olmedo, "Breaking of isospectrality of quasinormal modes in nonrotating loop quantum gravity black holes," *Phys. Rev. D* **105** no. 6, (2022) 064053, arXiv:2201.09584 [gr-qc].

[7] A. Einstein, "The Field Equations of Gravitation," *Sitzungsber. Preuss. Akad. Wiss. Berlin (Math. Phys.)* **1915** (1915) 844–847.

[8] A. Friedman, "On the Curvature of space," *Z. Phys.* **10** (1922) 377–386.

[9] A. Friedmann, "On the Possibility of a world with constant negative curvature of space," *Z. Phys.* **21** (1924) 326–332.

[10] G. Lemaitre, "A Homogeneous Universe of Constant Mass and Growing Radius Accounting for the Radial Velocity of Extragalactic Nebulae," *Annales Soc. Sci. Bruxelles A* **47** (1927) 49–59.

[11] H. P. Robertson, "Kinematics and World-Structure," *Astrophys. J.* **82** (1935) 284–301.

[12] H. P. Robertson, "Kinematics and World-Structure. 2," *Astrophys. J.* **83** (1935) 187–201.

[13] H. P. Robertson, "Kinematics and World-Structure. 3," *Astrophys. J.* **83** (1936) 257–271.

[14] A. G. Walker, "On Milne's Theory of World-Structure," *Proc. Lond. Math. Soc. s* **2-42** no. 1, (1937) 90–127.

[15] G. Gamow, "Expanding universe and the origin of elements," *Phys. Rev.* **70** (1946) 572–573.

[16] A. A. Penzias and R. W. Wilson, "A Measurement of excess antenna temperature at 4080-Mc/s," *Astrophys. J.* **142** (1965) 419–421.

[17] E. R. Harrison, "Fluctuations at the threshold of classical cosmology," *Phys. Rev. D* **1** (1970) 2726–2730.

[18] Y. B. Zeldovich, "A Hypothesis, unifying the structure and the entropy of the universe," *Mon. Not. Roy. Astron. Soc.* **160** (1972) 1P–3P.

[19] W. Rindler, "Visual Horizons in World Models," *Mon. Not. Roy. Astron. Soc.* **116** no. 6, (1956) 662–677.

[20] R. H. Dicke and P. J. E. Peebles, *The big bang cosmology: Enigmas and nostrums*. Univ. Pr., Cambridge, UK, 1979.

[21] G. 't Hooft, "Magnetic Monopoles in Unified Gauge Theories," *Nucl. Phys. B* **79** (1974) 276–284.

[22] K. S. Stelle, "Renormalization of Higher Derivative Quantum Gravity," *Phys. Rev. D* **16** (1977) 953–969.

[23] K. S. Stelle, "Classical Gravity with Higher Derivatives," *Gen. Rel. Grav.* **9** (1978) 353–371.

[24] A. A. Starobinsky, "A New Type of Isotropic Cosmological Models Without Singularity," *Phys. Lett. B* **91** (1980) 99–102.

[25] A. A. Starobinsky, "NONSINGULAR MODEL OF THE UNIVERSE WITH THE QUANTUM GRAVITATIONAL DE SITTER STAGE AND ITS OBSERVATIONAL CONSEQUENCES," in *Second Seminar on Quantum Gravity*. 1981.

[26] K. S. Kumar, "Inflationary cosmology: from effective field theory to quantum gravity." Institute of Cosmology and Gravitation, University of Portsmouth, UK, 2025. Lecture notes.

[27] L. Buoninfante, "Strict renormalizability as a paradigm for fundamental physics," `arXiv:2504.05900 [hep-th]`.

[28] L. Buoninfante *et al.*, "Visions in Quantum Gravity," `arXiv:2412.08696 [hep-th]`.

[29] **Planck** Collaboration, P. A. R. Ade *et al.*, "Planck 2015 results. XX. Constraints on inflation," *Astron. Astrophys.* **594** (2016) A20, `arXiv:1502.02114 [astro-ph.CO]`.

[30] **Planck** Collaboration, Y. Akrami *et al.*, "Planck 2018 results. X. Constraints on inflation," *Astron. Astrophys.* **641** (2020) A10, arXiv:1807.06211 [astro-ph.CO].

[31] **Planck** Collaboration, N. Aghanim *et al.*, "Planck 2018 results. VI. Cosmological parameters," *Astron. Astrophys.* **641** (2020) A6, arXiv:1807.06209 [astro-ph.CO]. [Erratum: Astron.Astrophys. 652, C4 (2021)].

[32] A. H. Guth, "The Inflationary Universe: A Possible Solution to the Horizon and Flatness Problems," *Phys. Rev. D* **23** (1981) 347–356.

[33] A. D. Linde, "Scalar Field Fluctuations in Expanding Universe and the New Inflationary Universe Scenario," *Phys. Lett. B* **116** (1982) 335–339.

[34] A. D. Linde, "Chaotic Inflation," *Phys. Lett. B* **129** (1983) 177–181.

[35] V. F. Mukhanov, H. A. Feldman, and R. H. Brandenberger, "Theory of cosmological perturbations. Part 1. Classical perturbations. Part 2. Quantum theory of perturbations. Part 3. Extensions," *Phys. Rept.* **215** (1992) 203–333.

[36] V. F. Mukhanov and G. V. Chibisov, "Quantum Fluctuations and a Nonsingular Universe," *JETP Lett.* **33** (1981) 532–535.

[37] S. W. Hawking, "The Development of Irregularities in a Single Bubble Inflationary Universe," *Phys. Lett. B* **115** (1982) 295.

[38] A. D. Dolgov and D. P. Kirilova, "ON PARTICLE CREATION BY A TIME DEPENDENT SCALAR FIELD," *Sov. J. Nucl. Phys.* **51** (1990) 172–177.

[39] J. H. Traschen and R. H. Brandenberger, "Particle Production During Out-of-equilibrium Phase Transitions," *Phys. Rev. D* **42** (1990) 2491–2504.

[40] Y. Shtanov, J. H. Traschen, and R. H. Brandenberger, "Universe reheating after inflation," *Phys. Rev. D* **51** (1995) 5438–5455, arXiv:hep-ph/9407247.

[41] L. Kofman, A. D. Linde, and A. A. Starobinsky, "Reheating after inflation," *Phys. Rev. Lett.* **73** (1994) 3195–3198, arXiv:hep-th/9405187.

[42] L. Kofman, A. D. Linde, and A. A. Starobinsky, "Towards the theory of reheating after inflation," *Phys. Rev. D* **56** (1997) 3258–3295, arXiv:hep-ph/9704452.

[43] K. Jedamzik, M. Lemoine, and J. Martin, "Collapse of Small-Scale Density Perturbations during Preheating in Single Field Inflation," *JCAP* **09** (2010) 034, arXiv:1002.3039 [astro-ph.CO].

[44] K. Jedamzik, M. Lemoine, and J. Martin, "Generation of gravitational waves during early structure formation between cosmic inflation and reheating," *JCAP* **04** (2010) 021, arXiv:1002.3278 [astro-ph.CO].

[45] J. Martin, T. Papanikolaou, and V. Vennin, "Primordial black holes from the preheating instability in single-field inflation," *Journal of Cosmology and Astroparticle Physics* **2020** (01, 2020) 024–024.

[46] J. Martin, T. Papanikolaou, L. Pinol, and V. Vennin, "Metric preheating and radiative decay in single-field inflation," *JCAP* **05** (2020) 003, arXiv:2002.01820 [astro-ph.CO].

[47] M. C. Guzzetti, N. Bartolo, M. Liguori, and S. Matarrese, "Gravitational waves from inflation," *Riv. Nuovo Cim.* **39** no. 9, (2016) 399–495, arXiv:1605.01615 [astro-ph.CO].

[48] D. Baumann, P. J. Steinhardt, K. Takahashi, and K. Ichiki, "Gravitational Wave Spectrum Induced by Primordial Scalar Perturbations," *Phys. Rev. D* **76** (2007) 084019, arXiv:hep-th/0703290.

[49] M. Maggiore, *Gravitational Waves. Vol. 1: Theory and Experiments*. Oxford University Press, 2007.

[50] H. Assadullahi and D. Wands, "Gravitational waves from an early matter era," *Phys. Rev. D* **79** (2009) 083511, arXiv:0901.0989 [astro-ph.CO].

[51] G. Franciolini, K. Kritos, E. Berti, and J. Silk, "Primordial black hole mergers from three-body interactions," *Phys. Rev. D* **106** no. 8, (2022) 083529, arXiv:2205.15340 [astro-ph.CO].

[52] P. Meszaros, "The behaviour of point masses in an expanding cosmological substratum," *Astron. Astrophys.* **37** (1974) 225–228.

[53] K. M. Belotsky, V. I. Dokuchaev, Y. N. Eroshenko, E. A. Esipova, M. Y. Khlopov, L. A. Khromykh, A. A. Kirillov, V. V. Nikulin, S. G. Rubin, and I. V. Svadkovsky, "Clusters of primordial black holes," *Eur. Phys. J. C* **79** no. 3, (2019) 246, arXiv:1807.06590 [astro-ph.CO].

[54] J. R. Chisholm, "Clustering of primordial black holes: basic results," *Phys. Rev. D* **73** (2006) 083504, arXiv:astro-ph/0509141.

[55] J. R. Chisholm, "Clustering of Primordial Black Holes. II. Evolution of Bound Systems," *Phys. Rev. D* **84** (2011) 124031, arXiv:1110.4402 [astro-ph.CO].

[56] V. De Luca, G. Franciolini, and A. Riotto, "Heavy Primordial Black Holes from Strongly Clustered Light Black Holes," *Phys. Rev. Lett.* **130** no. 17, (2023) 171401, arXiv:2210.14171 [astro-ph.CO].

[57] V. De Luca, G. Franciolini, P. Pani, and A. Riotto, "Constraints on Primordial Black Holes: the Importance of Accretion," *Phys. Rev. D* **102** no. 4, (2020) 043505, arXiv:2003.12589 [astro-ph.CO].

[58] V. De Luca, G. Franciolini, A. Kehagias, P. Pani, and A. Riotto, "Primordial black holes in matter-dominated eras: The role of accretion," *Phys. Lett. B* **832** (2022) 137265, arXiv:2112.02534 [astro-ph.CO].

[59] G. Domènech and J. Tränkle, "From formation to evaporation: Induced gravitational wave probes of the primordial black hole reheating scenario," arXiv:2409.12125 [gr-qc].

[60] G. Domènech, "Cosmological gravitational waves from isocurvature fluctuations," *AAPPS Bull.* **34** no. 1, (2024) 4, arXiv:2311.02065 [gr-qc].

[61] G. Domènech, C. Lin, and M. Sasaki, "Gravitational wave constraints on the primordial black hole dominated early universe," *JCAP* **04** (2021) 062, arXiv:2012.08151 [gr-qc]. [Erratum: JCAP 11, E01 (2021)].

[62] T. Papanikolaou, V. Vennin, and D. Langlois, "Gravitational waves from a universe filled with primordial black holes," *JCAP* **03** (2021) 053, arXiv:2010.11573 [astro-ph.CO].

[63] T. Papanikolaou, "Gravitational waves induced from primordial black hole fluctuations: the effect of an extended mass function," *JCAP* **10** (2022) 089, arXiv:2207.11041 [astro-ph.CO].

[64] B. J. Carr, K. Kohri, Y. Sendouda, and J. Yokoyama, "New cosmological constraints on primordial black holes," *Phys. Rev. D* **81** (2010) 104019, arXiv:0912.5297 [astro-ph.CO].

[65] A. S. Josan, A. M. Green, and K. A. Malik, "Generalised constraints on the curvature perturbation from primordial black holes," *Phys. Rev. D* **79** (2009) 103520, arXiv:0903.3184 [astro-ph.CO].

[66] T. L. Smith, E. Pierpaoli, and M. Kamionkowski, "A new cosmic microwave background constraint to primordial gravitational waves," *Phys. Rev. Lett.* **97** (2006) 021301, arXiv:astro-ph/0603144.

[67] M. Maggiore, "Gravitational wave experiments and early universe cosmology," *Phys. Rept.* **331** (2000) 283–367, arXiv:gr-qc/9909001.

[68] S. Schaffer, "John michell and black holes," *Journal for the History of Astronomy* **10** no. 1, (1979) 42–43, https://doi.org/10.1177/002182867901000104. https://doi.org/10.1177/002182867901000104.

[69] P. de Laplace, *Exposition Du Système Du Monde*. R. Phillips, 1796. https://books.google.es/books?id=6ddnzQEACAAJ.

[70] K. Schwarzschild, "On the gravitational field of a mass point according to Einstein's theory," *Sitzungsber. Preuss. Akad. Wiss. Berlin (Math. Phys.)* **1916** (1916) 189–196, arXiv:physics/9905030.

[71] G. D. Birkhoff and R. E. Langer, *Relativity and modern physics*. Harvard University Press, 1923.

[72] J. R. Oppenheimer and H. Snyder, "On Continued gravitational contraction," *Phys. Rev.* **56** (1939) 455–459.

[73] R. P. Kerr, "Gravitational field of a spinning mass as an example of algebraically special metrics," *Phys. Rev. Lett.* **11** (1963) 237–238.

[74] R. Penrose, "Gravitational collapse and space-time singularities," *Phys. Rev. Lett.* **14** (1965) 57–59.

[75] S. W. Hawking and R. Penrose, "The Singularities of gravitational collapse and cosmology," *Proc. Roy. Soc. Lond. A* **314** (1970) 529–548.

[76] S. Hawking, "Gravitationally collapsed objects of very low mass," *Mon. Not. Roy. Astron. Soc.* **152** (1971) 75.

[77] Y. B. Zel'dovich and I. D. Novikov, "The Hypothesis of Cores Retarded during Expansion and the Hot Cosmological Model," *Soviet Astron. AJ (Engl. Transl.),* **10** (1967) 602.

[78] B. J. Carr and S. W. Hawking, "Black holes in the early Universe," *Mon. Not. Roy. Astron. Soc.* **168** (1974) 399–415.

[79] B. J. Carr, "The Primordial black hole mass spectrum," *Astrophys. J.* **201** (1975) 1–19.

[80] E. de Jong, J. C. Aurrekoetxea, E. A. Lim, and T. França, "Spinning primordial black holes formed during a matter-dominated era," *JCAP* **10** (2023) 067, arXiv:2306.11810 [astro-ph.CO].

[81] P. Auclair and V. Vennin, "Primordial black holes from metric preheating: mass fraction in the excursion-set approach," *JCAP* **02** (2021) 038, arXiv:2011.05633 [astro-ph.CO].

[82] W. H. Press and P. Schechter, "Formation of galaxies and clusters of galaxies by selfsimilar gravitational condensation," *Astrophys. J.* **187** (1974) 425–438.

[83] S. W. Hawking, "Black hole explosions," *Nature* **248** (1974) 30–31.

[84] Y. B. Zel'dovich, "Generation of waves by a rotating body," *JETP Lett.* **14** (1971) 180. [Pisma Zh. Eksp. Teor. Fiz. 14, 270 (1971)].

[85] A. A. Starobinsky, "Amplification of waves reflected from a rotating "black hole".," *Sov. Phys. JETP* **37** no. 1, (1973) 28–32.

[86] D. N. Page and S. W. Hawking, "Gamma rays from primordial black holes," *Astrophys. J.* **206** (1976) 1–7.

[87] I. D. Novikov, A. G. Polnarev, A. A. Starobinskii, and I. B. Zeldovich, "Primordial black holes," *Astron. Astrophys.* **80** no. 1, (Nov., 1979) 104–109.

[88] B. V. Vainer and P. D. Naselskii, "Cosmological implications of the process of primordial black hole evaporation," *Sov. Astron.* **22** (Apr., 1978) 138–140.

[89] S. Miyama and K. Sato, "The Upper Bound of the Number Density of Primordial Black Holes From the Big Bang Nucleosynthesis," *Prog. Theor. Phys.* **59** (1978) 1012.

[90] S. W. Hawking, "Breakdown of Predictability in Gravitational Collapse," *Phys. Rev. D* **14** (1976) 2460–2473.

[91] B. J. Carr, J. H. Gilbert, and J. E. Lidsey, "Black hole relics and inflation: Limits on blue perturbation spectra," *Phys. Rev. D* **50** (1994) 4853–4867, arXiv:astro-ph/9405027.

[92] M. A. Markov and P. C. West, eds., *QUANTUM GRAVITY. PROCEEDINGS, 2ND SEMINAR, MOSCOW, USSR, OCTOBER 13-15, 1981.* 1984.

[93] J. H. MacGibbon, "Can Planck-mass relics of evaporating black holes close the universe?," *Nature* **329** (1987) 308–309.

[94] S. R. Coleman, J. Preskill, and F. Wilczek, "Quantum hair on black holes," *Nucl. Phys. B* **378** (1992) 175–246, arXiv:hep-th/9201059.

[95] K. S. Kumar and J. Marto, "Towards a Unitary Formulation of Quantum Field Theory in Curved Space-Time: The Case of the Schwarzschild Black Hole," *PTEP* **2024** no. 12, (2024) 123E01, arXiv:2307.10345 [hep-th].

[96] K. S. Kumar and J. Marto, "Hawking radiation with pure states," *Gen. Rel. Grav.* **56** no. 12, (2024) 143, arXiv:2407.18652 [gr-qc].

[97] H. Kodama, M. Sasaki, and K. Sato, "Abundance of Primordial Holes Produced by Cosmological First Order Phase Transition," *Prog. Theor. Phys.* **68** (1982) 1979.

[98] B. J. Carr and J. E. Lidsey, "Primordial black holes and generalized constraints on chaotic inflation," *Phys. Rev. D* **48** (1993) 543–553.

[99] P. Ivanov, P. Naselsky, and I. Novikov, "Inflation and primordial black holes as dark matter," *Phys. Rev. D* **50** (1994) 7173–7178.

[100] I. Stamou, "Mechanisms for Producing Primordial Black Holes from Inflationary Models beyond Fine-Tuning," *Universe* **10** no. 6, (2024) 241, arXiv:2404.14321 [astro-ph.CO].

[101] B. J. Carr and J. Silk, "Can graininess in the early universe make galaxies?," *Astrophys. J.* **268** (May, 1983) 1–16.

[102] K. Freese, R. Price, and D. N. Schramm, "Formation of population III stars and galaxies with primordial planetary-mass black holes," *Astrophys. J.* **275** (Dec., 1983) 405–412.

[103] B. J. Carr and M. J. Rees, "How large were the first pregalactic objects?," *Mon. Not. Roy. Astron. Soc.* **206** (1984) 2.315–325.

[104] P. Dayal, "Exploring a primordial solution for early black holes detected with JWST," *Astron. Astrophys.* **690** (2024) A182, arXiv:2407.07162 [astro-ph.GA].

[105] R. Maiolino *et al.*, "A small and vigorous black hole in the early Universe," *Nature* **627** no. 8002, (2024) 59–63, arXiv:2305.12492 [astro-ph.GA]. [Erratum: Nature 630, E2 (2024)].

[106] H.-L. Huang, Y.-T. Wang, and Y.-S. Piao, "Supermassive primordial black holes for the GHZ9 and UHZ1 observed by the JWST," arXiv:2410.05891 [astro-ph.GA].

[107] A. Bogdan *et al.*, "Evidence for heavy-seed origin of early supermassive black holes from a z $\approx$ 10 X-ray quasar," *Nature Astron.* **8** no. 1, (2024) 126–133, arXiv:2305.15458 [astro-ph.GA].

[108] R. Bean and J. Magueijo, "Could supermassive black holes be quintessential primordial black holes?," *Phys. Rev. D* **66** (2002) 063505, arXiv:astro-ph/0204486.

[109] D. Spolyar, K. Freese, and P. Gondolo, "Dark matter and the first stars: a new phase of stellar evolution," *Phys. Rev. Lett.* **100** (2008) 051101, arXiv:0705.0521 [astro-ph].

[110] K. Freese, P. Bodenheimer, D. Spolyar, and P. Gondolo, "Stellar Structure of Dark Stars: a first phase of Stellar Evolution due to Dark Matter Annihilation," *Astrophys. J. Lett.* **685** (2008) L101–L112, arXiv:0806.0617 [astro-ph].

[111] K. Freese, D. Spolyar, A. Aguirre, P. Bodenheimer, P. Gondolo, J. A. Sellwood, and N. Yoshida, "Dark Stars: Dark Matter in the First Stars leads to a New Phase of Stellar Evolution," *IAU Symp.* **255** (2008) 56–60, arXiv:0808.0472 [astro-ph].

[112] M. W. Choptuik, "Universality and scaling in gravitational collapse of a massless scalar field," *Phys. Rev. Lett.* **70** (1993) 9–12.

[113] J. C. Niemeyer and K. Jedamzik, "Near-critical gravitational collapse and the initial mass function of primordial black holes," *Phys. Rev. Lett.* **80** (1998) 5481–5484, arXiv:astro-ph/9709072.

[114] J. C. Niemeyer and K. Jedamzik, "Dynamics of primordial black hole formation," *Phys. Rev. D* **59** (1999) 124013, arXiv:astro-ph/9901292.

[115] I. Musco, J. C. Miller, and L. Rezzolla, "Computations of primordial black hole formation," *Class. Quant. Grav.* **22** (2005) 1405–1424, arXiv:gr-qc/0412063.

[116] I. Musco, J. C. Miller, and A. G. Polnarev, "Primordial black hole formation in the radiative era: Investigation of the critical nature of the collapse," *Class. Quant. Grav.* **26** (2009) 235001, arXiv:0811.1452 [gr-qc].

[117] I. Musco and J. C. Miller, "Primordial black hole formation in the early universe: critical behaviour and self-similarity," *Class. Quant. Grav.* **30** (2013) 145009, arXiv:1201.2379 [gr-qc].

[118] T. Harada, C.-M. Yoo, and K. Kohri, "Threshold of primordial black hole formation," *Phys. Rev. D* **88** no. 8, (2013) 084051, arXiv:1309.4201 [astro-ph.CO]. [Erratum: Phys.Rev.D 89, 029903 (2014)].

[119] T. Harada, C.-M. Yoo, K. Kohri, K.-i. Nakao, and S. Jhingan, "Primordial black hole formation in the matter-dominated phase of the Universe," *Astrophys. J.* **833** no. 1, (2016) 61, arXiv:1609.01588 [astro-ph.CO].

[120] T. Harada, C.-M. Yoo, K. Kohri, and K.-I. Nakao, "Spins of primordial black holes formed in the matter-dominated phase of the Universe," *Phys. Rev. D* **96** no. 8, (2017) 083517, arXiv:1707.03595 [gr-qc]. [Erratum: Phys.Rev.D 99, 069904 (2019)].

[121] M. Y. Khlopov and A. G. Polnarev, "PRIMORDIAL BLACK HOLES AS A COSMOLOGICAL TEST OF GRAND UNIFICATION," *Phys. Lett. B* **97** (1980) 383–387.

[122] M. Y. Khlopov and A. G. Polnarev, "SUPERHEAVY PARTICLES IN COSMOLOGY AND EVOLUTION OF INHOMOGENEITIES IN THE EARLY UNIVERSE," in *Nuffield Workshop on the Very Early Universe*. 1982.

[123] A. G. Polnarev and M. Y. Khlopov, "COSMOLOGY, PRIMORDIAL BLACK HOLES, AND SUPERMASSIVE PARTICLES," *Sov. Phys. Usp.* **28** (1985) 213–232.

[124] M. Y. Khlopov, "Primordial Black Holes," *Res. Astron. Astrophys.* **10** (2010) 495–528, arXiv:0801.0116 [astro-ph].

[125] A. G. Polnarev and M. Y. Khlopov, "Primordial Black Holes and the ERA of Superheavy Particle Dominance in the Early Universe," *Soviet Astronomy* **25** (Aug., 1981) 406.

[126] B. Carr, K. Kohri, Y. Sendouda, and J. Yokoyama, "Constraints on primordial black holes," *Rept. Prog. Phys.* **84** no. 11, (2021) 116902, arXiv:2002.12778 [astro-ph.CO].

[127] P. Gondolo, P. Sandick, and B. Shams Es Haghi, "Effects of primordial black holes on dark matter models," *Phys. Rev. D* **102** no. 9, (2020) 095018, arXiv:2009.02424 [hep-ph].

[128] T. D. Gomez-Aguilar, L. E. Padilla, E. Erfani, and J. C. Hidalgo, "Constraints on primordial black holes for nonstandard cosmologies," *JCAP* **11** (2024) 005, arXiv:2308.04642 [astro-ph.CO].

[129] M. Ricotti, J. P. Ostriker, and K. J. Mack, "Effect of Primordial Black Holes on the Cosmic Microwave Background and Cosmological Parameter Estimates," *Astrophys. J.* **680** (2008) 829, arXiv:0709.0524 [astro-ph].

[130] I. B. Zeldovich, A. A. Starobinskii, M. I. Khlopov, and V. M. Chechetkin, "Primordial black holes and the deuterium problem," *Soviet Astronomy Letters* **3** (June, 1977) 110–112.

[131] S. K. Acharya and R. Khatri, "CMB and BBN constraints on evaporating primordial black holes revisited," *JCAP* **06** (2020) 018, arXiv:2002.00898 [astro-ph.CO].

[132] M. Lemoine, "Moduli constraints on primordial black holes," *Phys. Lett. B* **481** (2000) 333–338, arXiv:hep-ph/0001238.

[133] O. Heaviside, "A gravitational and electromagnetic analogy," *The Electrician* **31** (1893) 281–282.

[134] H. Poincaré, "Sur la Dynamique de l'Electron," *Compte Rendus* **140** (1905) 1504–1508.

[135] J. L. Cervantes-Cota, S. Galindo-Uribarri, and G.-F. Smoot, "A Brief History of Gravitational Waves," *Universe* **2** no. 3, (2016) 22, arXiv:1609.09400 [physics.hist-ph].

[136] T. Rothman, "The Secret History of Gravitational Waves," *American Scientist* **106** (2018) 96–104.

[137] A. Einstein, "On the electrodynamics of moving bodies," *Annalen Phys.* **17** (1905) 891–921.

[138] A. Einstein, "Über die vom Relativitätsprinzip geforderte Trägheit der Energie," *Annalen Phys.* **23** no. 7, (1907) 371–384.

[139] A. Einstein, "Approximative Integration of the Field Equations of Gravitation," *Sitzungsber. Preuss. Akad. Wiss. Berlin (Math. Phys.)* **1916** (1916) 688–696.

[140] A. Einstein, "Über Gravitationswellen," *Sitzungsber. Preuss. Akad. Wiss. Berlin (Math. Phys.)* **1918** (1918) 154–167.

[141] A. Einstein and N. Rosen, "Two-Body Problem in General Relativity Theory," *Phys. Rev.* **49** (1936) 404–405.

[142] F. A. E. Pirani, "On the Physical significance of the Riemann tensor," *Acta Phys. Polon.* **15** (1956) 389–405.

[143] J. Weber, "Detection and Generation of Gravitational Waves," *Phys. Rev.* **117** (1960) 306–313.

[144] J. H. Taylor, L. A. Fowler, and P. M. McCulloch, "Measurements of general relativistic effects in the binary pulsar PSR 1913+16," *Nature* **277** (1979) 437–440.

[145] A. A. Starobinsky, "Spectrum of relict gravitational radiation and the early state of the universe," *JETP Lett.* **30** (1979) 682–685.

[146] **LIGO Scientific, Virgo** Collaboration, B. P. Abbott *et al.*, "Observation of Gravitational Waves from a Binary Black Hole Merger," *Phys. Rev. Lett.* **116** no. 6, (2016) 061102, arXiv:1602.03837 [gr-qc].

[147] **LIGO Scientific, Virgo** Collaboration, B. P. Abbott *et al.*, "GW170814: A Three-Detector Observation of Gravitational Waves from a Binary Black Hole Coalescence," *Phys. Rev. Lett.* **119** no. 14, (2017) 141101, arXiv:1709.09660 [gr-qc].

[148] K. Kuroda, W.-T. Ni, and W.-P. Pan, "Gravitational waves: Classification, Methods of detection, Sensitivities, and Sources," *Int. J. Mod. Phys. D* **24** no. 14, (2015) 1530031, arXiv:1511.00231 [gr-qc].

[149] N. Aggarwal *et al.*, "Challenges and opportunities of gravitational-wave searches at MHz to GHz frequencies," *Living Rev. Rel.* **24** no. 1, (2021) 4, arXiv:2011.12414 [gr-qc].

[150] P. Amaro-Seoane *et al.*, "Laser Interferometer Space Antenna," *arXiv preprint* (2017) , arXiv:1702.00786 [astro-ph.IM].

[151] W.-T. Ni, "ASTROD-GW: Overview and Progress," *Int. J. Mod. Phys. D* **22** (2013) 1341004, arXiv:1212.2816 [astro-ph.IM].

[152] J. Crowder and N. J. Cornish, "Beyond LISA: Exploring future gravitational wave missions," *Phys. Rev. D* **72** (2005) 083005, arXiv:gr-qc/0506015.

[153] S. Kawamura *et al.*, "The Japanese space gravitational wave antenna DECIGO," *Class. Quant. Grav.* **23** (2006) S125–S132.

[154] M. Maggiore *et al.*, "Science Case for the Einstein Telescope," *JCAP* **03** (2020) 050, arXiv:1912.02622 [astro-ph.CO].

[155] D. Reitze *et al.*, "Cosmic Explorer: The U.S. Contribution to Gravitational-Wave Astronomy beyond LIGO," *Bull. Am. Astron. Soc.* **51** (2019) 35, arXiv:1907.04833 [astro-ph.IM].

[156] D. Hooper, G. Krnjaic, J. March-Russell, S. D. McDermott, and R. Petrossian-Byrne, "Hot Gravitons and Gravitational Waves From Kerr Black Holes in the Early Universe," arXiv:2004.00618 [astro-ph.CO].

[157] A. S. Koshelev, K. S. Kumar, and A. A. Starobinsky, "Analytic infinite derivative gravity, R^2-like inflation, quantum gravity and CMB," *Int. J. Mod. Phys. D* **29** no. 14, (2020) 2043018, arXiv:2005.09550 [hep-th].

[158] A. Kehagias, A. Moradinezhad Dizgah, and A. Riotto, "Remarks on the Starobinsky model of inflation and its descendants," *Phys. Rev. D* **89** no. 4, (2014) 043527, arXiv:1312.1155 [hep-th].

[159] I. Musco, J. C. Miller, and L. Rezzolla, "Computations of primordial black-hole formation," *Classical and Quantum Gravity* **22** no. 7, (Apr., 2005) 1405–1424, arXiv:gr-qc/0412063 [gr-qc].

[160] G. Ballesteros and M. Taoso, "Primordial black hole dark matter from single field inflation," *Phys. Rev. D* **97** no. 2, (2018) 023501, arXiv:1709.05565 [hep-ph].

[161] S. Habib, A. Heinen, K. Heitmann, and G. Jungman, "Inflationary perturbations and precision cosmology," *Phys. Rev. D* **71** (2005) 043518, arXiv:astro-ph/0501130.

[162] I. Wolfson, *Numerical Analysis of the Primordial Power Spectrum for (Small Field) Inflationary Potentials*. PhD thesis, Ben Gurion U. of Negev, 2021. arXiv:2103.16594 [astro-ph.CO].

[163] S. M. C. V. Goncalves, "Black hole formation from massive scalar field collapse in the Einstein-de Sitter universe," *Phys. Rev. D* **62** (2000) 124006, arXiv:gr-qc/0008039.

[164] D. Maison, "Nonuniversality of critical behavior in spherically symmetric gravitational collapse," *Phys. Lett. B* **366** (1996) 82–84, arXiv:gr-qc/9504008.

[165] D. W. Neilsen and M. W. Choptuik, "Critical phenomena in perfect fluids," *Class. Quant. Grav.* **17** (2000) 761–782, arXiv:gr-qc/9812053.

[166] M. Snajdr, "Critical collapse of an ultrarelativistic fluid in the Gamma —> 1 limit," *Class. Quant. Grav.* **23** (2006) 3333–3352, arXiv:gr-qc/0508062.

[167] R. Kallosh and A. Linde, "Multi-field Conformal Cosmological Attractors," *JCAP* **12** (2013) 006, arXiv:1309.2015 [hep-th].

[168] R. Kallosh and A. Linde, "Universality Class in Conformal Inflation," *JCAP* **07** (2013) 002, arXiv:1306.5220 [hep-th].

[169] D. I. Kaiser and E. I. Sfakianakis, "Multifield Inflation after Planck: The Case for Nonminimal Couplings," *Phys. Rev. Lett.* **112** no. 1, (2014) 011302, arXiv:1304.0363 [astro-ph.CO].

[170] R. Kallosh and A. Linde, "Planck, LHC, and α-attractors," *Phys. Rev. D* **91** (2015) 083528, arXiv:1502.07733 [astro-ph.CO].

[171] O. Iarygina, E. I. Sfakianakis, D.-G. Wang, and A. Achucarro, "Universality and scaling in multi-field α-attractor preheating," *JCAP* **06** (2019) 027, arXiv:1810.02804 [astro-ph.CO].

[172] O. Iarygina, E. I. Sfakianakis, D.-G. Wang, and A. Achúcarro, "Multi-field inflation and preheating in asymmetric α-attractors," arXiv:2005.00528 [astro-ph.CO].

[173] T. Krajewski, K. Turzyński, and M. Wieczorek, "On preheating in α-attractor models of inflation," *Eur. Phys. J. C* **79** no. 8, (2019) 654, arXiv:1801.01786 [astro-ph.CO].

[174] K. D. Lozanov and M. A. Amin, "Self-resonance after inflation: oscillons, transients and radiation domination," *Phys. Rev. D* **97** no. 2, (2018) 023533, arXiv:1710.06851 [astro-ph.CO].

[175] E. I. Sfakianakis and J. van de Vis, "Preheating after Higgs Inflation: Self-Resonance and Gauge boson production," *Phys. Rev. D* **99** no. 8, (2019) 083519, arXiv:1810.01304 [hep-ph].

[176] G. Ballesteros, J. Iguaz Juan, P. D. Serpico, and M. Taoso, "Primordial black hole formation from self-resonant preheating?," arXiv:2406.09122 [astro-ph.CO].

[177] M. Shafi, E. J. Copeland, R. Mahbub, S. S. Mishra, and S. Basak, "Formation and decay of oscillons after inflation in the presence of an external coupling, Part-I: Lattice simulations," arXiv:2406.00108 [hep-ph].

[178] R. Mahbub and S. S. Mishra, "Oscillon formation from preheating in asymmetric inflationary potentials," *Phys. Rev. D* **108** no. 6, (2023) 063524, arXiv:2303.07503 [astro-ph.CO].

[179] Y. Sang and Q.-G. Huang, "Oscillons during Dirac-Born-Infeld preheating," *Phys. Lett. B* **823** (2021) 136781, arXiv:2012.14697 [hep-th].

[180] R. Zhang and S. Zheng, "Gravitational dark matter from minimal preheating," *JHEP* **02** (2024) 061, arXiv:2311.14273 [hep-ph].

[181] H. L. Child, J. T. Giblin, Jr, R. H. Ribeiro, and D. Seery, "Preheating with Non-Minimal Kinetic Terms," *Phys. Rev. Lett.* **111** (2013) 051301, arXiv:1305.0561 [astro-ph.CO].

[182] P. G. Drazin, *Nonlinear Systems*. Cambridge Texts in Applied Mathematics. Cambridge University Press, 1992.

[183] A. Nayfeh and D. Mook, *Nonlinear Oscillations*. Wiley Classics Library. Wiley, 2008. https://books.google.es/books?id=sj3ebg7jRaoC.

[184] T. Burton and M. Hamdan, "Analysis of non-linear autonomous conservative oscillators by a time transformation method," *Journal of Sound and Vibration* **87** no. 4, (1983) 543–554.

[185] Y. Cheung, S. Chen, and L. S.L., "A modified Lindstedt-Poincaré method for certain strongly non-linear oscillators," *International Journal of Non-Linear Mechanics* **26** no. 3, (1991) 367–378.

[186] I. Kovacic, L. Cveticanin, M. Zukovic, and Z. Rakaric, "Jacobi elliptic functions: A review of nonlinear oscillatory application problems," *Journal of Sound Vibration* **380** (Oct., 2016) 1–36.

[187] M. A. Amin, "Inflaton fragmentation: Emergence of pseudo-stable inflaton lumps (oscillons) after inflation," arXiv:1006.3075 [astro-ph.CO].

[188] M. P. Hertzberg, J. Karouby, W. G. Spitzer, J. C. Becerra, and L. Li, "Theory of self-resonance after inflation. I. Adiabatic and isocurvature Goldstone modes," *Phys. Rev. D* **90** (2014) 123528, arXiv:1408.1396 [hep-th].

[189] M. P. Hertzberg, J. Karouby, W. G. Spitzer, J. C. Becerra, and L. Li, "Theory of self-resonance after inflation. II. Quantum mechanics and particle-antiparticle asymmetry," *Phys. Rev. D* **90** (2014) 123529, arXiv:1408.1398 [hep-th].

[190] D. G. Figueroa, A. Florio, F. Torrenti, and W. Valkenburg, "The art of simulating the early Universe – Part I," *JCAP* **04** (2021) 035, arXiv:2006.15122 [astro-ph.CO].

[191] D. G. Figueroa, A. Florio, F. Torrenti, and W. Valkenburg, "CosmoLattice: A modern code for lattice simulations of scalar and gauge field dynamics in an expanding universe," *Comput. Phys. Commun.* **283** (2023) 108586, arXiv:2102.01031 [astro-ph.CO].

[192] E. J. Barroso, L. F. Demétrio, S. D. P. Vitenti, and X. Ye, "Primordial Black Hole Formation in a Dust Bouncing Model," arXiv:2405.00207 [astro-ph.CO].

[193] G. Domènech, "Scalar Induced Gravitational Waves Review," *Universe* **7** no. 11, (2021) 398, arXiv:2109.01398 [gr-qc].

[194] D. Baumann, P. J. Steinhardt, K. Takahashi, and K. Ichiki, "Gravitational Wave Spectrum Induced by Primordial Scalar Perturbations," *Phys. Rev. D* **76** (2007) 084019, arXiv:hep-th/0703290.

[195] K. N. Ananda, C. Clarkson, and D. Wands, "The Cosmological gravitational wave background from primordial density perturbations," *Phys. Rev. D* **75** (2007) 123518, arXiv:gr-qc/0612013.

[196] T. C. Gehrman, B. Shams Es Haghi, K. Sinha, and T. Xu, "Baryogenesis, primordial black holes and MHz–GHz gravitational waves," *JCAP* **02** (2023) 062, arXiv:2211.08431 [hep-ph].

[197] L. Iacconi, M. Fasiello, J. Väliviita, and D. Wands, "Novel CMB constraints on the α parameter in alpha-attractor models," *JCAP* **10** (2023) 015, arXiv:2306.00918 [astro-ph.CO].

[198] K. Alam, M. Bastero-Gil, K. Dutta, and H. V. Ragavendra, "Non-thermal moduli production during preheating in α-attractor inflation models," *JCAP* **11** (2023) 095, arXiv:2303.17383 [astro-ph.CO].

[199] P. Chen, Y. C. Ong, and D.-h. Yeom, "Black Hole Remnants and the Information Loss Paradox," *Phys. Rept.* **603** (2015) 1–45, arXiv:1412.8366 [gr-qc].

[200] Y. Aharonov, A. Casher, and S. Nussinov, "The Unitarity Puzzle and Planck Mass Stable Particles," *Phys. Lett. B* **191** (1987) 51.

[201] J. D. Barrow, E. J. Copeland, and A. R. Liddle, "The Cosmology of black hole relics," *Phys. Rev. D* **46** (1992) 645–657.

[202] D. N. Page and S. W. Hawking, "Gamma rays from primordial black holes.," *Astrophys. J.* **206** (May, 1976) 1–7.

[203] B. Carr and F. Kuhnel, "Primordial Black Holes as Dark Matter: Recent Developments," *Ann. Rev. Nucl. Part. Sci.* **70** (2020) 355–394, arXiv:2006.02838 [astro-ph.CO].

[204] B. Carr and F. Kuhnel, "Primordial black holes as dark matter candidates," *SciPost Phys. Lect. Notes* **48** (2022) 1, arXiv:2110.02821 [astro-ph.CO].

[205] T. Harada, C.-M. Yoo, and K. Kohri, "Threshold of primordial black hole formation," arXiv:1309.4201 [astro-ph.CO].

[206] J. C. Niemeyer, "Small-scale structure of fuzzy and axion-like dark matter," arXiv:1912.07064 [astro-ph.CO].

[207] R. R. R. Reis, "Domain of validity of the evolution of perturbations in Newtonian cosmology with pressure," *Phys. Rev. D* **67** (2003) 087301. [Erratum: Phys.Rev.D 68, 089901 (2003)].

[208] A. Escrivà, "PBH Formation from Spherically Symmetric Hydrodynamical Perturbations: A Review," *Universe* **8** no. 2, (2022) 66, arXiv:2111.12693 [gr-qc].

[209] J. Martin, T. Papanikolaou, L. Pinol, and V. Vennin, "Metric preheating and radiative decay in single-field inflation," arXiv:2002.01820 [astro-ph.CO].

[210] J. C. Niemeyer and K. Jedamzik, "Dynamics of primordial black hole formation," *Phys. Rev. D* **59** (1999) 124013, arXiv:astro-ph/9901292.

[211] A. M. Green and A. R. Liddle, "Critical collapse and the primordial black hole initial mass function," *Phys. Rev. D* **60** (1999) 063509, arXiv:astro-ph/9901268.

[212] A. D. Gow, C. T. Byrnes, P. S. Cole, and S. Young, "The power spectrum on small scales: Robust constraints and comparing PBH methodologies," *JCAP* **02** (2021) 002, arXiv:2008.03289 [astro-ph.CO].

[213] R. Kallosh, A. Linde, and D. Roest, "Superconformal Inflationary α-Attractors," *JHEP* **11** (2013) 198, arXiv:1311.0472 [hep-th].

[214] J. J. M. Carrasco, R. Kallosh, A. Linde, and D. Roest, "Hyperbolic geometry of cosmological attractors," *Phys. Rev. D* **92** no. 4, (2015) 041301, arXiv:1504.05557 [hep-th].

[215] M. Y. Khlopov and A. G. Polnarev, "Primordial black holes as a cosmological test of grand unification," *Physics Letters B* **97** no. 3-4, (Dec., 1980) 383–387.

[216] A. G. Polnarev and M. Y. Khlopov, "Primordial Black Holes and the ERA of Superheavy Particle Dominance in the Early Universe,".

[217] A. G. Polnarev and M. Y. Khlopov, "Dustlike Stages in the Early Universe and Constraints on the Primordial Black-Hole Spectrum,".

[218] A. Linde, "Inflationary Cosmology after Planck 2013," in *100e Ecole d'Ete de Physique: Post-Planck Cosmology*, pp. 231–316. 2015. arXiv:1402.0526 [hep-th].

[219] J. Ellis, D. V. Nanopoulos, and K. A. Olive, "Starobinsky-like Inflationary Models as Avatars of No-Scale Supergravity," *JCAP* **10** (2013) 009, arXiv:1307.3537 [hep-th].

[220] R. Kallosh and A. Linde, "Escher in the Sky," *Comptes Rendus Physique* **16** (2015) 914–927, arXiv:1503.06785 [hep-th].

[221] **BICEP, Keck** Collaboration, P. A. R. Ade *et al.*, "Improved Constraints on Primordial Gravitational Waves using Planck, WMAP, and BICEP/Keck Observations through the 2018 Observing Season," *Phys. Rev. Lett.* **127** no. 15, (2021) 151301, arXiv:2110.00483 [astro-ph.CO].

[222] M. Tristram *et al.*, "Improved limits on the tensor-to-scalar ratio using BICEP and Planck data," *Phys. Rev. D* **105** no. 8, (2022) 083524, arXiv:2112.07961 [astro-ph.CO].

[223] M. A. Page *et al.*, "Gravitational wave detectors with broadband high frequency sensitivity," *Commun. Phys.* **4** (2021) 27, arXiv:2007.08766 [physics.optics].

[224] V. Dandoy, T. Bertólez-Martínez, and F. Costa, "High Frequency Gravitational Wave Bounds from Galactic Neutron Stars," arXiv:2402.14092 [gr-qc].

[225] R. Anantua, R. Easther, and J. T. Giblin, "GUT-Scale Primordial Black Holes: Consequences and Constraints," *Phys. Rev. Lett.* **103** (2009) 111303, arXiv:0812.0825 [astro-ph].

[226] J. L. Zagorac, R. Easther, and N. Padmanabhan, "GUT-Scale Primordial Black Holes: Mergers and Gravitational Waves," *JCAP* **06** (2019) 052, arXiv:1903.05053 [astro-ph.CO].

[227] A. Addazi, A. S. Koshelev, S. Pi, and A. Tokareva, "Secondary Gravitational Waves in Non-local Starobinsky inflation," arXiv:2408.04004 [gr-qc].

[228] N. Aggarwal, G. P. Winstone, M. Teo, M. Baryakhtar, S. L. Larson, V. Kalogera, and A. A. Geraci, "Searching for New Physics with a Levitated-Sensor-Based Gravitational-Wave Detector," *Phys. Rev. Lett.* **128** no. 11, (2022) 111101, arXiv:2010.13157 [gr-qc].

[229] M. Goryachev and M. E. Tobar, "Gravitational Wave Detection with High Frequency Phonon Trapping Acoustic Cavities," *Phys. Rev. D* **90** no. 10, (2014) 102005, arXiv:1410.2334 [gr-qc]. [Erratum: Phys.Rev.D 108, 129901 (2023)].

[230] M. Goryachev, W. M. Campbell, I. S. Heng, S. Galliou, E. N. Ivanov, and M. E. Tobar, "Rare Events Detected with a Bulk Acoustic Wave High Frequency Gravitational Wave Antenna," *Phys. Rev. Lett.* **127** no. 7, (2021) 071102, arXiv:2102.05859 [gr-qc].

[231] J. Mizuno, *Comparison of optical configurations for laser-interferometric gravitational-wave detectors*. PhD thesis, Hannover U., 1995.

[232] **Holometer Collaboration** Collaboration, A. S. Chou, R. Gustafson, C. Hogan, B. Kamai, O. Kwon, R. Lanza, S. L. Larson, L. McCuller, S. S. Meyer, J. Richardson, C. Stoughton, R. Tomlin, and R. Weiss, "Mhz gravitational wave constraints with decameter michelson interferometers," *Phys. Rev. D* **95** (Mar, 2017) 063002. https://link.aps.org/doi/10.1103/PhysRevD.95.063002.

[233] E. Armengaud *et al.*, "Conceptual Design of the International Axion Observatory (IAXO)," *JINST* **9** (2014) T05002, arXiv:1401.3233 [physics.ins-det].

[234] A. Ringwald, J. Schütte-Engel, and C. Tamarit, "Gravitational Waves as a Big Bang Thermometer," *JCAP* **03** (2021) 054, arXiv:2011.04731 [hep-ph].

[235] V. Domcke and C. Garcia-Cely, "Potential of radio telescopes as high-frequency gravitational wave detectors," *Phys. Rev. Lett.* **126** no. 2, (2021) 021104, arXiv:2006.01161 [astro-ph.CO].

[236] A. Lella, F. Calore, P. Carenza, and A. Mirizzi, "Constraining gravitational-wave backgrounds from conversions into photons in the Galactic magnetic field," *Phys. Rev. D* **110** no. 8, (2024) 083042, arXiv:2406.17853 [hep-ph].

[237] G. Galloni, N. Bartolo, S. Matarrese, M. Migliaccio, A. Ricciardone, and N. Vittorio, "Updated constraints on amplitude and tilt of the tensor primordial spectrum," *JCAP* **04** (2023) 062, arXiv:2208.00188 [astro-ph.CO].

[238] T. Papanikolaou, X.-C. He, X.-H. Ma, Y.-F. Cai, E. N. Saridakis, and M. Sasaki, "New probe of non-Gaussianities with primordial black hole induced gravitational waves," *Phys. Lett. B* **857** (2024) 138997, arXiv:2403.00660 [astro-ph.CO].

[239] X.-C. He, Y.-F. Cai, X.-H. Ma, T. Papanikolaou, E. N. Saridakis, and M. Sasaki, "Gravitational waves from primordial black hole isocurvature: the effect of non-Gaussianities," *JCAP* **12** (2024) 039, arXiv:2409.11333 [astro-ph.CO].

[240] L. Frosina and A. Urbano, "Inflationary interpretation of the nHz gravitational-wave background," *Phys. Rev. D* **108** no. 10, (2023) 103544, arXiv:2308.06915 [astro-ph.CO].

[241] D. G. Figueroa and E. H. Tanin, "Ability of LIGO and LISA to probe the equation of state of the early Universe," *JCAP* **08** (2019) 011, arXiv:1905.11960 [astro-ph.CO].

[242] C. Caprini and D. G. Figueroa, "Cosmological Backgrounds of Gravitational Waves," *Class. Quant. Grav.* **35** no. 16, (2018) 163001, arXiv:1801.04268 [astro-ph.CO].

[243] V. Sahni, M. Sami, and T. Souradeep, "Relic gravity waves from brane world inflation," *Phys. Rev. D* **65** (2002) 023518, arXiv:gr-qc/0105121.

[244] V. Sahni, "The Energy Density of Relic Gravity Waves From Inflation," *Phys. Rev. D* **42** (1990) 453–463.

[245] S. S. Mishra, V. Sahni, and A. A. Starobinsky, "Curing inflationary degeneracies using reheating predictions and relic gravitational waves," *JCAP* **05** (2021) 075, arXiv:2101.00271 [gr-qc].

[246] **LiteBIRD** Collaboration, T. Hasebe *et al.*, "Sensitivity Modeling for LiteBIRD," *J. Low Temp. Phys.* **211** no. 5-6, (2023) 384–397.

[247] **LiteBIRD** Collaboration, T. Namikawa *et al.*, "LiteBIRD science goals and forecasts: improving sensitivity to inflationary gravitational waves with multitracer delensing," *JCAP* **06** (2024) 010, arXiv:2312.05194 [astro-ph.CO].

[248] K. Inomata, K. Kohri, T. Nakama, and T. Terada, "Gravitational Waves Induced by Scalar Perturbations during a Gradual Transition from an Early Matter Era to the Radiation Era," *JCAP* **10** (2019) 071, arXiv:1904.12878 [astro-ph.CO]. [Erratum: JCAP 08, E01 (2023)].

[249] K. Inomata, K. Kohri, T. Nakama, and T. Terada, "Enhancement of Gravitational Waves Induced by Scalar Perturbations due to a Sudden Transition from an Early Matter Era to the Radiation Era," *Phys. Rev. D* **100** (2019) 043532, arXiv:1904.12879 [astro-ph.CO]. [Erratum: Phys.Rev.D 108, 049901 (2023)].

[250] A. Chakraborty, S. Clery, M. R. Haque, D. Maity, and Y. Mambrini, "Generalizing the Bogoliubov vs Boltzmann approaches in gravitational production," arXiv:2503.21877 [gr-qc].

[251] **CMB-S4** Collaboration, S. Belkner, J. Carron, L. Legrand, C. Umiltà, C. Pryke, and C. Bischoff, "CMB-S4: Iterative Internal Delensing and r Constraints," *Astrophys. J.* **964** no. 2, (2024) 148, arXiv:2310.06729 [astro-ph.CO].

[252] **CMB-S4** Collaboration, K. N. Abazajian *et al.*, "CMB-S4 Science Book, First Edition," arXiv:1610.02743 [astro-ph.CO].

[253] L. Iacconi, H. Assadullahi, M. Fasiello, and D. Wands, "Revisiting small-scale fluctuations in α-attractor models of inflation," *JCAP* **06** no. 06, (2022) 007, arXiv:2112.05092 [astro-ph.CO].

[254] I. Dalianis, A. Kehagias, and G. Tringas, "Primordial black holes from α-attractors," *JCAP* **01** (2019) 037, arXiv:1805.09483 [astro-ph.CO].

[255] J. Garcia-Bellido and E. Ruiz Morales, "Primordial black holes from single field models of inflation," *Phys. Dark Univ.* **18** (2017) 47–54, arXiv:1702.03901 [astro-ph.CO].

[256] M. P. Hertzberg and M. Yamada, "Primordial Black Holes from Polynomial Potentials in Single Field Inflation," *Phys. Rev. D* **97** no. 8, (2018) 083509, arXiv:1712.09750 [astro-ph.CO].

[257] K. Inomata, E. McDonough, and W. Hu, "Amplification of primordial perturbations from the rise or fall of the inflaton," *JCAP* **02** no. 02, (2022) 031, arXiv:2110.14641 [astro-ph.CO].

[258] I. Dalianis, "Features in the Inflaton Potential and the Spectrum of Cosmological Perturbations," *arXiv e-prints* (10, 2023) , arXiv:2310.11581 [astro-ph.CO].

[259] I. Dalianis, G. P. Kodaxis, I. D. Stamou, N. Tetradis, and A. Tsigkas-Kouvelis, "Spectrum oscillations from features in the potential of single-field inflation," *Phys. Rev. D* **104** no. 10, (2021) 103510, arXiv:2106.02467 [astro-ph.CO].

[260] Y.-F. Cai, X.-H. Ma, M. Sasaki, D.-G. Wang, and Z. Zhou, "One small step for an inflaton, one giant leap for inflation: A novel non-Gaussian tail and primordial black holes," *Phys. Lett. B* **834** (2022) 137461, arXiv:2112.13836 [astro-ph.CO].

[261] Y. Aldabergenov, A. Addazi, and S. V. Ketov, "Inflation, SUSY breaking, and primordial black holes in modified supergravity coupled to chiral matter," *Eur. Phys. J. C* **82** no. 8, (2022) 681, arXiv:2206.02601 [astro-ph.CO].

[262] M. Braglia, D. K. Hazra, F. Finelli, G. F. Smoot, L. Sriramkumar, and A. A. Starobinsky, "Generating PBHs and small-scale GWs in two-field models of inflation," *JCAP* **08** (2020) 001, arXiv:2005.02895 [astro-ph.CO].

[263] S. Pi and M. Sasaki, "Primordial black hole formation in nonminimal curvaton scenarios," *Phys. Rev. D* **108** no. 10, (2023) L101301, arXiv:2112.12680 [astro-ph.CO].

[264] X. Wang, Y.-l. Zhang, and M. Sasaki, "Enhanced curvature perturbation and primordial black hole formation in two-stage inflation with a break," *JCAP* **07** (2024) 076, arXiv:2404.02492 [astro-ph.CO].

[265] Z. Zhou, J. Jiang, Y.-F. Cai, M. Sasaki, and S. Pi, "Primordial black holes and gravitational waves from resonant amplification during inflation," *Phys. Rev. D* **102** no. 10, (2020) 103527, arXiv:2010.03537 [astro-ph.CO].

[266] N. E. Mavromatos, V. C. Spanos, and I. D. Stamou, "Primordial black holes and gravitational waves in multiaxion-Chern-Simons inflation," *Phys. Rev. D* **106** no. 6, (2022) 063532, arXiv:2206.07963 [hep-th].

[267] A. Afzal and A. Ghoshal, "Primordial black holes and scalar-induced gravitational waves in radiative hybrid inflation," *Eur. Phys. J. C* **84** no. 9, (2024) 983, arXiv:2402.06613 [astro-ph.CO].

[268] V. C. Spanos and I. D. Stamou, "Gravitational waves and primordial black holes from supersymmetric hybrid inflation," *Phys. Rev. D* **104** no. 12, (2021) 123537, arXiv:2108.05671 [astro-ph.CO].

[269] M. Braglia, A. Linde, R. Kallosh, and F. Finelli, "Hybrid α-attractors, primordial black holes and gravitational wave backgrounds," *JCAP* **04** (2023) 033, arXiv:2211.14262 [astro-ph.CO].

[270] S. Clesse and J. García-Bellido, "Massive Primordial Black Holes from Hybrid Inflation as Dark Matter and the seeds of Galaxies," *Phys. Rev. D* **92** no. 2, (2015) 023524, arXiv:1501.07565 [astro-ph.CO].

[271] Y. Tada and M. Yamada, "Stochastic dynamics of multi-waterfall hybrid inflation and formation of primordial black holes," *JCAP* **11** (2023) 089, arXiv:2306.07324 [astro-ph.CO].

[272] P. Villanueva-Domingo, O. Mena, and S. Palomares-Ruiz, "A brief review on primordial black holes as dark matter," *Front. Astron. Space Sci.* **8** (2021) 87, arXiv:2103.12087 [astro-ph.CO].

[273] B. Carr, K. Kohri, Y. Sendouda, and J. Yokoyama, "Constraints on primordial black holes," *Rept. Prog. Phys.* **84** no. 11, (2021) 116902, arXiv:2002.12778 [astro-ph.CO].

[274] R. Allahverdi *et al.*, "The First Three Seconds: a Review of Possible Expansion Histories of the Early Universe," *The Open Journal of Astrophysics* (6, 2020) , arXiv:2006.16182 [astro-ph.CO].

[275] A. Kalaja, N. Bellomo, N. Bartolo, D. Bertacca, S. Matarrese, I. Musco, A. Raccanelli, and L. Verde, "From Primordial Black Holes Abundance to Primordial Curvature Power Spectrum (and back)," *JCAP* **10** (2019) 031, arXiv:1908.03596 [astro-ph.CO].

[276] R. Murgia, G. Scelfo, M. Viel, and A. Raccanelli, "Lyman-α Forest Constraints on Primordial Black Holes as Dark Matter," *Phys. Rev. Lett.* **123** no. 7, (2019) 071102, arXiv:1903.10509 [astro-ph.CO].

[277] J. Chluba, A. L. Erickcek, and I. Ben-Dayan, "Probing the inflaton: Small-scale power spectrum constraints from measurements of the CMB energy spectrum," *Astrophys. J.* **758** (2012) 76, arXiv:1203.2681 [astro-ph.CO].

[278] C. T. Byrnes, P. S. Cole, and S. P. Patil, "Steepest growth of the power spectrum and primordial black holes," *JCAP* **06** (2019) 028, arXiv:1811.11158 [astro-ph.CO].

[279] R. Mahbub, "Primordial black hole formation in α-attractor models: An analysis using optimized peaks theory," *Phys. Rev. D* **104** no. 4, (2021) 043506, arXiv:2103.15957 [astro-ph.CO].

[280] K. Sravan Kumar and P. Vargas Moniz, "Conformal GUT inflation, proton lifetime and non-thermal leptogenesis," *Eur. Phys. J. C* **79** no. 11, (2019) 945, arXiv:1806.09032 [hep-ph].

[281] L. Husdal, "On Effective Degrees of Freedom in the Early Universe," *Galaxies* **4** no. 4, (2016) 78, arXiv:1609.04979 [astro-ph.CO].

[282] K. Saikawa and S. Shirai, "Primordial gravitational waves, precisely: The role of thermodynamics in the Standard Model," *JCAP* **05** (2018) 035, arXiv:1803.01038 [hep-ph].

[283] S. Hannestad, "What is the lowest possible reheating temperature?," *Phys. Rev. D* **70** (2004) 043506, arXiv:astro-ph/0403291.

[284] F. L. Bezrukov and D. S. Gorbunov, "Distinguishing between R^2-inflation and Higgs-inflation," *Phys. Lett. B* **713** (2012) 365–368, arXiv:1111.4397 [hep-ph].

[285] D. S. Gorbunov and A. G. Panin, "Scalaron the mighty: producing dark matter and baryon asymmetry at reheating," *Phys. Lett. B* **700** (2011) 157–162, arXiv:1009.2448 [hep-ph].

[286] H. Jeong, K. Kamada, A. A. Starobinsky, and J. Yokoyama, "Reheating process in the R^2 inflationary model with the baryogenesis scenario," *JCAP* **11** (2023) 023, arXiv:2305.14273 [hep-ph].

[287] T. Kokubu, K. Kyutoku, K. Kohri, and T. Harada, "Effect of Inhomogeneity on Primordial Black Hole Formation in the Matter Dominated Era," *Phys. Rev. D* **98** no. 12, (2018) 123024, arXiv:1810.03490 [astro-ph.CO].

[288] D. N. Page, "Particle Emission Rates from a Black Hole: Massless Particles from an Uncharged, Nonrotating Hole," *Phys. Rev. D* **13** (1976) 198–206.

[289] D. Hooper, G. Krnjaic, and S. D. McDermott, "Dark Radiation and Superheavy Dark Matter from Black Hole Domination," *JHEP* **08** (2019) 001, arXiv:1905.01301 [hep-ph].

[290] G. W. Gibbons and S. W. Hawking, "Action Integrals and Partition Functions in Quantum Gravity," *Phys. Rev. D* **15** (1977) 2752–2756.

[291] J. W. York, Jr., "Role of conformal three geometry in the dynamics of gravitation," *Phys. Rev. Lett.* **28** (1972) 1082–1085.

[292] Y. B. Zel'dovich, "Gravitational instability: An approximate theory for large density perturbations.," *Astron. & Astrophys.* **5** (Mar., 1970) 84–89.

[293] M. Shibata and M. Sasaki, "Black hole formation in the Friedmann universe: Formulation and computation in numerical relativity," *Phys. Rev. D* **60** (1999) 084002, arXiv:gr-qc/9905064.

[294] A. Kehagias, D. Perrone, and A. Riotto, "Why the universal threshold for primordial black hole formation is universal," *Class. Quant. Grav.* **42** no. 5, (2025) 055010, arXiv:2405.05208 [astro-ph.CO].

[295] T. Harada, C.-M. Yoo, and Y. Koga, "Revisiting compaction functions for primordial black hole formation," *Phys. Rev. D* **108** no. 4, (2023) 043515, arXiv:2304.13284 [gr-qc].

[296] The GRChombo Collaboration, "Grchombo." https://www.grtlcollaboration.org/.

[297] J. C. Aurrekoetxea, K. Clough, and F. Muia, "Oscillon formation during inflationary preheating with general relativity," *Phys. Rev. D* **108** no. 2, (2023) 023501, arXiv:2304.01673 [gr-qc].

[298] D. Baumann, "Inflation," in *Theoretical Advanced Study Institute in Elementary Particle Physics: Physics of the Large and the Small*, pp. 523–686. 2011. arXiv:0907.5424 [hep-th].

[299] D. Baumann, "TASI Lectures on Inflation," *arXiv e-prints* (July, 2009) arXiv:0907.5424, arXiv:0907.5424 [hep-th].

[300] M. A. G. Garcia, K. Kaneta, Y. Mambrini, and K. A. Olive, "Inflaton Oscillations and Post-Inflationary Reheating," *JCAP* **04** (2021) 012, arXiv:2012.10756 [hep-ph].

[301] J. A. R. Cembranos, A. L. Maroto, and S. J. Núñez Jareño, "Cosmological perturbations in coherent oscillating scalar field models," *JHEP* **03** (2016) 013, arXiv:1509.08819 [astro-ph.CO].

[302] V. Mukhanov, *Physical Foundations of Cosmology*. Cambridge University Press, Oxford, 2005.

[303] A. de la Macorra and H. H. Vucetich, "Causality, stability and sound speed in scalar field models," arXiv:astro-ph/0212302.

[304] O. F. Piattella, J. C. Fabris, and N. Bilić, "Note on the thermodynamics and the speed of sound of a scalar field," *Class. Quant. Grav.* **31** (2014) 055006, arXiv:1309.4282 [gr-qc].

[305] A. Aviles and J. L. Cervantes-Cota, "Dark degeneracy and interacting cosmic components," *Phys. Rev. D* **84** (2011) 083515, arXiv:1108.2457 [astro-ph.CO]. [Erratum: Phys.Rev.D 84, 089905 (2011)].

[306] G. B. Arfken and H. J. Weber, *Mathematical methods for physicists; 4th ed.* Academic Press, San Diego, CA, 1995. https://cds.cern.ch/record/379118.

[307] S. Banerjee, T. Papanikolaou, and E. N. Saridakis, "Constraining F(R) bouncing cosmologies through primordial black holes," *Phys. Rev. D* **106** no. 12, (2022) 124012, arXiv:2206.01150 [gr-qc].

[308] J. D. Barrow and B. J. Carr, "Primordial black hole formation in an anisotropic Universe.," *Mon. Not. R. astr. Soc.* **182** (Feb., 1978) 537–558.

[309] J. R. Klauder, ed., *MAGIC WITHOUT MAGIC - JOHN ARCHIBALD WHEELER. A COLLECTION OF ESSAYS IN HONOR OF HIS 60TH BIRTHDAY*. Freeman, San Francisco, 1972.

[310] C. W. Misner, K. S. Thorne, and J. A. Wheeler, *Gravitation*. W. H. Freeman, San Francisco, 1973.

[311] A. G. Doroshkevich, "Spatial structure of perturbations and origin of galactic rotation in fluctuation theory," *Astrophysics* **6** (1970) 1573–8191.

[312] T. Harada, C.-M. Yoo, K. Kohri, and K.-I. Nakao, "Spins of primordial black holes formed in the matter-dominated phase of the Universe," *Phys. Rev. D* **96** no. 8, (2017) 083517, arXiv:1707.03595 [gr-qc]. [Erratum: Phys.Rev.D 99, 069904 (2019)].